MANCHESTER 1824
The University of Manchester

2D Materials Complex Architectures for Energy Applications

A thesis submitted to

The University of Manchester

For the degree of

Doctor of Philosophy

In the Faculty of Science and Engineering

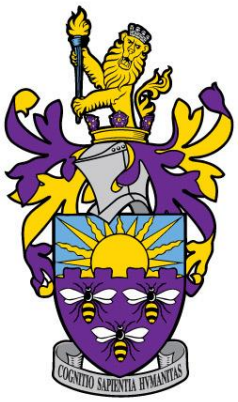

2021

Wenji Yang

School of Natural Sciences, Department of Materials

List of Contents

List of Figures*

***Please note that the figures for each manuscript are self-contained, and thus not listed here.**

List of Tables*

***Please note that the tables for each manuscript are self-contained, and thus not listed here.**

List of Abbreviations*

2D	Two dimensional
3D	Three dimensional
MILD	Minimally invasive layer delamination
MOF	Metal organic frameworks
COF	Covalent organic frameworks
BN	Boron nitride
GaN	Gallium nitride
DFT	Density functional theory
CVD	Chemical vapor deposition
EES	Electrochemical energy storage
EDLCs	Electrical double-layer capacitors
PPy	Polypyrrole
CNT(s)	Carbon nanotube(s)
RGO/rGO	Reduced graphene oxide
LDH	Layered double hydroxide
CV	Cyclic voltammetry
EMI-TFSI	(1-ethyl-3methylimidazolium bis(trifluoromethylsulfonyl) imide
LIB(s)	Lithium-ion battery(ies)
PVP	Polyvinylpyrrolidone
G'	Elastic (storage) modulus
G''	Viscous (loss) modulus
AM	Additive manufacturing
SLA	Sterolithography
SLS	Selective laser sintering
GO	Graphene oxide
DIB	1,3-diisopropenylbenzene
SAP	Superabsorbent polymer
EG	Exfoliated graphene
PANI	Polyaniline
CN	Cellulose nanofiber

SEM	Scanning electron microscopy
EDS/EDX	Energy dispersive X-ray spectroscopy
XRD	X-ray diffraction
MSC(s)	Micro-supercapacitor(s)
CC	Current collector
SI	Supporting(Supplementary) information
AFM	Atomic force microscopy
BET	Brunauer-Emmett-Teller
SSA	Specific surface area
PVA	Poly (vinyl alcohol)
GCD	Galvanostatic charge-discharge
EIS	Electrochemical impedance spectroscopy
ESR	Equivalent series resistance
XCT	X-ray computed tomography
FaTC	Freeze-assisted tape casting
DIW	Direct-ink writing
TEM	Transmission electron microscopy
STEM	Scanning transmission electron microscope
HRTEM	High resolution TEM
PDF	Powder diffraction file
HDPE	High density polyethylene
DI	Deionized
CCD	Charge-coupled device
EDXRF	Energy-dispersive X-ray fluorescence
***h*BN**	Hexagonal boron nitride
THT	$Ti_3C_2T_x$-*h*BN-$Ti_3C_2T_x$
EC	Ethylene carbonate
DEC	Diethyl carbonate
PET	Polyethylene terephthalate

2D Materials Complex Architectures for Energy Applications

A these submitted to The University for the degree of Doctor of Philosophy (PhD) in the Faculty of Science and Engineering

2021

Wenji Yang

Department of Materials, School of Natural Sciences

Abstract

Graphene, Mxene and related 2D materials have the potential to open new engineering opportunities in a wide range of technological applications. In particular, 2D materials could provide an alternative to conventional electrode materials by improving the storage capacity and lifetimes of energy storage devices. However, the practical application of these materials in energy will require assembly into 3D structures with tuned architectures to truly maximise their available surface area for reactions, fluid transport or the distribution of functional sites. This research project focuses on the development of novel electrode materials with multi-scale architectures via advanced manufacturing approaches such as 3D printing, freeze casting and tape casting. Overall, the study will comprise the following endeavours: 1) fundamental research on the synthesis, chemical stability, and rheological properties of 2D materials: MXene; 2) Design of novel inks with optimized viscoelastic performance for freeze casting, tape casting and extrusion-based printing; 3) Investigate the structure-property evolution of the material during and after manufacturing via advanced characterization techniques; 4) Study of the electrochemical performance of relevant electrodes in energy storage devices (supercapacitor).

Declaration

I hereby declare that no portion of this work referred to in the thesis has been submitted in support of an application for another degree or qualification of this or any university or other institute of learning.

Copyright Statement

Acknowledgements

Firstly, I would like to extend my sincere gratitude to my supervisors, Prof. Suelen Barg and Prof. Sarah Haigh. Having had no experience outside of China, Suelen helped me to climatise to a new culture and environment. She has continued to inspire me to push the limitations of research in the area and provided me with the platform to freely be creative in my approach to my research. I would also like to thank Sarah, for introducing me the field fo transmission electron microscopy and extending an invitation to expand my skillset within this field.

I would also like to thank the University of Manchester, as I was honoured to be selected to be on a Presidential Doctorate Scholarship. It was enriched my experience as a PhD student, and I was grateful to be part of a rewarding community.

I am grateful to my parents and my family for their unconditional love and continuing support throughout my studies.

I would like to convey my appreciation towards those I have collaborated with during my time in Manchester. I especially thank Mr. Jae Jong Byun, Mr. Jie Yang, Mr. Francis Moissinac, Dr. Yudong Peng, and Dr. Pei Yang for the discussion we have had, from which we have shared our knowledge, idea and experience.

My colleges have established a welcoming and comfortable working environment, and I would like to sincerely thank their patience and generosity especially during difficult times.

Finally, I would like to thank the committee members for their valuable time for reading, reviewing and discussing of my thesis.

Publications

1. **W. Yang**, J. J. Byun, J. Yang, F. P. Moissinac, Y. Ma, H. Ding, W. Sun, R. A. W. Dryfe, S. Barg, **All-in-one MXene-Boron Nitride-MXene "OREO" with Vertically Aligned Channels for Flexible Structural Supercapacitor Design** [J]. *ACS Applied Energy Materials*, 2021, 4: 7959-7972. (Included as Chapter 5)

2. Y. Peng, J. Cao, Y. Sha, **W. Yang**, L. Li, Z. Liu, **Laser Solid-phase Synthesis of Single-atom Catalysts** [J]. *Light: Science & Applications*, 2021, 10:168.

3. M. Greaves, M. Nebde, J. Wang, **W. Yang**, S. Barg, **Rheological Characteristics of 2D Titanium Carbide (MXene) Dispersions: Better Than We Thought** [J]. *Journal of Materials Research*, 2021, doi.org/10.1557/s43578-021-00282-7.

4. **W. Yang**, J. J. Byun, J. Yang, F. P. Moissinac, Y. Peng, G. Tontini, R. A. W. Dryfe, S. Barg, **Freeze-assisted Tape Casting of Vertically Aligned MXene Films for High Rate Performance Supercapacitors** [J]. *Energy Environmental Materials*, 2020, 3: 380-388. (Included as Chapter 4)

5. J. Yang, J. Cao, Y. Peng, **W. Yang**, S. Barg, Z. Liu, I. A. Kinloch, M. A. Bissett, R. A. W. Dryfe, **Unravelling the Mechanism of Rechargeable Aqueous Zn-MnO_2 Batteries: Implementation of Charging Process by Electrodeposition of MnO_2** [J]. *ChemSusChem*, 2020, 13: 1-9.

6. Y. Peng, J. Cao, J. Yang, **W. Yang**, C. Zhang, X. Li, R. A. W. Dryfe, L. Li, I. A. Kinloch, Z, Liu, **Laser Assisted Solution Synthesis of High Performance Graphene Supported Electrocatalysts** [J]. *Advanced Functional Materials*, 2020, 30: 2001756.

7. **W. Yang**, J. Yang, J. J. Byun, F. P. Moissinac, J. Xu, S. J. Haigh, M. Domingos, M. A. Bissett, R. A. W. Dryfe, S. Barg. **3D printing of freestanding MXene architectures for current-collector-free supercapacitors** [J]. *Advanced Materials*, 2019: 1902725. (Included as Chapter 3)

8. H. Li, L. Jiang, Q. Feng, Z. Huang, H. Zhou, Y. Gong, Z. Hou, **W. Yang**, C. Fu, Y. Kuang. **Ultra-fast transfer and high storage of Li^+/Na^+ in MnO quantum dots@ carbon hetero**

nanotubes: Appropriate quantum dots to improve the rate [J]. *Energy Storage Materials*, 2019, 17: 157-166.

9. H. Li, S. Ma, H. Cai, H. Zhou, Z. Huang, Z. Hou, J. Wu, **W. Yang**, H. Yi, C. Fu, Y. Kuang. **Ultra-thin Fe3C nanosheets promote the adsorption and conversion of polysulfides in lithium-sulfur batteries** [J]. *Energy Storage Materials*, 2019, 18: 338-348.

10. Z. Huang, H. Pan, **W. Yang**, H. Zhou, N. Gao, C. Fu, S. Li, H. Li, Y. Kuang. ***In situ*** **self-template synthesis of Fe-N-doped double-shelled hollow carbon microspheres for oxygen reduction reaction** [J]. *ACS nano*, 2018, 12(1): 208-216.

Chapter 1. General Introduction

1.1 Background

Dimensionality is a word referring to the number of independent space-time coordinates. Two-dimension (2D) is essentially a plane made of length and width, and thus materials, which only have two dimensions, are denoted as 2D materials. P.R. Wallace theorised the concept of single carbon layer and Hanns-Peter Boehm introduced the term 'graphene' in 1986 [1]. Geim's research group from the University of Manchester was the first to isolate 2D graphene from graphite in 2004, which lead to the increase in popularity of 2D materials in academia and industry. Concurrently, a diverse family of 2D materials started to be explored, including transition metal carbides/nitrides or carbonitrides (e.g. $Ti_3C_2T_x$, Ti_3CNT_x) [2], Xenes (e.g. borophene, germanene, stanene) [3], organic materials [4], transition metal dichalcogenide (TMD) [5] and Nitrides [6], etc. They all have certain similarities: 1) Generally, the scale of their third dimension is comprised of a single to a few atomic layers i.e. 2D; 2) their specific ordered structure; 3) their structure is extended in the 2D plane from nano to micrometre scale.

In terms of 2D materials with a single atomic layer, almost all the atoms are exposed, remarkably increasing the atomic efficiency. One of the eventual goals with 2D materials has been to control their energy band structure and electrical properties to optimize performance characteristics for targeted applications. This can be achieved through exfoliation of multilayer 2D materials and post-treatment processes such as, functionalisation through heteroatom doping, inducing defects or used as an additive in composites. 2D materials can be utilised as a conductor, a semi-conductor, or an insulator. Additionally, they can be chemical inert but also can be modified by other chemicals. All of the aforementioned, 2D materials have potential when it comes to exploiting their distinct novel properties as graphene has done in different chemical, physical, electronic and optical fields within applications such as electronic/photonic, energy storage, energy conversion and, sensory devices.

Every 2D material, has their corresponding precursors, which is typically a laminated structure composed of layers of the respective 2D material, where electrostatic force plays an important bonding role between each layer, such as graphite with graphene, and MAX Phase with MXene [7]. Notwithstanding, the converse is possible in which isolated atomic planes can also be

reassembled layer by layer to grow heterostructures, which demonstrates the attractive nature of 2D materials and the many mysteries yet to be discovered within this field [8].

The transition from the 3D precursor to the 2D material leads to significant changes in properties. For example, the electronic property can be augmented due to the confinement of the electrons in the 2D plane, while strong in-plane covalent bonds and atomic-layer thickness contributes to the excellent mechanical property, optical transparency, and flexibility. Further, the obtained 2D layer has an expansive specific surface area and large aspect ratio of lateral size to thickness with some defects or terminal groups on the surface. Although this increase in surface area enhances the potential for functional efficiency, it also makes the 2D materials unstable. According to the second law of thermodynamics, the nano-thin flake needs to rid itself of the energy by spontaneous agglomeration in order to reach a stable state [9]. For applications in energy storage or conversion devices, this phenomenon would severely affect electrolyte ion transportation and expose less surface active sites. In order to address this challenge, most of the research focuses on improving the stability of the 2D materials modification during or after the exfoliation process from precursors. So far, several methods have been used and listed as follows:

1) The addition of surfactant. In this way, zeta potential in the dispersion would be changed, consequently avoid the agglomeration to some extent [10].
2) Functionalization of 2D materials' surface/edges by heteroatomic doping or defect manipulation [11,12].
3) Changing the morphological shape of the 2D materials [13].
4) Post-manufacturing process like freeze drying [14].

Specifically, MXene is a typical 2D material exfoliated from a three-dimensional (3D) bulk precursor. Therefore, re-agglomeration after delamination also needs to be prevented. In 2015, Yan et al. reported the mixture of $Ti_3C_2T_x$ and carbon nanotubes (CNTs) suspensions. In this way, one-dimensional material CNTs between individual $Ti_3C_2T_x$ layers could impede the restacking of the 2D sheets [15]. Alternatively, additive manufacturing is another method used in graphene research to build 3D microstructures to prevent agglomeration. In regard to MXenes, it is still a comparatively new type of material. Therefore, there are only a few related works reported about 3D printing and the fundamental development of MXene based inks. Thus, the 3D printing of MXene is explored in this thesis. Conventionally, electrode fabrication of 2D sheets easily causes restacking of the material, which limits the electrochemical

performance of the energy storage devices. In the same year, Hu et al. investigated one facile 'dropping-mild-baking' method to acquire $Ti_3C_2T_x$ film-coated nickel foam and used it directly as the electrode for supercapacitors. By assembling the $Ti_3C_2T_x$ flakes on the nickel skeleton, restacking problems can be somewhat mitigated [16], but when the loading/thickness of the materials on the foam increase, it is still hard to ensure there is no/partial agglomeration. In 2018, Xia et al. proposed a mechanical shearing method and obtained vertically aligned liquid crystalline MXenes, which can make the thickness of the electrode increase to about 200 micrometres without suffering too much with regards to electrochemical performance. Although the method showed promising results, it is hard to scale up to the industrial production level. As shown in Bayram's work, freeze casting was chosen to build tuneable MXene aerogels with lamellae architectures. After freeze-drying, the structure shows porous channels after the removal of ice-template [17]. Based on their work on freeze casting MXene structures, fabrication of vertical alignment within the electrode microstructure is investigated using freeze-assisted tape-casting manufacturing method, which combines conventional tape-casting with freeze-casting technologies.

1.2 Research Objectives

Investigation of fundamental characteristics is the precondition required before successive research in functionalizing and using those 2D materials. In addition to this, the structural design and manufacturing methods for the products are also important factors to be considered. In this study, $Ti_3C_2T_x$, one of the MXenes demonstrating promising potential across the literature, is chosen as the material of interest due to its good electric conductivity and excellent electrochemical performance for energy storage applications. 3D printing and tape casting are selected for further structural design and manufacturing. Thus, the study of the rheological and mechanical properties of $Ti_3C_2T_x$ also becomes a necessary part of this research. The specific objectives of the thesis are listed below:

1) To synthesize delaminated $Ti_3C_2T_x$ flakes from Ti_3AlC_2 MAX phases of different quality and primary flake sizes (purchased from different companies) and the development of their inks for colloidal processing.
2) To investigate the effect of $Ti_3C_2T_x$ flake size and the concentration on the rheological properties of inks and slurries and so establish suitable formulations for 3D printing and freeze-assisted tape casting (FaTC).

3) To establish a processing route to build 3D architectures of complex shape with $Ti_3C_2T_x$ based on 3D printing and investigate the corresponding processing parameters to enable manufacturing such as needle size, printing speed, printing gap etc.
4) To develop a processing route based on tape and freeze casting for the fabrication of electrode films with a vertical arrangement of 2D materials and investigate the effect of film thickness on the performance of electrodes.
5) To establish if electrochemical performance of electrode films is improved by the internal microstructural alignment of 2D materials produced via FATC and how this related to thickness.
6) To develop an all-in-one multi-material supercapacitor device demonstrator based on FaTC, and to investigate its electrochemical performance and mechanical property.

1.3 Thesis Structure

The aim of this PhD study is to develop the processing capabilities to build a three-dimensional architecture based on $Ti_3C_2T_x$. This would involve developing inks/slurries using the two-dimensional material and studying the rheological properties. The project started with developing a basic understanding of the synthesis method of delaminated $Ti_3C_2T_x$, looking at different flake sizes. Then, with the delaminated $Ti_3C_2T_x$, apply two manufacturing approaches: the direct ink writing method (3D Printing) and freeze-assisted tape casting (FaTC) to fabricate 3D architectures. This, in turn, prevented the agglomeration of the 2D material and facilitated electrochemical reactions. The manuscripts and data in this thesis consist of three separate papers already published or under review in three different peer-reviewed journals (in sequence: *Advanced Materials*, *Energy Environmental Materials* and *ACS Applied Energy Materials*), which have self-contained figures, tables and citations. These works and results were mainly completed by the first author with some assistance from the collaborators. The contributions are clarified at the beginning of each corresponding chapters.

The thesis constitutes of six chapters, and they are as follows:

Chapter 1. Introduction. An overview of the thesis and a brief introduction of the work carried out in this project, including the selection of materials, manufacturing techniques and fields of application, as well as highlighting some existing problems and solutions.

Chapter 2. Literature Review. This chapter provides an introduction to 2D materials development (characteristics, synthesis methods, modification etc.) along with their research

evolution and applications. An introduction to MXenes is provided with focus on $Ti_3C_2T_x$. Subsequently a brief introduction of the manufacturing methods/designs for electrode and the energy storage configuration, including additive manufacturing and freeze-assisted tape-casting is outlined.

Chapter 3. 3D printing of Freestanding MXene Architectures for Current Collector-Free Supercapacitors. In this chapter, the MILD (minimally invasive layer delamination) method was used to obtain single/few-layer $Ti_3C_2T_x$ flakes with average 8 μm lateral size. $Ti_3C_2T_x$ aqueous inks with different concentrations were prepared and studied to reach the rheological performance required in additive manufacturing: 3D printing. By adjusting the storage and loss modulus of the corresponding inks with the printing parameters, it was the first time 3D printing of additive-free MXene was accomplished in this research area. The printed structure is able to retain its original structure, even reaching over 25 layers without collapsing. The printed intercalated electrode can be assembled to a micro-supercapacitor with the addition of solid electrolyte and connecting silver wire leads.

Chapter 4. Freeze-assisted Tape Casting of vertically aligned MXene films for high rate performance supercapacitors. In this chapter, delaminated $Ti_3C_2T_x$ with ~3.7 μm flake size was synthesized by the MILD method but with different reaction temperature and etchant/precursor ratio. Freeze-assisted tape-casting was used to build the vertically aligned microstructure for the $Ti_3C_2T_x$ electrode, followed by freeze-drying. The chosen manufacturing route facilitated the retention of the delaminated state of the 2D material after exfoliation whilst the resultant the designed structure can facilitate the transportation of the electrolyte ions, thus improving the rate performance. In the case of increasing the thickness from 150 μm to 700 μm of the electrode, the specific capacitance was maintained at a fixed scan rate.

Chapter 5. All-in-one Mxene-Boron Nitride-Mxene "OREO" for flexible supercapacitor design with integrated structural and functional properties. In this chapter, combining the same manufacturing method for the electrode in **Chapter 4**, an all-in-one integrated supercapacitor configuration was presented, in which fabrication and assembly of the electrodes and separator were simultaneous. The device was able to function immediately after applying electrolyte and connecting circuitry without further processing. In this way, freestanding $Ti_3C_2T_x$ films have a good bonding with the boron nitride separator. Thus, the symmetric supercapacitor cell can accomplish independently from the structural material to create a structural supercapacitor. This allows for a minimalistic design philosophy and

mutability in which the electrochemical energy storage device itself provides some form of the structural framework of the product whilst facilitating a function.

Chapter 6. Conclusions and Perspectives. The final chapter consists of a summary of these projects, further consideration, and viewpoints about future improvement.

Chapter 2. Literature Review

Overcoming developmental hurdles in translating novel research into practical solutions to address environmental concerns and energy accessibility has been a recent pith of societal technological sustainability. With an urgent requirement for clean and sustainable energy sources such as hydrogen, wind and solar a complementary need for specialised storage devices that accounts for system variability is essential.

Among energy storage technologies, electrochemical energy storage systems, such as batteries [18,19], supercapacitors [20,21] and their hybrid devices [22,23] are considered to be promising ways to build sustainable energy systems in which generated electrical energy can be converted by relatively efficient electrochemical reactions into chemical energy via electron and ion transfer in electrodes. These devices can be used to power electric vehicles, portable electronic devices and aircrafts, etc. However, the performance of existing electrochemical energy storage devices cannot meet the growing demand for large-scale energy storage solutions. This is because they are unable to provide both high power density and high energy density. In order to tackle this issue, it is urgent to seek new materials with better performance and new efficient manufacturing technologies for energy storage systems [24,25].

Three-dimensional (3D) printing has attracted much attention for the fabrication of advanced functional materials, novel frameworks and complex systems, with broad applications for energy storage in recent years [26,27]. The development of inks is an essential component for 3D printing. It relates to the materials, the printing method, and the structures of the final 3D-printed products. MXenes, 2D transition-metal carbides and nitrides, have shown promising properties for energy storage capacitance [28,29]. However, highly stacked MXene flakes cannot fully exhibit their merits. If we can build tuned porous networks through 3D printing, this will increase the specific surface area and be beneficial to the infiltration of electrolyte to achieve enhanced energy storage capabilities.

2.1 Introduction to 2D material

2.1.1 Introduction

Since graphene's discovery in 2010, its marketing towards the general public and important impact in academic research culminated in the Nobel Prize for its discovery. Researchers began

to explore its supreme mechanical, electrical and thermal characteristics. Concurrently, a large number of novel 2D materials were developed and altered scientists' perceptions of materials in the material science field, amongst many others. Looking at elemental distribution on the periodic table, those 2D materials mainly contain at least one of the atoms from a transition metal, carbon group, chalcogens etc. Similar to graphene, those materials have completely different emergent properties compared with their corresponding bulk phase precursors. Single layer 2D materials have almost all the surficial atoms exposed which consequently leads to higher atomic efficiencies. The energy band structure and electronic characteristics can be easily controlled by regulating thickness and heteroatomic doping. They can act as conductor, semi-conductor, as well as insulator. Interestingly, with regards to chemical activity, they can be modified by other chemicals but also can exhibit chemical inertness. In summary, they have three key advantages which is as follows:

1) They are conducive to chemical modification, which can adjust the electronic or electrochemical performance.
2) Their structures are more beneficial to electron transportation as opposed to bulk crystals, which can contribute to enhanced performance capabilities of the related electronics or energy storage devices.
3) They have high flexibility and transparency, which have prospects in the field development of wearable smart devices and flexible energy storage.

Apart from graphene, there are five primary groups of 2D materials: MXenes, Xenes, Organic materials, Transition Metal Dichalcogenides (TMDC) and Nitrides. They are hot topics in the scientific community (shown in **Fig. 2-1** and **Fig. 2-2**).

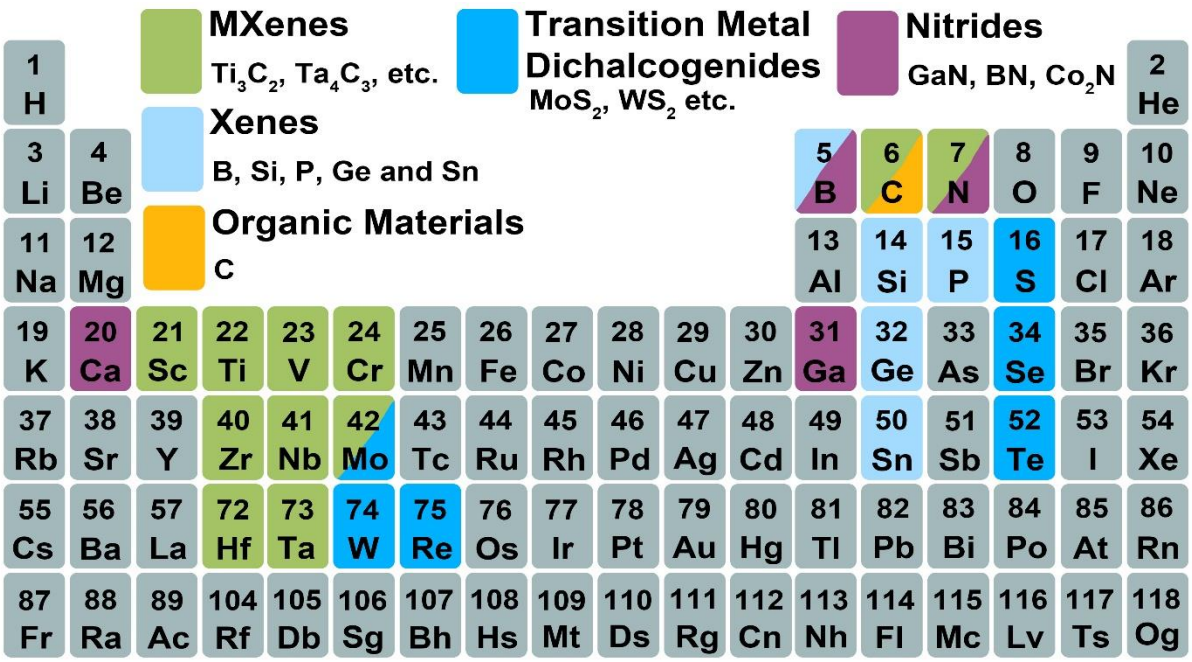

Figure 2- 1 Five primary categories of 2D materials.

After the exploration of graphene, elements adjacent to carbon have been explicitly explored such as boron, silicon, phosphorus, germanium and tin etc. and referred to as Xenes, where X represents the element and -ene is from graphene. These materials' atoms are arranged as buckled sheets in a honeycomb pattern. Xene's bandgap and charge-transport properties make them candidates for fast, flexible electronics and energy storage devices. In 2015, researchers from America and Italy collaborated and prepared the super-thin two-dimensional silene by Al_2O_3 capping [30]. With regards to organic materials, studies are being focused on 2D metal-organic frameworks (MOF), and covalent organic frameworks (COF), which can be obtained by sonication or ion exchange techniques to delaminate MOFs or COFs with weak force [31]. Those covalent organic frameworks and other organic compounds are promising candidates for nanoporous filters and membranes, biosensors and optoelectronic devices. MoS_2 and WS_2 represent another kind of 2D material, which is called Transition Metal Dichalcogenides (TMDC) [32]. Due to their pronounced band gaps, these sheet-like semiconductors have been used to fabricate transistors and have seen significant development in lightweight integrated electronic devices applications as the key components in the circuits for lightweight, etc. However, the scalability of production has been a problem. The fourth type of 2D materials are nitrides, which include boron nitride (BN), gallium nitride (GaN) and so on. This group of materials has potential as both an electrical insulators or/and conductors that could be used in

high-speed, transparent, flexible electronics [33]. The last group of 2D materials, which will be the main focus of this thesis is, MXene.

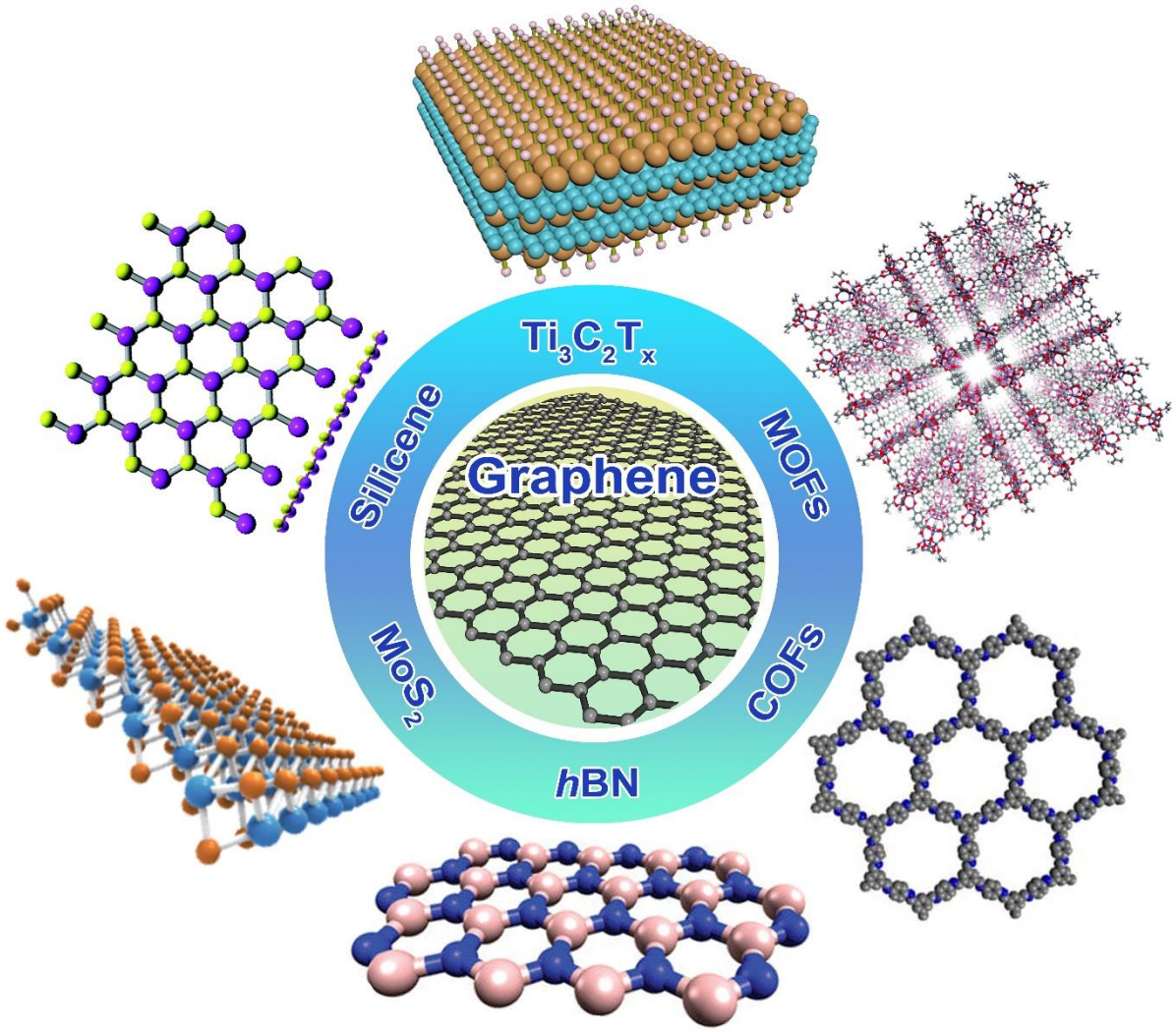

Figure 2- 2 Six more representative 2D materials except for graphene from five primary categories.

2.1.2 MXenes

Ten years ago, a new class of two-dimensional (2D) early transition metal carbides, nitrides or carbonitrides with laminated micro-structure, was discovered and named as MXene (pronounced "max-enes") [34,35]. The general formula for MXene is $M_{n+1}X_nT_x$ (n=1-3), where n+1 layers of M, which represents the early transition metal such as Sc, Ti, Zr, V, Nb, Cr and Mo, are interleaved (interspersed) with n layers of carbon or nitrogen (X). The T_x bonds are present on the outer M layers, representing the surface terminations, such as oxygen (O), hydroxyl (OH), fluorine (F) and/or chlorine (Cl) atoms. The first member from the big family of MXene: $Ti_3C_2T_x$, was first synthesized at the University of Drexel in Professor Yury

Gogotsi's group with Professor Michel W. Barsoum. Thus far, over 70 % of MXene related works have focused primarily on $Ti_3C_2T_x$. At least 100 stoichiometric MXene compositions and a large amount of solid solutions can offer not only unique combinations of properties but also methods to tune their characteristics by changing the ratios of M or X elements [34].

In Gogotsi's group, during the early stages researchers were working on the selective etching method to prepare 2D materials. In 2006, a Nano Letter publication showed the synthesis of 5-10 nm thickness SiC laminated nanosheets from the anisotropic etching of bulk SiC [36]. In the same way, MXenes also originated from this type of selective etching. MAX phase is one kind of laminated ceramic material, where M, A and X represents a transition metal, an atom from group IIIA or IVA on the periodic table and carbon/nitrogen, respectively [28]. Due to the co-existence of strong covalent bond and metallic bond between the layers in structure, MAX phase is hard to be exfoliated, unlike graphite, which is maintained by comparatively weaker Van der Waals's force. MAX phases have a layered hexagonal structure with P63/mmc symmetry, in which the M layers are closed packed, the X atoms fill the octahedral sites, and the layers of "A" atoms interleave in $M_{n+1}X_n$ layers. Compared with M–X bonds, the M–A bonds are weaker [37]. Thus, by taking advantage of the differences in character and relative strengths of M–A and M–X bonds, the "A" atoms layers can be selectively etched chemically without destroying the M–X bonds (as shown in **Fig. 2-3**). Michael Nguib from Gogotsi's group placed the Ti_3AlC_2 into HF solution and found that the Al was etched by HF and leaving behind Ti_3C_2. After density functional theory (DFT) calculations, it was confirmed that Ti_3C_2 has a stable configuration and possesses metallic properties. Microstructural characterization further supports the observed 2D laminated structure. This work has been firstly published in the Journal of Advanced Materials, where they announced the birth of the first MXene: $Ti_3C_2T_x$ [35]. Since MXene (Ti_3C_2) was first reported in 2011, more than 70 kinds of MAX phases have been successfully synthesized in experiments [38]. MXene has been confirmed to show exceptional properties, including metallic conductivity (up to 6,500 S cm^{-1}), surface hydrophilicity, and excellent ion intercalation behaviour [39]. This new family has shown promise in a wide array of applications, particularly $Ti_3C_2T_x$, which exhibits great application potential in batteries and supercapacitors for electrochemical energy storage.

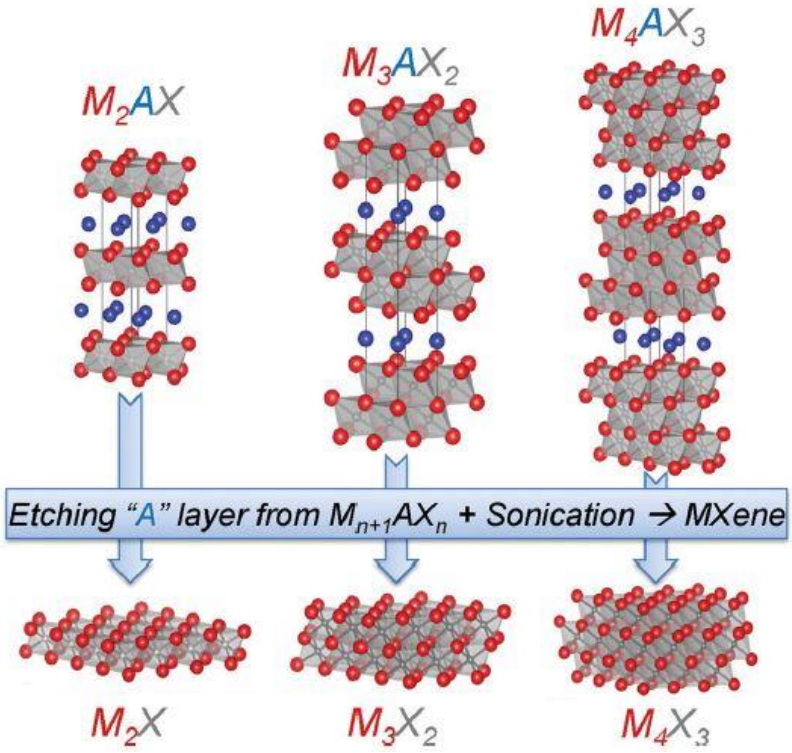

Figure 2- 3 Structure of MAX phases and the corresponding MXenes [40].

2.1.3 Structure of MXenes

It is important to investigate the MXene structures in order to understand the potential of their properties. MXene can be seen as stacked layers of hexagonal MAX phases without the A atoms layer, which is similar to graphene flakes. After selectively extracting the A layer, the M atoms are arranged in close-packed arrays while the X atoms occupy the body centre of MX octahedrons [40]. In reality, pure MXenes without surface terminating groups is hard to synthesize experimentally without any post-processing because of the use of fluoride/chloride-based etchants. The as-prepared MXenes by selective etching will always possess a O, OH, F, and/or Cl terminating groups. Meanwhile, OH functional groups are not stable since the H atoms can be replaced by alkali metals (such as Li, Na and K), alkaline earth metals (such as Mg and Ca) or transition metals (such as Pb) and can be removed at high temperature (-OH groups transforms into -O groups). Therefore, the surface chemistry of MXene would be complex with a heterogeneous/homogeneous dispersion of terminating groups, thus understanding the surface groups of MXene is particularly important as it is impossible to avoid the surface functionalization in experiments. In previous work, Zhou's group first reported two distinct configurations (I and II in **Fig. 2-4**) based on $Ti_3C_2T_2$ [28]. For configuration I, the T groups point directly toward the Ti atoms on both sides of the $Ti_3C_2T_2$ layers. For configuration

II, the T groups are positioned above the C atoms on both sides of the $Ti_3C_2T_2$ layers. Besides, there is a mixed structure, in which one side of the sheet is in configuration I and the opposing side is in configuration II, named as configuration III. The stabilities of these configuration were investigated using DFT, based on $Ti_3C_2F_2$ and $Ti_3C_2(OH)_2$ configurations. The results showed that the structural stabilities decrease in the order I > II as the steric repulsion between T groups and the underlying C atoms makes configuration II less stable. Therefore, this result suggests that both F and OH groups tend to adopt configuration I. However, it is necessary to point out that the MXenes prepared experimentally may have mixed functional groups (such as OH, O and F) on their surfaces that may affect their configurations. According to the theoretical calculation of Gibbs free energy from Rina's work [41], the formation of mixed terminations is favourable, although there is no report on MXenes configurations with mixed surface functional groups to date [28]. At the same time, they also approached the conclusion that pH of the etching solvent has some effect on the formation of the terminal groups, with the observation that more -F group terminations will form at lower pH.

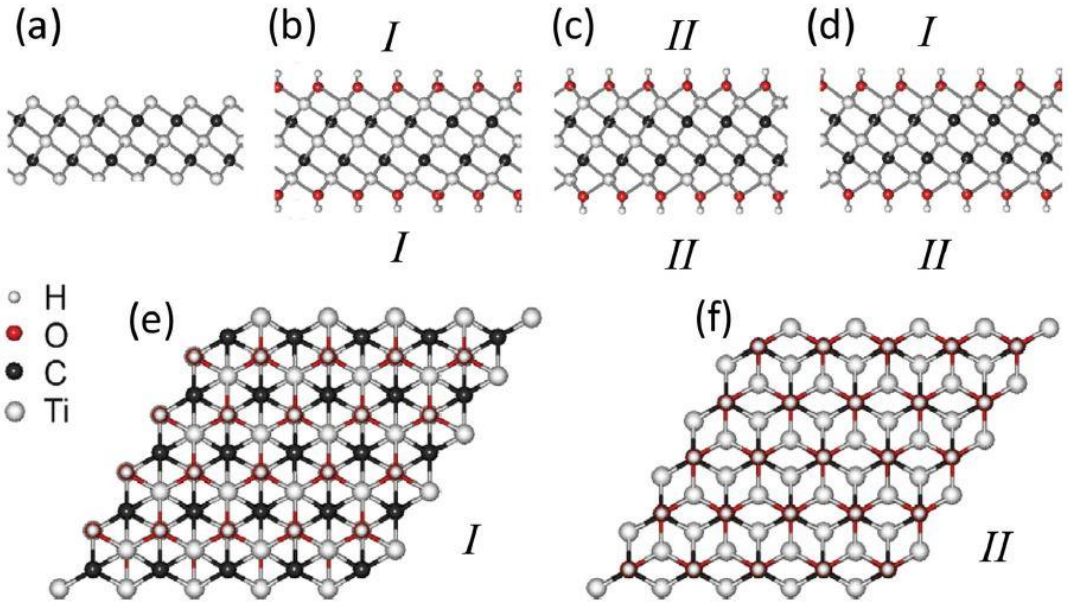

Figure 2- 4 Configurations of functionalized MXenes with different arrangements of the surface atoms: side views of a) bare Ti_3C_2, b) I- $Ti_3C_2(OH)_2$, c) II-$Ti_2C(OH)_2$, and d) III-$Ti_3C_2(OH)_2$, e,f) top views of I-$Ti_3C_2(OH)_2$ and II-$Ti_3C_2(OH)_2$. As configuration III is a mixture of I and II, its top view is not shown [28].

2.1.4 Synthesis of MXenes

As mentioned above, the first obtained MXene, $Ti_3C_2T_x$, was derived by selectively etching the Al atomic layers from the precursors, Ti_3AlC_2. After continuous trials, it is found that the common method for producing MXenes is selectively etching out the A layers from corresponding MAX phases. As reported, there are over 70 MAX phases has been investigated so far, which made of layers of M_{n+1} and X_n as well as the intercalated A layer [38], meanwhile more than 30 different MXenes have been reported [28]. A developmental journey of MXene synthesis methods from 2011 to the end of 2017 is shown in **Fig. 2-5**. The etching method has been improved gradually by changing the etching conditions, includes the ratio between the reactants, the temperature, the reaction duration and also the agitation. In 2011, the first MXene multi-layered powder ($Ti_3C_2T_x$) was made by selective etching Al from Ti_3AlC_2 using hydrofluoric acid (HF), which was reported by Naguib et al. [35]. In essence, the MAX phase powder was stirred in aqueous HF for a certain amount of time followed by centrifugation of the mixture to separate the solid from the supernatant, and then exfoliation via sonication treatment. The etching reactions are shown by following equations (1-1, 1-2, 1-3, 1-4):

Ti_3AlC_2 (s) + 3HF (aq.) = AlF_3 (aq.) + Ti_3C_2 (s) +3/2 H_2 (g) --------- (1-1)

Ti_3C_2 (s) +2H_2O (aq.) = $Ti_3C_2(OH)_2$ (s) + H_2 (g) --------- (1-2)

Ti_3C_2 (s) +2HF (aq.) = $Ti_3C_2F_2$ (s) + H_2 (g) --------- (1-3)

$Ti_3C_2(OH)_2$ (s) = $Ti_3C_2O_2$ (s) + H_2 (g) --------- (1-4)

Through the above treatment, the obtained MXene was decorated with O, OH or F terminations, which was denoted as $M_{n+1}X_nT_x$, where T implies surface functional groups (-OH, -F, -O-, etc.). Subsequently, researchers successfully obtained a series of $M_{n+1}X_nT_x$ with the same etchant, including Ti_2CT_x, $TiNbCT_x$, $Ti_3CN_xT_x$, $Ta_4C_3T_x$, Nb_2CT_x, V_2CT_x, $Nb_4C_3T_x$, Mo_2CT_x, $(Nb_{0.8}Ti_{0.2})_4C_3T_x$, $(Nb_{0.8}Zr_{0.2})_4C_3T_x$, $Zr_3C_2T_x$ and $Hf_3C_2T_x$, meanwhile the connection between the strength of M-A bonds and the etching conditions were investigated systematically [42]. After etching, accordion-like MXene is obtained with loosely packed multi-layered structure. In order to do further conversion to get single/few layer MXene, a post-delamination process is required by intercalating metal ions [43], organic molecules (such as urea, dimethyl sulfoxide) followed by sonication or mechanical shaking [44]. In addition, NH_4HF_2 and the mixture of HCl and LiF were also reported as etchant to etch "A" atoms layers. In the process of treatment with NH_4HF_2, NH_3 and NH^{4+} species is released by NH_4HF_2 which can intercalate in MXene layers that lead to a 25 % larger *c* lattice parameter than those of the samples etched with HF. The latter resulted in $Ti_3C_2T_x$ with clay-like behaviour and is called the clay method.

With sonication of $Ti_3C_2T_x$ clay in water, submicrometer lateral-size single flakes of $Ti_3C_2T_x$ were isolated [42]. Comparatively, the route with HCl and LiF as the etchant, the obtained MXene flakes did not have nanometer size defects due to the much milder nature of LiF and HCl compared with HF (as shown in equation 1-5, 1-6, 1-7, 1-8, 1-9) [45], but this reaction still builds an *in situ* HF environment. In 2015, tetrabutylammonium hydroxide (TBAOH) and amine were reported to be used as the assistant for further delamination [46]. Additionally, double-transition metal carbides: the subfamily of MXenes where two different transition metals occupy different atomic layers, were discovered. As a result, there were 25 more potential new species added to enlarge the MXene family, such as $Mo_2TiC_2T_x$, $Cr_2TiC_2T_x$, $Mo_2Ti_2C_3T_x$) [47]. In 2016, an upgraded etching method by using LiF/HCl to delaminate and obtain the single layer $Ti_3C_2T_x$ with large flakes (>2 μm) were explored. This method was referred to minimally intensive layer delamination (MILD), and in this method, ultra-sonication is not required to exfoliate the multi-flakes, resulting in larger flakes with better electric conductivity [48]. In 2017, by synthesizing in-plane double transition metal MAX phase ($(Mo_{2/3}Sc_{1/3})_2AlC$) and etching one of the transition metals, MXene with ordered di-vacancies ($Mo_{1.3}CT_x$) was synthesized [49]. At the beginning, the etchant was concentrated hydrofluoric acid. With the gradually established etching process, researchers started to explore additional fluoride-based etchants, which would not only contribute to the surface chemistry and properties but also bring in greater reaction safety with lower associated environmental risks. Moreover, there are a small number of non-HF methods used to obtain MXene, such as chemical vapor deposition (CVD) [50], high-temperature alkali liquor treatment [51], electrochemical etching and molten-salt etching [52,53], which has not accomplished scaled-up production at this moment. These methods can etch and remove the A layers but has difficulties in delamination and exfoliation. Geng et al. successfully prepared Mo_2C MXene by CVD [50]. This method could better control the thickness of Mo_2C crystals and opens a new approach for the preparation of MXene-based materials. Li et al. believed that some MAX phases like Ti_3AlC_2 can react with OH- from a thermodynamic viewpoint. Therefore, they used NaOH to successfully remove the Al layers at 270 ℃ and obtained $Ti_3C_2T_x$ with 92 wt% purity [51]. In 2017, Sun et al. found a way to etch Ti_2AlC using an electrochemical method in a low-concentration HCl solution [53]. Li et al. reported an element replacement approach by using lewis acidic molten salts, which resulted in a substitution in the precursor MAX phase and yielded Cl-terminated MXenes [52]. In 2018, Asia et al. found that MXene can be applied to radio frequency antennas for wireless communication and fabricated a 100 nm-think translucent MXene antenna with a reflection coefficient of less than 10 dB. When they increase

the thickness to 8 μm, a reflection coefficient of 65 dB was achieved. Related MXene RF identification device tag could also reach a reading distance of 8 m at 860 MHz [54]. Nine years after MXene was first time obtained, the challenge of industrial quantity manufacture of this material was overcome [55]. Afterwards, in 2021, there are more MXenes have been discovered and synthesized. Besides, MXenes with better quality and lower cost have also been achieved by using modified precursors. One batch of $Ti_3C_2T_x$ synthesis has been increased from 1 gram to 50 grams.

$$2Ti_3AlC_2 + 6LiF + 6HCl = Li_3AlF_6 + AlCl_3 + 3LiCl + 3H_2 + 2Ti_3C_2 \quad \text{---------} \quad (1\text{-}5)$$

$$Ti_3C_2 + 2H_2O = Ti_3C_2(OH)_2 + H_2 \quad \text{---------} \quad (1\text{-}6)$$

$$Ti_3C_2 + 2HCl = Ti_3C_2Cl_2 + H_2 \quad \text{---------} \quad (1\text{-}7)$$

$$Ti_3C_2 + 2HF = Ti_3C_2F_2 + H_2 \quad \text{---------} \quad (1\text{-}8)$$

$$Ti_3C_2(OH)_2 = Ti_3C_2O_2 + H_2 \quad \text{---------} \quad (1\text{-}9)$$

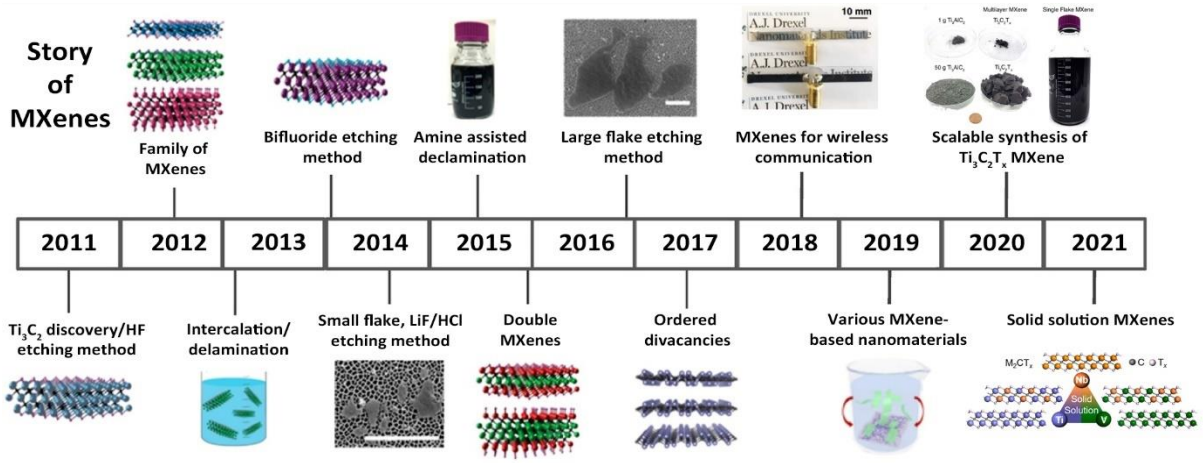

Figure 2- 5 Timeline of MXene from 2011 to 2019 [2][55][56].

Table 2- 1 Mxene synthesis methods

Precursors	MXene	Etching Methods	Yield (%)	Ref.
Ti_3AlC_2	$Ti_3C_2T_x$	50 wt% HF, RT, 2 hours	100	[35]
Ti_2AlC	Ti_2CT_x	10 wt% HF, RT, 10 hours	80	[57]
Ti_3AlCN	Ti_3CNT_x	30 wt% HF, RT, 18 hours	80	[58]
V_2AlC	V_2CT_x	50 wt%, RT, 90 hours	60	[59]
Ti_2AlN	Ti_2NT_x	5% wt%, RT, 24 hours	NA	[60]
Ti_3AlC_2	$Ti_3C_2T_x$	3 M LiF + 6 M HCl, 40 °C, 45 hours	100	[61]

Ti_2AlC	Ti_2CT_x	0.9 M LiF + 6 M HCl, 40 ℃, 15 hours	NA	[62]
Ti_3AlCN	Ti_3CNT_x	0.66 g LiF + 6 M HCl, 35 ℃, 12 hours	NA	[63]
V_2AlC	V_2CT_x	2 g LiF + 40 M HCl, 90 ℃, 48 hours	NA	[64]
Ti_3AlC_2	$Ti_3C_2T_x$	1 M NH_4HF_2, 80 ℃, 12 hours	NA	[65]
Ti_3AlC_2	$Ti_3C_2T_x$	NH_3F, 150 ℃, 24 hours	NA	[66]
Ti_4AlN_3	$Ti_4N_3T_x$	59 % KF + 29 % LiF + 12 % NaF, 550 ℃, 0.5 hours	NA	[67]
/	Mo_2C	Mo foil + CH_4, 1100 ℃, 2 hours	NA	[50]
Ti_3AlC_2	$Ti_3C_2T_x$	27.5 M NaOH, 270 ℃, 12 hours	92 wt	[51]
Ti_2AlC	Ti_2CT_x	HCl (1 M or 2 M), RT, 1/5/14 days	NA	[53]
Ti_3AlC_2	$Ti_3C_2Cl_2$	1.05 g $ZnCl_2$, 550 ℃, 2 hours	67	[52]

2.2 MXenes properties

2.2.1 Introduction

Starting with the discovery of the MXenes from 2011, there has been a large increase in publications and development for application in various areas. Up to now, the research areas of MXenes have covered numerous fields (as shown in **Fig. 2-6**) such as catalysis, separation membranes, medicine, optical devices, energy storage, electronics etc. Consequently, this has garnered more global attraction from various research communities. Several reasons listed below can explain the rapid development of MXene is those areas.

1. MXenes have a unique combination of high electric-conductivity and good mechanical characteristics of the transition metal carbides/nitrides.
2. MXenes have functional terminations on its surface, which can make them hydrophilic and easily modifiable by various groups.
3. MXenes are relatively easy to process and to form a stable colloidal solution because of the negative zeta potential.
4. MXenes can effectively adsorb electromagnetic waves.

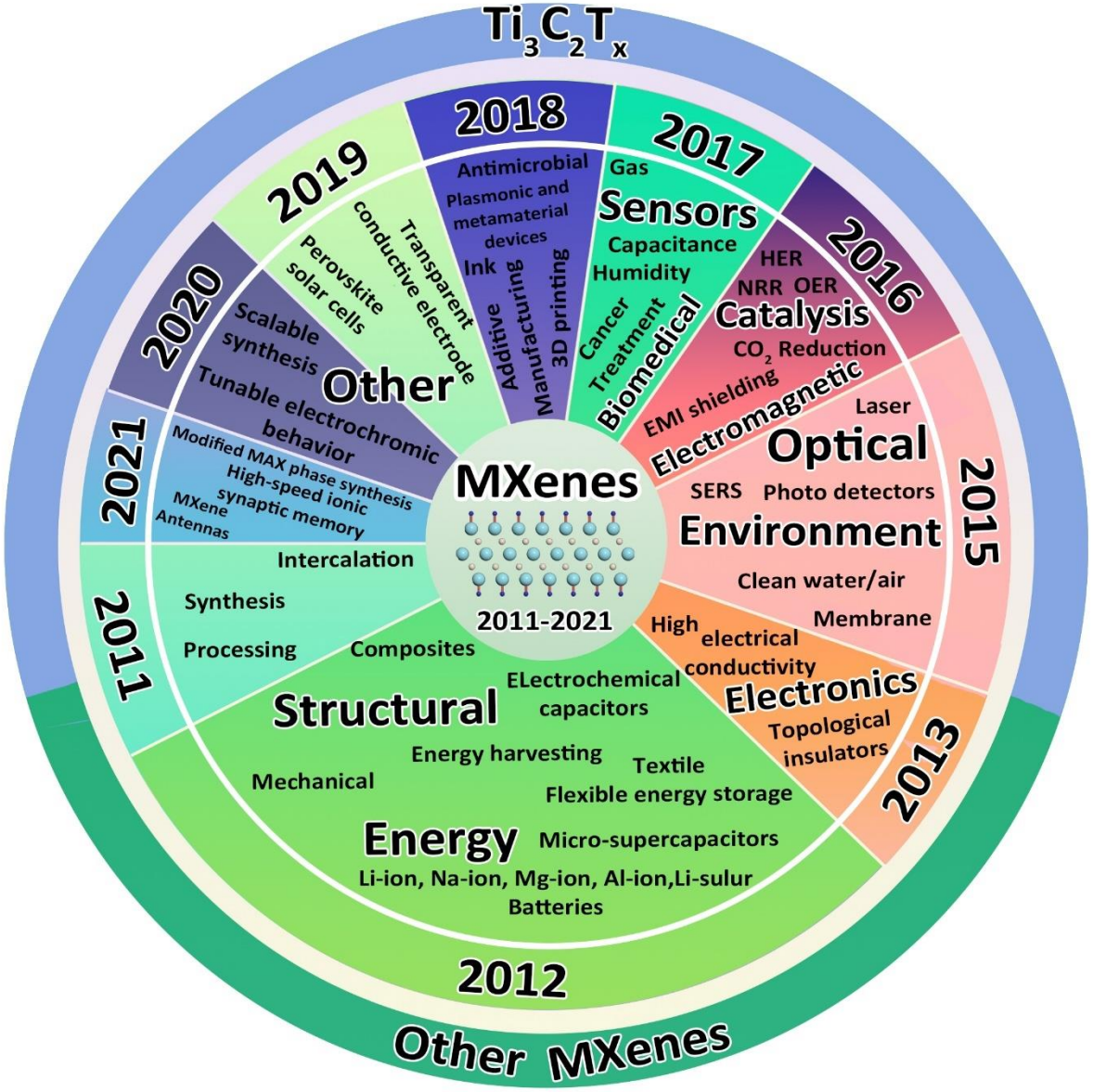

Figure 2- 6 Timeline of the explored research areas and applications of MXenes from 2011-2021, which also illustrates the ratio of the various works [34].

The first and most developed application of MXenes is energy storage, with some novel explorations in catalysis and electronics as well. To meet expanding electrification in society, renewable energy generated from sunlight, wind, waves/tides, and geothermal heat are becoming dominant sources. As a consequence, energy storage devices are required to capture the charge from these energy harvesting devices. At the same time, corresponding electronics, such as sensors, are also important to deliver information and execute corresponding reactions to help optimize grid systems.

2.2.2 Electronic and electrochemical properties of MXenes

Most of the MXenes exhibit a metallic behaviour, thus most of them have high electronic conductivity [68]. Researchers have made a lot of effort to investigate the physical properties of MXene and to enhance the metallic conductivity. Acting as one of the most promising candidates for energy storage and electronic applications, MXenes have become attractive electrode materials and conductive materials for such reasons:

1. The inner conductive transition metal carbide layers enable fast electron transportation.
2. Terminations on the surface and edges, and the transitional metal oxide-like surface are effective active sites for redox reactions.
3. High electric-conductivity of mono-layer up to 11,000 S cm^{-1} [69], and high volumetric capacitance at ultra-high rate capability in acidic electrolyte.

In terms of the most common studied MXene $Ti_3C_2T_x$, it can process diverse chemical and physical properties due to various intrinsic structural features and compositions caused by different etching and processing methods. Electronic conductivity of the electrode plays a very important role in an electrochemical energy device's usage. Bare MXenes exhibit metallic features, similar to the corresponding MAX phases. But after etching, there are terminated groups anchored on the flake surface, which can affect the electrical conductivity [70]. For example, Ti_2CO_2 which terminates with O, has its d band lifted above Fermi level and makes it semi-conducting, while Ti_2CF_2 still retains its Fermi energy at the d band of Ti layers, thus can remain metallic [70]. In practical research, the prepared MXenes are always terminated with mixed groups. Additionally, MXenes' electronic properties are also related to the type of transition metal M. Specifically, some MXenes which contain heavy elements such as Mo and W, are predicted to be topological insulators [71]. Carbonitride and nitride MXenes exhibit stronger metallic properties than carbide MXenes since N possesses an additional free electron. Experimental results show that $Ti_3CN(OH)_2$ exhibits greater metallic property than $Ti_3C_2(OH)_2$ although they have similar structures. Up to now, $Ti_3C_2T_x$ exhibits the highest electrical conductivity, and this makes it a good candidate for supercapacitor applications [58,72]. For the same type of MXene, the electrical conductivity will change according to the preparation method, flake size and sample state (such as oxidation state). As reported, an individual monolayer $Ti_3C_2T_x$ has an electrical conductivity of 11,000 S cm^{-1}, a high breakdown current density of $1.2*10^8$ A cm^{-2}, and an improved mobility up to 6 cm^2 V^{-1} s^{-1} [69]. It has been observed that one pure $Ti_3C_2T_x$ film with large flake size has exhibited a high conductivity of roughly 15,100 S cm^{-1} [73]. Furthermore, the thin layer MXene enables it to possess both conductivity and transparency, which allows it to be applied for transparent conductive applications [39].

Kayali et al. have found the different electrochemical properties existing between MXenes with diverse lateral flake size distribution. Comparatively, the MXene with larger flakes show higher electrical conductivity, as the smaller 2D sheets has more contact resistance between flakes and more defects on the edges [74]. Centrifugation is commonly used to relegate the size distribution. Normally, the smaller flakes are located on the top part of the suspension while the larger flakes are settled to the bottom part [75].

2.2.3 Other properties of MXenes

In terms of the mechanical property, as a result of the high Ti-O bonding strength, MXenes have very good stiffness, and the mechanical properties can be adjusted by changing the surface terminated groups [76]. Magnuson et al. believed the length of the Ti-C bond has potential to affect the elastic property of the MXene, i.e. MXene's elasticity can also be modified by adjusting the strength of the bonds [77]. According to theoretical calculations, Yorulmaz et al. ascertained that the higher the mass of the transition metal, the stiffer the MXene is [78]. Despite MXene generally exhibiting lower strength and stiffness as graphene does, the majority of carbide-based MXenes are regarded as mechanically stable [28]. With regard to magnetic properties, the majority of the common MXenes are non-magnetic, which is attributed to the strong covalent bond between the M and X atoms [79]. However, some bare MXenes have been predicted to show intrinsical magnetism, such as Cr_2C [80], Mn_2C and so on [81]. Besides this, some MXenes have demonstrated optical transparency, plasmonic behaviour, and efficient photothermal conversion, which also are attributed to the surface terminated groups [68].

2.2.4 Chemical stability of MXenes

So far, colloidal solutions of MXenes have been widely used to process films, complex patterns or 3D printed structures. Thus, it is important to investigate the stability of MXene based suspensions. According to thermodynamic theory, MXenes have the tendency to be oxidized due to the lower oxidation number of M in MXenes compared to corresponding oxides. Oxidation starts from the edges of the 2D sheets and spreads through to the whole basal plane, which automatically occurs in air, liquid or solid media at varying speeds. This would result in altered composition as well as destroyed flake structure, which affects their processability and functional properties. Generally, flake size also affects the speed of the oxidation. Flakes with smaller size and thinner layers have more specific active area, which results in faster oxidation.

Zhang et al. have reported that putting the $Ti_3C_2T_x$ colloidal in an ambient environment, for over 2 weeks (15 days) resulted in 100 % of it converted to primarily anatase TiO_2 due to the abundant oxygen in the water and air [82]. Therefore, if oxygen can be eliminated from the solvent, the oxidation rate can be slowed down. In addition, drying MXene is another temporal way to mitigate this situation, as it can prevent severe oxidation from large amounts of O_2 dissolved in the water, slowing down the degradation process. Additionally, exposure to light can also accelerate the speed of oxidation. Extended storage of MXene powder or film in a cold (~5 °C), dry and inert-gas environment can lead to comparatively less oxidation. Besides this, there are also chemical ways to protect MXenes from oxidation. As reported previously, Zhao et al. added sodium L-ascorbate into the $Ti_3C_2T_x$ colloidal as an antioxidant. Whether in a colloid or as a dehydrated film (of the colloid), a chemical antioxidant defends against oxidation to a certain degree. The composition, micro-morphology, electrical conductivity of $Ti_3C_2T_x$ is still retained after the sodium-L-ascorbate treatment. Composition and environment are two key factors that influence MXenes' chemical stability, so if they can be controlled appropriately, we can extend the lifetime of MXenes' functional properties. Another way to extend the storing duration is submerging MXenes in organic solvents [83].

2.3 MXene based energy storage applications

2.3.1 Introduction

Due to their unique chemical construction, morphologies, excellent electronic conductivities and ease of processibility, MXenes are considered to be a fascinating candidate for many applications, including catalysts, electronic devices, electromagnetic shielding and electrochemical energy storage materials. Particularly, many researchers focus on exploring the use of MXenes in electrochemical energy storage applications, such as electrode materials for batteries and supercapacitors [28,29]. For storing energy, different kinds of batteries such as lithium-ion batteries, are good choice as they possess a high energy density. However, the limited cycling duration requires batteries to have periodic maintenance or replacement. Furthermore, comparatively low power density limits their applications in high-speed charging-discharging circumstances. In order to address the limitation of batteries, another considered electrochemical energy storage (EES) device are supercapacitors (electrochemical capacitors), which can potentially become the supportive alternative to batteries, combining the prominent characteristics from electric double-layer capacitance and pseudo-capacitance.

For the energy storage infrastructure, retaining a sustainable energy supply is not the only singular key point to be considered. A necessary requirement is the ability to sustain the high charging flow during peak periods. Therefore, rather than viewing supercapacitors as a competing product, it should be viewed as a supportive technology. They can be used synergistically to optimize the performance of an energy storage unit. The Ragone plot in **Fig. 2-7** illustrates the energy & power densities of different energy storage devices. Batteries and fuel cells have the highest energy density and lowest power density, while supercapacitors have comparatively higher power supply capability, losing out on energy density and bridging the gap between the conventional capacitor and the battery with long cycling life.

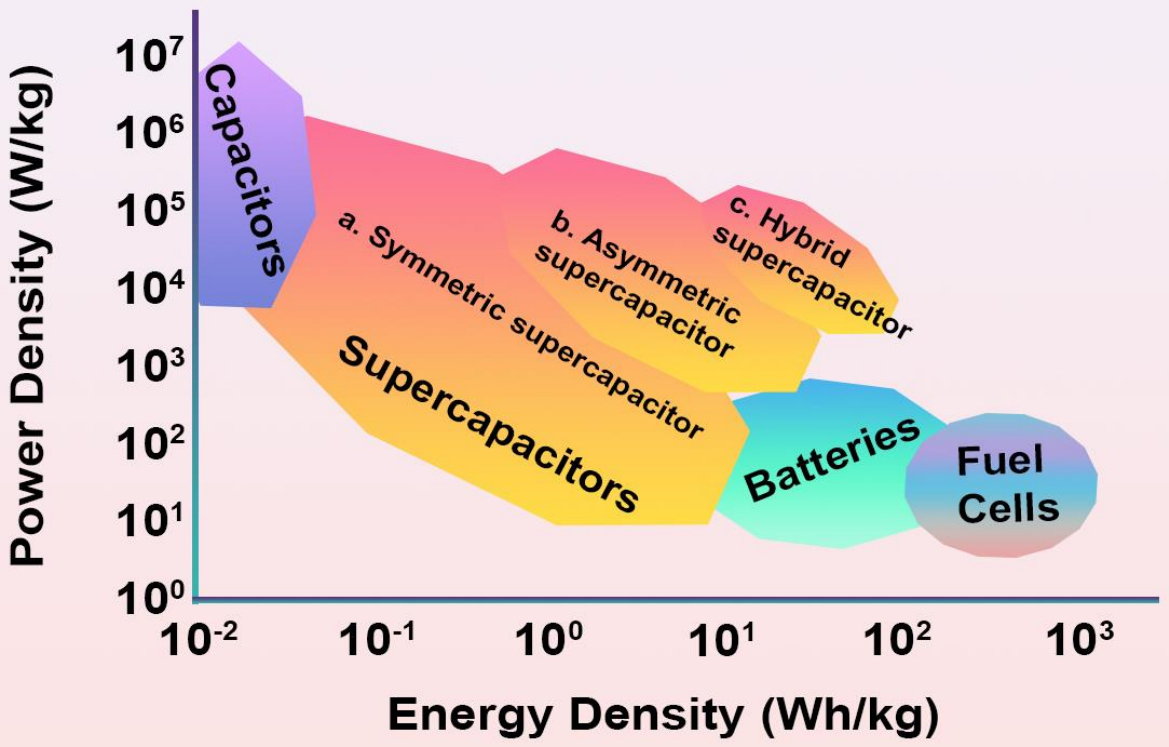

Figure 2- 7 Ragone plot shows the energy density and power density comparison of supercapacitors with the other energy storage devices.

2.3.2 MXene for Supercapacitor

In recent years, supercapacitors have attracted greater attention because of their high power density, excellent rate performance and long cyclic stability. In practice, supercapacitors are generally applied in start-stop control systems of hybrid electric vehicles and fuel cell vehicles due to their rapid charge/discharge. Therefore, supercapacitors also play a significant role in future energy storage systems. There are two kinds of supercapacitors, based on two working

mechanisms: electrical double-layer capacitance and pseudo-capacitance. In the former, capacitance is generated from reversible desorption/adsorption of ions and electrons on both sides of electrode materials' surface to form double-layer charging walls, which is highly dependent on the high specific surface area and conductivity of the active material. The latter, normally generates the pseudo-capacitance by fast reversible electrochemical reactions on the surface or near-surface of the material [84]. It occupies a middle-ground between electrical double-layer capacitors (EDLCs) and batteries, which typically rely on intercalation of ions and Faradaic electron transfer. It can be driven by three kinds of reactions: (1) fast redox reaction from metal oxides such as RuO_2 and MnO_2 etc., which has two or more redox states, *via* Faradaic electron transfer or non-Faradaic charge storage. This type of reactions mostly happens in aqueous electrolyte; (2) Intercalation pseudo-capacitance, which normally arises from multilayer electrode materials, such as Nb_2O_5, and the reactions are suitable in non-aqueous electrolyte; (3) Underpotential deposition, which mainly happens on the surface of noble metals, such as Au.

MXene possesses a unique 2D layer structure, large surface area and excellent electronic properties, which make MXene-based materials a promising candidate for potential applications in supercapacitors. Lukatskaya et al. for the first time reported intercalation behaviour of cations (Na^+, K^+, NH^{4+}, Mg^{2+} and Al^{3+}) from electrolyte solutions into $Ti_3C_2T_x$ MXene layers [85]. With KOH as electrolyte, $Ti_3C_2T_x$ paper electrodes can exhibit a volumetric capacitance of 340 F cm^{-3} at 2 mV s^{-1} and no obvious degradation after 10,000 cycles at 1 A g^{-1}. The results open a new door for the development and application of MXene in supercapacitors. Furthermore, Hu et al. investigated the capacitance mechanism of $Ti_3C_2T_x$ MXene with *in-situ* Raman spectroscopy [86]. The results showed that $Ti_3C_2T_x$ exhibited mainly pseudocapacitive behaviour in sulfuric acid, in which the hydronium in H_2SO_4 electrolyte takes part in bonding/debonding with the terminated -O groups on $Ti_3C_2T_x$ surface during discharging/charging processes while the $Ti_3C_2T_x$ electrode only showed electric double layer capacitance in $(NH_4)_2SO_4$ and $MgSO_4$ electrolytes. $Ti_3C_2T_x$ MXenes are the most popular electrode material investigated in applications for supercapacitors [87]. Ghidiu et al. first prepared clay-like $Ti_3C_2T_x$ MXene as supercapacitor electrodes, and the obtained $Ti_3C_2T_x$ electrode exhibit a capacitance of 900 F cm^{-3} (245 F g^{-1}) at 2 mV s^{-1} in H_2SO_4 solution [61]. Among all intercalating cations, H^+ ion can provide more energy for storage in the same space due to the smaller ionic size. Meanwhile, the more open interlayer spacing of the as-synthetized MXene and the associated surface redox reaction processes will also contribute to increased

capacitance. Hu et al. prepared self-assembled $Ti_3C_2T_x$ films with a dropping-mild baking approach, and the obtained $Ti_3C_2T_x$ electrode exhibited a high gravimetric capacitance of 499 F g^{-1} and excellent cyclic stability in acidic solutions [16]. Xu et al. proposed a binder-free $Ti_3C_2T_x$ MXene electrode by a modified electrophoretic deposition method, which also exhibited excellent electrochemical performances as supercapacitors [88]. In addition, Zhang et al. applied the highly transparent and conductive $Ti_3C_2T_x$ as solid-state supercapacitor electrodes. The results demonstrated that the $Ti_3C_2T_x$ electrode displayed remarkable volumetric capacitance of 676 F cm^{-3} with rapid charging/discharging [87]. Lukatskaya et al. prepared a macro-porous $Ti_3C_2T_x$ MXene electrode for supercapacitors (**Fig. 2-8**), which exhibited a high capacitance of 210 F g^{-1} at 10 V s^{-1} and 100 F g^{-1} at 40 V s^{-1} [89]. In addition, $Ti_3C_2T_x$ MXene hydrogels were also obtained and showed an outstanding volumetric capacitance of 1,500 F cm^{-3} [89].

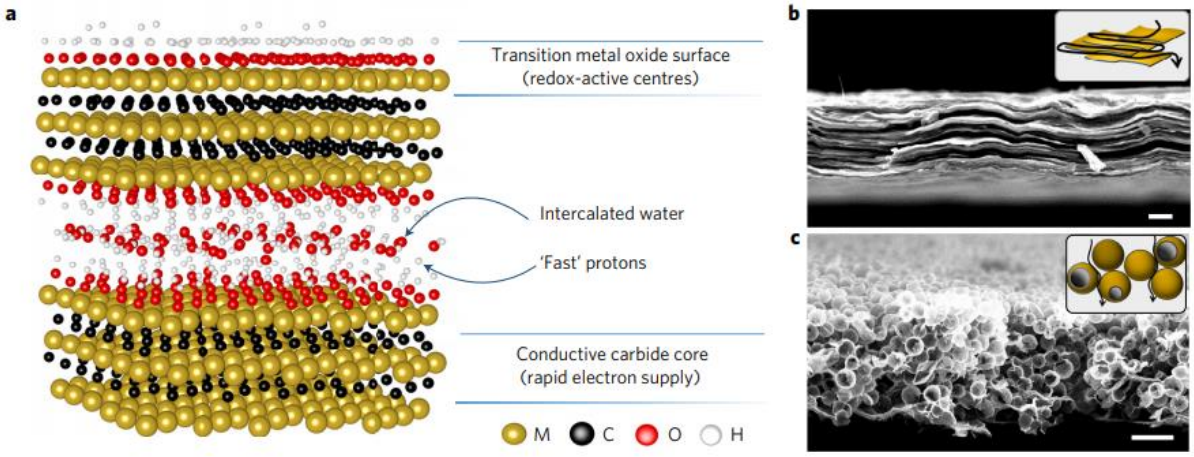

Figure 2- 8 Schematic illustration and scanning electron microscopy (SEM) images of microporous $Ti_3C_2T_x$ MXene electrode for supercapacitors [89].

Recently, Wen et al. reported that the c-lattice parameter of $Ti_3C_2T_x$ would increase by doping N atoms, and the as-prepared N-doped $Ti_3C_2T_x$ MXene (N-TiC_2T_x) exhibits improved capacitances of 192 F g^{-1}, which is higher than that of un-doped MXene materials [90]. For the preparation process of MXenes, the influence of HF etching time on the electrochemical performances of MXene was also investigated. The results showed that the electrochemical performances of $Ti_3C_2T_x$ were maximised at an etching time approaching 216 hours [91]. Levi et al. investigated the electrochemical behaviours (energy storage mechanism) of $Ti_3C_2T_x$ MXene electrodes in the charge and discharge processes [92]. The results show that the cation inserts very fast in $Ti_3C_2T_x$ MXene, in which cations were adsorbed at the solid-liquid interfaces with the structure of MXene particles going through extensive deformation. The

adsorbed cations are electrochemically inserted into the MXene layers, leading to swelling of MXene particles. It is noteworthy to point out that the cation was absorbed in the shallow and deep layers of the MXene simultaneously, which results in high rate performance and a high capacitance.

In addition, the combination of MXene and polymer as electrodes for supercapacitors is a useful strategy for improving electrochemical performance since polymers can not only provide increased capacity but also modify the MXenes. Ling et al. reported $Ti_3C_2T_x$/polymer (polydiallyldimethyl ammonium chloride or polyvinyl alcohol) composite films as electrodes of a supercapacitor (**Fig. 2-9**), which exhibited high volumetric capacitance in KOH solution [93]. Boota et al. prepared $Ti_3C_2T_x$/polypyrrole (PPy) composites [94], in which PPy intercalates into MXene layers to expand the interlayer space and also behaves as a conductive polymer contributing to pseudo-capacitance. The obtained PPy/$Ti_3C_2T_x$ electrode exhibited a volumetric capacitance of 1,000 F cm^{-3} and a capacitance retention of 92 % after 25,000 cycles.

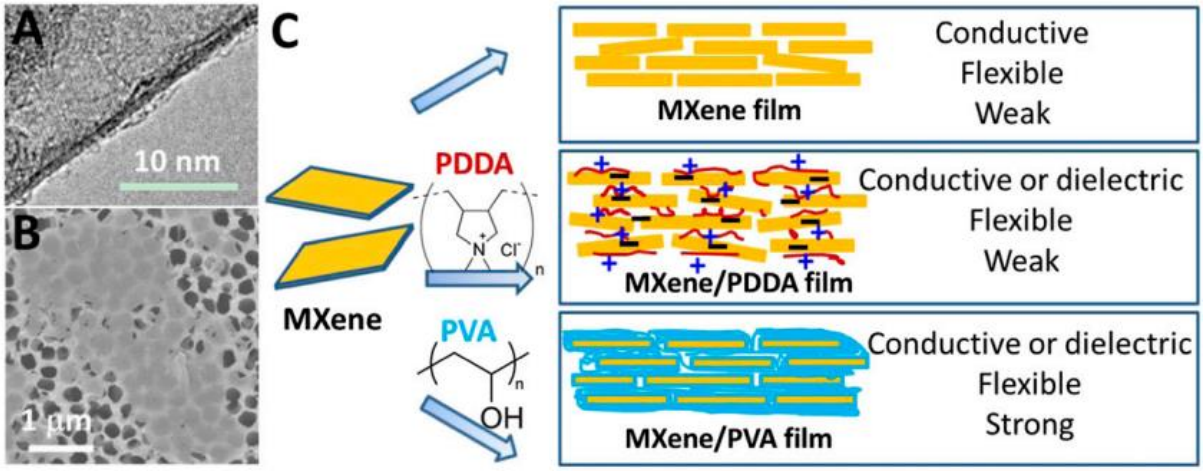

Figure 2- 9 (a,b) SEM and transmission electron microscopy (TEM) images of delaminated MXene. (c) Schematic illustration of the preparation of MXene functional films [93].

Furthermore, carbon-based materials can also be applied as a composite material with MXenes for supercapacitors. Zhao et al. prepared a sandwich-like MXene/CNT composite paper electrodes, which exhibited excellent electrochemical performance in 1 M $MgSO_4$ electrolyte for supercapacitors [95]. Using the same method, sandwich-like MXene/ onion-like carbon and MXene/ Reduced graphene oxide (RGO) composite electrodes were also obtained [95]. Besides this, transition metal oxides were also formed into composites with MXene to enhance the electrochemical performance. Wang et al. combined $Ti_3C_2T_x$ MXene and nickel-aluminium layered double hydroxide (LDH) by *in-situ* growth of LDH on a MXene substrate [96]. The

obtained MXene/LDH composite electrode exhibited a high specific capacitance of 1,061 F g^{-1} at 1 A g^{-1}. The fast ion transport and large reaction area of this supercapacitor can be attributed to the unique 3D structure formed by the composite.

MXenes were also directly applied in areal energy storage devices. Kurra et al. prepared MXene-on-paper co-planar micro-supercapacitors by a coating and laser machining process, which exhibited excellent electrochemical performance [97]. Peng et al. produced solid-state on-chip micro-supercapacitors by applying two layers of $Ti_3C_2T_x$ with different flake sizes as electrode materials (**Fig. 2-10**) [98]. These micro-supercapacitors exhibited high areal volumetric capacitances of ~27 mF cm^{-2} and ~357 F cm^{-3} at 20 mV s^{-1} and capacitance retention of 100 % after 10,000 cycles at 50 mV s^{-1}.

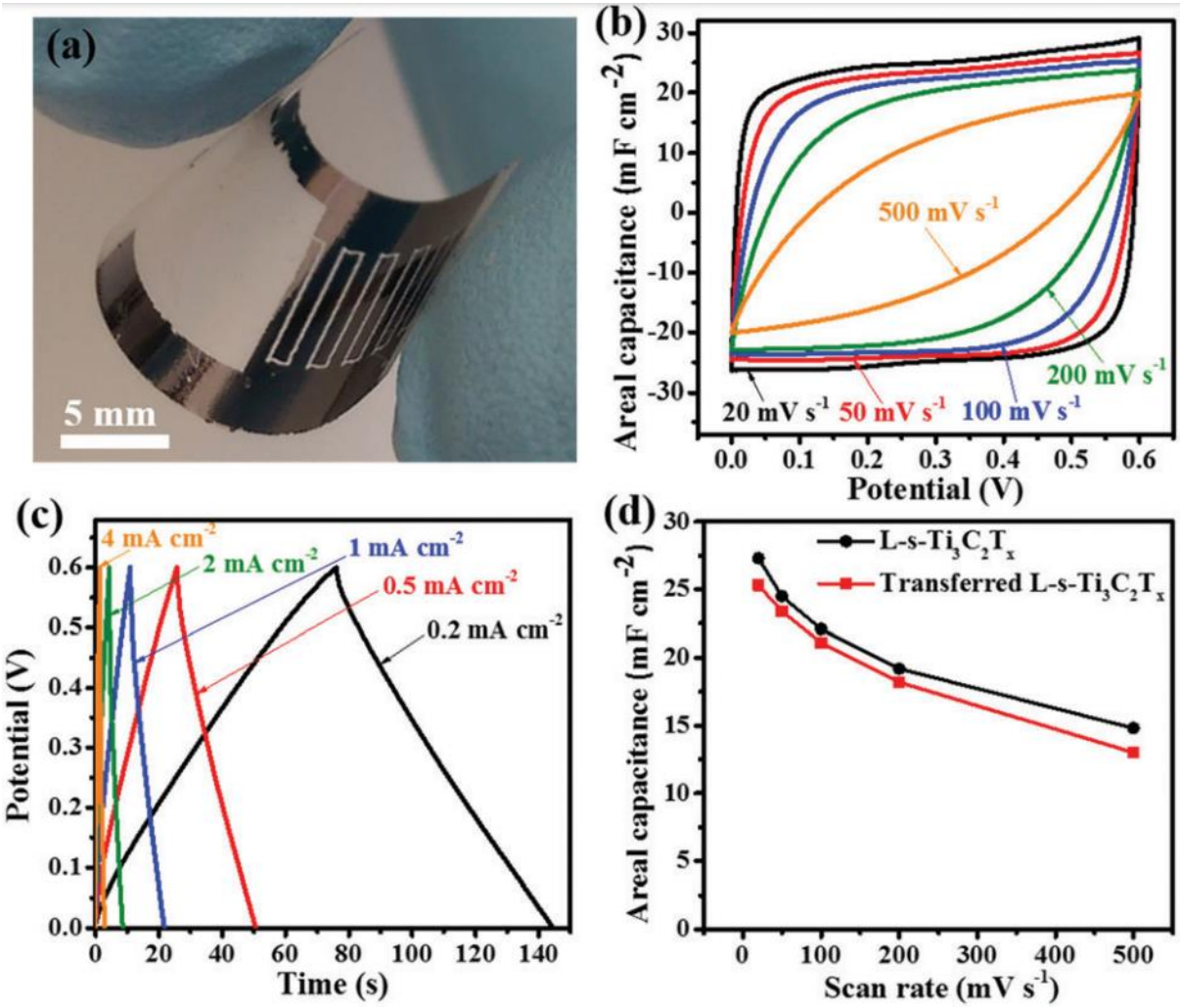

Figure 2- 10 (a) Digital photo of MXene based on-chip micro-supercapacitor. (b-d) Cyclic voltammetry (CV), charge-discharge curves and rate performance of the micro-supercapacitor [98].

Meanwhile, Li et al. also fabricated an on-chip micro-supercapacitor with MXene nanosheets and electrochemically exfoliated graphene [99]. The device demonstrated areal and volumetric capacitances of 2.26 mF cm^{-2} and 33 F cm^{-3} at 5 mV s^{-1} respectively. Besides this, Lin et al. were the first to report the application of $Ti_3C_2T_x$ MXene as supercapacitor electrodes with ionic liquid electrolytes (1-ethyl-3methylimidazolium bis(trifluoromethylsulfonyl) imide (EMI-TFSI)) with a large voltage window of 3 V (**Fig. 2-11**) [100].

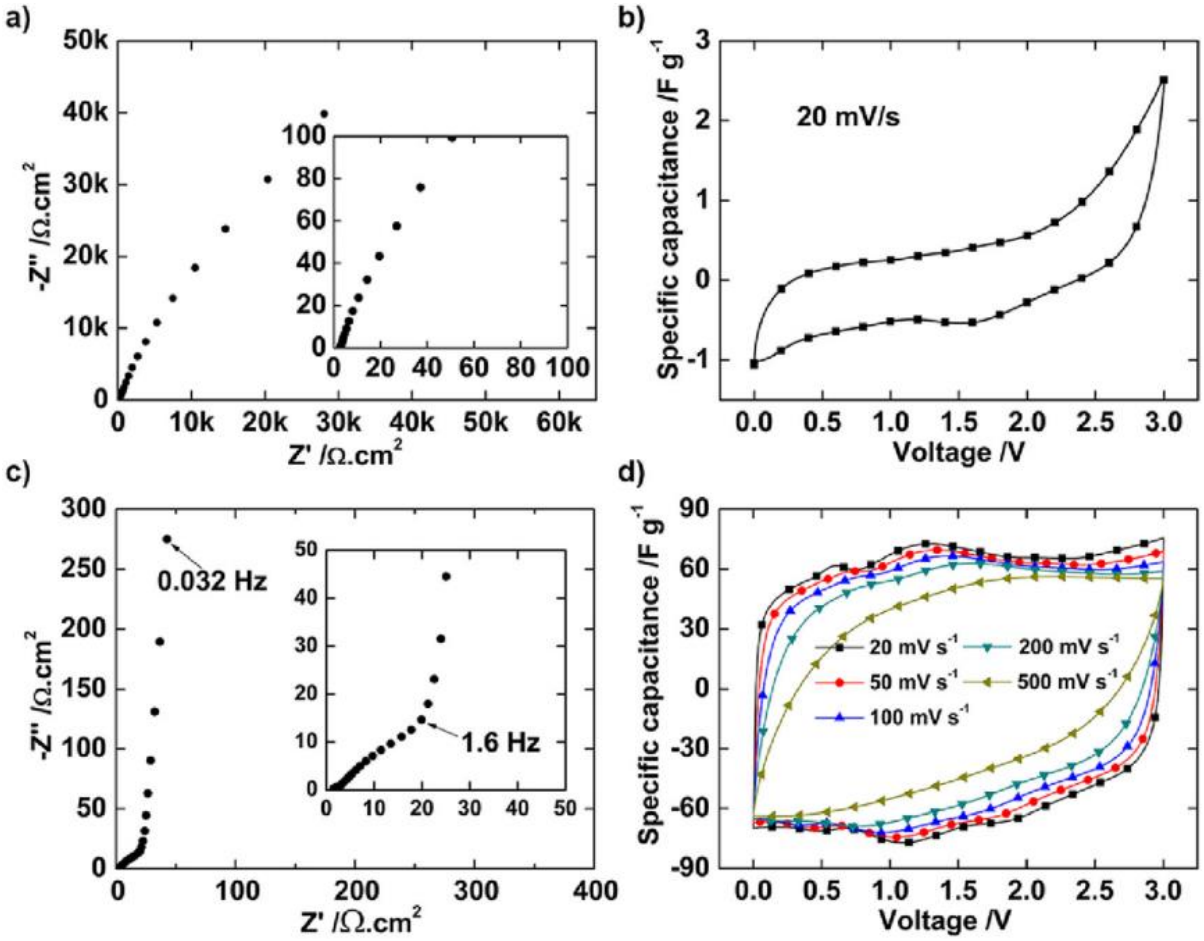

Figure 2- 11 (a) Nyquist plot (b) CV of $Ti_3C_2T_x$ film tested in ionic liquid electrolyte. (c,d) were tested in a two-electrode Swagelok [100].

In addition, Ti_2CT_x has also been frequently studied for supercapacitors. Particularly, post-etching methods was proposed to modify Ti_2CT_x MXenes. Rakhi et al. obtained Ti_2CT_x MXene which went through post-etch annealing in Ar, N_2, N_2/H_2 and ambient air as symmetric supercapacitors, which showed a specific capacitance of 51 F g^{-1} at 1 A g^{-1} because of high carbon content and low fluorine content on the surface [101]. Kajiyama et al. applied steric chloride as intercalating agent in Ti_2CT_x to expand its interlayer space, resulting in a high gravimetric and volumetric capacitance of 300 F g^{-1} and 130 F cm^{-3} at 0.2 mV s^{-1} [62].

Meanwhile, Ti_2CT_x has been fabricated into wire-type supercapacitors which exhibited a high specific length capacitance of 3.09 mF cm^{-1} and high length-specific energy density of 210 nWh cm^{-1} with good cycling stability [102].

2.3.3 MXene for Lithium-Ion Battery

Nowadays, rechargeable Lithium-ion batteries (LIBs) are the most widely used commercial electrochemical energy storage device. Graphite is most commonly used as the anode material of LIBs [103]. However, graphite suffers from some disadvantages, including low capacities and swelling problems, which results in its inability to meet the growing demands of energy storage devices. Therefore, exploitation of new anode materials is urgent for the evolution of LIBs. As mentioned above, pure MXene and MXene with surface functionalized groups exhibit metallic or semiconducting character with a narrow band gap, resulting in inherent advantages with regards to electronic conductivity.

In 2011, Naguib et al. first reported the feasibility of using Ti_3C_2 MXene as the anode material for LIBs [35]. Whereafter, the performances of $Ti_3C_2T_x$ as the anode material for LIBs were systematically investigated with experimental and theoretical calculations. Tang et al. reported the performance of $Ti_3C_2T_x$ anodes for LIBs by investigating the adsorption and migration of Li^+ on the surface of pure, -F and -OH terminated Ti_3C_2 MXene, with results showing that Ti_3C_2 MXene as anodes of a LIB exhibit excellent performance with low operating voltage and diffusion barrier [104]. Subsequently, Xie et al. reported that the MXene with -O groups showed the highest capacity since O-terminated groups can adsorb an extra Li ion [105]. Besides, the dynamic charge storage mechanism of $Ti_3C_2(OH)_2$ electrodes was investigated by molecular dynamic simulation and the results showed that $Ti_3C_2(OH)_2$ electrodes with narrower pores would exhibit excellent energy storage performance [106].

In experiments, Mashtalir et al. prepared a kind of $Ti_3C_2T_x$ "paper" as LIB anodes, and the as-prepared MXene "paper" anode exhibited a high capacity of 410 mAh g^{-1} at 1 C rate [107]. Sun et al. proposed Ti_3C_2 intercalated with dimethyl sulfoxide and it showed a capacity of 123.6 mAh g^{-1} at 260 mA g^{-1} and a coulombic efficiency of 47 % [108]. Meanwhile, Kim et al. proposed that Ti_3C_2 as anodes for LIBs exhibited an areal capacity of 5.9 mAh cm^{-2} at 1.5 mA cm^{-1} after 50 cycles [109]. An effective method to promote the electrochemical performance of MXene is delaminating multilayer MXene into paper-like structures because of a more opened structure and large specific surface area. However, the delaminating process will lead to potential

structural collapse and flakes stacking, resulting in the decrease of electrical conductivity and surfaces accessibility to electrolytes. Furthermore, Ren et al. used a kind of chemical etching method to introduce pores into MXene flakes, which can further increase the specific surface areas and optimize the structures. They prepared porous $Ti_3C_2T_x$ (p-$Ti_3C_2T_x$)/carbon nanotubes (CNTs) composite electrode for LIB, which exhibited a high capacity of 1,250 mAh g^{-1} at 32 mA g^{-1} [110].

Luo et al. prepared polyvinylpyrrolidone (PVP)/Ti_3C_2 nanocomposites decorated with Sn^{4+} ions (PVP-Sn(IV)@ Ti_3C_2) by a liquid-phase immersion method [111]. The Sn^{4+} ions inserted into the layers of alkalization intercalated Ti_3C_2 to contributing to a "pillar effect", which can aid the insertion of Li ions. Thus, the synergistic effect between Sn ions and Ti_3C_2 layers could further increase the capacity. The results showed that the as-prepared composite materials exhibited an ultrahigh reversible capacity of 1,375 mAh cm^{-3} (635 mAh g^{-1}) at 216.5 mA cm^{-3} (100 mA g^{-1}) with excellent rate and cycling performance. These experimental results bring a new perspective to further improve the capacity of MXene-based anodes by increasing the interlayer spacing with pillared structures. MXene with an appropriately selected inserted precursor will attain suitable interlayer spacing and pillared structures will be obtained [112]. The pillared MXene can exhibit better electrochemical performance since proper interlayer spacing can facilitate the adsorption and intercalation of ions in electrolytes (**Fig. 2-12**).

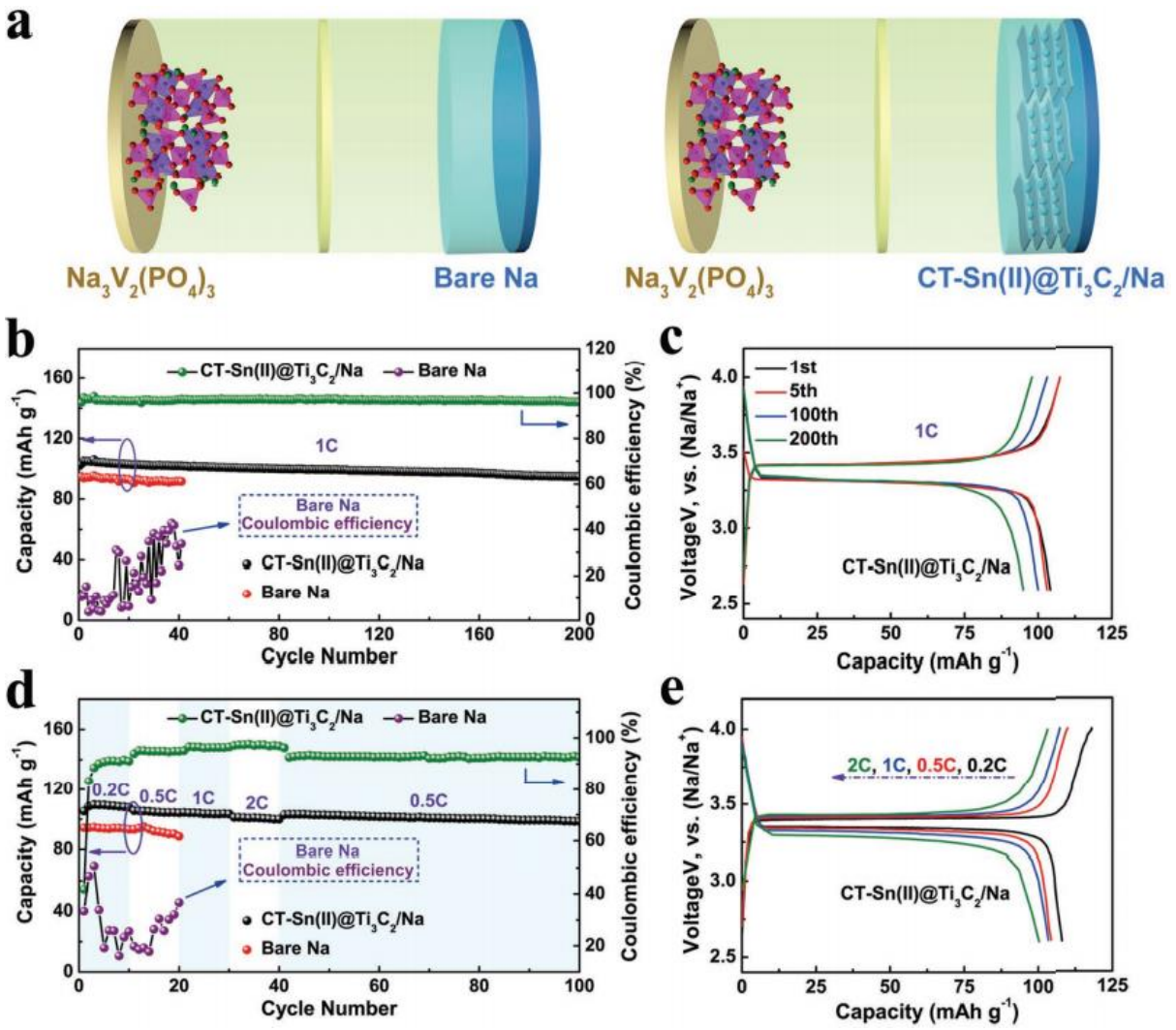

Figure 2- 12 (a) Full-cell configuration of MXene based sodium metal battery. (b-e) Electrochemical performance of the cell, including cycling performance, charge-discharge curves and rate performance [112].

Metal oxides have also been applied to enhance MXene as an anode material of LIBs. Particularly, SnO_2 is an appropriate enhancing material because of its high theoretical capacity, low cost and environmental friendliness. Wang et al. prepared SnO_2 nanoparticle embellished Ti_3C_2 MXene (SnO_2-Ti_3C_2) composite materials by a hydrothermal method and the obtained SnO_2-Ti_3C_2 exhibited a capacity of 1,030 mAh g^{-1} at 100 mA g^{-1} at the first cycle, and retained 360 mAh g^{-1} after 200 cycles [113]. However, since MXene is easily oxidized which could lead to the collapse of the structure during hydrothermal treatment, so this method might not be the best strategy to modify MXene with metal oxides. Ahmed et al. used low-temperature atomic layer deposition to modify SnO_2 particle on MXene (SnO_2/MXene), which is followed by coating with a conformal thin passivation layer of inactive HfO_2. The obtained HfO_2 coated

SnO_2/MXene anode exhibited a specific capacity of 843 mAh g^{-1} at 500 mA g^{-1} after 50 cycles. Carbon coating is another effective strategy to stabilize the structural of MXene [114]. Wu et al. prepared a kind of $MoS_2/Ti_3C_2/C$ composite with unique 2D hierarchical structure by assembling carbon coated MoS_2 on carbon stabilized Ti_3C_2 MXene. The obtained $MoS_2/Ti_3C_2/C$ anode exhibited a capacity of 580 mAh g^{-1} at 20 A g^{-1} with 95 % capacity retention after 3,000 cycles [114].

In theory, MXene materials with lower molecular weights will exhibit higher gravimetric capacity. Xie et al. investigated the Li ions storage capacity of some MXenes with lower formula weights (Compared with $Ti_3C_2T_x$, including Sc_2C, Ti_2C, Ti_3C_2, V_2C, Cr_2C and Nb_2C) using DFT theoretical calculations, and the results showed that Ti_2C MXene exhibited the highest theoretical capacity [115]. Meanwhile, the electrochemical performance of other kinds of functionalized M_2CT_x MXene (M=Ti, V, Cr, Mn, Fe, Co, Ni, Nb and Mo) were investigated as electrode materials for LIBs. Sun et al. investigated the Li ion insertion behaviors of V_2CO_2 and the structural transformation by DFT calculation [116]. The lithium storage capacity of nitride and carbonitride MXene as anodic materials of LIBs were also investigated.

2.3.5 Summary

Because of the excellent thermal, optical, electrical and mechanical properties of MXenes, they are considered as one of the most promising materials in a massive range of research and application areas, especially energy storage. Researchers expended a lot of effort to investigate the structural, properties and electrochemical application of MXenes by experiment and theoretical calculation and the former has verified those superior properties of MXene proposed in the simulations. The results demonstrated that MXenes exhibited large potential application for electrochemical energy storage devices including Li-ion batteries and supercapacitors. Besides, there are many breakthroughs for the application of MXene-based materials to the field of electrochemical energy storage. However, there is definitely a long way to go to improve both the preparation and applications of MXene. Further investigations are still desirable to shed light on the practical applications of MXene-based materials in electrochemical energy storage.

2.4 Manufacturing Methods for MXene based electrodes

2.4.1 Introduction

There are numerous economically efficient and eco-friendly manufacturing methods of MXene for energy storage, sensor, electronics or other wide variety of applications, such as vacuum filtration, spray coating, spin coating, screen printing, 3D printing and tape-casting. With these methods they can be processed as thin films, free-standing paper, and also complex structures like fibers and interdigital patterns. Based on first-principle calculations, compared with the bare MXenes without any terminated groups, those with terminations are more likely to have negative enthalpy of formation with significant thermodynamic stability [117]. The surface states of the materials have significant influence on the attractive force within the dispersion [118]. The negative zeta potential and hydrophilicity leads to a stable MXene suspension, slurry or ink without further addition of other additives or surfactants. Therefore, the formulation of stable MXene dispersions with specific rheological properties play an important role in the processability of these systems (**Fig. 2-13**).

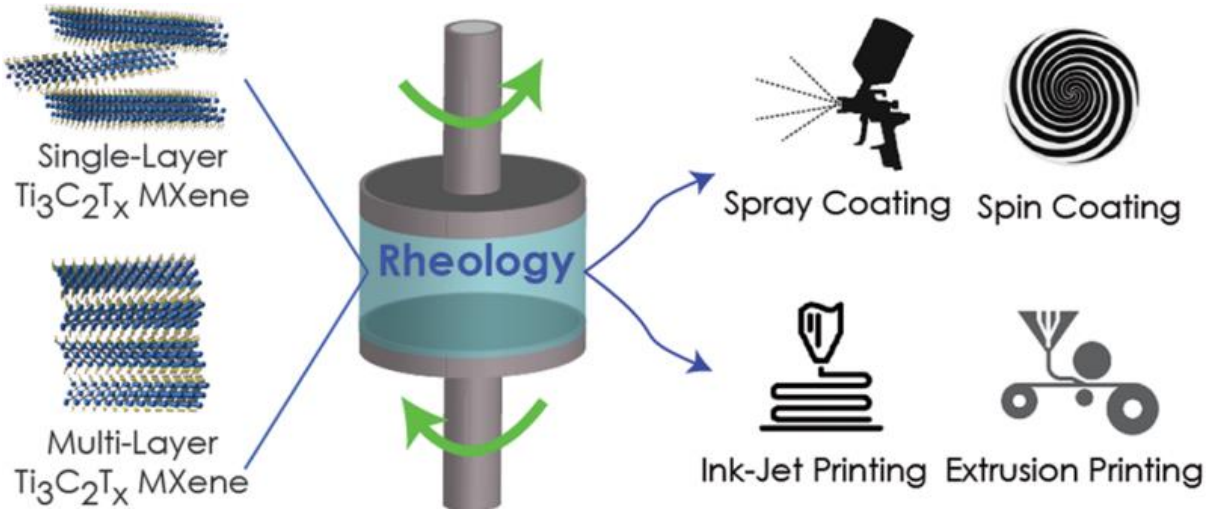

Figure 2- 13 A guide for processing MXenes [119].

2.4.1.1 Rheological Properties of MXene

Investigating the rheological behaviour of MXene enables further processing, scalable fabrication and integration into to complex 3D architectures by coating, tape casting and printing techniques. The high negative surface charge and polar terminations make $Ti_3C_2T_x$ and some other MXenes display superior hydrophilicity and facilitates easy preparation into colloids, slurries, and inks in polar solvents for post manufacturing processes. Foremostly, viscosity is a critical parameter to understand more about the flow properties of MXene colloids. After evaluating the viscosity, a study of viscoelastic behaviour is also useful to further understand the fundamental research motivations as well as suitability of practical

applications. In particular, shear-thinning is a prerequisite for printing and coating techniques, e.g. screen printing, extrusion-printing, tape-casting, spray coating. The ratio of elastic (storage) modulus (G') to viscous (loss) modulus (G'') can also contribute in determining the rheological performance of a dispersion (as shown in **Fig. 2-14**) [119].

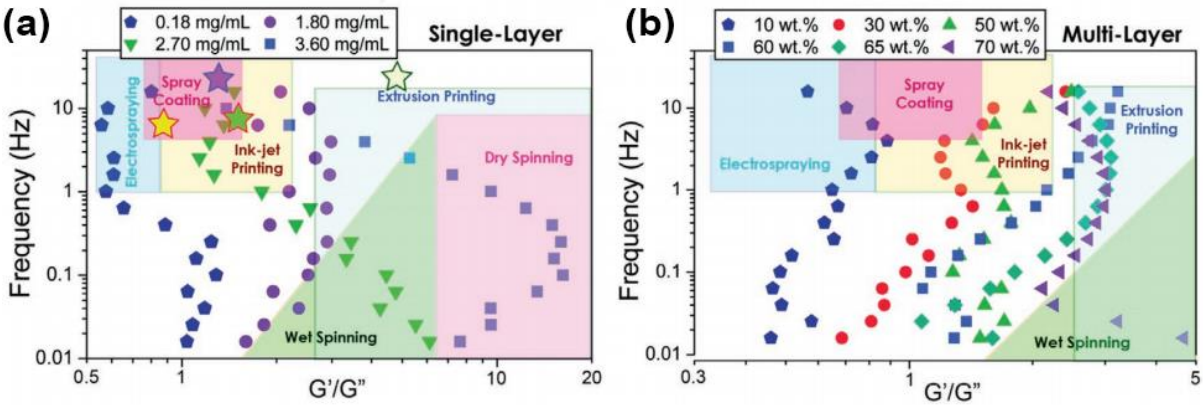

Figure 2- 14 Frequency versus the G'/G'' ratio for aqueous (a) single-layered MXene and (b) multi-layered MXene based inks for various printing techniques [119].

In 2018, Akuzum et al. investigated the viscosity and viscoelasticity of $Ti_3C_2T_x$ dispersions in deionized water [119]. In this work, the rheological properties of a wide range of concentrations and different flake states (single-layer and multi-layer flakes) were explored (**Fig. 2-15**). For the first time they showed the shear-thinning and viscoelasticity of aqueous bare $Ti_3C_2T_x$ dispersions. According to their results, $Ti_3C_2T_x$ dispersions with different flake states should be regarded as two separate systems to be investigated, and they all exhibited distinct rheological properties offering versatile performance in fabrication. The single layered MXene ink showed evidence of elasticity even when the concentration was lower than 0.2 mg mL^{-1}, which may be caused by few reasons: 1. negative surface charge; 2. hydrophilicity; 3. comparatively lower mass and packing density. For the multi-layered MXene, even though the loading is increased to 70 wt%, it still has observable flowability, which can achieve higher viscosity and elasticity by using higher solid loading [119].

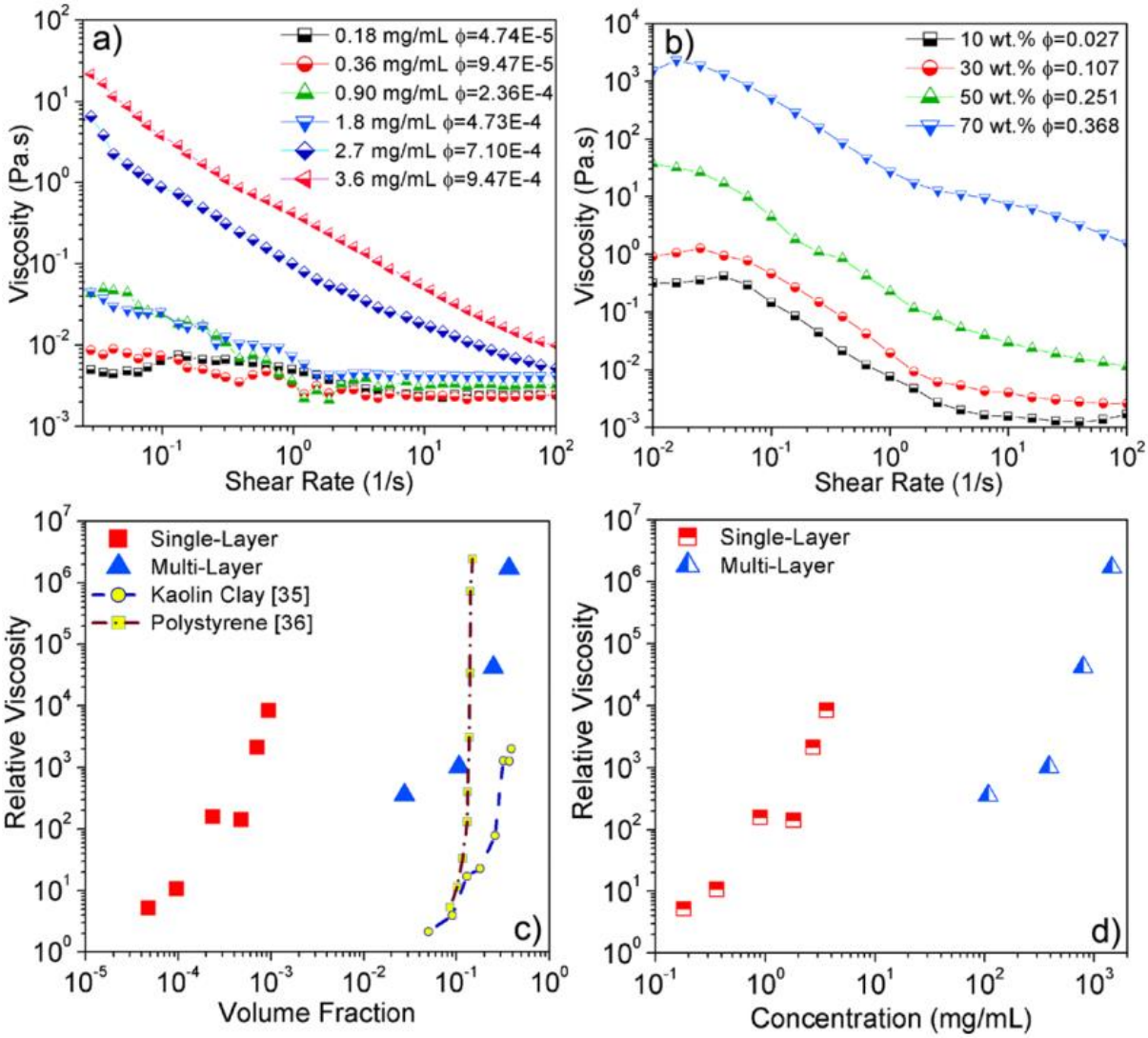

Figure 2- 15 Rheological properties of $Ti_3C_2T_x$ with various concentrations. (a) and (b) measured viscosity versus shear rate of MXene susoensions with single-layered flakes and multi-layered flakes, respectively [119].

For various printing, coating or alternative methods, the rheological requirements vary from a gel-like paste for extrusion printing, low viscosity slurry for screen printing and tape casting, and further low concentration dispersions for spray coating. For spray coating, higher G'' is needed to process faster, while 3D printing requires higher G' to maintain the shape of the printed pattern [118]. After the first MXene related review paper concerning rheology was published, there has been more research on the rheological behaviour of MXenes. Zhang et al. investigated additive free $Ti_3C_2T_x$ ink for direct printing, including extrusion printing with aqueous inks and inkjet printing with organic inks [120]. All the organic inks demonstrated non-Newtonian characteristics and pseudoplastic behaviour. In our first published work [121], 15 mg mL^{-1} $Ti_3C_2T_x$ ink made of single/few 2D flakes with larger aspect ratio can achieve similar

order of magnitude of viscosity as 70 wt% multi-layered $Ti_3C_2T_x$ did [119]. Afterwards, Yu et al. reported a N-doped MXene ink for screen printing and 3D printing. Their ink exhibited high viscosity of over 10^4 Pa·s at an initial shear rate of 0.05 s^{-1}, which ensured a fixed shape [122].

In conclusion, to exert control over the rheological properties of the MXene ink, adjusting the flake size and volume fraction of 2D sheets are key. Based on the excellent rheological properties of MXenes, their suitability as base materials for functional applications as well as additives to support processing are substantiated. Malchik et al. reported a method to use few-layer delaminated $Ti_3C_2T_x$ as the conductive agent and also binder to fabricate freestanding $NaTi_2(PO_4)_3$ film for sodium-ion battery anodes, which showed good energy density, rate performance and superior cycling stability [123]. As long as the rheological behaviours of MXene can be understood and controlled, various printing/coating processing methods (**Fig. 2-16**) can be more easily adapted for diverse applications [118].

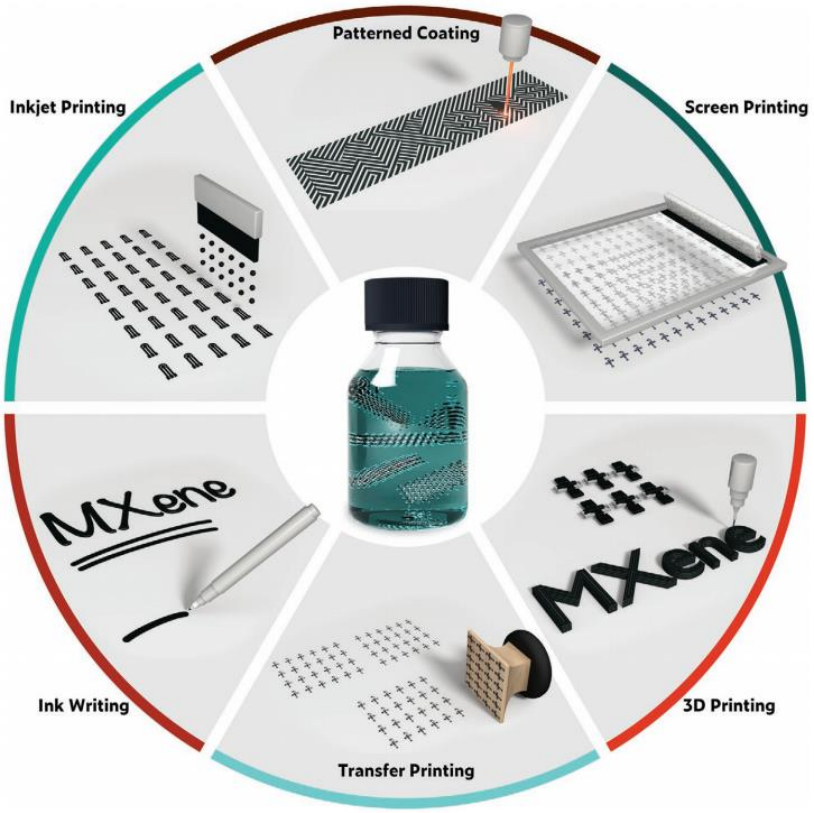

Figure 2- 16 Different manufacturing methods to prepare MXene films, which are relied on the rheological properties of the MXene dispersions [118].

2.4.1.2 Chemical stability of MXene inks

Since MXenes show very promising dispersion stability in water, the oxygen dissolved in water can also affect their stability significantly by chemically degrading the delaminated MXene flakes [82,124]. Typically, more oxidation is prone to happen when the flake is more exfoliated, especially single layer MXene, which has the largest surface area-to-volume ratio [118]. The degradation leads to structural breakdown due to the formation of non-2D (amorphous) metal oxides, resulting in irreversible effects on the MXene inks. After structural deformation, even if the concentration of the MXene suspension is kept the same as its initial, the rheological behaviour cannot reach its previous characteristics. In addition, high temperature, sonication and long exposure to sunlight can also accelerate oxidation speed [42,125]. Many challenges still exist that hinder the ability to store water based MXene inks for long durations. In order to achieve similar rheological behaviour, fabrication parameters, and obtain comparable data, all the MXene inks have to be used as soon as possible when they are freshly prepared and successively dried after it has been processed. Furthermore, a promising path would be if the application can allow the MXene to be stored in organic solvents. As Kathleen et al. indicated, well suspended MXene dispersions in the organic solvents can remain stable for several months [83].

2.4.2 Manufacturing methods

2.4.2.1 3D printing

3D printing, also known as additive manufacturing (AM), continuous extrusion printing, is one of the most common manufacturing techniques to build 3D complex architectures digitally followed by physically printing it out, which allows the fabrication of the desired objects with accurate shapes and economical application of materials. There are two main categories of 3D printing methods. One exploits the light/temperature sensitivity characteristics of the material, while the other is based on the rheological properties of the ink itself [126]. The first method is a more mature technique with high resolutions achieved by printing photopolymerizable resins or thermoplastic polymer powders, such as stereolithography (SLA) and selective laser sintering (SLS) [126], as shown in **Fig. 2-17**. The ink-based method, relies on the material itself or the substantial addition of binders, thus development is still at a laboratory scale. Typically, after drying, the printed electrodes have 3D porous microstructure with large specific surface area, which allows for shorter charge transport routes and faster diffusion of electrolyte ions during charging and discharging. Referred to as continuous extrusion initially, high viscosity,

high yield stress under shear and compression, and well-controlled viscoelasticity are strict necessities. Besides this, shear thinning (pseudoplastic) behaviour ensures that when the force is applied, the ink can flow through the needle smoothly. In addition, the ink requires thixotropic properties to ensure the printed rods recover to its previous high viscosity immediately after leaving the needle without an externally applied force. Therefore, controlling and tuning the rheology behaviour of the ink are very essential steps in this research.

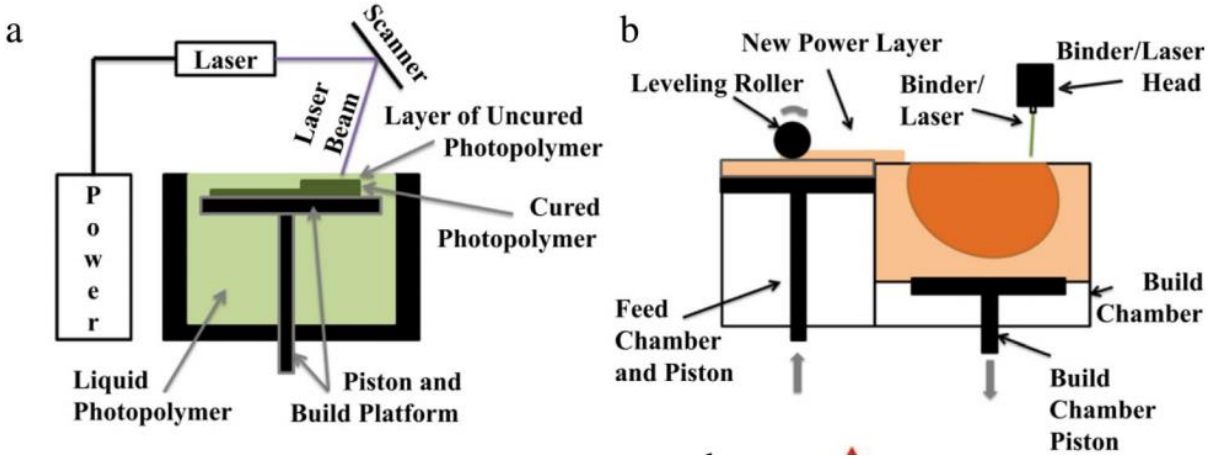

Figure 2- 17 Schematic of (a) stereolithography and (b) selevtive laser sintering [126].

There are already many papers reporting printed micro-energy storage devices via this method. Graphene oxide (GO)/graphene and other exfoliated 2D materials like MXenes are the next generation material choices to prepare functional inks for 3D printing. As reported, GO/graphene based inks exhibited shear-thinning behaviour [127,128]. In order to attain suitable G' to avoid the collapse of the printed structure, high mass fraction of GO/graphene has to be prepared or adding additives such as polymeric binders [129,130] and/or inorganic particles [131]. **Fig. 2-18a** demonstrates the apparent viscosity of GO suspension as a function of shear rate. GO suspensions with concentration of 20 and 40 mg mL^{-1} were investigated [131]. It was found that, when increasing the GO suspension concentration, there is an apparently increase in viscosity even at higher shear rate manifesting in better printability of the ink. Additionally, the influence of binder was also investigated. Silica filler was added into GO suspension to increase the viscosity. Based on **Fig. 2-18b**, 20 mg mL^{-1} GO suspensions showed poorer printability (G', G''), while 40 mg mL^{-1} GO suspensions with silica filler increased by over one order of magnitude, which proved that the GO suspensions of higher concentration with higher amount of silica filler could improve the printability of the inks.

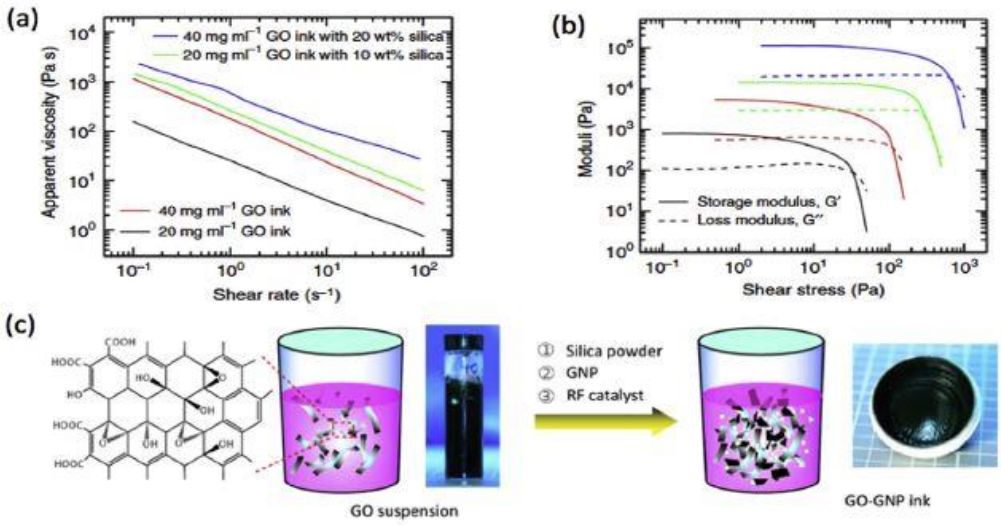

Figure 2- 18 (a) Viscosity as a function of shear rate of GO/GO composite; (b) G', G''/Pa as a function of shear stress of GO/GO composite suspension; (c) Schematic of the ink preparation [131].

Shen et al. developed sulfur copolymer-graphene inks for lithium-sulfur batteries by adding sublimed sulfur and 1,3-diisopropenylbenzene (DIB) to GO solution [132]. The prepared inks show excellent shear-thinning behaviour, which can used to print the as-designed architectures. Besides this, the plateau of G' is an order of magnitude higher than G'', indicating elastically controlled behaviour. With the shear stress increased to over 10^3 Pa, viscosity plays a dominant role, which makes the ink exhibit liquid like behaviour, as shown in **Fig. 2-19**.

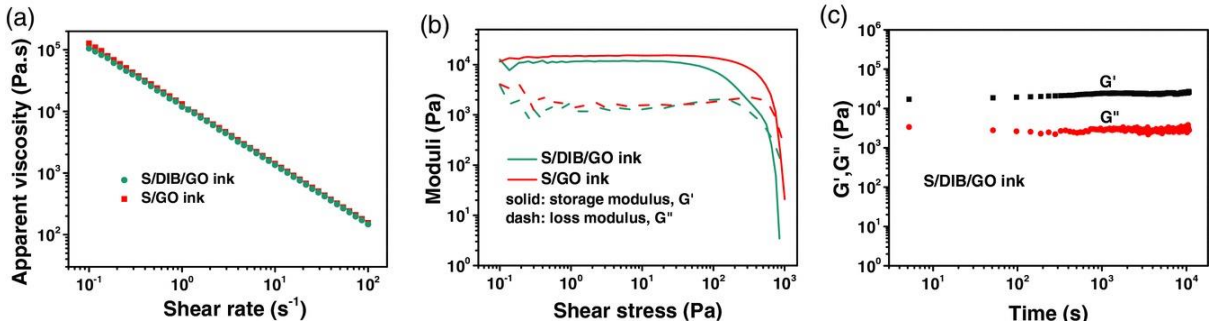

Figure 2- 19 Rheological properties of inks. a) Apparent viscosities of S/DIB/GO and S/GO inks. b) G' and G'' at a shear stress from 10^{-1} to 10^3 Pa for S/DIB/GO and S/GO inks. c) Aging properties of the S/DIB/GO ink [132].

In order to maximize the electrical, thermal and further functionality of the printed ink, usage of additives should be avoided. Ideally, the 2D materials can be dispersed uniformly in a water-based solvent without setting or re-agglomeration. Our first work has shown the possibility of additive-free $Ti_3C_2T_x$ aqueous inks for 3D printing. After MILD method etching, thin $Ti_3C_2T_x$ 2D sheets with ~8 μm flake size were used to formulate homogeneous inks, which showed

ideal viscoelastic properties for extrusion-based 3D printing [121]. Soon afterwards, Orangi et al. demonstrated $Ti_3C_2T_x$ ink with high concentration (290 mg mL^{-1}) for ultra- high energy density supercapacitor application [133]. After etching, superabsorbent polymer (SAP) beads were used to concentrate their inks, and then a gel-like ink can be printed on a substrate with layer-by-layer structure (**Fig. 2-20**).

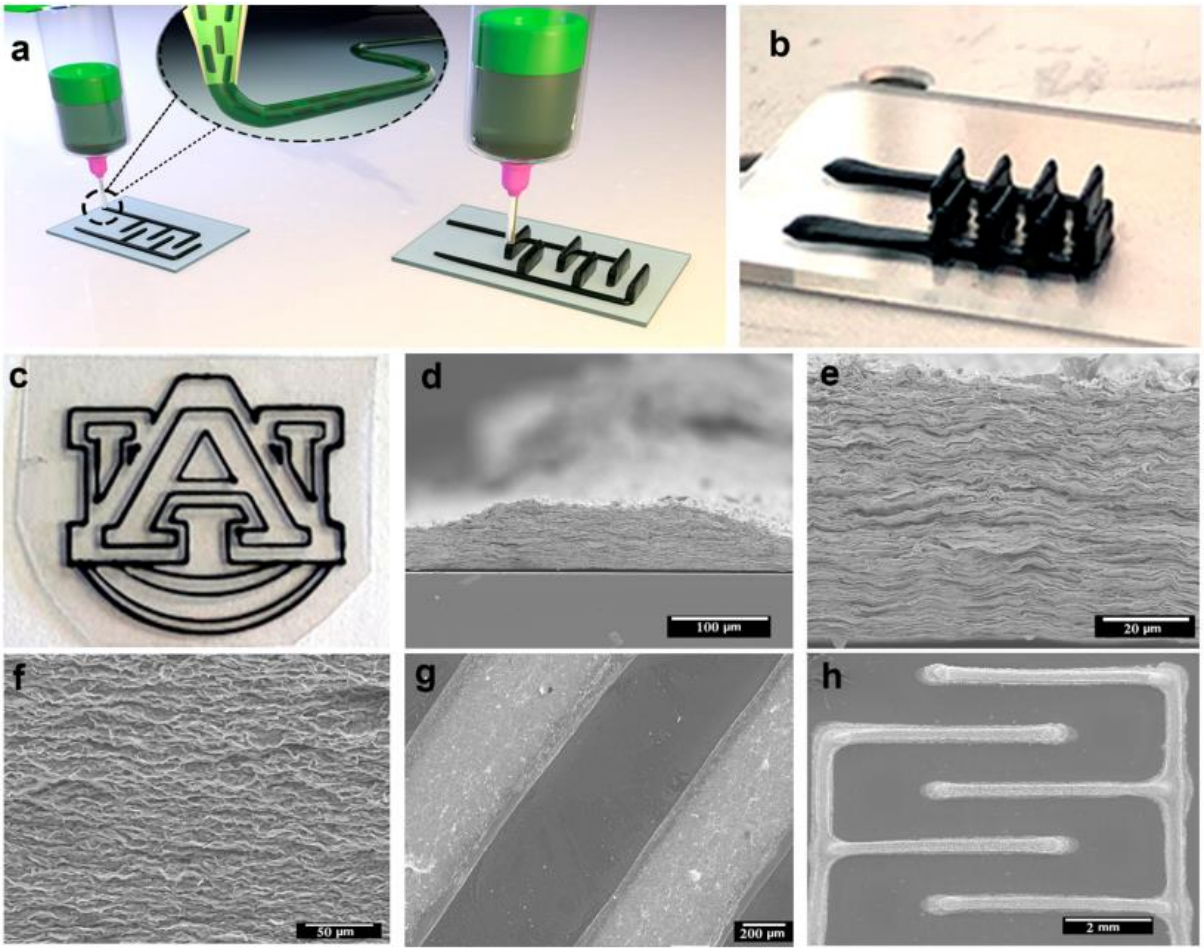

Figure 2- 20 (a-c) Schematic and digital photos of the 3D printed electrode for micro supercapacitors. (d-h) SEM images of the printed structures [133].

Fan et al. reported nitrogen-doped $Ti_3C_2T_x$ inks to 3D print the anode part for sodium-ion hybrid capacitor applications [134]. Carbon nanotubes (CNTs) and GO were also added to improve the rheological performance of the ink (**Fig. 2-21**). The printed structure showed open pores and uniform N-doping distribution, resulting in faster ion pathways during electrochemical reactions and superior Na-ion storage behaviour.

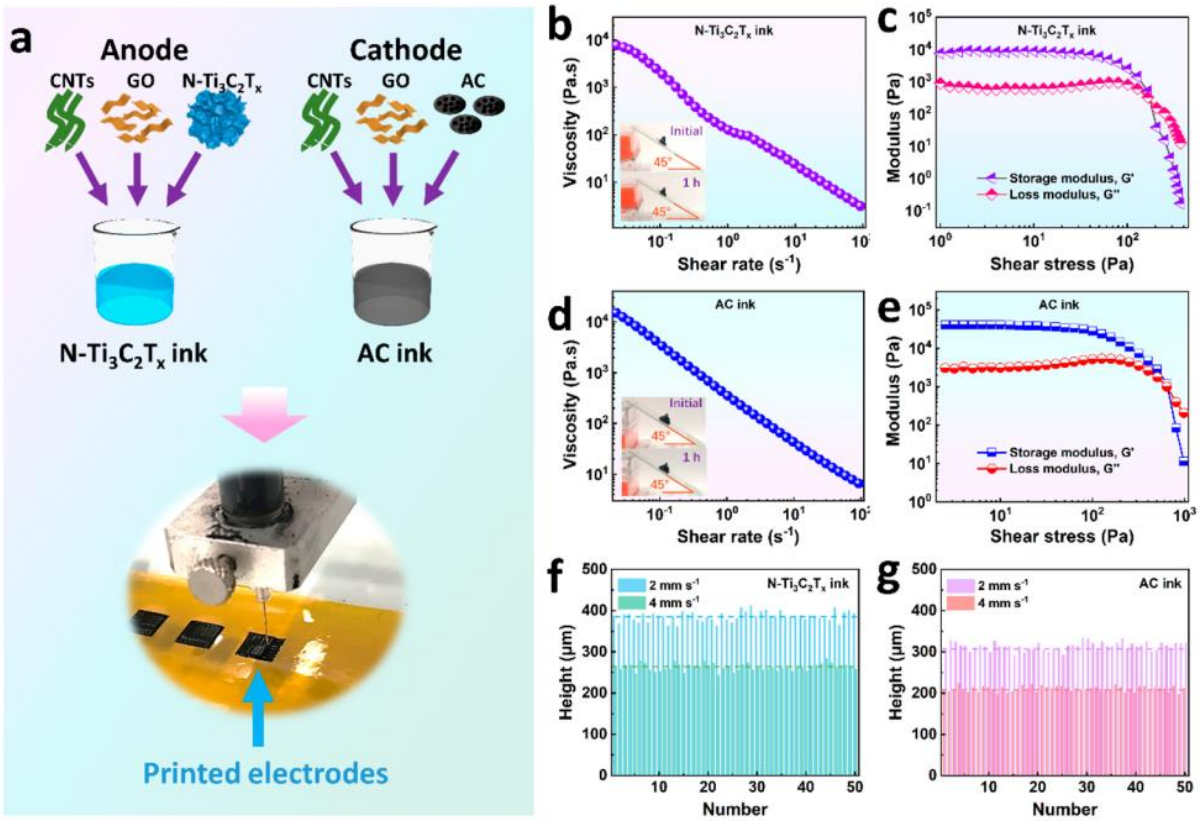

Figure 2- 21 (a) Schematic of the ink preparation. (b-e) Rheological performance of the inks. (f,g) Height distribution of the 2D printed filaments [134].

2.4.2.2 Tape casting/Freeze-assisted tape casting

Freeze-templating also commonly referred to as freeze-casting has been a popular method in manufacturing porous electrodes for energy storage devices due to its simplicity and potential scalability which will allow for high volume production. This process utilizes the crystallisation of a liquid phase during solidification within an aqueous dispersion to template the microstructure of a hydrogel. This can then be subject to drying methods to remove water thereby forming a highly porous aerogel foam.

Practically, a stable colloid is casted onto a cooling bed which induces a directional temperature gradient. This will initiate freezing of the colloidal dispersion, in which the more energetically favourable heterogeneous nucleation will occur [135]. The thermal gradient will consequently result in ice crystals growing with a lamellar morphology which exerts a force on the flakes and/or particulates within the colloid, segregating them between the ice-crystals [136,137]. An illustration of particle interactions at the freeze-front of the growing ice-crystals can be seen in **Fig. 2-22**. Once the solvent has been removed, the result is an anisotropic microstructure which

typically has lamellar channels in the direction of the thermal gradient and circular pores perpendicular to the thermal gradient.

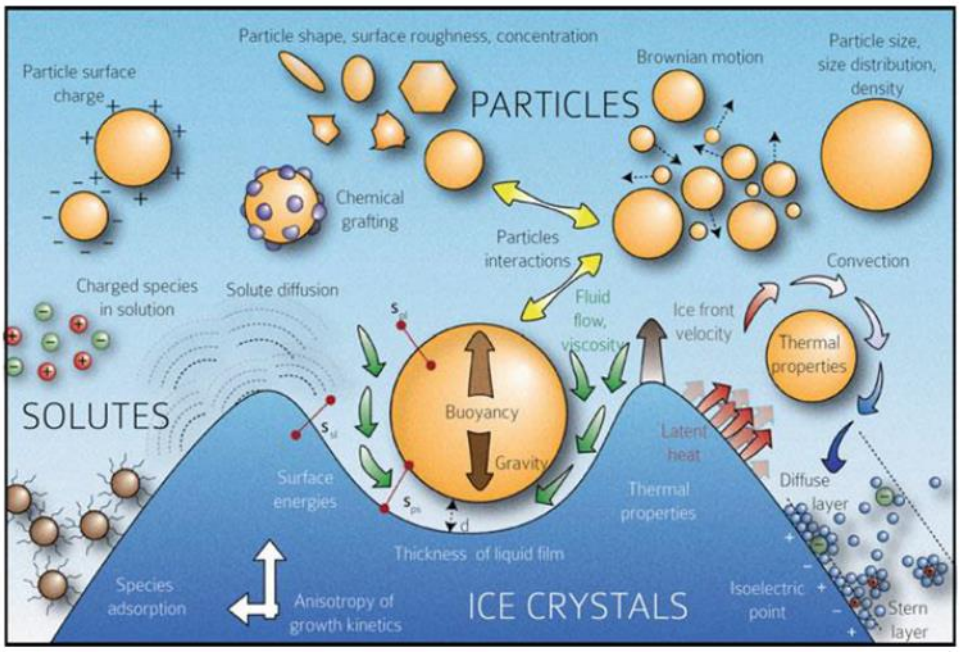

Figure 2- 22 Illustration of various particle interactions that occur at the freeze-front of a colloid that is being freeze-templated [135].

Within the last few years, although often not explicitly stated, freeze-casting has been a widely applied as a facile method together with hydrothermal synthesis to form highly porous electrodes for energy storage devices. An example of this is in the work of Yuanlong Shao et. al. who fabricated '3D' freeze-casted cellular graphene films for ultrahigh power density supercapacitors [138]. In their work, a hierarchically porous graphene film was fabricated by a combination of vacuum filtering and freeze-casting partially reduced graphene oxide. The morphology of this film can be observed in **Fig. 2-23**. This as-fabricated film managed an impressive gravimetric capacitance of 284.2 F g^{-1} at a current density of 1 A g^{-1} and retained 61.2 % of the initial capacitance once the current density was raised to 500 A g^{-1}, with 1 M H_2SO_4 as the electrolyte.

Contrastingly, an RGO film that had not integrated the freeze-casting step only achieved a gravimetric capacitance of 181.3 F g^{-1} at 1 A g^{-1} with a retention of only 27.8 % at 500 A g^{-1}. This performance discrepancy elucidates the potential benefits of a templated porous architecture, which would have less re-stacked RGO sheets and higher accessible surface area which could contribute to final electrode capacitance.

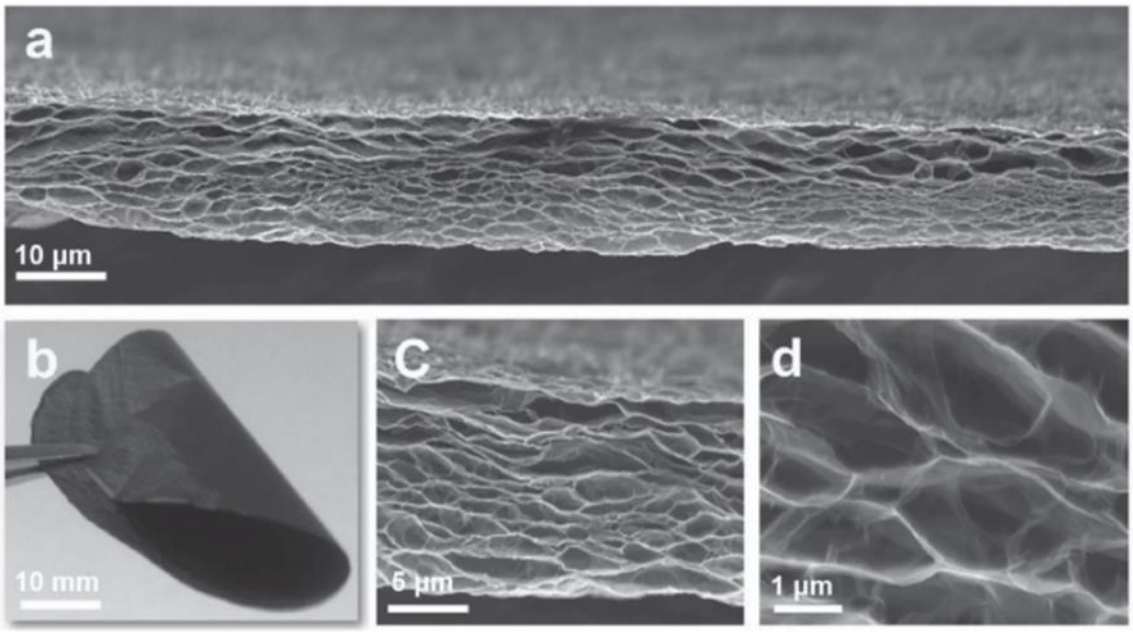

Figure 2- 23 Morphology of 3D porous RGO films a) cross-section SEM image of 3D porous RGO film after long-term reduction b) Photograph of a bent 3D porous RGO film c,d) Partially enlarged views of (a) under higher magnification [138].

In a similar approach, Peng Zhang et. al. used an in-situ ice template approach to fabricate '3D' flexible MXene film-based electrodes for high performance supercapacitors [139]. In their work, porous films of $Ti_3C_2T_x$ MXene with interspersed carbon nanotubes (CNT) were formed by freeze-drying the hydrated films. This resulted in a porous networked supercapacitor electrode which was able to deliver a capacitance of 375 F g^{-1} at 5 mV s^{-1} and retain 251.2 F g^{-1} at a scan rate of 1,000 mV s^{-1}. As a symmetrical supercapacitor, the device managed an energy density of 9.2 Wh kg^{-1}. The work showcases how an in-situ templating strategy aids in mitigating restacking of 2D nanomaterial sheets [140], with the CNTs acting as functional spacers within the porous network.

Further to this, an interesting application of freeze-casting can be seen in the work by Qingrong Wang et. al., in which they were able to design typographical supercapacitors with an integrated architecture [141]. The resultant flexible integrated supercapacitor structure was formed by exfoliated graphene (EG) current collectors, symmetric polyaniline/reduced graphene oxide (PANI/rGO) electrodes and a cellulose nanofiber (CN) separator (seen in **Fig. 2-24b**). It was elucidated that the integrated film with compressed porous structures had higher tensile strength and Young's modulus than that of the individual components and a conventional stacked device (seen in **Fig. 2-24c**). This was hypothesized to be due to strong interfacial strength between neighbouring layers which could lead to effective load transfer (as can be

seen in **Fig. 2-24d**) [141]. This feature is especially important for implementation in flexible electronics which would require robust flexible energy storage devices. The fabricated device with a mass ratio of PANI to rGO of 1 managed an appreciable specific capacitance of 511 F g^{-1} with a retention of 275.9 F g^{-1} at 10 A g^{-1} and energy density of 6.13 Wh kg^{-1} at a power density of 9.60 kW kg^{-1} (when calculated with mass of electrode). This work provides some insight on potential benefits an integrated structure fabricated with freeze-casting might provide for a flexible energy storage device.

Looking through literature, a generalisation can be made that freeze-casting is inherently employed in fabricating porous energy storage device components (such as the electrode) in discretized and/or monolithic manufacturing steps. Commercially, this is not very ideal as roll-to-roll manufacturing of films are a more appropriate medium for scalable manufacturing of electrode stacks. Therefore, tape casting can be combined with this templating method in the process called freeze-tape casting to facilitate roll-to-roll manufacturing. Tape casting is a well-established process in which a doctor blade is used to govern the thickness of a colloid that is being cast onto a substrate [142].

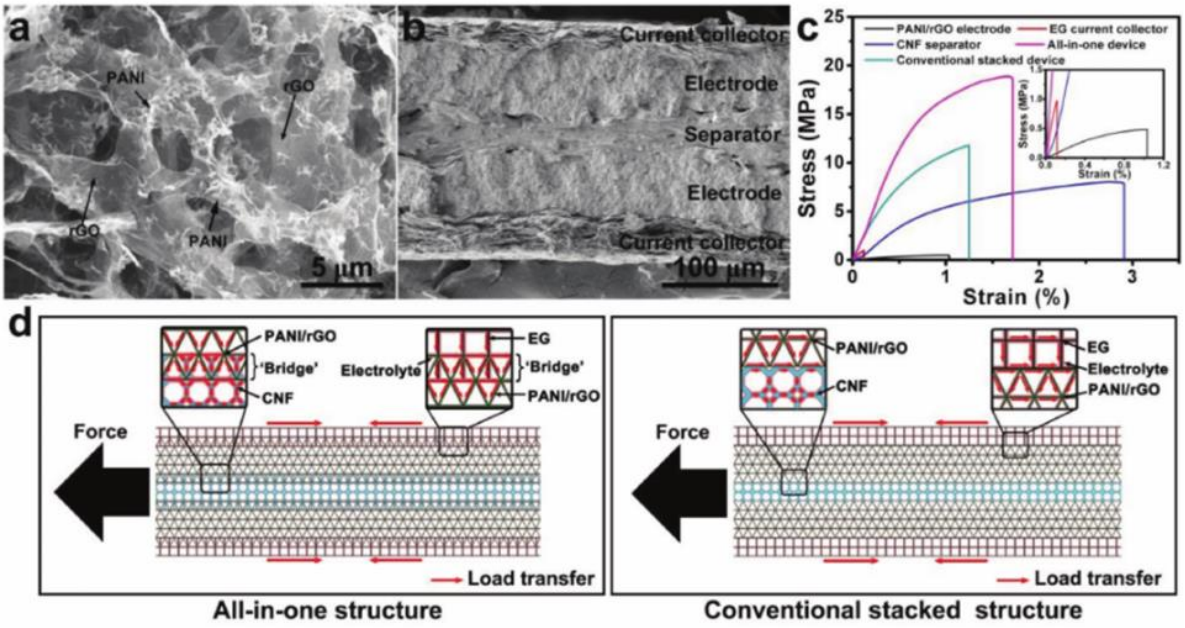

Figure 2- 24 a) SEM micrograph of PANI/rGO composite (1.0 mass ratio) b) Cross-section SEM micrograph of the all in one device with EC current collector, PANI/rGO electrodes and CN separator c) Stress-strain plot of the respective discrete device components, conventionally stacked device and integrated all-in-one device d) Proposed load transfer mechanism of the all-in-one and conventionally stacked structure [141].

Literature surrounding the application of freeze-tape casting of 2D nanomaterials for energy storage devices currently, is sparse [143–146]. Most works to be found apply heuristic fabrication methods such as formation of the electrode film with vacuum filtration such as in the previously mentioned work [138]. This can potentially lead to the restacking of the 2D nanosheets [140], which will then require supplementary processes or additives to mitigate. An area of interest that would require further research and method development is in utilizing this freeze-tape casting fabrication route to prevent restacking of the 2D nanosheets within the electrode material and form integrated device structures such as in [141]. A good example of this method being applied is in work by Yoon Hwa et. al. in which directional freeze-tape casting was used to create aligned sulfur-graphene oxide electrodes for a Li-S cell [147]. The resultant cell fabricated with this electrode demonstrated extended cycling capabilities (4 % retention after 200 cycles) as opposed to a conventionally prepared tape-casted electrode. It was ascertained that the low tortuosity of the electrode and the confining influence of GO on soluble polysulphides influenced its stability and performance. Similar performance benefits of using such a manufacturing method can be observed in work by Milad Ghadkolai et. al. in which thick Mo doped $Li_4Ti_5O_{12}$ electrodes were freeze tape casted for lithium-ion batteries [148]. The resultant cells demonstrated improved specific capacity and rate performance despite being thicker than conventionally tape casted electrodes.

The highlighted works serve as a good origination for this research theme. The benefits and fundamental principles of this manufacturing method to develop complex architectures for electrodes is evident. Furthermore, a gap can be perceived in understanding the ability of such a method in forming integrated hierarchical structures, with 2D nanomaterials and especially with MXenes. Thus, this is a domain that will be addressed in this research.

2.5 Summary

As an active material for energy storage, MXenes have shown high electronic conductivity, high packing density, tunable interlayer distance and outstanding electrochemical capacitance over other conductive 2D materials for supercapacitors. However, as might be expected, there are also restacking problem when we process them, which existed in almost all the few-layer exfoliated 2D materials. Compared with the authentic 2D sheets, agglomoration causes insufficient usage of the active materials and longer ion transport pathways for the electrolyte ions, leading to lower specific capacitance and lower rate performance especially in a thick electrode. As the active component of energy storage devices, thicker MXene electrodes are

required to achieve higher specific areal energy density. Thus, novel MXene nanostructures with porous framework has become desirable to boost the energy storage application by facilitating ion diffusion during electrochemical reaction. Due to the hydrophilicity and abundant highly negatively charged groups on the surface of MXene flakes, they can be easily processed to a stable colloidal dispersion in water and also in various organic solvents, which can be applied to efficient integration and direct fabrication to controllably manufacture the energy devices.

Reference

[1] A. K. Geim, *Phys. Scr.* **2012**, *T146*, 014003.

[2] M. Alhabeb, K. Maleski, B. Anasori, P. Lelyukh, L. Clark, S. Sin, Y. Gogotsi, *Chem. Mater.* **2017**, *29*, 7633.

[3] Q. Jiang, Y. Lei, H. Liang, K. Xi, C. Xia, H. N. Alshareef, *Energy Storage Mater.* **2020**, *27*, 78.

[4] J. W. Colson, A. R. Woll, A. Mukherjee, M. P. Levendorf, E. L. Spitler, V. B. Shields, M. G. Spencer, J. Park, W. R. Dichtel, **2011**, *332*, 228.

[5] M. Chhowalla, H. S. Shin, G. Eda, L. J. Li, K. P. Loh, H. Zhang, *Nat. Chem.* **2013**, *5*, 263.

[6] X. Xiao, H. Yu, H. Jin, M. Wu, Y. Fang, J. Sun, Z. Hu, T. Li, J. Wu, L. Huang, Y. Gogotsi, J. Zhou, *ACS Nano* **2017**, *11*, 2180.

[7] Y. U. Yi-jun, Z. Yuan-bo, **2017**, *46*, 205.

[8] A. K. Geim, I. V. Grigorieva, *Nature* **2013**, *499*, 419.

[9] S. V. Sokolov, E. Kätelhön, R. G. Compton, *J. Phys. Chem. C* **2015**, *119*, 25093.

[10] S. Chuah, W. Li, S. J. Chen, J. G. Sanjayan, W. H. Duan, *Constr. Build. Mater.* **2018**, *161*, 519.

[11] L. K. Putri, W. J. Ong, W. S. Chang, S. P. Chai, *Appl. Surf. Sci.* **2015**, *358*, 2.

[12] O. Dyck, M. Yoon, L. Zhang, A. R. Lupini, J. L. Swett, S. Jesse, *ACS Appl. Nano Mater.* **2020**, *3*, 10855.

[13] A. Eftekhari, P. Jafarkhani, *J. Phys. Chem. C* **2013**, *117*, 25845.

[14] C. Ding, Y. Zhao, D. Yan, Y. Zhao, H. Zhou, J. Li, H. Jin, *Electrochim. Acta* **2016**, *221*, 124.

[15] P. Yan, R. Zhang, J. Jia, C. Wu, A. Zhou, J. Xu, X. Zhang, *J. Power Sources* **2015**, *284*, 38.

[16] M. Hu, Z. Li, H. Zhang, T. Hu, C. Zhang, Z. Wu, X. Wang, *Chem. Commun.* **2015**, *51*, 13531.

[17] V. Bayram, M. Ghidiu, J. J. Byun, S. D. Rawson, P. Yang, S. A. McDonald, M. Lindley, S. Fairclough, S. J. Haigh, P. J. Withers, M. W. Barsoum, I. A. Kinloch, S. Barg, *ACS Appl. Energy Mater.* **2020**, *3*, 411.

[18] R. Marom, S. F. Amalraj, N. Leifer, D. Jacob, D. Aurbach, *J. Mater. Chem.* **2011**, *21*, 9938.

[19] Y. Yang, S. Bremner, C. Menictas, M. Kay, *Renew. Sustain. Energy Rev.* **2018**, *91*, 109.

[20] L. Zhang, X. Hu, Z. Wang, F. Sun, D. G. Dorrell, *Renew. Sustain. Energy Rev.* **2018**, *81*, 1868.

[21] A. Borenstein, O. Hanna, R. Attias, S. Luski, T. Brousse, D. Aurbach, *J. Mater. Chem. A* **2017**, *5*, 12653.

[22] H. Liu, X. Liu, S. Wang, H. K. Liu, L. Li, *Energy Storage Mater.* **2020**, *28*, 122.

[23] A. Muzaffar, M. B. Ahamed, K. Deshmukh, J. Thirumalai, *Renew. Sustain. Energy Rev.* **2019**, *101*, 123.

[24] F. Zhang, M. Wei, V. V. Viswanathan, B. Swart, Y. Shao, G. Wu, C. Zhou, *Nano Energy* **2017**, *40*, 418.

[25] N. Kittner, F. Lill, D. M. Kammen, *Nat. Energy* **2017**, *2*, 1.

[26] M. Cheng, R. Deivanayagam, R. Shahbazian-Yassar, *Batter. Supercaps* **2020**, *3*, 130.

[27] T. Gao, Z. Zhou, J. Yu, J. Zhao, G. Wang, D. Cao, B. Ding, Y. Li, *Adv. Energy Mater.* **2019**, *9*, 1.

[28] B. Anasori, M. R. Lukatskaya, Y. Gogotsi, *Nat. Rev. Mater.* **2017**, *2*, 16098.

[29] D. Xiong, X. Li, Z. Bai, S. Lu, *Small* **2018**, *14*, 1.

[30] L. Tao, E. Cinquanta, D. Chiappe, C. Grazianetti, M. Fanciulli, M. Dubey, A. Molle, D. Akinwande, *Nat. Nanotechnol.* **2015**, *10*, 227.

[31] S. Zhao, Y. Wang, J. Dong, C. T. He, H. Yin, P. An, K. Zhao, X. Zhang, C. Gao, L. Zhang, J. Lv, J. Wang, J. Zhang, A. M. Khattak, N. A. Khan, Z. Wei, J. Zhang, S. Liu, H. Zhao, Z. Tang, *Nat. Energy* **2016**, *1*, 1.

[32] K. Kang, S. Xie, L. Huang, Y. Han, P. Y. Huang, K. F. Mak, C. J. Kim, D. Muller, J. Park, *Nature* **2015**, *520*, 656.

[33] S. K. Kang, S. W. Hwang, H. Cheng, S. Yu, B. H. Kim, J. H. Kim, Y. Huang, J. A. Rogers, *Adv. Funct. Mater.* **2014**, *24*, 4427.

[34] Y. Gogotsi, B. Anasori, *ACS Nano* **2019**, *13*, 8491.

[35] M. Naguib, M. Kurtoglu, V. Presser, J. Lu, J. Niu, M. Heon, L. Hultman, Y. Gogotsi, M. W. Barsoum, *Adv. Mater.* **2011**, *23*, 4248.

[36] G. Z. Cambaz, G. N. Yushin, Y. Gogotsi, V. G. Lutsenko, *Nano Lett.* **2006**, *6*, 548.

[37] Y. Liu, J. Yu, D. Guo, Z. Li, Y. Su, *J. Alloys Compd.* **2020**, *815*, 152403.

[38] X. Zhang, Z. Zhang, Z. Zhou, *J. Energy Chem.* **2018**, *27*, 73.

[39] A. D. Dillon, M. J. Ghidiu, A. L. Krick, J. Griggs, S. J. May, Y. Gogotsi, M. W. Barsoum, A. T. Fafarman, *Adv. Funct. Mater.* **2016**, *26*, 4162.

[40] N. K. Chaudhari, H. Jin, B. Kim, D. San Baek, S. H. Joo, K. Lee, *J. Mater. Chem. A* **2017**, *5*, 24564.

[41] R. Ibragimova, M. J. Puska, H. P. Komsa, *ACS Nano* **2019**, *13*, 9171.

[42] M. Alhabeb, K. Maleski, B. Anasori, P. Lelyukh, L. Clark, S. Sin, Y. Gogotsi, *Chem. Mater.* **2017**, *29*, 7633.

[43] N. C. Osti, M. Naguib, A. Ostadhossein, Y. Xie, P. R. C. Kent, B. Dyatkin, G. Rother, W. T. Heller, A. C. T. Van Duin, Y. Gogotsi, E. Mamontov, *ACS Appl. Mater. Interfaces* **2016**, *8*, 8859.

[44] M. Boota, M. Pasini, F. Galeotti, W. Porzio, M. Q. Zhao, J. Halim, Y. Gogotsi, *Chem. Mater.* **2017**, *29*, 2731.

[45] T. Zhang, L. Pan, H. Tang, F. Du, Y. Guo, T. Qiu, J. Yang, *J. Alloys Compd.* **2017**, *695*, 818.

[46] M. Naguib, R. R. Unocic, B. L. Armstrong, J. Nanda, *Dalt. Trans.* **2015**, *44*, 9353.

[47] B. Anasori, Y. Xie, M. Beidaghi, J. Lu, B. C. Hosler, L. Hultman, P. R. C. Kent, Y. Gogotsi, M. W. Barsoum, *ACS Nano* **2015**, *9*, 9507.

[48] M. Malaki, A. Maleki, R. S. Varma, *J. Mater. Chem. A* **2019**, *7*, 10843.

[49] Q. Tao, M. Dahlqvist, J. Lu, S. Kota, R. Meshkian, J. Halim, J. Palisaitis, L. Hultman, M. W. Barsoum, P. O. Å. Persson, J. Rosen, *Nat. Commun.* **2017**, *8*, 1.

[50] D. C. Geng, X. X. Zhao, Z. X. Chen, W. W. Sun, W. Fu, J. Y. Chen, W. Liu, W. Zhou, K. P. Loh, *Adv. Mater.* **2017**, *29*, 1.

[51] T. Li, L. Yao, Q. Liu, J. Gu, R. Luo, J. Li, X. Yan, W. Wang, P. Liu, B. Chen, W. Zhang, W. Abbas, R. Naz, D. Zhang, *Angew. Chemie - Int. Ed.* **2018**, *57*, 6115.

[52] M. Li, J. Lu, K. Luo, Y. Li, K. Chang, K. Chen, J. Zhou, J. Rosen, L. Hultman, P. Eklund, P. O. Å. Persson, S. Du, Z. Chai, Z. Huang, Q. Huang, *J. Am. Chem. Soc.* **2019**, *141*, 4730.

[53] W. Sun, S. A. Shah, Y. Chen, Z. Tan, H. Gao, T. Habib, M. Radovic, M. J. Green, *J. Mater. Chem. A* **2017**, *5*, 21663.

[54] A. Sarycheva, A. Polemi, Y. Liu, K. Dandekar, B. Anasori, Y. Gogotsi, *Sci. Adv.* **2018**, *4*, 1.

[55] C. E. Shuck, A. Sarycheva, M. Anayee, A. Levitt, Y. Zhu, S. Uzun, V. Balitskiy, V. Zahorodna, O. Gogotsi, Y. Gogotsi, *Adv. Eng. Mater.* **2020**, *22*, 1.

[56] L. Wang, M. Han, C. E. Shuck, X. Wang, Y. Gogotsi, *Nano Energy* **2021**, *88*, 106308.

[57] K. Zhu, Y. Jin, F. Du, S. Gao, Z. Gao, X. Meng, G. Chen, Y. Wei, Y. Gao, *J. Energy Chem.* **2019**, *31*, 11.

[58] M. Naguib, O. Mashtalir, J. Carle, V. Presser, J. Lu, L. Hultman, Y. Gogotsi, M. W. Barsoum, *ACS Nano* **2012**, *6*, 1322.

[59] A. Vahidmohammadi, A. Hadjikhani, S. Shahbazmohamadi, M. Beidaghi, *ACS Nano* **2017**, *11*, 11135.

[60] B. Soundiraraju, B. K. George, *ACS Nano* **2017**, *11*, 8892.

[61] M. Ghidiu, M. R. Lukatskaya, M. Q. Zhao, Y. Gogotsi, M. W. Barsoum, *Nature* **2015**, *516*, 78.

[62] S. Kajiyama, L. Szabova, H. Iinuma, A. Sugahara, K. Gotoh, K. Sodeyama, Y. Tateyama, M. Okubo, A. Yamada, *Adv. Energy Mater.* **2017**, *7*, 1.

[63] F. Du, H. Tang, L. Pan, T. Zhang, H. Lu, J. Xiong, J. Yang, C. (John) Zhang, *Electrochim. Acta* **2017**, *235*, 690.

[64] F. Liu, J. Zhou, S. Wang, B. Wang, C. Shen, L. Wang, Q. Hu, Q. Huang, A. Zhou, *J. Electrochem. Soc.* **2017**, *164*, A709.

[65] J. Halim, M. R. Lukatskaya, K. M. Cook, J. Lu, C. R. Smith, L. Å. Näslund, S. J. May, L. Hultman, Y. Gogotsi, P. Eklund, M. W. Barsoum, *Chem. Mater.* **2014**, *26*, 2374.

[66] L. Wang, H. Zhang, B. Wang, C. Shen, C. Zhang, Q. Hu, A. Zhou, B. Liu, *Electron. Mater. Lett.* **2016**, *12*, 702.

[67] P. Urbankowski, B. Anasori, T. Makaryan, D. Er, S. Kota, P. L. Walsh, M. Zhao, V. B. Shenoy, M. W. Barsoum, Y. Gogotsi, *Nanoscale* **2016**, *8*, 11385.

[68] K. A. Papadopoulou, A. Chroneos, D. Parfitt, S. R. G. Christopoulos, *J. Appl. Phys.* **2020**, *128*, 170902.

[69] A. Lipatov, A. Goad, M. J. Loes, N. S. Vorobeva, J. Abourahma, Y. Gogotsi, A. Sinitskii, *Matter* **2021**, *4*, 1413.

[70] M. Hu, H. Zhang, T. Hu, B. Fan, X. Wang, Z. Li, *Chem. Soc. Rev.* **2020**, *49*, 6666.

[71] M. Khazaei, A. Ranjbar, M. Arai, S. Yunoki, *Phys. Rev. B* **2016**, *94*, 125152.

[72] J. L. Hart, K. Hantanasirisakul, A. C. Lang, B. Anasori, D. Pinto, Y. Pivak, J. T. van Omme, S. J. May, Y. Gogotsi, M. L. Taheri, *Nat. Commun.* **2019**, *10*, 1.

[73] J. Zhang, N. Kong, S. Uzun, A. Levitt, S. Seyedin, P. A. Lynch, S. Qin, M. Han, W. Yang, J. Liu, X. Wang, Y. Gogotsi, J. M. Razal, *Adv. Mater.* **2020**, *32*, 1.

[74] E. Kayali, A. Vahidmohammadi, J. Orangi, M. Beidaghi, *ACS Appl. Mater. Interfaces* **2018**, *10*, 25949.

[75] J. Kang, V. K. Sangwan, J. D. Wood, M. C. Hersam, *Acc. Chem. Res.* **2017**, *50*, 943.

[76] Y. Bai, K. Zhou, N. Srikanth, J. H. L. Pang, X. He, R. Wang, *RSC Adv.* **2016**, *6*, 35731.

[77] M. Magnuson, J. Halim, L. Å. Näslund, *J. Electron Spectros. Relat. Phenomena* **2018**, *224*, 27.

[78] U. Yorulmaz, A. Özden, N. K. Perkgöz, F. Ay, C. Sevik, *Nanotechnology* **2016**, *27*, 335702.

[79] M. Khazaei, A. Ranjbar, M. Arai, T. Sasaki, S. Yunoki, *J. Mater. Chem. C* **2017**, *5*, 2488.

[80] C. Si, J. Zhou, Z. Sun, *ACS Appl. Mater. Interfaces* **2015**, *7*, 17510.

[81] L. Hu, X. Wu, J. Yang, *Nanoscale* **2016**, *8*, 12939.

[82] C. J. Zhang, S. Pinilla, N. McEvoy, C. P. Cullen, B. Anasori, E. Long, S. H. Park, A. Seral-Ascaso, A. Shmeliov, D. Krishnan, C. Morant, X. Liu, G. S. Duesberg, Y. Gogotsi, V. Nicolosi, *Chem. Mater.* **2017**, *29*, 4848.

[83] K. Maleski, V. N. Mochalin, Y. Gogotsi, *Chem. Mater.* **2017**, *29*, 1632.

[84] Y. Gogotsi, R. M. Penner, *ACS Nano* **2018**, *12*, 2081.

[85] M. R. Lukatskaya, O. Mashtalir, C. E. Ren, Y. Dall'Agnese, P. Rozier, P. L. Taberna, M. Naguib, P. Simon, M. W. Barsoum, Y. Gogotsi, *Science.* **2013**, *341*, 1502.

[86] M. Hu, Z. Li, T. Hu, S. Zhu, C. Zhang, X. Wang, *ACS Nano* **2016**, *10*, 11344.

[87] J. Zhang, S. Seyedin, S. Qin, Z. Wang, S. Moradi, F. Yang, P. A. Lynch, W. Yang, J. Liu, X. Wang, J. M. Razal, *Small* **2019**, *15*, 1.

[88] S. Xu, G. Wei, J. Li, Y. Ji, N. Klyui, V. Izotov, W. Han, *Chem. Eng. J.* **2017**, *317*, 1026.

[89] M. R. Lukatskaya, S. Kota, Z. Lin, M. Q. Zhao, N. Shpigel, M. D. Levi, J. Halim, P. L. Taberna, M. W. Barsoum, P. Simon, Y. Gogotsi, *Nat. Energy* **2017**, *2*, 17105.

[90] Y. Wen, T. E. Rufford, X. Chen, N. Li, M. Lyu, L. Dai, L. Wang, *Nano Energy* **2017**, *38*, 368.

[91] Y. Tang, J. Zhu, C. Yang, F. Wang, *J. Electrochem. Soc.* **2016**, *163*, A1975.

[92] M. D. Levi, M. R. Lukatskaya, S. Sigalov, M. Beidaghi, N. Shpigel, L. Daikhin, D. Aurbach, M. W. Barsoum, Y. Gogotsi, *Adv. Energy Mater.* **2015**, *5*, 1.

[93] Z. Ling, C. E. Ren, M.-Q. Zhao, J. Yang, J. M. Giammarco, J. Qiu, M. W. Barsoum, Y. Gogotsi, *Proc. Natl. Acad. Sci.* **2014**, *111*, 16676.

[94] M. Boota, B. Anasori, C. Voigt, M. Q. Zhao, M. W. Barsoum, Y. Gogotsi, *Adv. Mater.* **2016**, *28*, 1517.

[95] M. Q. Zhao, C. E. Ren, Z. Ling, M. R. Lukatskaya, C. Zhang, K. L. Van Aken, M. W. Barsoum, Y. Gogotsi, *Adv. Mater.* **2015**, *27*, 339.

[96] Y. Wang, H. Dou, J. Wang, B. Ding, Y. Xu, Z. Chang, X. Hao, *J. Power Sources* **2016**, *327*, 221.

[97] N. Kurra, B. Ahmed, Y. Gogotsi, H. N. Alshareef, *Adv. Energy Mater.* **2016**, *6*, 1.

[98] Y. Y. Peng, B. Akuzum, N. Kurra, M. Q. Zhao, M. Alhabeb, B. Anasori, E. C. Kumbur, H. N. Alshareef, M. Der Ger, Y. Gogotsi, *Energy Environ. Sci.* **2016**, *9*, 2847.

[99] J. Li, S. Sollami Delekta, P. Zhang, S. Yang, M. R. Lohe, X. Zhuang, X. Feng, M. Östling, *ACS Nano* **2017**, *11*, 8249.

[100] Z. Lin, D. Barbara, P. L. Taberna, K. L. Van Aken, B. Anasori, Y. Gogotsi, P. Simon, *J. Power Sources* **2016**, *326*, 575.

[101] R. B. Rakhi, B. Ahmed, M. N. Hedhili, D. H. Anjum, H. N. Alshareef, *Chem. Mater.* **2015**, *27*, 5314.

[102] K. Krishnamoorthy, P. Pazhamalai, S. Sahoo, S. J. Kim, *J. Mater. Chem. A* **2017**, *5*, 5726.

[103] T. Deng, X. Zhou, *J. Solid State Electrochem.* **2016**, *20*, 2613.

[104] Q. Tang, Z. Zhou, P. Shen, *J. Am. Chem. Soc.* **2012**, *134*, 16909.

[105] Y. Xie, M. Naguib, V. N. Mochalin, M. W. Barsoum, Y. Gogotsi, X. Yu, K. W. Nam, X. Q. Yang, A. I. Kolesnikov, P. R. C. Kent, *J. Am. Chem. Soc.* **2014**, *136*, 6385.

[106] K. Xu, H. Shao, Z. Lin, C. Merlet, G. Feng, J. Zhu, P. Simon, *Energy Environ. Mater.* **2020**, *3*, 235.

[107] O. Mashtalir, M. Naguib, V. N. Mochalin, Y. Dall'Agnese, M. Heon, M. W. Barsoum, Y. Gogotsi, *Nat. Commun.* **2013**, *4*, 1.

[108] D. Sun, M. Wang, Z. Li, G. Fan, L. Z. Fan, A. Zhou, *Electrochem. commun.* **2014**, *47*, 80.

[109] S. J. Kim, M. Naguib, M. Zhao, C. Zhang, H. T. Jung, M. W. Barsoum, Y. Gogotsi, *Electrochim. Acta* **2015**, *163*, 246.

[110] C. E. Ren, M. Q. Zhao, T. Makaryan, J. Halim, M. Boota, S. Kota, B. Anasori, M. W. Barsoum, Y. Gogotsi, *ChemElectroChem* **2016**, *3*, 689.

[111] J. Luo, X. Tao, J. Zhang, Y. Xia, H. Huang, L. Zhang, Y. Gan, C. Liang, W. Zhang, *ACS Nano* **2016**, *10*, 2491.

[112] J. Luo, C. Wang, H. Wang, X. Hu, E. Matios, X. Lu, W. Zhang, X. Tao, W. Li, *Adv. Funct. Mater.* **2019**, *29*, 1805946.

[113] H. Wang, Y. Wu, X. Yuan, G. Zeng, J. Zhou, X. Wang, J. W. Chew, *Adv. Mater.* **2018**, *30*, 1.

[114] X. Wu, Z. Wang, M. Yu, L. Xiu, J. Qiu, *Adv. Mater.* **2017**, *29*, 1.

[115] Y. Xie, Y. Dall'Agnese, M. Naguib, Y. Gogotsi, M. W. Barsoum, H. L. Zhuang, P. R. C. Kent, *ACS Nano* **2014**, *8*, 9606.

[116] D. Sun, Q. Hu, J. Chen, X. Zhang, L. Wang, Q. Wu, A. Zhou, *ACS Appl. Mater. Interfaces* **2016**, *8*, 74.

[117] M. Ashton, K. Mathew, R. G. Hennig, S. B. Sinnott, *J. Phys. Chem. C* **2016**, *120*, 3550.

[118] Y. Z. Zhang, Y. Wang, Q. Jiang, J. K. El-Demellawi, H. Kim, H. N. Alshareef, *Adv. Mater.* **2020**, *32*, 1.

[119] B. Akuzum, K. Maleski, B. Anasori, P. Lelyukh, N. J. Alvarez, E. C. Kumbur, Y. Gogotsi, *ACS Nano* **2018**, *12*, 2685.

[120] C. (John) Zhang, L. McKeon, M. P. Kremer, S. H. Park, O. Ronan, A. Seral-Ascaso, S. Barwich, C. Coileáin, N. McEvoy, H. C. Nerl, B. Anasori, J. N. Coleman, Y. Gogotsi, V. Nicolosi, *Nat. Commun.* **2019**, *10*, 1.

[121] W. Yang, J. Yang, J. J. Byun, F. P. Moissinac, J. Xu, S. J. Haigh, M. Domingos, M. A. Bissett, R. A. W. Dryfe, S. Barg, *Adv. Mater.* **2019**, *31*, 1902725.

[122] L. Yu, Z. Fan, Y. Shao, Z. Tian, J. Sun, Z. Liu, *Adv. Energy Mater.* **2019**, *9*, 1.

[123] F. Malchik, N. Shpigel, M. D. Levi, T. R. Penki, B. Gavriel, G. Bergman, M. Turgeman, D. Aurbach, Y. Gogotsi, *Nano Energy* **2021**, *79*, 105433.

[124] O. Mashtalir, K. M. Cook, V. N. Mochalin, M. Crowe, M. W. Barsoum, Y. Gogotsi, *J. Mater. Chem. A* **2014**, *2*, 14334.

[125] X. Li, Z. Huang, C. Zhi, *Front. Mater.* **2019**, *6*, 2.

[126] B. Bhushan, M. Caspers, *Microsyst. Technol.* **2017**, *23*, 1117.

[127] X. Yun, B. Lu, Z. Xiong, B. Jia, B. Tang, H. Mao, T. Zhang, X. Wang, *RSC Adv.* **2019**, *9*, 29384.

[128] W. Tesfai, P. Singh, Y. Shatilla, M. Z. Iqbal, A. A. Abdala, *J. Nanoparticle Res.* **2013**, *15*, 1.

[129] E. García-T ͡On, S. Barg, J. Franco, R. Bell, S. Eslava, E. D'Elia, R. C. Maher, F. Guitian, E. Saiz, *Adv. Mater.* **2015**, *27*, 1688.

[130] Q. Zhang, F. Zhang, S. P. Medarametla, H. Li, C. Zhou, D. Lin, *Small* **2016**, *12*, 1702.

[131] C. Zhu, T. Y. J. Han, E. B. Duoss, A. M. Golobic, J. D. Kuntz, C. M. Spadaccini, M. A. Worsley, *Nat. Commun.* **2015**, *6*, 1.

[132] K. Shen, H. Mei, B. Li, J. Ding, S. Yang, *Adv. Energy Mater.* **2018**, *8*, 1.

[133] J. Orangi, F. Hamade, V. A. Davis, M. Beidaghi, *ACS Nano* **2020**, *14*, 640.

[134] Z. Fan, C. Wei, L. Yu, Z. Xia, J. Cai, Z. Tian, G. Zou, S. X. Dou, J. Sun, *ACS Nano* **2020**, *14*, 867.

[135] S. Deville, *Freezing Colloids: Observations, Principles, Control, and Use*, **2017**.

[136] S. Deville, E. Saiz, A. P. Tomsia, *Acta Mater.* **2007**, *55*, 1965.

[137] S. Deville, E. Maire, A. Lasalle, A. Bogner, C. Gauthier, J. Leloup, C. Guizard, *J. Am. Ceram. Soc.* **2009**, *92*, 2489.

[138] Y. Shao, M. F. El-Kady, C. W. Lin, G. Zhu, K. L. Marsh, J. Y. Hwang, Q. Zhang, Y. Li, H. Wang, R. B. Kaner, *Adv. Mater.* **2016**, *28*, 6719.

[139] P. Zhang, Q. Zhu, R. A. Soomro, S. He, N. Sun, N. Qiao, B. Xu, *Adv. Funct. Mater.* **2020**, *30*, 2000922.

[140] T. Hu, M. Hu, Z. Li, H. Zhang, C. Zhang, J. Wang, X. Wang, *Phys. Chem. Chem. Phys.* **2016**, *18*, 20256.

[141] Q. Wang, X. Wang, F. Wan, K. Chen, Z. Niu, J. Chen, *Small* **2018**, *14*, 1.

[142] S. Korkut, J. D. Roy-Mayhew, D. M. Dabbs, D. L. Milius, I. A. Aksay, *ACS Nano* **2011**, *5*, 5214.

[143] L. Ren, Y. P. Zeng, D. Jiang, *J. Am. Ceram. Soc.* **2007**, *90*, 3001.

[144] L. M. Wang, Z. F. Tang, J. Lin, X. D. He, C. S. Chen, C. H. Chen, *J. Mater. Chem. A* **2019**, *7*, 17376.

[145] A. Daraghmeh, S. Hussain, L. Servera, E. Xuriguera, M. Blanes, F. Ramos, A. Cornet, A. Cirera, *Mater. Res. Express* **2017**, *4*, 025007.

[146] R. A. Susantyoko, F. Parveen, I. Mustafa, S. Almheiri, *Ionics (Kiel).* **2019**, *25*, 265.

[147] Y. Hwa, E. Yi, H. Shen, Y. Sung, J. Kou, K. Chen, D. Y. Parkinson, M. M. Doeff, E. J. Cairns, *Nano Lett.* **2019**, *19*, 4731.

[148] M. A. Ghadkolai, S. Creager, J. Nanda, R. K. Bordia, *J. Electrochem. Soc.* **2017**, *164*, A2603.

Chapter 3. 3D Printing of Freestanding MXene Architectures for Current-Collector-Free Supercapacitors

3.1 Chapter Introduction

Very recently, extrusion-based 3D printing, as an emerging technology, has been successfully demonstrated to construct complex structures with a wide application in various areas, such as electronic, biomedical, and energy storage fields. To develop suitable inks with high viscosities and shear-thinning rheological properties, it is essential to print ideal architectures without collapse. Among these, fabrication of functional components or devices for microelectronic systems with 3D printing technologies is still promising. Recently, a series of 3D printed functional components and devices for electronics have been reported, especially with the widely used direct ink writing 3D printing. The revelation of novel characteristics found in MXenes have directed significant interest for its use in rising fields, particularly in electrochemical energy storage. Although research on MXenes have seen dramatic progress in recent years, materials performance is hindered. This is attributed to limitations in the design and fabrication of electrodes with tuned architectures. MXene aqueous inks could be employed in commercial pens for direct writing functional films and thus be integrated into customised 3D device architectures. This chapter will explore the rheological properties of aqueous MXene inks and, in addition, the suitability for direct ink writing. The MXene inks will be used to print interdigitated single layer devices to show the potential for printed micro-supercapacitors, whilst demonstrating the potential for a truly 3D printed supercapacitor devices.

In this work, the thesis author conceived this study carried out materials fabrication, SEM / Energy dispersive X-ray spectroscopy (EDS) / X-ray diffraction (XRD) / Rheology and data analysis, printing of MXene inks and wrote MXene inks, and writing the paper. Yang Jie assisted with electrochemical measurements. All authors contributed to the review of the manuscript. The original manuscript is presented in the following sections.

Paper: 3D printing of Freestanding MXene Architectures for Current Collector-Free Supercapacitors

Wenji Yang[†], Jie Yang[‡§], Jae Jong Byun[†] Francis Moissinac[†], Jiaqi Xu[†], Sarah J Haigh[†], Marco Domingos[δ], Mark A. Bissett[†], Robert A.W. Dryfe[‡§], Suelen Barg[†]

† Department of Materials, School of Natural Sciences, University of Manchester, Oxford Road, Manchester, M13 9PL, U.K.

‡ National Graphene Institute, University of Manchester, Oxford Road, Manchester, M13 9PL, U.K.

§ Department of Chemistry, School of Natural Sciences, University of Manchester, Oxford Road, Manchester M13 9PL, U.K.

δ Department of Mechanical, Aerospace and Civil Engineering, University of Manchester, Oxford Road, Manchester M13 9PL, U.K.

KEYWORDS: MXene; Aqueous Inks, Rheology; 3D printing; Supercapacitors

3.2 Abstract

Additive Manufacturing (AM) technologies appear to be a paradigm for the scalable manufacture of electrochemical energy storage (EES) devices, where complex three-dimensional (3D) architectures are typically required but hard to achieve using conventional techniques. The combination of these technologies and innovative material formulations that maximize surface area accessibility and ion transport within electrodes while minimizing space are of growing interest. Herein, we formulate aqueous inks composed of atomically thin (1-3 nm) 2D $Ti_3C_2T_x$ with large lateral size of about 8 μm possessing ideal viscoelastic properties for extrusion-based 3D printing of freestanding, high-specific surface area architectures. The MXene inks were 3D printed into interdigitated electrodes to determine the viability of manufacturing energy storage devices. The 3D printed device with active material loading of about 8.5 mg cm^{-2} achieved areal capacitance as high as 2.1 F cm^{-2} at 1.7 mA cm^{-2} and gravimetric capacitance of 242.5 F g^{-1} at 0.2 A g^{-1} with retention of above 90 % capacitance for 10,000 cycles. It also exhibited a high energy density of 0.0244 mWh cm^{-2} and power density of 0.64 mW cm^{-2} at a current density of 4.3 mA cm^{-2}. We anticipate that the sustainable printing and design approach developed in this work can be applied to fabricate high performance bespoke multi-scale and multi-dimensional 3D architectures of functional and structural materials for integrated devices in energy, catalysis and transportation applications.

3.3 Introduction

The performance and application of electrochemical energy storage (EES) devices increasingly relies on the development of scalable manufacturing routes and innovative materials formulations that can maximize surface area accessibility and ion transport within electrodes while minimizing space and environmental impact. Consequently, Additive Manufacturing (AM) technologies, which are capable of printing three-dimensional (3D) objects and complex structures, offer unique possibilities to bring novel electrode materials into high performance EES devices. Among the AM technologies, continuous extrusion-based 3D printing (also called direct ink-writing or robocasting) is a versatile and cost-effective processing route where the formulation and properties of colloidal inks directly control the printability and architecture of printed parts. It further offers the ability to integrate functional materials of different surface chemistry and dimensionality into EES devices [1] such as Li-ion batteries [2–4], micro-supercapacitors (MSCs) [5,6] and wearable electronics [7,8].

Recently, two-dimensional (2D) transition metal carbides, called MXenes ($M_{n+1}X_nT_x$, with M representing an early transition metal, X representing C and/or N and, T_x representing the terminal functional groups) [9,10], have shown huge potential as electrode materials for supercapacitors [11,12]. Their combination of metallic conductivity, high density (3.8 ± 0.3 g cm^{-3}) and redox active, negatively charged surfaces can lead to superior charge storage and transfer capabilities when compared to other 2D materials. Their surface functional groups (-O, -OH and -F) further render them hydrophilic allowing them to be easily dispersed into aqueous suspensions and inks for processing electrodes using different approaches such as vacuum filtration [10,13], spin coating [14,15], screen-printing [16,17], stamping [18], and spraying [19–21]. While these approaches show the potential of MXene for water-based processing of EES devices, limitations remain with respect to architectural control, scalability or cost-effectiveness that could be addressed by employing 3D printing technologies. Although MXene aqueous inks have been recently employed in commercial pens for direct writing functional films [22], the development of 3D printable MXene inks and their integration into customised 3D device architectures is still unexplored. In order to realize this challenge, these materials need to be integrated into inks with very specific rheological properties that allow smooth flow through narrow nozzles while still enabling the extruded filaments to retain their shape even after multiple layers are printed. Furthermore, the optimised ink formulation and

processing route should allow the properties of the 2D MXene to be efficiently translated to their 3D printed architecture.

Herein, we formulate aqueous inks with 2D $Ti_3C_2T_x$ (the most studied MXene material) with ideal viscoelastic properties for extrusion-based 3D printing of freestanding, high-specific surface area architectures of different size and shapes (**Fig. 1**). Previous studies show that high aspect ratio materials with high surface charge, such as clay, Graphene Oxide (GO) and MXene are effective in tuning the rheological properties for wet processing when compared to conventional colloidal systems [23–25]. In particular, the bi-dimensionality of MXenes in combination with their highly negatively charged surfaces and more positive edges [26] render them electrostatic properties and the capability to intercalate water that is similar to some clays [27]. Here we extend this knowledge to develop 3D printable inks solely based on large lateral size, few-layer thick MXene flakes in water without the necessity of using normally employed sacrificial additives [28–31] to control the rheological properties. We further apply the inks to directly print interdigitated symmetric MSCs with a solid electrolyte using $Ti_3C_2T_x$ as both the electrode material and the current collector (CC). This eliminates the need to employ noble metals [32] or other metallic materials used as CC in 3D printed electrode designs [4,26,30]. The electrodes with an active material loading of about 8.5 mg cm^{-2} exhibited an areal capacitance of 2.1 F cm^{-2} and gravimetric capacitance of 242 F g^{-1} at 0.2 A g^{-1}, high power and energy densities and capacitance retention above 90 % for 10,000 cycles. While this work represents a feasibility study, we anticipate that this sustainable printing and design approach can be applied to fabricate customized MXene-based architectures and integrated devices for a wide range of applications from energy storage and transfer, catalysis, electromagnetic shielding, environmental cleaning to advanced composite manufacturing.

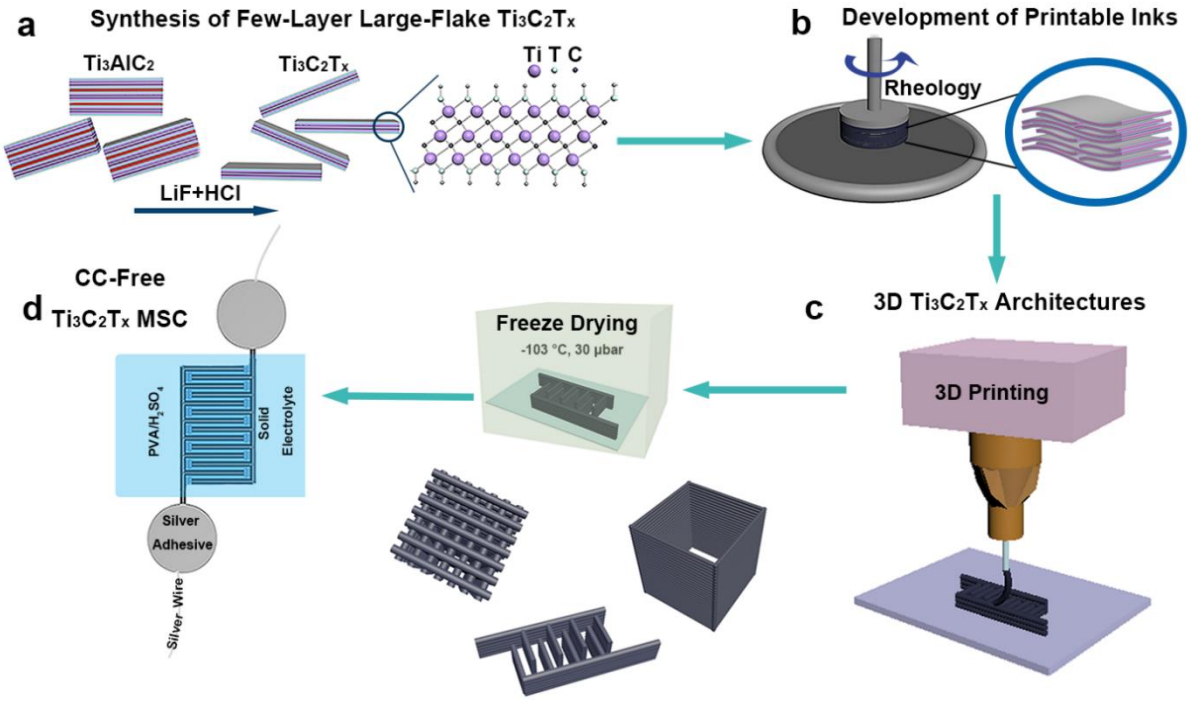

Figure 1 Schematic representation of the manufacturing strategy developed for 3D printing of freestanding MXene architectures and MSC demonstrators. (a) Synthesis of 2D $Ti_3C_2T_x$ following a less aggressive approach with multiple purifications and no sonication steps to allow the formation of few-layers large flakes. (b) Development of $Ti_3C_2T_x$ aqueous inks at neutral pH and study of their suitability for 3D printing via specific rheological characterizations (e.g. viscous properties under shear and their viscoelastic fingerprints); (c) 3D printing of inks with suitable viscoelastic fingerprints layer-by-layer to produce different 3D designs. The subsequent freeze-drying gives rise to freestanding 3D architectures that retain their shape and dimensions; (d) Probing the suitability of the 3D printable inks to develop high performance symmetrical current collector-free (CC-Free) $Ti_3C_2T_x$ solid-state MSCs.

3.4 Results and Discussion

In order to probe the suitability of 2D MXenes for extrusion-based 3D printing, we synthesised $Ti_3C_2T_x$ flakes that are both large (8 µm average lateral size) and thin (1-3 nm thick) giving a mean length to thickness ratio of approx. 4,000 (**Fig. 2a-c, Fig. S1**). During the synthesis (Experimental Section - SI), the Ti_3AlC_2 precursor is selectively etched in a LiF and HCl mixture (with in-situ formation of HF as the etchant) and the subsequent delamination is achieved by the intercalation of water and Li ions within the negatively charged surface resulting in a volume increase as previously described [27]. We followed a less aggressive etching and delamination protocol [34,35], with no sonication steps (**Fig. 1a** and SI) to allow the synthesis of 2D flakes of preserved lateral size. After purification and centrifugation steps, the

large 1-3 nm thick $Ti_3C_2T_x$ flakes can be readily formulated into homogeneous aqueous inks at neutral pH (Zeta potential of -41 mV with standard deviation of 2 mV) (**Fig. S2**). A rheological study of the developed inks was subsequently carried out to probe their suitability for 3D printing (**Fig. 2d-f**). The ink's viscosity and viscoelastic properties depend on the $Ti_3C_2T_x$ flakes concentration in water and the inks present a clear shear-thinning behaviour as previously reported for 2D materials systems [23,36,37]. The viscosity recovery of the shear-thinning inks over time shows their potential for continuous extrusion during the 3D printing process (**Fig. 2e**). By applying alternate low (0.01 s^{-1}) and high (1,000 s^{-1}) shear rates to the inks over time we can observe the viscosity drop at higher rates (simulating the extrusion through narrow nozzles) and the instantaneous recovery of viscosity when the shear stress is reduced (simulating post printing recovery of the inks rheological properties). Interestingly, the 15 mg mL^{-1} inks present viscosity values in the order of magnitude as reported for highly concentrated (2.33 g mL^{-1}, 70 wt%) [38] multi-layered $Ti_3C_2T_x$ suspensions, which indicates that high aspect ratio $Ti_3C_2T_x$ flakes are effective in tuning rheology at low concentrations.

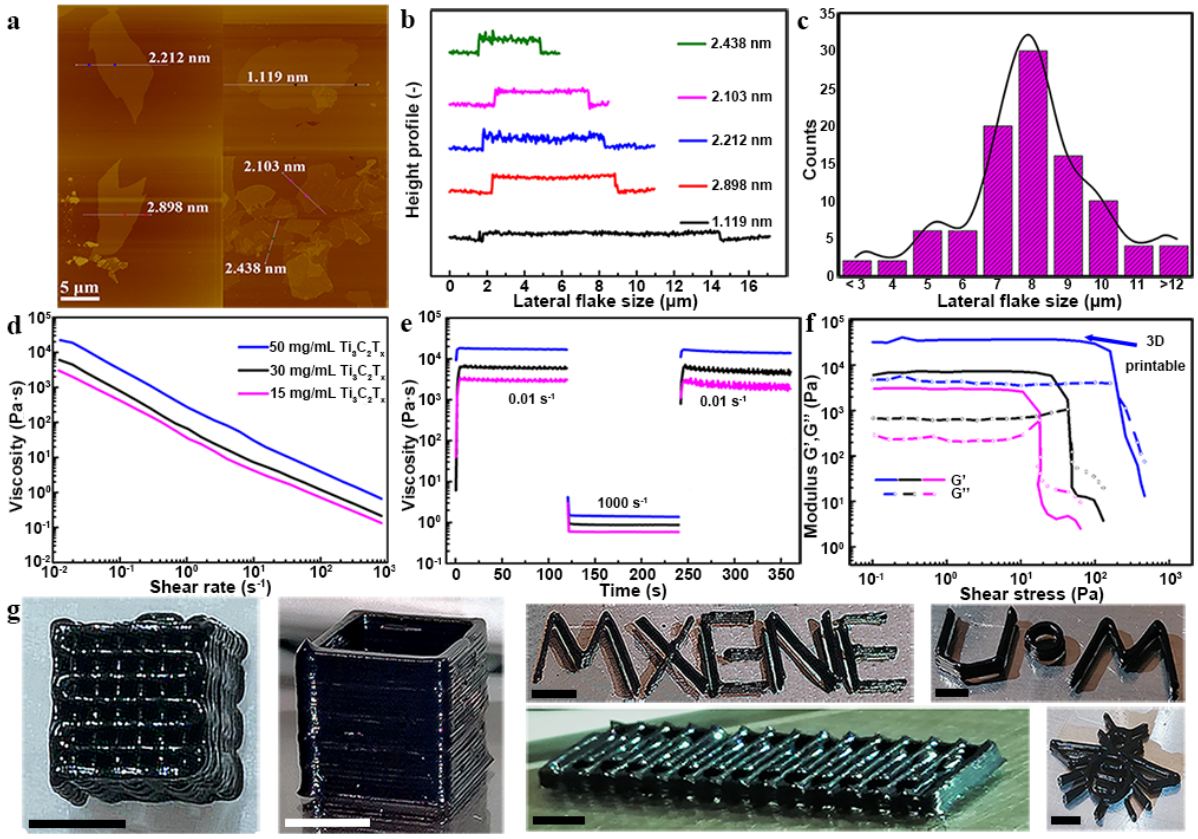

Figure 2 $Ti_3C_2T_x$ flakes dimensional analysis via atomic force microscopy (AFM) (a-b) and scanning electron microscopy (SEM) (c), inks rheological characterization (d-e) and wet stage 3D printed structures (g). a-b) Flake thicknesses ranging from approximately 1 to 3 nm. Large area and thin flakes

with aspect ratios above 10,000 can be synthesised (a representative 1.1 nm thick, 12 μm lateral size flake is represented by the black line). c) Histogram of $Ti_3C_2T_x$ flakes lateral size obtained from SEM imaging of diluted inks (**Fig. S1**). The mean lateral flake size is 8 μm with a standard deviation of 2.7 μm. d) Inks shear thinning behaviour appropriate for continuous extrusion through printing nozzles as narrow as 250 μm diameter. Inset legend refers to line colours used in panels d-f. e) Inks viscosity evolution over time for alternate low (0.01 s^{-1}) and high shear rate (1,000 s^{-1}) showcasing appropriate viscosity drop and post-printing recovery. f) Inks viscoelastic fingerprints showing their solid-like behavior with large plateau regions (where G' is independent of stress) and yield stresses (cross over point between G' and G'') that increase as the inks become more concentrated. In particular, 50 mg mL^{-1} inks demonstrate an elastic modulus of 3,747 Pa and extendable plateau regions with yield stress of 206 Pa enabling them to be 3D printable. Inks at 15, 30 and 50 mg mL^{-1} correspond to 1.5, 2.9 and 4.8 wt% $Ti_3C_2T_x$, respectively. g) Illustration of 3D printed architectures: clock-wise: 3D printed micro-lattice and rectangular hollow prism printed through 330 and 250 μm nozzles respectively (both 25 printed layers); MXene (4 layers), UoM (5 layers), bee (3 layers) and interdigitated (4 layers) designs all printed through a 330 μm nozzle. All structures used a printing speed of 6 - 10 mm s^{-1}. All scale bars in g) correspond to 3 mm.

The inks viscoelastic fingerprints (**Fig. 2f**) show predominantly solid-like behaviour with a high storage modulus (G') at the plateau region (region where G' is independent of stress) indicating the formation of a highly percolated $Ti_3C_2T_x$ network. The viscoelastic network breaks and flows when a critical stress is applied (the yield stress at the cross over point between G' and loss modulus (G'')) resulting in a liquid-like behaviour (G'' > G') that enables continuous extrusion through micrometre-sized nozzles. The magnitude of the elastic modulus and yield stress increases as the inks become more concentrated with 2D flakes, indicating an increase in suitability for shape retention upon continuous extrusion. The elastic modulus and yield stress for inks with 50 mg mL^{-1} concentration reaches 36,507 Pa and 206 Pa, respectively, falling within the range for printable inks reported for other systems [2,39–41]. Furthermore, inks with increased material loading maintained sufficient viscoelastic characteristics to be printable and led to a proportional increase in bulk densities of printed parts (**Fig. S3**). These inks can easily flow through narrow nozzles and instantaneously recover their solid-like behaviour, retaining the nozzle's filamentary shape after extrusion. Consequently, it is possible to successfully fabricate 3D architectures by the continuous extrusion of additive-free large $Ti_3C_2T_x$ aqueous inks layer-by-layer following different structural designs (**Fig. 2g** and **S4**). Freestanding wet $Ti_3C_2T_x$ 3D woodpile, hollow rectangular prism, interdigitated electrode

configurations and other constructs have been 3D printed directly in air with the shapes retained after the printing process.

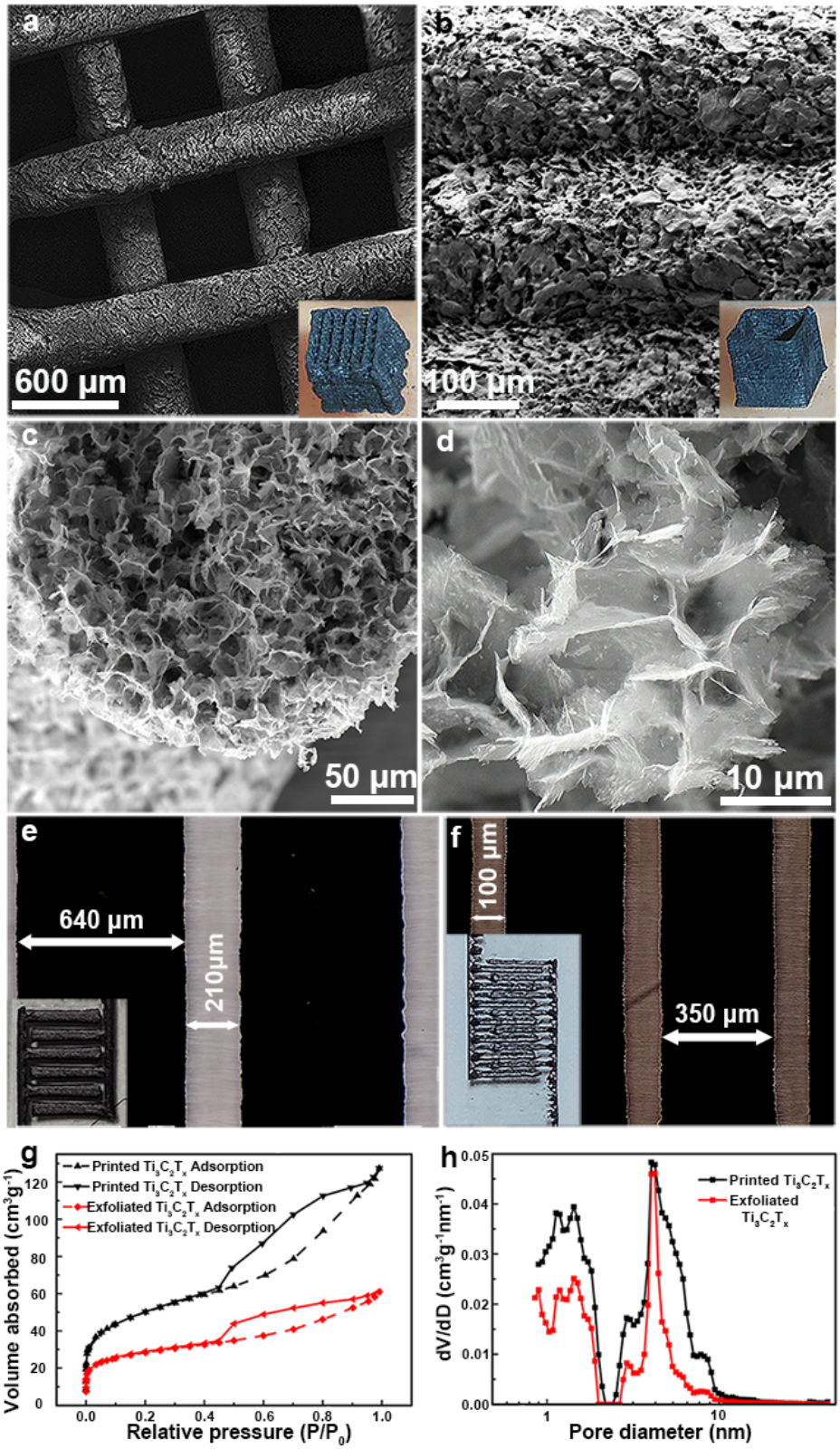

Figure 3 3D printed multi-scale architectures after freeze-drying. SEM and optical micrographs (inset) of free-standing $Ti_3C_2T_X$ micro-lattice (a) and hollow rectangular prism (b) printed through 330 and 250

μm nozzles, respectively; The cross-sectional SEM images of one filament within the micro-lattice in (a) show the retention of shape and formation of porous internal structures upon freeze-drying (c-d). e-f) Optical micrographs (inset) of 3D printed interdigitated designs with a $Ti_3C_2T_X$ finger thicknesses and finger gaps of 640 and 210 μm (e) and 350 and 100 μm (f), respectively. g-h) N_2 adsorption and desorption isotherms and the pore size distribution of vacuum dried 2D $Ti_3C_2T_x$ (SSA of 100 m^2g^{-1}) and 3D printed $Ti_3C_2T_x$ architectures (SSA of 177 m^2g^{-1}). The preserved surface area of few-layer and large vacuum dried 2D $Ti_3C_2T_x$ is further improved upon 3D printing and freeze-drying. The inset printed structures in (a), (b), (e) and (f) all have lateral sizes of 5 mm.

The wet 3D structures are subsequently freeze-dried to give freestanding $Ti_3C_2T_x$ architectures without the necessity of any further thermal or chemical treatments as are normally required when using additives or GO [28,37,42]. Freeze-drying protects the internal integrity and the external shape of the structures with low shrinkage resulting in $Ti_3C_2T_x$ 3D architectures of well-defined shapes (**Fig. 3a-d**) and filaments in the micrometre range. The process parameters, i.e. the nozzle internal diameter, printing speed and pressure, can be tuned in order to obtain printed filaments that are similar to the internal diameter of the nozzle. The SEM micrograph of the micro-lattice structure (**Fig. 3a**) shows individual printed filaments of 326 ± 13 μm in diameter forming the interlaced configuration without bending. Side view imaging of the printed rectangular prism (**Fig. 3b**) shows the boundaries between individual printed filament layers without any overlap or internal collapse. These results demonstrate the $Ti_3C_2T_x$ inks viscoelastic properties are highly appropriate for 3D printing of freestanding architectures.

Cross-sectional images through the filaments (**Fig. 3c-d**) reveal an internal network of $Ti_3C_2T_x$ flakes with interconnected pores in the range of 12 - 35 μm and smaller openings between them in the range of 3 - 5 μm. While porosity can lead to more accessible surfaces for the electrolyte and improved rate performances, it can also sacrifice the volumetric capacitance and volumetric energy density to some extent [10]. Thus, the optimization of porosity is a big challenge in electrode design.

Our synthesis approach resulted in large, few-layers flakes with a Brunauer-Emmett-Teller (BET) specific surface area (SSA) of 100 $m^2\ g^{-1}$ (vacuum dried etched dispersion), which is considerably higher than previously reported (SSA for $Ti_3C_2T_x$ is normally between 4.2 - 55.06 $m^2\ g^{-1}$ [43–46]). The SSA of the 3D printed $Ti_3C_2T_x$ architectures was calculated as 177 $m^2\ g^{-1}$ (**Fig. 3g**). The post 3D printing freeze-drying approach assembles the 2D flakes into a porous architecture within the filaments preventing the normal restacking of 2D flakes during drying [47]. This further improves their surface area accessibility compared to conventional techniques

(e.g. casting or vacuum filtration). The $Ti_3C_2T_x$ samples present a typical type IV N_2 adsorption/desorption isotherm, indicating their predominantly mesoporous internal structures [48]. Based on the Density Functional Theory model [49], the pore size distribution is determined to be from 0.8 nm to 9 nm (**Fig. 3h**). Elemental mapping of the 3D printed $Ti_3C_2T_x$ structures (**Fig. S5**) show them to be mainly composed of homogeneously distributed Ti, C, O and F elements and XRD analysis (**Fig. S6**) shows very similar peaks to delaminated $Ti_3C_2T_x$ flakes, indicating that the materials do not change crystal structure upon printing and post-printing processes.

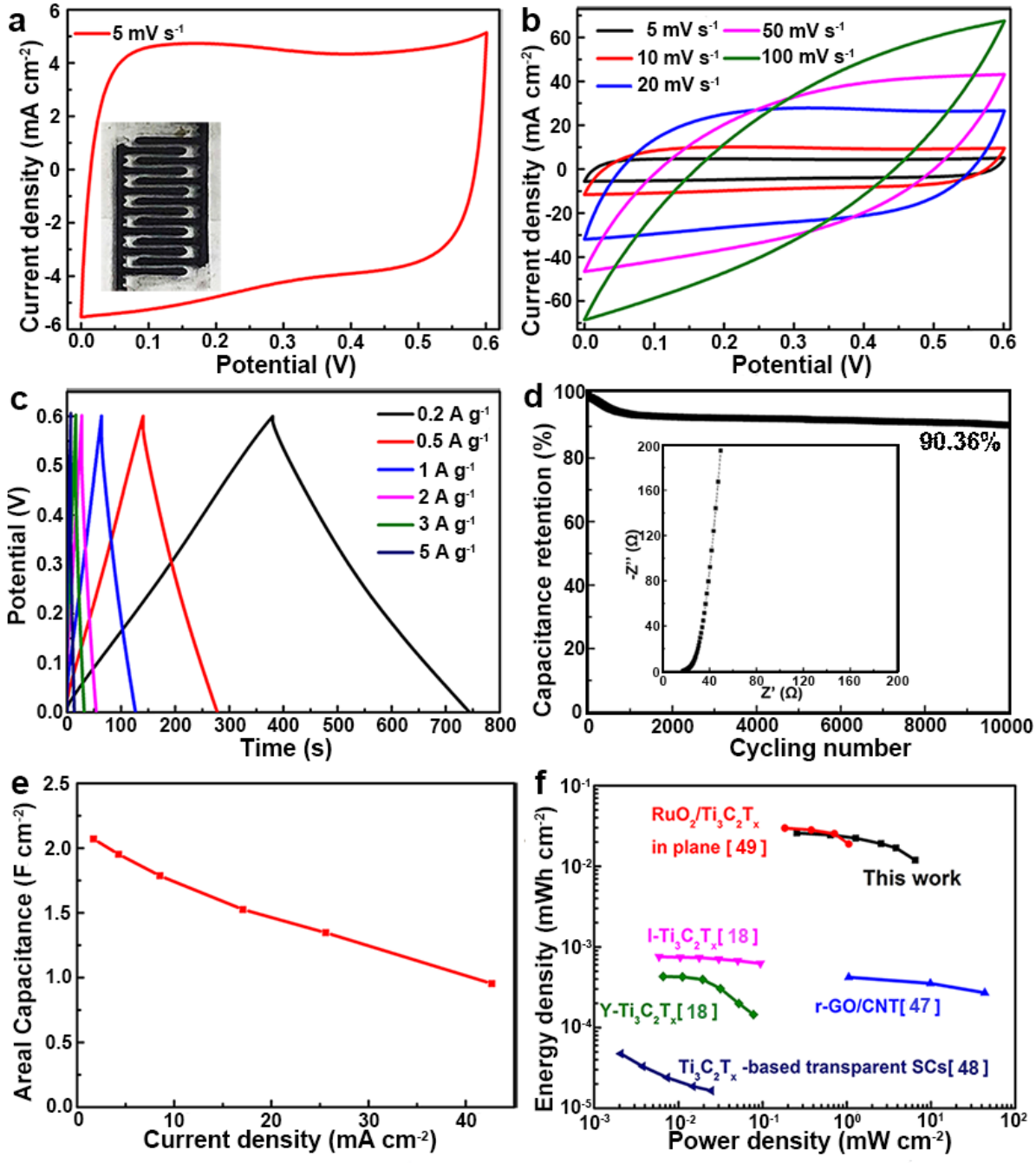

Figure 4 Electrochemical performance of 3D printed few-layer large-flake $Ti_3C_2T_x$ interdigitated electrodes integrated into current-collector free symmetric MSCs (finger diameter of 326 μm and gap distance of 187 μm). a) cyclic voltammetry (CV) at 5 mV s^{-1} showing the ideal capacitive behaviour. The MSC MXene interdigitated electrode configuration is shown in the inset (5 mm smallest lateral size). b) CVs collected at scan rates of 5 mV s^{-1} to 100 mV s^{-1}; c) galvanostatic charge-discharge (GCD) profiles collected at different current densities ranging from 0.2 A g^{-1} to 5 A g^{-1}; d) Cycling stability test showing over 90 % capacitance retention after 10,000 cycles at 1 A g^{-1}. e) Areal capacitance *versus* different areal current densities (2 - 44 mA cm^{-2}); f) Ragone plots of the 3D printed $Ti_3C_2T_x$ supercapacitors together with other reported values for comparison. MSCs tested presented a loading of 8.5 mg cm^{-2}.

In order to demonstrate the potential of our MXene inks for the manufacturing of energy storage devices, we 3D printed interdigitated $Ti_3C_2T_x$ electrodes with tuneable finger thickness and with finger gaps that can be as small as 100 μm (**Fig. 3e-f** and **S4**). We further assembled symmetrical all MXene solid-state MSCs (using solid electrolyte, a mixture of poly (vinyl alcohol) (PVA) and sulfuric acid) to test the electrochemical performance of 3D printed interdigitated electrode architectures (**Fig. 1**, **4a-f**, **S7** and **S8**). The assembled demonstrators were composed of about 8.5 mg cm^{-2} active material loaded in 326 μm diameter fingers separated by 187 μm gaps allowing a short distance between electrodes without short-circuiting the devices (**Fig. 4a** inset and **Fig. S8**). The materials present an ideal capacitive behaviour showing a quasi-rectangular CV curve shape (5 - 20 mV s^{-1}) maintaining a good performance at higher rates (**Fig. 4a-b**). The discharging profile in galvanostatic charge-discharge (GCD) curves shows a triangular shape, revealing typical capacitive characteristics and efficient charge storage ability. The devices present gravimetric capacitances ranging between 242.5 and 117.7 F g^{-1} (for current densities between 0.2 and 5 A g^{-1}, as shown is **Fig. S7**) with capacitance retention above 90 % after 10,000 cycles at 1 A g^{-1} (**Fig. 4d**).

The kinetics of ion transport and charge transfer in the 3D-printed $Ti_3C_2T_x$ micro-supercapacitor was further investigated by electrochemical impedance spectroscopy (EIS) with a frequency range from 0.01 Hz to 100 kHz. The Nyquist plot shows a semicircle in the high-frequency region and nearly vertical line at the low-frequency region (indicating a good capacitive behaviour and fast ion diffusion). The intercept of the curve with the real axis shows the equivalent series resistance (ESR) of 16.83 Ω (which includes the resistance of the electrode materials, solid electrolyte and contact resistance between the electrode materials with current collector).

The areal capacitance is a critical metric to evaluate the performance of MSCs. The 3D printed devices with active material loading of about 8.5 mg cm^{-2} achieve areal capacitance as high as 2.1 F cm^{-2} at 1.7 mA cm^{-2} and 1.0 F cm^{-2} when the current density is increased by 25-fold (at 42.7 mA cm^{-2}), surpassing the capacitance performance of MXene MSCs produced by other methods (e.g. 42.5 mF cm^{-2} at 0.8 mA cm^{-2}) [18]. The Ragone plot (**Fig. 4f**) further showcases the potential of 3D printed MXene interdigitated electrodes for high energy density and power density supercapacitors. At a current density of 4.3 mA cm^{-2}, the MSC exhibits an energy density of 0.0244 mWh cm^{-2} and a power density of 0.64 mW cm^{-2}. By increasing the current density to 44 mA cm^{-2}, 50 % of the energy density is retained (0.012 mWh cm^{-2}) while the power density increases to 6.50 mW cm^{-2} (a 10-fold increase). The 3D printed $Ti_3C_2T_x$ MSCs exhibit two orders of magnitude higher energy density with comparable power densities to graphene/CNT hybrids [50]; higher power and energy densities compared to $Ti_3C_2T_x$ supercapacitors [51]; reaching similar performance as $RuO_2/Ti_3C_2T_x$ hybrid materials [52]. It should be noted that the relatively narrow voltage window limits the energy density to some degree. Therefore, to overcome the voltage window limitation, the use of ionic liquid or organic electrolyte and designing asymmetric supercapacitors with other materials like graphene will be further explored as effective strategies to enhance the energy density.

3.5 Conclusion

In this work we have developed additive-free aqueous inks based on large area, thin $Ti_3C_2T_x$ flakes that enable the formation of strong "solid-like" $Ti_3C_2T_x$ networks with ideal rheological properties for layer-by-layer printing of freestanding 3D architectures. The developed manufacturing route enables a good translation of properties from the 2D material into 3D, resulting in architectures with significantly improved SSA compared to other approaches. We have employed the optimized inks to 3D print MSCs with $Ti_3C_2T_x$ interdigitated fingers of tuneable thickness and gap size in the micrometre range. 3D printed devices with a solid electrolyte and active material loading of 8.5 mg cm^{-2} have achieved areal capacitance as high as 2.1 F cm^{-2} at 1.7 mA cm^{-2} with superior energy and power density (e.g. 0.0244 mWh cm^{-2} at 0.64 mW cm^{-2}) compared to previously report symmetric 2D material-based MSCs. The unique rheological properties achieved by the 2D MXene inks combined with the sustainability of the approach can serve as a base to explore other applications requiring controlled 3D architectures and the methodology could be expanded to incorporate other functional and structural materials into MXene-based 3D printable inks. We anticipate that the capability to

print customized MXene architectures in three-dimensions that has been demonstrated in this work, will open new opportunities to realise high performance multi-scale and multi-dimensional devices, as required for many different energy, catalysis and transportation applications.

Acknowledgement

W.Y. and J.Y. contributed equally to this work. This work was supported by the Henry Royce Institute for Advanced Materials, funded through EPSRC grants EP/R00661X/1, EP/S019367/1, EP/P025021/1 and EP/P025498/1. S.B. would like to thank Heilongjiang Huasheng Graphite Co. Ltd. for funding. W.Y. And S.B. Acknowledge the University of Manchester for the President's Doctoral Scholar Award. S.J.H. thanks the European Research Council (Starter Grant EvoluTEM) and EPSRC (grant EP/P009050/1). R.A.W.D. thanks EPSRC for funding through the grants EP/R023034/1 and EP/N032888/1. The authors also acknowledge Gary Harrison and Dr. John E. Warren from the Department of Materials X-ray Diffraction Suite at the University of Manchester.

Received: 29 April 2019

Revised: 13 June 2019

Published online: 10 September 2019

Reference

[1] C. W. Foster, M. P. Down, Y. Zhang, X. Ji, S. J. Rowley-Neale, G. C. Smith, P. J. Kelly, C. E. Banks, Sci. Rep. **2017**, *7*, 42233.

[2] J. A. Lewis, Adv. Funct. Mater. **2006**, *16*, 2193.

[3] K. Sun, T. S. Wei, B. Y. Ahn, J. Y. Seo, S. J. Dillon, J. A. Lewis, Adv. Mater. **2013**, *25*, 4539.

[4] T. S. Wei, B. Y. Ahn, J. Grotto, J. A. Lewis, Adv. Mater. **2018**, *30*, 1703027.

[5] D. Shen, G. Zou, L. Liu, W. Zhao, A. Wu, W. W. Duley, Y. N. Zhou, ACS Appl. Mater. Interfaces **2018**, *10*, 5404.

[6] W. Yu, H. Zhou, B. Q. Li, S. Ding, ACS Appl. Mater. Interfaces **2017**, *9*, 4597.

[7] Y. Wang, C. Chen, H. Xie, T. Gao, Y. Yao, G. Pastel, X. Han, Y. Li, J. Zhao, K. K. Fu, L. Hu, Adv. Funct. Mater. **2017**, *27*, 1703140.

[8] W. Honda, S. Harada, T. Arie, S. Akita, K. Takei, Adv. Funct. Mater. **2014**, *24*, 3299.

[9] B. Anasori, M. R. Lukatskaya, Y. Gogotsi, Nat. Rev. Mater. **2017**, *2*, 16098.

[10] M. R. Lukatskaya, S. Kota, Z. Lin, M. Q. Zhao, N. Shpigel, M. D. Levi, J. Halim, P. L. Taberna, M. W. Barsoum, P. Simon, Y. Gogotsi, Nat. Energy **2017**, *2*, 17105.

[11] J. Yan, C. E. Ren, K. Maleski, C. B. Hatter, B. Anasori, P. Urbankowski, A. Sarycheva, Y. Gogotsi, Adv. Funct. Mater. **2017**, *27*, 1701264.

[12] Y. Wen, T. E. Rufford, X. Chen, N. Li, M. Lyu, L. Dai, L. Wang, Nano Energy **2017**, *38*, 368.

[13] Y. Xia, T. S. Mathis, M. Q. Zhao, B. Anasori, A. Dang, Z. Zhou, H. Cho, Y. Gogotsi, S. Yang, Nature **2018**, *557*, 409.

[14] G. Ying, A. D. Dillon, A. T. Fafarman, M. W. Barsoum, Mater. Res. Lett. **2017**, *5*, 391.

[15] G. Ying, S. Kota, A. D. Dillon, A. T. Fafarman, M. W. Barsoum, FlatChem **2018**, *8*, 25.

[16] S. Xu, Y. Dall'Agnese, G. Wei, C. Zhang, Y. Gogotsi, W. Han, Nano Energy **2018**, *50*, 479.

[17] H. Hu, T. Hua, J. Mater. Chem. A **2017**, *5*, 19639.

[18] C. J. Zhang, M. P. Kremer, A. Seral-Ascaso, S. H. Park, N. McEvoy, B. Anasori, Y. Gogotsi, V. Nicolosi, Adv. Funct. Mater. **2018**, 28, 1705506.

[19] K. Hantanasirisakul, M. Q. Zhao, P. Urbankowski, J. Halim, B. Anasori, S. Kota, C. E. Ren, M. W. Barsoum, Y. Gogotsi, Adv. Electron. Mater. **2016**, *2*, 1600050.

[20] A. Sarycheva, A. Polemi, Y. Liu, K. Dandekar, B. Anasori, Y. Gogotsi, Sci. Adv. **2018**, *4*, eaau0920.

[21] Z. Wang, H. Kim, H. N. Alshareef, Adv. Mater. **2018**, *30*, 1706656.

[22] E. Quain, T. S. Mathis, N. Kurra, K. Maleski, K. L. Van Aken, M. Alhabeb, H. N. Alshareef, Y. Gogotsi, Adv. Mater. Technol. **2019**, *4*, 1800256.

[23] B. Akuzum, K. Maleski, B. Anasori, P. Lelyukh, N. J. Alvarez, E. C. Kumbur, Y. Gogotsi, ACS Nano **2018**, *12*, 2685.

[24] M. J. Solomon, A. S. Almusallam, K. F. Seefeldt, A. Somwangthanaroj, P. Varadan, Macromolecules **2001**, *34*, 1864.

[25] S. Naficy, R. Jalili, S. H. Aboutalebi, R. A. Gorkin, K. Konstantinov, P. C. Innis, G. M. Spinks, P. Poulin, G. G. Wallace, Mater. Horiz. **2014**, *1*, 326.

[26] V. Natu, M. Sokol, L. Verger, M. W. Barsoum, J. Phys. Chem. C **2018**, *122*, 27745.

[27] M. Ghidiu, M. R. Lukatskaya, M. Q. Zhao, Y. Gogotsi, M. W. Barsoum, Nature **2015**, *516*, 78.

[28] E. García-T On, S. Barg, J. Franco, R. Bell, S. Eslava, E. D'Elia, R. C. Maher, F. Guitian, E. Saiz, Adv. Mater. **2015**, *27*, 1688.

[29] V. G. Rocha, E. García-Tuñón, C. Botas, F. Markoulidis, E. Feilden, E. D'Elia, N. Ni, M. Shaffer, E. Saiz, ACS Appl. Mater. Interfaces **2017**, *9*, 37136.

[30] B. G. Compton, J. A. Lewis, Adv. Mater. **2014**, *26*, 5930.

[31] W. Wu, A. Deconinck, J. A. Lewis, Adv. Mater. **2011**, *23*, H178.

[32] Y. Y. Peng, B. Akuzum, N. Kurra, M. Q. Zhao, M. Alhabeb, B. Anasori, E. C. Kumbur, H. N. Alshareef, M. Der Ger, Y. Gogotsi, Energy Environ. Sci. **2016**, *9*, 2847.

[33] W. Li, Y. Li, M. Su, B. An, J. Liu, D. Su, L. Li, F. Li, Y. Song, J. Mater. Chem. A **2017**, *5*, 16281.

[34] M. Alhabeb, K. Maleski, B. Anasori, P. Lelyukh, L. Clark, S. Sin, Y. Gogotsi, Chem. Mater. **2017**, *29*, 7633.

[35] A. Lipatov, M. Alhabeb, M. R. Lukatskaya, A. Boson, Y. Gogotsi, A. Sinitskii, Adv. Electron. Mater. **2016**, *2*, 1600255.

[36] C. Bao, H. Zhang, C. A. Wilkie, S. Bi, X. Z. Tang, J. Wu, J. Yang, Carbon **2016**, *107*, 774.

[37] E. García-Tuñón, E. Feilden, H. Zheng, E. D'Elia, A. Leong, E. Saiz, ACS Appl. Mater. Interfaces **2017**, *9*, 32977.

[38] B. Akuzum, K. Maleski, B. Anasori, P. Lelyukh, N. J. Alvarez, E. C. Kumbur, Y. Gogotsi, ACS Nano **2018**, *12*, 2685.

[39] S. Roh, D. P. Parekh, B. Bharti, S. D. Stoyanov, O. D. Velev, Adv. Mater. **2017**, *29*, 1701554.

[40] E. Koos, N. Willenbacher, Science **2011**, *331*, 897.

[41] E. García-T On, S. Barg, J. Franco, R. Bell, S. Eslava, E. D'Elia, R. C. Maher, F. Guitian, E. Saiz, Adv. Mater. **2015**, *27*, 1688.

[42] A. J. Blake, R. R. Kohlmeyer, J. O. Hardin, E. A. Carmona, B. Maruyama, J. D. Berrigan, H. Huang, M. F. Durstock, Adv. Energy Mater. **2017**, *7*, 1602920.

[43] Y. Fang, Z. Liu, J. Han, Z. Jin, Y. Han, F. Wang, Y. Niu, Y. Wu, Y. Xu, Adv. Energy Mater. **2019**, *9*, 1803406.

[44] S. Xu, G. Wei, J. Li, Y. Ji, N. Klyui, V. Izotov, W. Han, Chem. Eng. J. **2017**, *317*, 1026.

[45] Y. Zhang, B. Guo, L. Hu, Q. Xu, Y. Li, D. Liu, M. Xu, J. Alloys Compd. **2018**, *732*, 448.

[46] L. Wang, H. Zhang, B. Wang, C. Shen, C. Zhang, Q. Hu, A. Zhou, B. Liu, Electron. Mater. Lett. **2016**, *12*, 702.

[47] Q. Zhang, F. Zhang, S. P. Medarametla, H. Li, C. Zhou, D. Lin, Small **2016**, *12*, 1702.

[48] B. Chen, Z. Zhu, J. Hong, Z. Wen, J. Ma, Y. Qiu, J. Chen, Dalton Trans. **2014**, *43*, 10767.

[49] J. Jagiello, M. Thommes, Carbon **2004**, *42*, 1227.

[50] M. Beidaghi, C. Wang, Adv. Funct. Mater. **2012**, *22*, 4501.

[51] C. J. Zhang, B. Anasori, A. Seral-Ascaso, S. H. Park, N. McEvoy, A. Shmeliov, G. S. Duesberg, J. N. Coleman, Y. Gogotsi, V. Nicolosi, Adv. Mater. **2017**, *29*, 1702678.

[52] Q. Jiang, N. Kurra, M. Alhabeb, Y. Gogotsi, H. N. Alshareef, Adv. Energy Mater. **2018**, *8*, 1703043.

3.6 Experimental Section

Preparation of few-layer large-flake $Ti_3C_2T_x$ (T=F/OH) and ink preparations

Firstly, LiF powder was dispersed into 6 M HCl at room temperature. The mixture was stirred for several minutes until LiF dissolved completely. Subsequently, Ti_3AlC_2 powders (flake size < 38 μm) were added slowly into the LiF/HCl mixture over the course of 5 mins while stirring. Mass ratio of LiF, $Ti_3C_2T_x$ and HCl is set as 2:3:6.6. The reaction was allowed to proceed under continuous stirring at 30 °C for 24 hours. The as-synthesized mixture was washed with deionized water by centrifugation at 3,500 rpm for 5 mins, and the black viscous supernatant was collected. The material was collected and washed with deionized water several times at high-speed centrifugation of 10,000 rpm. During this procedure the water molecules intercalate the layers to exfoliate the flakes. The intercalation of water within the high aspect ratio and negatively charged flakes (Zeta potential of -41 mV with standard deviation of 2 mV) results in a clay-like state. When the system reaches a pH of around 7 the clay-like sediment was collected to prepare inks of various concentrations.

Preparation of $Ti_3C_2T_x$ ink of different concentrations and rheology test.

The sediment collected after 10,000 rpm washing was used to prepare inks. Firstly, the concentration of the final sediment was directly calculated (between 30 and 90 mg mL^{-1}). In order to adjust the concentration of the inks (e.g. at 15, 30, 50 mg mL^{-1}) the required amount of water is added or removed by vacuum drying at room temperature. The homogenisation of the inks was achieved using speed mixer (SpeedMixer DAC 150 SP) at 2,000-3,500 rpm for 10-20 mins.

Since the $Ti_3C_2T_x$ inks used in this work are made of few-layer large flakes (high aspect ratio) with repulsive negative functional groups the flakes are dispersed homogeneously in an aqueous solution ensuring the printed filaments present a uniform micromorphology. Afterwards, $Ti_3C_2T_x$ inks with various concentrations (15 mg mL^{-1}, 30 mg mL^{-1}, 50 mg mL^{-1}) were prepared to explore the rheological properties, using a TA Instruments rheometer with 20 mm parallel plate geometry (gap=1,000 μm).

3D printing of $Ti_3C_2T_x$ architectures.

Printable $Ti_3C_2T_x$ inks (minimum concentration of 50 mg mL^{-1}) were loaded into a 30 mL syringe attached to a stainless steel nozzle. A computer program converted the input 3D model

(drew by 3ds MAX) into the machine command and controlled the nozzle jetting (applied pressure of 1-5 MPa) and motion (printing speed of 6-10 mm sec^{-1}). The programmed 3D structures were printed (envisiontec 3D-BIOPLOTTER) on top of a glass slide. After 3D printing, the samples were immediately transferred into a dry ice box and frozen samples were subsequently freeze dried (Labconco FreeZone 4.5L -105C Benchtop Freeze Dryer) for 24 h.

The assembly of $Ti_3C_2T_x$ based MSCs.

3D interdigitated architectures were printed on glass slides, and after drying we obtained interdigitated symmetric electrodes. The solid electrolyte was prepared by dissolving 6 g poly (vinyl alcohol) (PVA) powder in 30 mL deionized water at 90 °C, followed by the addition of 6 g 98 wt% sulfuric acid (H_2SO_4). Two silver wires were connected separately with two electrodes by conductive silver glue. After the glue dried completely, the electrolyte gel was casted onto the whole electrodes without touching the conductive silver glue (**Fig. S3**).

Characterization of structures and properties.

The surface morphology images and chemical composition of the as-prepared samples were acquired by scanning electron microscope (SEM, TESCAN Mira3 LC) with an energy dispersive spectroscopy (EDX) microprobe and atomic force microscope (AFM, Dimension 3100). The crystal structures were characterized through X-ray diffraction (XRD) taking on a Bruker D8 Advanced diffractometer using Cu Kα radiation (λ=0.15406 nm). Specific surface area of the prepared material was calculated using Brunauer-Emmett-Teller (BET) method (ASAP 2020m, Micromeritics, USA). The density of the $Ti_3C_2T_x$ powder was measured by Helium Pycnometer. Cycle voltammetry (CV), galvanostatic charge/discharge and electrochemical impedance spectroscopy (EIS) measurements were carried out with an Autolab electrochemical workstation and a Battery Test System (Germany). The gravimetric specific capacitance of single electrode is C_s (F g^{-1}), which was calculated based on following equations: $C_s = \frac{2I*\triangle t}{m*\triangle V}$, where I (A) is the discharge current, $\triangle t$ (s) is the discharge duration, $\triangle V$ (V) represents the voltage change during the discharge process, and m (g) is the weight of active material. $C_A = \frac{2I*\triangle t}{A*\triangle V}$, Where C_A is geometric surface normalized capacitance (F cm^{-2}), A is the geometric surface of the electrode (cm^2). The EIS curves were recorded by applying a sine wave with 5 mV amplitude under the frequency range of 10^5 Hz to 10^{-2} Hz.

3.7 Supplementary Information

Supplementary Figures

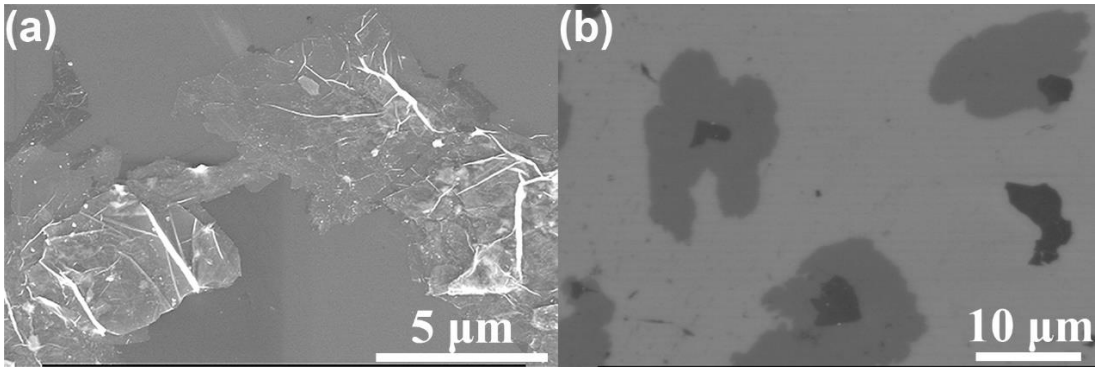

Figure S1 SEM images of exfoliated $Ti_3C_2T_x$.

Figure S2 Image of 3D printable inks showing the viscous nature. Inks have been printed through nozzles as small as 250 µm in diameter, and extruded filaments were strong enough to support their own weight and 25 subsequent layers without deflection (printed wet structures in **Fig. 2g**).

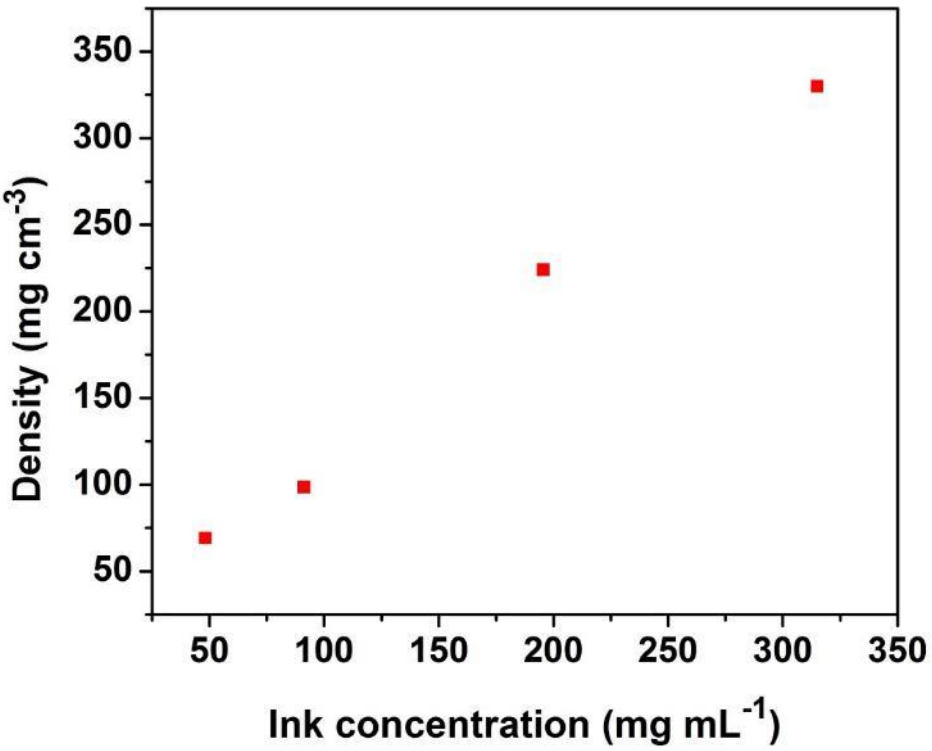

Figure S3 Bulk densities of freeze-dried printed filaments as a function of ink concentration.

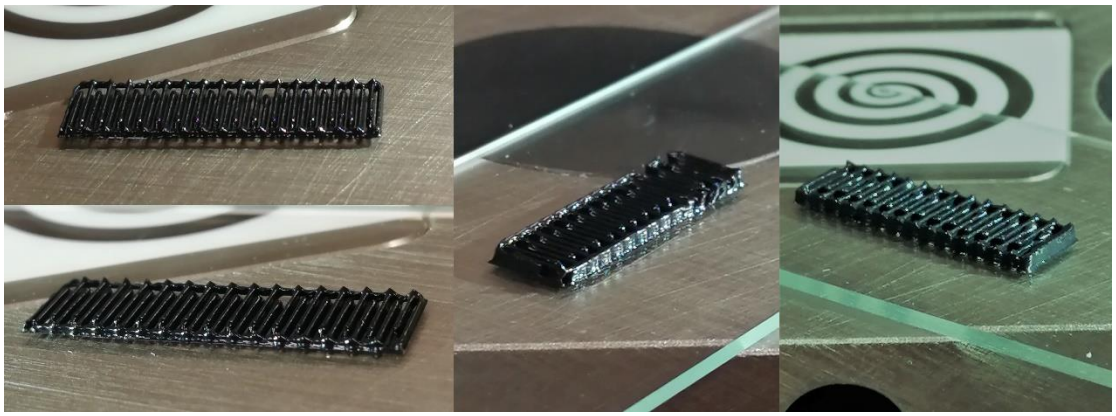

Figure S4 Photographs of the 3D printed interdigitated electrodes with variable number of layers in height. Clockwise: 2, 4, 4, and 2 printed layers. Samples are 5 x 25 mm lateral dimensions. All samples were printed with a printing speed of 6-10 mm/sec and 330 um nozzle internal diameter.

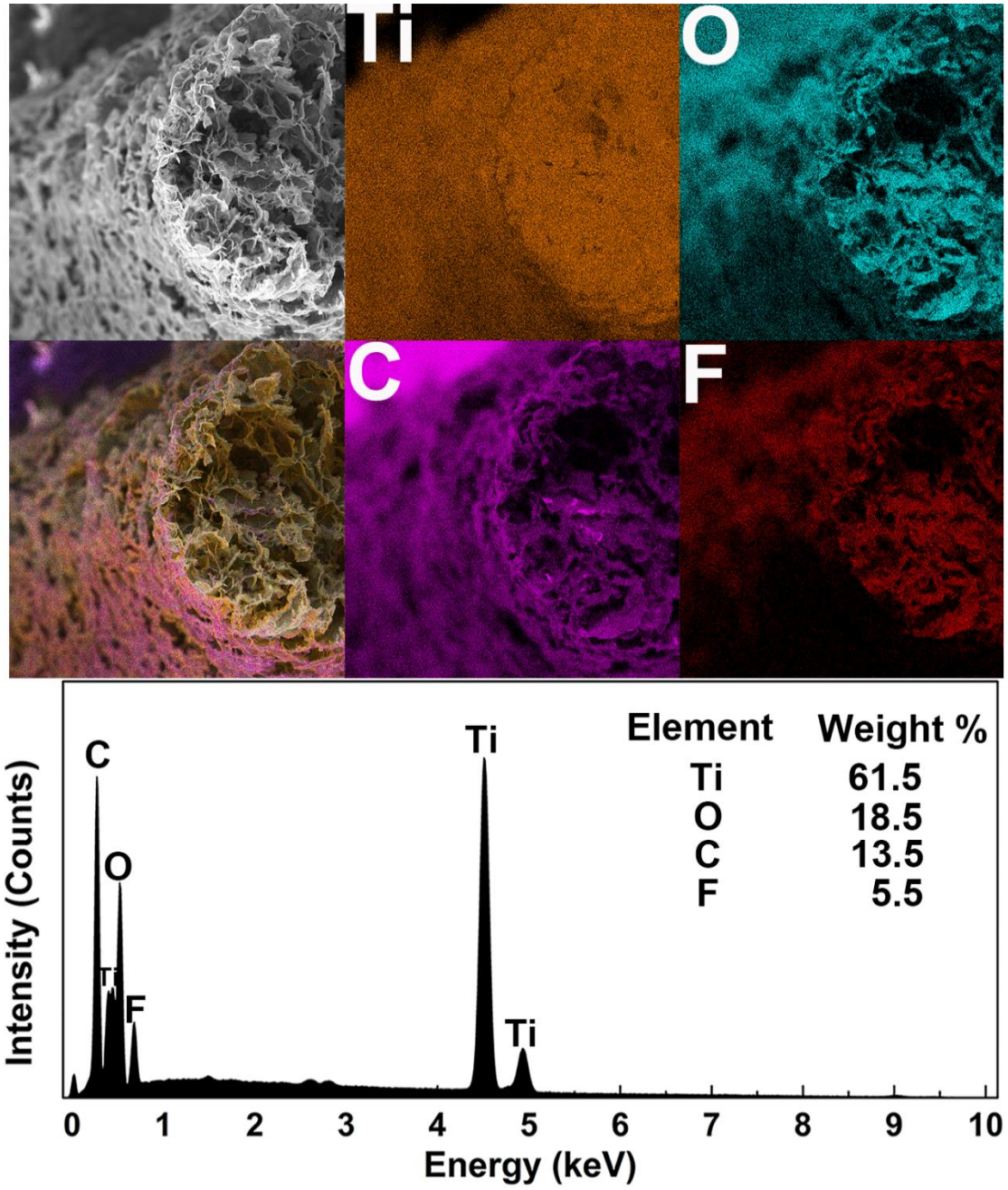

Figure S5 SEM image of printed few-layer large-flake $Ti_3C_2T_X$ string and corresponding elemental maps of titanium, oxygen, carbon and fluorine via Energy-dispersive X-ray spectroscopy (EDX). The results demonstrated that the few-layer large-flake $Ti_3C_2T_X$ was mainly composed of Ti, C, O and F elements well distributed in the printed structure.

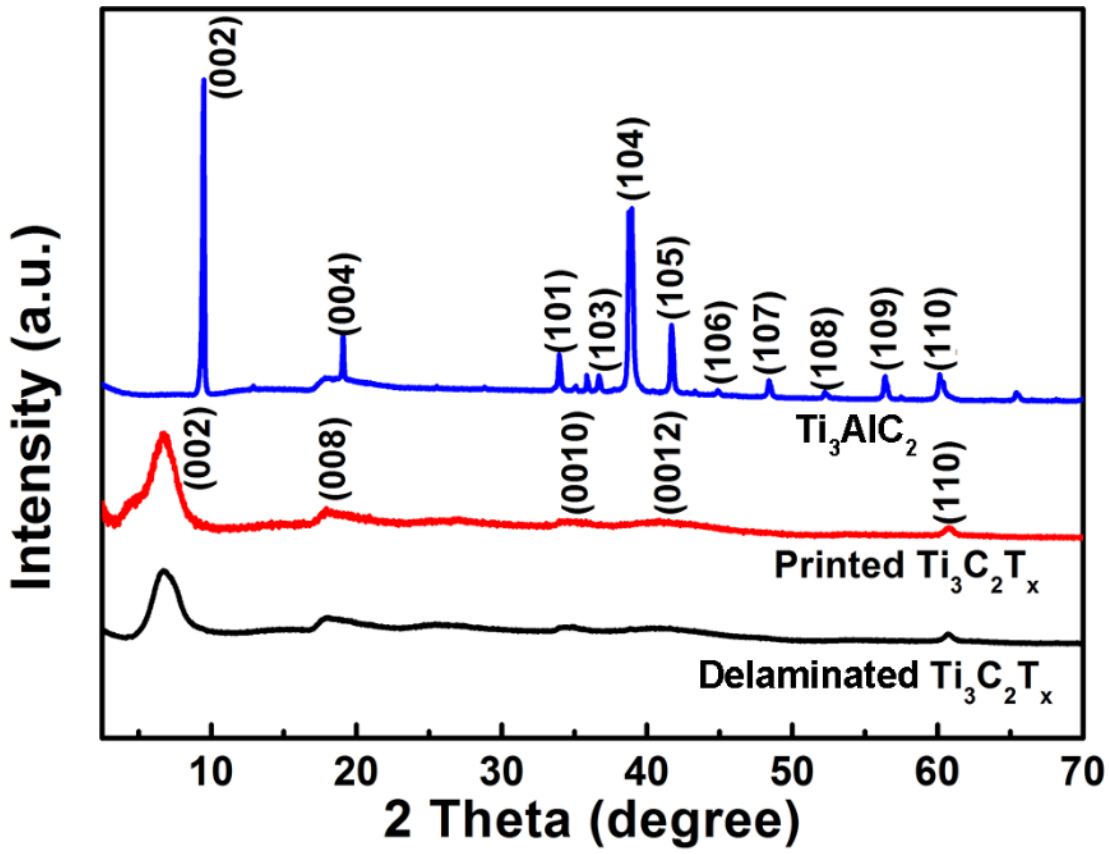

Figure S6 XRD diffraction patterns of exfoliated Ti_3AlC_2, printed Ti_3AlC_2 and Ti_3AlC_2 precursor. The XRD pattern with peaks at 9.5°, 19.2°, 34.0°, 36.8°, 39.1°, 41.8°, 44.9°, 48.5°, 52.4°, 56.5° and 60.3° is well assigned to the (002), (004), (101), (103), (104), (105), (106), (107), (108), (109) and (110) planes of Ti_3AlC_2 precursor (JCPDS No. 52-0875), respectively. After the etching and delamination process, the typical diffraction peaks of Ti_3AlC_2 have changed significantly and the peaks of $Ti_3C_2T_x$ emerge. In particular, the sharp peak at 39.1° is broadened indicating the removal of Al layers from Ti_3AlC_2 and the formation of $Ti_3C_2T_x$. After the Al layers are removed and replaced by other oxygen-containing functional groups such as -OH, -O and -F, the (002) peak shifts to a lower angle and becomes broadened. It is noted that the printed $Ti_3C_2T_x$ shows very similar XRD with delaminated $Ti_3C_2T_x$ powder.

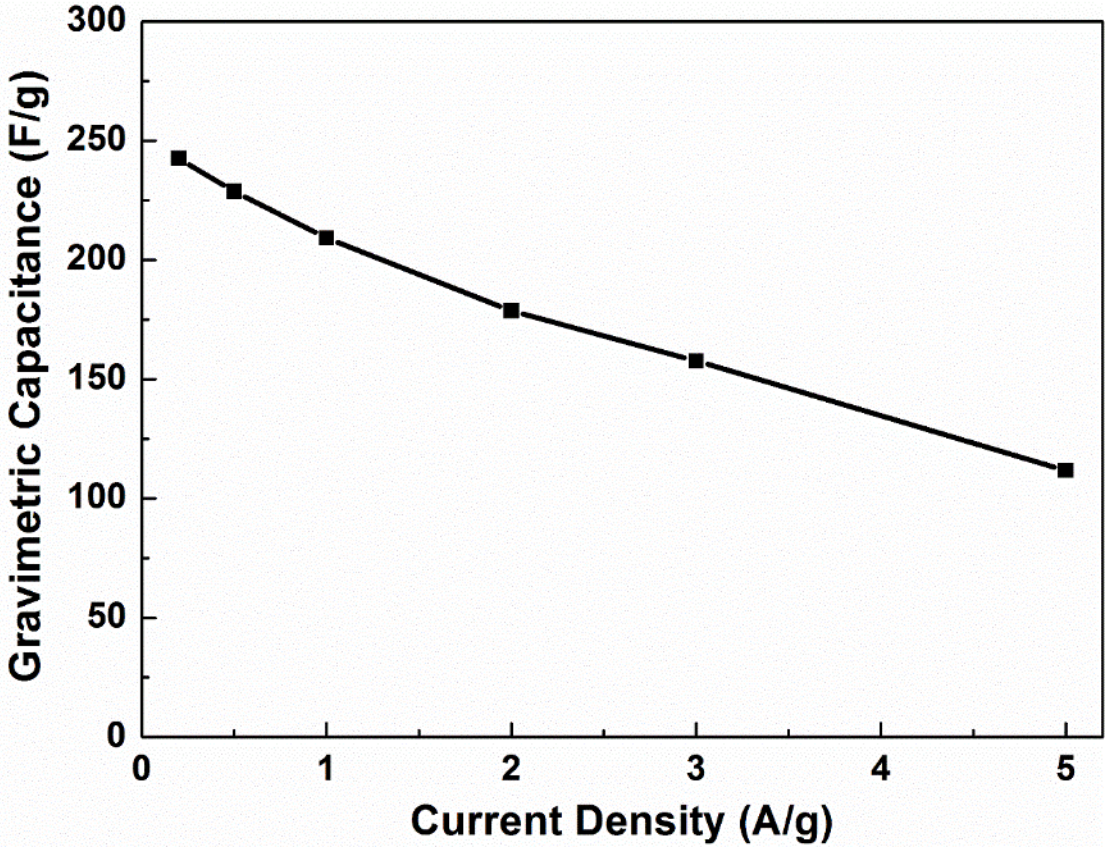

Figure S7 Gravimetric capacitance *versus* different areal current densities (0.2-5 A g^{-1})

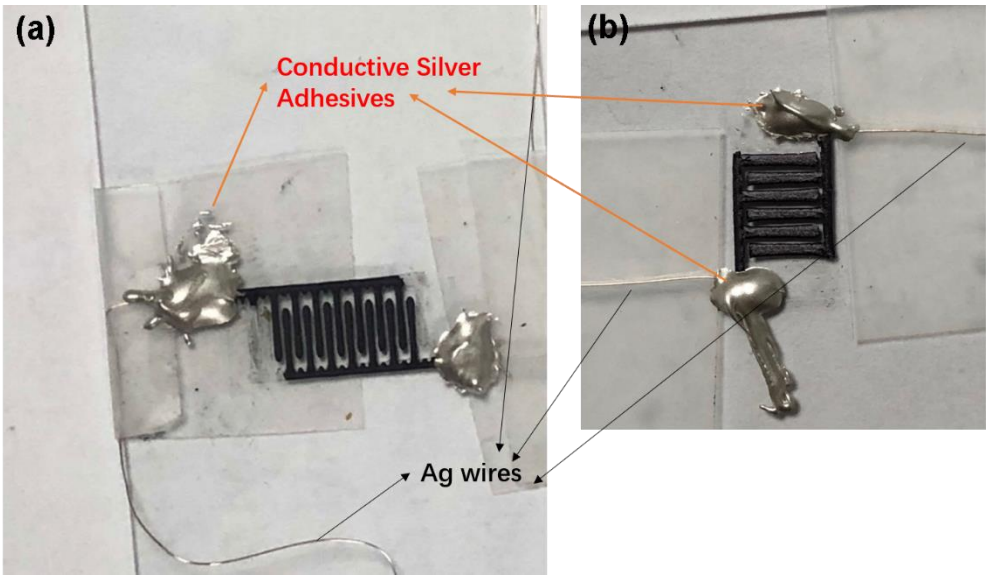

Figure S8 Photographs of 3D-printed interdigitated electrodes and assembly of micro-supercapacitor configuration (Corresponding to **Fig. 3e-f**). Various interdigitated electrode with different leg diameter values and variable gaps between two legs can be printed. In the images, the 3D printed interdigitated designs have a combination of $Ti_3C_2T_X$ finger thickness and gap of 326 and 187 μm (a) and 640 and 316 μm (b). Electrodes have 5 mm in the smallest lateral size.

In the recent review paper with my colleagues about the rheology of MXene dispersions for colloidal processing [1], we have fitted the viscosity, η (Pa s) of these inks prepared in this work and also some data collected from literatures to an equation:

$$\eta \approx 1.1 \cdot Z^{1.5} C^{1.5} \dot{\gamma}^{-0.9} \equiv \eta_m$$

where Z (μm) is the average lateral size of the MXene flake, C (wt%) represents the concentration of the MXene inks, $\dot{\gamma}$ (s^{-1}) is the applied shear rate. The accuracy of this fitting to different published datasets is presented in **Fig. S9**. Almost all of the data are accurately fitted by this model to within a factor of 2. The Cox-Merz rule, i.e. the correspondence between the steady state shear viscosity, η, and the magnitude of the complex viscosity, $\eta*$ (= G∗/iω, where ω is the angular frequency). The degree of adherence to the Cox-Merz rule provides insight into the nature of colloidal microstructures under shear, and where it is adhered to, η or $\eta*$ can be predicted when only data on the other are available. For example, cone/plate rheometers often cannot reach the *ca.* 10^6 s^{-1} steady shear rates experienced during inkjet printing without unwanted sample ejection, so oscillatory shear could be used to estimate η at such a high rate [2].

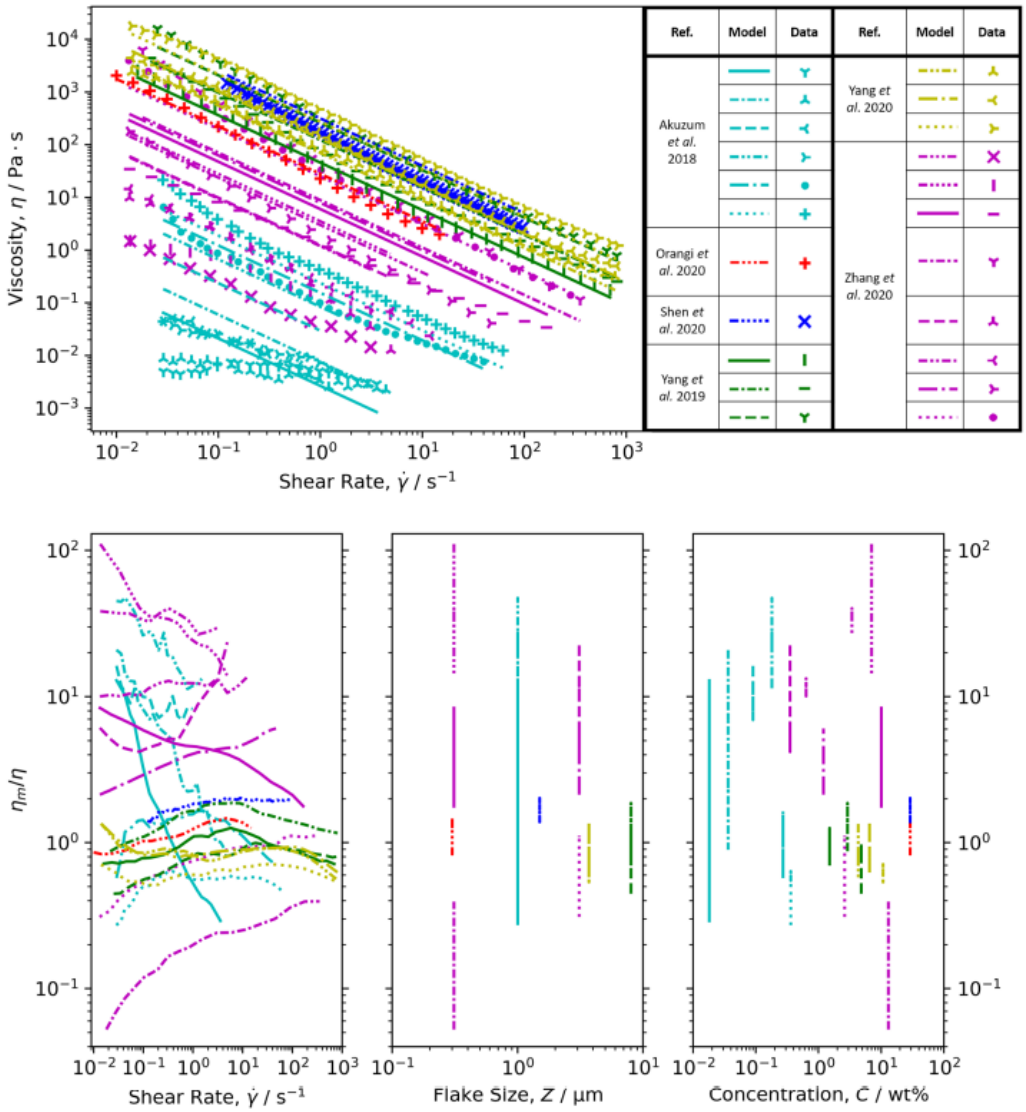

Figure S9 Published viscosity, η, data (symbols) plotted as a function of shear rate, $\dot{\gamma}$, alongside the viscosities predicted by the Equation above [3][4][5][6][7][8]. Below is the accuracy of η_m (measured as the quotient η_m/η) plotted as a function of the three parameters used in its calculation: $\dot{\gamma}$, Z and C [1].

Reference

[1] M. Greaves, M. Mende, J. Wang, W. Yang, S. Barg, *J. Mater. Res.* **2021**, DOI 10.1557/s43578-021-00282-7.

[2] S. Uzun, M. Schelling, K. Hantanasirisakul, T. S. Mathis, R. Askeland, G. Dion, Y. Gogotsi, *Small* **2021**, *17*, 1.

[3] W. Yang, J. Yang, J. J. Byun, F. P. Moissinac, J. Xu, S. J. Haigh, M. Domingos, M. A. Bissett, R. A. W. Dryfe, S. Barg, *Adv. Mater.* **2019**, *31*, 1.

[4] K. Shen, B. Li, S. Yang, *Energy Storage Mater.* **2020**, *24*, 670.

[5] B. Akuzum, K. Maleski, B. Anasori, P. Lelyukh, N. J. Alvarez, E. C. Kumbur, Y. Gogotsi, *ACS Nano* **2018**, *12*, 2685.

[6] J. Zhang, S. Uzun, S. Seyedin, P. A. Lynch, B. Akuzum, Z. Wang, S. Qin, M. Alhabeb, C. E. Shuck, W. Lei, E. C. Kumbur, W. Yang, X. Wang, G. Dion, J. M. Razal, Y. Gogotsi, *ACS Cent. Sci.* **2020**, *6*, 254.

[7] J. Orangi, F. Hamade, V. A. Davis, M. Beidaghi, *ACS Nano* **2020**, *14*, 640.

[8] W. Yang, J. J. Byun, J. Yang, F. P. Moissinac, Y. Peng, G. Tontini, R. A. W. Dryfe, S. Barg, *Energy Environ. Mater.* **2020**, *3*, 380.

Chapter 4. Freeze-assisted Tape Casting of vertically aligned MXene films for high rate performance supercapacitors

4.1 Chapter Introduction

The practical potential of MXenes (two-dimensional, a few atoms thick layers of transition-metal carbides, nitrides, and carbonitrides) as supercapacitor electrodes has become more promising with the successful vertical alignment of MXene nanosheets on substrates. These electrodes exhibit excellent rate performance. The conventional configuration is composed of horizontally stacked MXene sheets that are undesirable for fast-rate charging as ion diffusion through the sheets is severely impeded by the compact-film configuration. The sluggish ion movement leads to deterioration of energy storage capacity at elevated charging rates. This problem is exacerbated when the film thickness approaches or exceeds 10 μm, far less than the industrial thickness standard of 100 μm for active materials used in supercapacitors. To resolve this issue, developing electrodes with straight ion-movement channels extending from the electrode surface to the substrate is critical.

A potential solution is by attaching a surfactant, hexaethylene glycol monododecyl ether (C12E6), onto the surface of $Ti_3C_2T_x$ through hydrogen bonds, which turns the $Ti_3C_2T_x$ nanosheets into high-order liquid crystals, coined lamellar nematic. Upon applying a shear force, these surface-modified $Ti_3C_2T_x$ sheets "stand" straight on the substrate, forming orderly distributed arrays, as suggested by liquid-crystal theory. These vertical arrays were maintained after the C12E6 surfactants were removed. This structure contains abundant inter-sheet slits that serve as ion-movement "expressways" to allow quick ion diffusion [1].

Chemical vapor deposition (CVD) and filtration are the commonly used methods to prepare freestanding composite electrodes. These techniques are associated with high capital and operating costs and long processing time and require energy-intensive equipment. Recently, Susantyoko et al. have developed a surface engineered tape-casting fabrication technique to produce MWCNT-based freestanding sheets; the technique is characterized by being low-cost, high-throughput, scalable, largescale, and capable of roll-to-roll processing [2]. In the conventional casting method, electrode materials are cast onto a metal current collector and

always tend to stick to the substrate and almost impossible to peel as a perfect sheet. In contrast, surface-engineered tape-casting fabrication technique allows easy separation of the active material from the supporting substrate to produce mechanically strong freestanding sheets. In this chapter I propose a method which will allow easy detachment of MXene electrodes from a substrate This is accomplished by ensuring the following criteria are met: (i) enough difference between active material and substrate surface energies, and (ii) casting on a substrate with favourable pore structure morphology.

In this work, the thesis author conceived this study carried out materials fabrication, SEM/EDS/XRD/Rheology and data analysis, making and casting of the MXene slurries, and finally wrote the paper. Jae Jong Byun assisted with X-ray computed tomography (XCT) and Yang Jie assisted with electrochemical measurements. All authors contributed to discussing and review of the manuscript. The original manuscript is presented in the following sections.

[1] C. Wang, X. Wang, L. Zhang, *J. Phys. Energy* **2020**, *2*, 041002.

[2] R. A. Susantyoko, Z. Karam, S. Alkhoori, J. *Mater. Chem. A* **2017**, *5*, 19255.

Paper: Freeze-assisted Tape Casting of vertically aligned MXene films for high rate performance supercapacitors

Wenji Yang†*, Jae Jong Byunδ†, Jie Yang‡§, Francis Peter Moissinac†, Yudong Peng†, Gustavo Tontini†, Robert A.W. Dryfe‡§, Suelen Barg†*

†Royce Institute and Department of Materials, University of Manchester, Oxford Road, Manchester, M13 9PL, U.K.

δ Department of Electrical and Electronic Engineering, University of Manchester, Sackville Street Building, Manchester M1 3BB, U.K.

‡ National Graphene Institute, University of Manchester, Oxford Road, Manchester, M13 9PL, U.K.

§ Department of Chemistry, University of Manchester, Oxford Road, Manchester M13 9PL, U.K.

* Corresponding authors: wenji.yang@manchester.ac.uk; suelen.barg@manchester.ac.uk

KEYWORDS: Freeze-Assisted Tape Casting; Thickness-Independent Capacitance; Vertically Aligned Electrodes; MXene; Supercapacitors

4.2 Abstract

Conventional electrode preparation techniques of supercapacitors such as tape-casting or vacuum filtration often lead to the restacking or agglomeration of two-dimensional (2D) materials. As a result, tortuous paths are created for the electrolyte ions and their adsorption onto the surfaces of the active materials can be prevented. Consequently, maintaining high rate performance whilst increasing the thickness of electrodes has been a challenge. Herein, a facile freeze-assisted tape casting (FaTC) method is reported for the scalable fabrication of flexible MXene ($Ti_3C_2T_x$) supercapacitor electrode films of up to 700 μm thickness, exhibiting homogeneous ice-template microstructure composed of vertically aligned MXene walls within lamellar pores. The efficient ion transport created by the internal morphology allows for fast electrochemical charge-discharge cycles and near thickness-independent performance at up to 3,000 mV s^{-1} for films of up to 300 μm in thickness. By increasing the scan rate from 20 to 10,000 mV s^{-1}, $Ti_3C_2T_x$ films of 150 μm in thickness sustain 50 % of its specific capacitance (222.9 F g^{-1}). When the film thickness is doubled to 300 μm, its capacitance is still retained by 60 % (at 213.3 F g^{-1}) when the scan rate is increased from 20 to 3,000 mV s^{-1}, with a capacitance retention above 97.7 % for over 14,000 cycles at 10 A g^{-1}. They also showed a remarkably high gravimetric and areal power density of 150 kW kg^{-1} at 1,000 A g^{-1} and 667 mW cm^{-2} at 4,444 mA cm^{-2}, respectively. FaTC has the potential to provide industry with a viable way to fabricate electrodes formed from 2D materials on a large scale, whilst providing promising performance for use in a wide range of applications, such as flexible electronics and wearable energy storage devices.

4.3 Introduction

Expanding the electrification of the automotive and aerospace industry, in addition to increasing the supply of renewable energy within electrical grids, calls for large-scale storage of electrochemical energy. Although batteries are the electrochemical energy storage (EES) devices commonly employed due to their high energy density, their shortcomings are that they tend to be relatively heavy and their slow charge-discharge cycles are unsuitable for certain high-performance applications [1]. Supercapacitors are alternative EES devices that could potentially overcome the limitations of batteries in some circumstances, by combining the prominent characteristics from electric double-layer capacitors which are not limited by solid-state diffusion, and pseudo-capacitors which stores energy by a faradaic process.

Supercapacitors demonstrate high power densities [1], fast charge-discharge profiles, relative lightness (as opposed to batteries) and durability (ability to sustain capacitance for many cycles), which make them suited to meet the growing energy demand. However, application of these devices necessitates materials and associated fabrication methods that facilitate the creation of electrodes with high energy and power densities.

Two-dimensional (2D) materials are an ideal candidate electrode material due to their large specific surface areas [2–4]. Of recent interest are MXenes [2,3] (2D carbides and nitrides (X) of a transition metal (M)) with titanium carbide ($Ti_3C_2T_x$) being a material that falls in this classification. In addition to its high electrical conductivity [5] and aspect ratio (lateral size to thickness), $Ti_3C_2T_x$ demonstrates hydrophilicity due to the terminal functional groups (-F, -OH) anchored to the surface during the etching reaction, resulting in the ability to be spontaneously intercalated by polar organic molecules. This facilitates its processability and allows it to participate in electrochemical reactions, making it an ideal supercapacitor electrode material [2,3,6]. Despite this, there are several challenges in the fabrication of devices that effectively utilize the properties of 2D materials.

Two common and facile methods in assembling electrodes are tape casting and vacuum filtration of a solution through a porous membrane [7,8]. These typically create a thin film electrode assembly with good flexibility and relatively strong mechanical properties [9,10]. However, the nature of these methods typically leads to a restacking of the 2D material [11] which reduces the accessible surface area and limits ion transport in thicker films. This results in electrodes whose electrochemical performance highly depends on the thickness of the film. The problem is further compounded by the in-plane alignment of 2D sheets which also lead to the formation of tortuous paths, impacting rate performance [12–14]. Limiting film thickness is a common way to avoid the accumulated stacking of 2D sheets in thicker films and induce enhanced performances in the resultant electrode [6,7,12]. However, other metrics of electrochemical performance such as areal capacitance might be hindered as a result.

Other varied strategies are employed to mitigate these limitations and facilitate ion transport. For one, the interlayer spacing between 2D sheets can be increased by intercalating with ions in a process commonly referred to as ‘pillaring’ [15–18]. Alternatively, introducing porosity into the 2D sheets by designing nano-architectures such as ‘holes’ [19–21], has also been proposed to facilitate ion transport. Nonetheless, these methods would still result in materials that have low

volumetric energy storage or complex ion transport pathways that will impede the performance of the device at high charge-discharge rates [12,13].

Another fabrication method involves creating highly porous foam-like electrodes[22,23] composed of the 2D materials [22,23]. This can be seen in our previous work where a combination of lyophilisation and additive manufacturing namely, direct-ink writing (DIW) was used to synthesize interdigitated MXene electrodes as current-collector free supercapacitors [24]. The electrodes had limited degrees of restacking and retained high porosity, which maximised surface area accessibility and ion transport. The electrodes fabricated via this method indicated promising performance with a high areal capacitance of 2.1 F cm^{-2} at 1.7 mA cm^{-2} and gravimetric capacitance of 242.5 F g^{-1} at 0.2 A g^{-1}, with a retention of 90 % for 10,000 cycles [24]. A further variety of unique assembly techniques of three-dimensional (3D) porous structures have been reported [25], seeking to increase ion mobility within the structures.

Whilst the mentioned fabrication methods demonstrate promising performance, the optimal assembly configuration for 2D materials is the vertical alignment of 2D sheets [12,26,27]. This would enable directional ion transport leading to thickness-independent electrochemical performance in thick films. This is seen in an earlier work carried out by Yu Xia et. al. [12]. The authors managed to maintain over 75 % of the capacitance (at scan rate of 2,000 mV s^{-1}) of films ranging from 40 µm to 200 µm in thickness by using a novel method of mechanically shearing a discotic lamellar liquid-crystal phase of $Ti_3C_2T_x$ with a non-ionic surfactant to enhance molecular interactions between the sheets. Although the vertical alignment of 2D materials has shown promise in sustaining high rate performance with increased electrode thickness [12,26,27], their performance is limited with losses at higher rates, especially for films that approach the industrial standard of approximately 100 µm [12].

Within this work, freeze-assisted tape casting (FaTC) is applied to overcome the stacking challenges found in fabricating 2D material electrodes, whilst maintaining vertical alignment of the 2D sheets. In addition, its ease of integration into current manufacturing supply chains, relatively low cost and scalable roll-to-roll processing makes it an appealing method for fabricating supercapacitor electrodes formed from 2D materials with three-dimensional architecture.

FaTC is a combination of two manufacturing techniques: tape casting and ice-templating. Tape casting is a process involving a doctor blade regulating the thickness of a film formed by an aqueous colloid or slurry, on a carrier substrate, followed by some sort of drying or post-

treatment processing. Korkut et. al. [10] fabricated tough, high conductive functionalized graphene films by tape casting an aqueous dispersion of functionalized graphene sheets and polymeric surfactants.

The other facet of FaTC is ice-templating. This aspect of the fabrication process is critical in ensuring the vertical alignment of the 2D sheets. By reducing the temperature of the casting bed of the film being tape-cast, a directional temperature gradient is induced. This will initiate the freezing of the tape-cast colloid. As it is more energetically favourable, ice-crystals will be formed via heterogeneous nucleation on the surface of the casting-bed and in some cases, on the surface of the material sheet. The directional growth of ice-crystals along the thermal gradient is used to template the microstructure of the film. Growth of lamellar ice-crystals exerts a force which segregates the MXene sheets at the solid-liquid interface, concentrating them between the ice crystals [28,29]. This solid-liquid phase separation is further aided by a quasi-liquid layer of oriented water molecules which decreases the surface energy of the ice and acts as a lubricating layer [30]. Ice-templating has been employed to develop high performance supercapacitor films with MXene, such as in the work demonstrated by Zhang Peng et. al. which showcases a $Ti_3C_2T_x$/CNT film with an internal porous network, exposing a greater amount of surface active sites[31,32].

FaTC is a popular manufacturing method for functionally graded structures and porous ceramics [33–38]. For example, Yu Chen et. al. [33] fabricated functionally graded acicular electrodes for solid oxide fuel cells using this method, achieving enhanced electrochemical performance. Although there has been work done on applying tape casting to nanomaterials for flexible electronics and EES devices [37–40], the effectiveness of this method to produce electrodes with thickness independent performance and its application to other functional 2D materials beyond graphene, is still to be realised. Yoon Hwa et. al. [41] successfully applied the FaTC method in creating aligned graphene-oxide-sulphur cathodes, to mitigate sulphur reconstruction and facilitate lithium ion transport in lithium-sulphur batteries.

In this work, we demonstrate the feasibility of FaTC for the scalable manufacturing of electrodes composed of vertically aligned 2D MXene microstructures. Based on the single or few layer $Ti_3C_2T_x$ preparation and exfoliation method developed in our previous work [24], we formulated viscoelastic $Ti_3C_2T_x$ aqueous slurries suitable for FaTC without the addition of binders or conductive agents. By adjusting ice-templating parameters within the freeze-tape casting bed, vertically aligned $Ti_3C_2T_x$ films with thickness of 150, 200, 300, 400, 500 and 700

μm were obtained and evaluated with electrochemical performance testing. Supercapacitors constructed with electrodes with thicknesses between 150 and 300 μm exhibited near thickness-independent electrochemical performance for current densities of up to 100 A g^{-1} and scan rates of up to 3,000 mV s^{-1}. As a consequence of the meticulous quality control steps during the $Ti_3C_2T_x$ exfoliation and the vertical aligned microstructural design of the films, these electrodes showed a gravimetric and areal energy density of 2.8 Wh Kg^{-1} and 1.8 μWh cm^{-2} for 150 μm films; and 2.6 Wh Kg^{-1} and 11.3 μWh cm^{-2} for 700 μm films. They further achieved a gravimetric power density of 150 kW kg^{-1} at 1,000 A g^{-1} and an areal power density of 667 mW cm^{-2} at 4,444 mA cm^{-2} (700 μm). The vertically aligned $Ti_3C_2T_x$ films further retain good flexibility and mechanical properties demonstrating their potential in a broad range of application areas, such as flexible electronics and wearable energy storage devices.

4.4 Results and Discussion

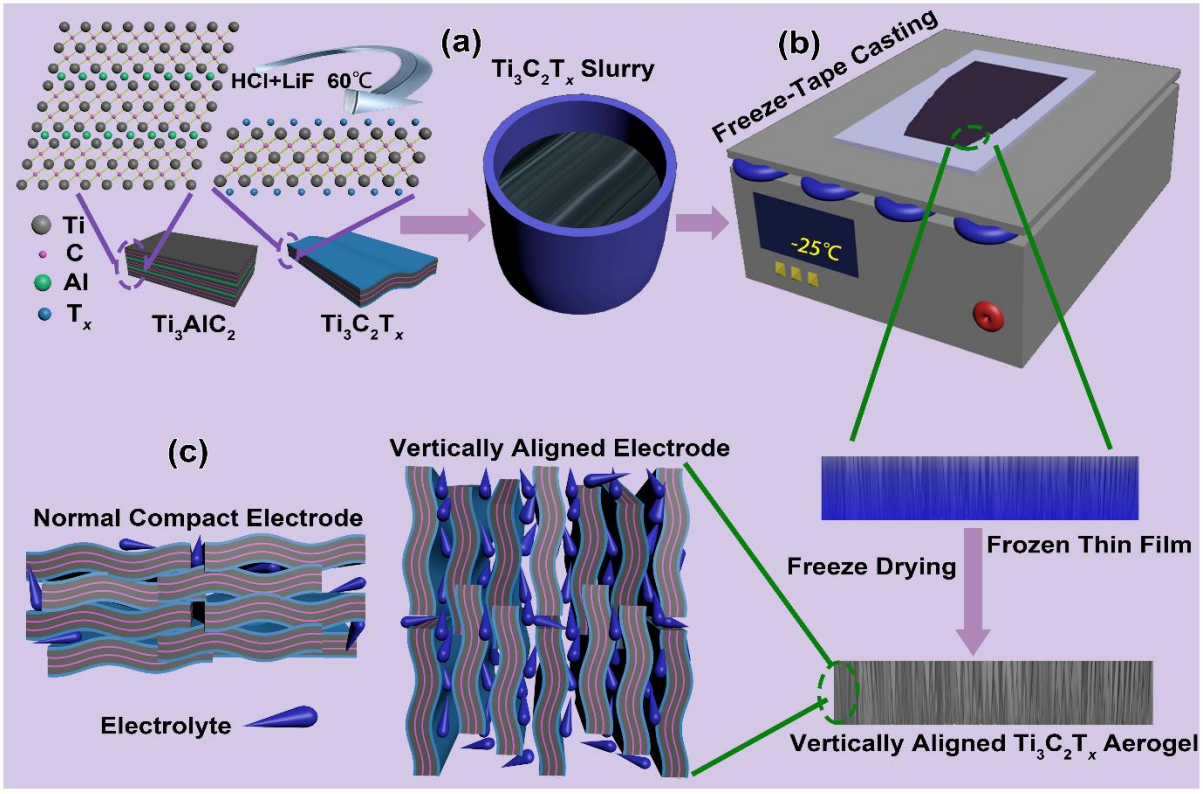

Figure 1 Schematic representation of the manufacturing process of vertically aligned $Ti_3C_2T_x$ films through unidirectional freezing assisted tape casting (FaTC). a) MILD (Minimal Intensity Layer Delamination) synthesis of few layers $Ti_3C_2T_x$ at 60 ℃ and their formulation into castable slurries; b) FaTC of MXene slurries into vertically aligned aerogel films; c) representation of electrolyte impregnation and path within the aligned electrodes developed in this work in comparison with traditional compact morphologies.

The manufacturing strategy of the 3D porous $Ti_3C_2T_x$ aerogel films with the vertically aligned microstructure is illustrated in **Fig. 1**. Firstly, the MILD method [42,43] was chosen to etch the precursor Ti_3AlC_2 (flakes < 10 μm) to the delaminated single or few layered $Ti_3C_2T_x$ at 60 °C (**Fig. 1a**). After the concentrated single or few layered $Ti_3C_2T_x$ aqueous paste were produced, slurries with specific concentrations (45, 70 and 120 mg mL^{-1}) were prepared for the subsequent casting (**Fig. 1b**). During FaTC, the $Ti_3C_2T_x$ slurry was deposited on the upper surface of a pre-cooled aluminium plate (at –25 °C) using a doctor blade to spread the slurry with a fixed thickness, and the film was frozen onto the substrate. The frozen $Ti_3C_2T_x$ films were subsequently freeze-dried to obtain the vertically aligned $Ti_3C_2T_x$ aerogels. A schematic comparison between stacked electrodes typically made by conventional methods and a vertically aligned porous electrode as made by our method (**Fig. 1c**) represents the improved

accessibility of the electrolyte in the latter allowing for a larger surface of active material to be reached by ions, improving the efficiency of electrochemical mechanisms.

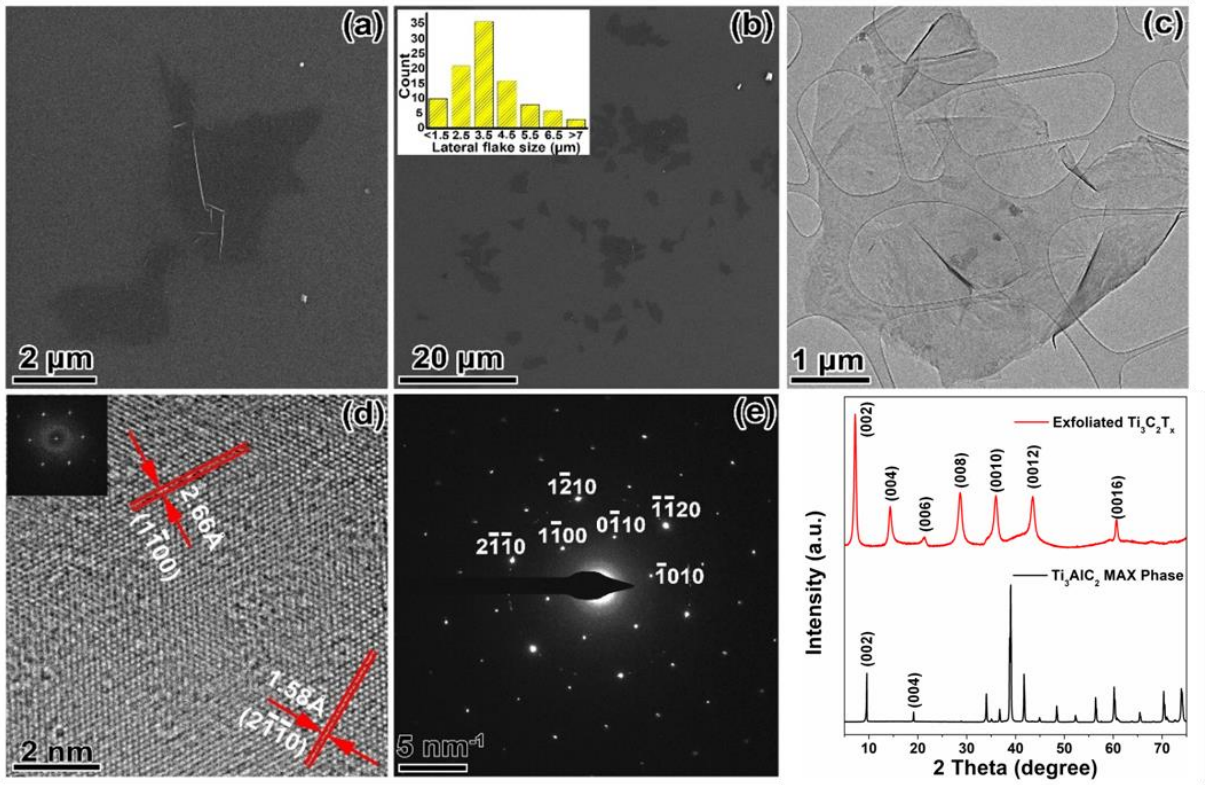

Figure 2 Characterization of exfoliated $Ti_3C_2T_x$ flakes. (a-b) SEM images of $Ti_3C_2T_x$ flakes prepared by drop casting from a dilute $Ti_3C_2T_x$ solution in water on silica plates. The inset in (b) shows the lateral size distribution of $Ti_3C_2T_x$ flakes, measured from SEM images of over 100 flakes. (c) Low-magnification TEM image, (d) HRTEM (high-resolution TEM) and (e) SAED patterns of the delaminated $Ti_3C_2T_x$ flakes. (f) XRD patterns of the exfoliated $Ti_3C_2T_x$ and precursor Ti_3AlC_2.

The typical morphology of the $Ti_3C_2T_x$ flakes obtained by the etching process is shown in **Fig. 2a-b**. An average lateral flake size of 3.7 µm is obtained from the size distribution measured from scanning electron microscopy (SEM) (inset of **Fig. 2b**). The low-magnification TEM image reveals a quite thin and transparent flake on the lacey carbon grid (**Fig. 2c**). The HRTEM image in **Fig. 2d** shows the single crystallinity of the $Ti_3C_2T_x$ flake basal plane, and the measured interplanar spacings in the figure are 2.66 Å and 1.58 Å corresponding to the $(0\bar{1}10)$ and $(2\bar{1}\bar{1}0)$ lattice planes, respectively. The selective area electron diffraction (SAED) pattern (**Fig. 2e**) shows that the $Ti_3C_2T_x$ flakes in this area maintain crystallinity and the hexagonal symmetry of the basal planes of the precursor Ti_3AlC_2 MAX phase. The XRD patterns of the exfoliated $Ti_3C_2T_x$ and precursor Ti_3AlC_2 and are shown in **Fig. 2f**. The $Ti_3C_2T_x$ sediment is separated from the exfoliated $Ti_3C_2T_x$ during exfoliation and post etching washing process. In

terms of the diffraction pattern for exfoliated $Ti_3C_2T_x$, all identified peaks can be attributed to the basal planes of $Ti_3C_2T_x$ as assigned and in accordance to the literature for MILD synthesis [44]. The large d-spacing of ~ 12.3 Å observed for the (002) plane at 7.19 degrees and the absence of non-basal reflections indicate the successful exfoliation of the flakes. Meanwhile, although also exhibiting the (002) peak of the exfoliated $Ti_3C_2T_x$ phase, the XRD pattern of the sediment (**Fig. S1**) also indicates the presence of the precursors Ti_3AlC_2 (PDF 04-012-0632 [45]) and LiF (PDF 00-004-0857 [46]), by-product α-Al_2O_3 (PDF 04-004-2852 [47]), and $TiC_{0.62}$ (PDF 04-017-1603 [48]). Since this mixed product influences negatively both the control of the FaTC process and the electrochemical properties of the material, it is crucial to highlight the importance of a thorough washing process.

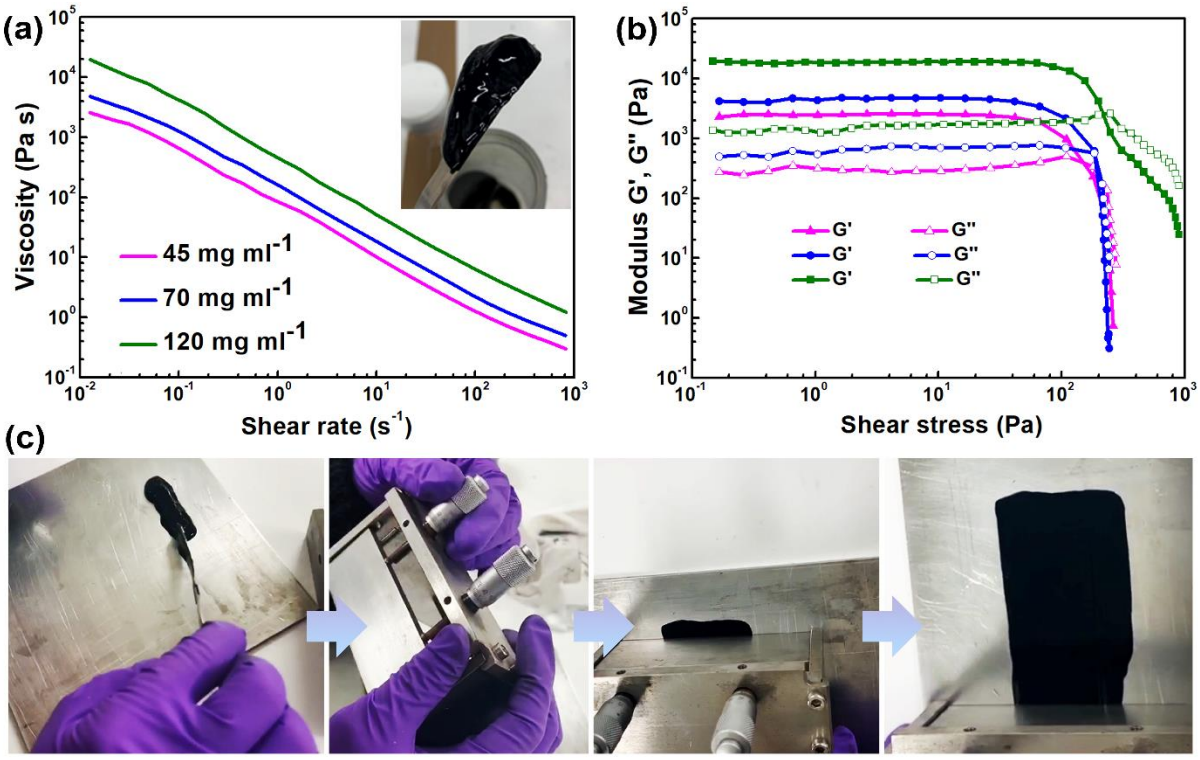

Figure 3 (a-b) Rheological properties of $Ti_3C_2T_x$ slurries prepared with 45, 70 and 120 mg mL^{-1} flakes concentration. (a) Viscosity *versus* shear rate (inset optical camera image depicts the viscous feature of 45 mg mL^{-1} ink), (b) Viscoelastic properties (storage and loss modulus as a function of shear stress. (c) Optical camera images of the processing of a $Ti_3C_2T_x$ slurry into a film via FaTC. From left to right: slurry cast onto the aluminium plate; doctor blade adjusted to produce the desired film thickness; slurry spread onto the aluminium plate at –25 °C to fabricate film with vertically aligned MXene porous structure.

Rheological properties such as viscosity and viscoelastic properties are key to enable the fabrication of homogeneous films of controllable thicknesses via FaTC method. Therefore, rheological investigations were carried out to identify the processability of the water based $Ti_3C_2T_x$ slurries at concentrations of 45, 70 and 120 mg mL^{-1} (**Fig. 3**). According to the viscosity versus shear rate curves in **Fig. 3a**, all slurries of varying concentrations show distinct shear thinning behaviour. The shear thinning behaviour of the slurries ensures that the MXene flakes are spread evenly during the tape casting process [42]. In order to define the linear and non-linear viscoelastic properties of these slurries, the variation tendency of both the storage modulus (G') and the loss modulus (G") were investigated regarding the applied shear stress in the range 0.1 to 1,000 Pa at a constant angular frequency of 10 rad s^{-1} (**Fig. 3b**). Until a critical oscillation stress (above 100 Pa), both moduli stay level with G' presenting higher values than G''. Since the small shear stress oscillation demanded minor structure deformation, the slurries behave in a more elastic than viscous manner and show a linear viscoelastic behaviour. After the crossover point (150.5, 186.1 and 216.7 Pa for 45, 70 and 120 mg mL^{-1} slurries respectively), all three slurries exhibited non-linear viscoelasticity where the storage moduli dropped rapidly due to the breakdown of the weak force acting between the single/few-layer $Ti_3C_2T_x$ flakes as a result of the applied shear stress [49]. A sufficient storage modulus allows the films to retain their thickness, even after removal of the applied shear force [50]. The storage modulus in the linear elastic region increases with increased concentration of the MXene flakes (reaching 18, 991 Pa for 120 mg mL^{-1}). However, even with the lowest concentration of 45 mg mL^{-1}, the storage modulus is high enough to allow the slurries to retain its shape after casting.

The developed $Ti_3C_2T_x$ slurries have shown favourable rheological properties to produce homogeneous films of adjustable thickness between 150-700 µm, while simultaneously enabling the formation of lamella ice crystals that template pores between vertically orientated MXene interconnected flakes (**Figs. 3c**, **4 and S2**). However, the highest concentration of $Ti_3C_2T_x$ investigated in this work, induced swifter freezing of the slurries, due to the lower water content. Therefore, thinner films were more difficult to produce with the highest concentrations (120 mg mL^{-1}). This could be overcome by controlling the casting speed (the speed at which the doctor blade was applied to slurries) by the development of an automated casting system.

Typically, tape-casting process requires a relatively high-loading of colloids [49], but this could have adverse effects on ice-templating. During freezing of concentrated colloids at low growth

velocities, the fraction of 2D sheets at the interface increases, which may lead to increased loading of the sheets at the freeze front. This may induce ice-crystal growth perpendicular to the thermal gradient in a phenomenon called ice-lensing [51,52]. Consequently, the resultant material would have alternating layers of ice and re-stacked 2D sheets. These cumulative factors need to be carefully considered when developing the fabrication method to manufacture vertically aligned MXene sheets via FaTC.

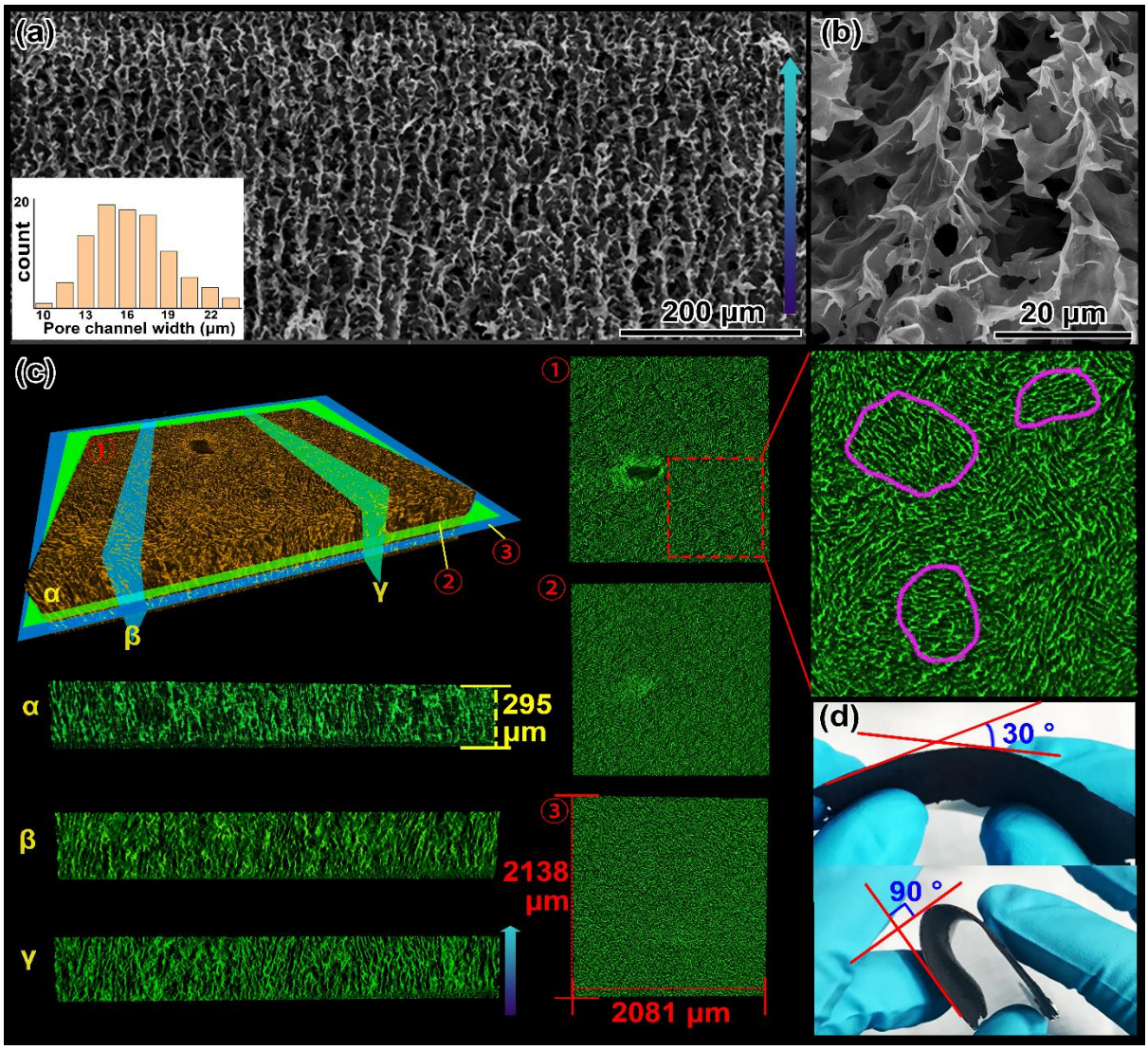

Figure 4 Microstructural and flexibility investigation of vertical aligned $Ti_3C_2T_x$ films produced from FaTC of 70 mg mL^{-1} slurry. (a, b) SEM cross-sectional images of the film's internal microstructure. The inset in (a) depicts the pore width distribution. (c) X-ray CT images of the $Ti_3C_2T_x$ film showing: The 3D reconstruction of a volume of interest within the sample; Views onto ①-③ (corresponding approximately to the view perpendicular to the freezing direction) demonstrate the alignment of the pores and the domains organization (purple rings) within the structure; Views onto α-γ (corresponding to the view parallel to the freezing direction) show the lamellae architecture with the alignment of the

$Ti_3C_2T_x$ sheets within the region. The arrow in SEM and CT images represent the freezing direction. (d) Digital photographs of a $Ti_3C_2T_x$ film with a thickness of 300 μm, showing its flexibility during bending.

The control of the solids loading in the slurry provides direct control of the density of freeze-dried films, and so represent an opportunity to control their physical and electrochemical properties via the FaTC approach. Slurries of 45 and 70 mg mL^{-1} resulted in films of average 43.1 and 71.7 mg cm^{-3} density, respectively. The morphology of typical films produced from 70 mg mL^{-1} is shown in **Fig. 4.** The cross-sectional SEM image (parallel to the freezing direction) of a ~ 400 μm thick sample (observing a decrease in the final thickness of the film after freeze drying; final thicknesses are listed in **Table.S1**) reveals the three-dimensionally uniform porous lamellar microstructure composed of vertically aligned $Ti_3C_2T_x$ flakes (**Figs. 4a** and **4b**). The lamellae channels are 16.2 μm wide on average as measured from the SEM micrographs (the size distribution is depicted in the inset of **Fig. 4a**). These channel between $Ti_3C_2T_x$ vertically aligned walls offer significant advantages for the absorptions of the electrolyte and transportation of the ions, especially for the furthest part to the opposite electrode.

The interconnected-lamellar/cellular structures observed in **Figs. 4a** and **4b** are a result of the growth of lamellar ice-crystals and segregation of the MXene sheets within it, which is dependent on the freeze-front (interface of growing ice-crystals and colloid) velocity[53]. This is governed by the cooling rate of the casting bed (aluminium plate) i.e. the induced thermal gradient. At low growth velocities, the freeze-front is planar [53,54], and as such the 2D sheets would be pushed to the top surface of the tape-casted film. However, this planar interface can be destabilized by Mullins-Sekerka instabilities, which are a sinusoidal perturbation arising from the interface at the solidification front [55]. They are the result of isotherms being compressed in front of a protrusion with the consequent latent heat produced diffusing more readily in this area. This results in faster growth of the protrusion to a certain direction [55] (stabilized by surface tension), resulting in the desired directional lamellar ice morphology. At rapid interface velocities, the freeze-front will become planar again, as the 2D sheets will be engulfed by the ice crystals preventing redistribution or ice-templating effects [53,54]. Ascertaining from the obtained morphology of the films (**Figs. 4a, 4b and S2**) from the FaTC process, and given an average MXene flake size of 3.7 μm, we can infer an intermediate freeze front velocity that is between unstable and metastable regimes [54]. To further analyse the morphology and 3D homogeneity of a ~ 300 μm thick $Ti_3C_2T_x$ film, X-ray CT was performed (**Fig. 4c**)**.** The analysis enabled the reconstruction of a large sample volume of ~ 300 μm

thickness (the actual film thickness) and ~ 2 mm sides. Although X-ray CT's resolution cannot define the MXene sheets as well as the SEM micrographs, cross-sectional views parallel to the freezing direction (views onto α-γ) show similar vertical lamellae alignment throughout the investigated 2 mm volume of the film. Furthermore, tomography top views perpendicular to the freezing direction (Views onto ①-③) show the formation of incoherently aligned orientation domains (examples of domains are identified with the purple boundaries drawn in the enlarged view onto ①). This is predominantly caused by the heterogeneous nucleation of the ice-crystals on the substrate and their anisotropic growth behaviour further imposing constraints to the nucleation and growth of adjacent crystals, generating clusters with short-range orientation [28,56]. Bai et al. proposed a dual temperature gradient method to control these domains achieving both vertical and horizontal alignment [57].

The developed films are flexible and mechanically robust, which plays an advantage in order to maximize the utilization of the $Ti_3C_2T_x$ electrode films in wide areas, like for the fabrication of wearable supercapacitors. As exemplified in **Fig. 4d**, a 300 μm thick $Ti_3C_2T_x$ film can be bent at an angle of nearly 180 degrees, remaining macroscopically undamaged, demonstrating its robustness for potential application in flexible and wearable devices.

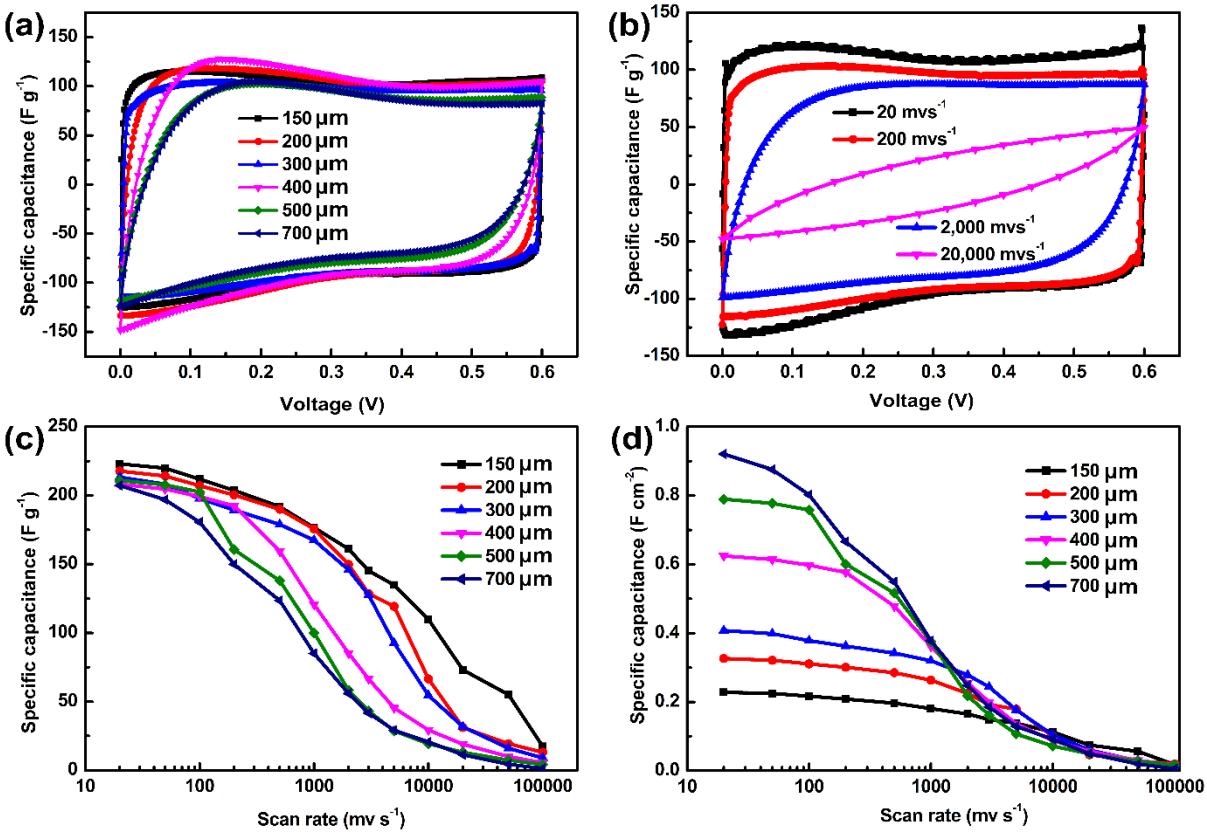

Figure 5 Electrochemical analysis of the vertically aligned $Ti_3C_2T_x$ films with thickness of 150, 200, 300, 400, 500 and 700 µm (produced from 70 mg mL^{-1} slurry). (a) Cyclic voltammograms (CV) of the samples at the scan rate of 200 mV s^{-1}. (b) CV of the 300 µm thick $Ti_3C_2T_x$ film at scan rates of 20, 200, 2,000 and 20,000 mV s^{-1}. (c, d) Rate performance (including gravimetric and areal) of the films at scan rates ranging from 20 to 100,000 mV s^{-1}.

To investigate the effectiveness of our approach for high rate performance applications, we have prepared two-electrode supercapacitor devices based on vertically aligned $Ti_3C_2T_x$ films produced from 70 mg mL^{-1} slurries with thickness of 150, 200, 300, 400, 500 and 700 µm. The cyclic voltammograms of the corresponding two-electrode supercapacitors based on films with varying thicknesses at a scan rate of 200 mV s^{-1} with a 3 M H_2SO_4 solution as the electrolyte are depicted in **Fig. 5a**. Almost all the CVs have maintained the typical rectangular shape, and the curves almost overlap when the thickness of the electrode varies from 150 to 400 µm. When the electrode thickness was increased to 500 and 700 µm, a slight shrinkage in the CV shape is observed due to the rising resistance. The electrochemical behaviour of the ordered vertically aligned porous structure shows an efficient mass transfer of the electrolyte ions despite the increase in the thickness of the electrode. Considering that the conventional electrode thickness is usually less than 100 µm [58–60], the modified structure created by the FaTC method shows a

great advantage in increasing the electrode thickness without sacrificing the electrochemical performance. **Fig. 5b** shows the CVs of a 300 μm thick sample at a large range of representative scan rates from 20 to 20,000 mV s^{-1}. When the scan rate was gradually increased from 20 to 3,000 mV s^{-1}, the rectangular shapes of the CV curves are retained, indicating the high rate performance of $Ti_3C_2T_x$ with this vertical porous structure (**Figs. 5b** and **S3**). The gravimetric and areal capacitance of samples with various thicknesses at different scan rates are shown in **Figs. 5c** and **5d**, respectively. With the enhancement of the scan rate value, the corresponding specific gravimetric capacitance of all thickness show very modest distortion, especially below 100 mV s^{-1}. For film thicknesses up to 300 μm, and scan rates up to 3,000 mV s^{-1}, the electrodes are still able to yield a comparatively high specific capacitance (127.4 F g^{-1}). The areal rate performance of the films shows that for thicknesses of up to 300 μm the capacitance is well maintained when the scan rate is increased up to 3,000 mV s^{-1}.

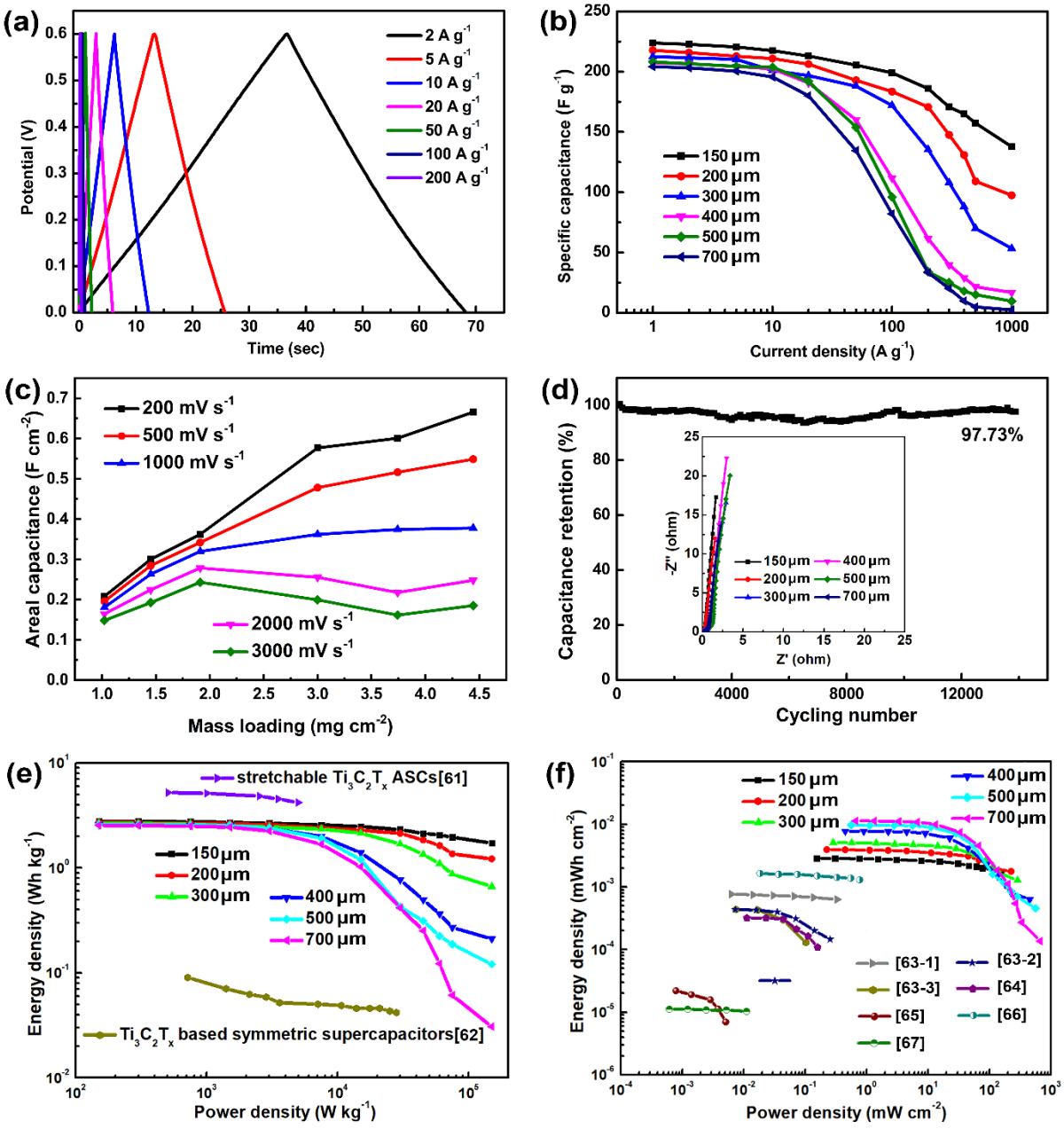

Figure 6 Electrochemical performance of the vertically aligned $Ti_3C_2T_x$ films with thicknesses of 150, 200, 300, 400, 500 and 700 µm (produced from 70 mg mL^{-1} slurry). (a) Galvanostatic charge-discharge profiles of the 300 µm thickness $Ti_3C_2T_x$ film at 2, 5, 10, 20, 50, 100, 200 A g^{-1}. (b) Gravimetric rate performance of the vertically aligned $Ti_3C_2T_x$ films at current densities ranging from 1 to 1,000 A g^{-1}. (c) Areal capacitance as a function of the mass loading at scan rates from 200 to 3,000 mV s^{-1}. The mass loading points (from left to right) correspond to films of 150, 200, 300, 400, 500 and 700 µm thickness. (d) Cycling stability of a vertically aligned $Ti_3C_2T_x$ electrode (thickness of 300 µm) tested by galvanostatic cycling at a current density of 10 A g^{-1} showing over 97 % capacitance retention after 14,000 cycles. The inset shows Nyquist plots of electrochemical impedance spectroscopy (EIS) for different thicknesses of vertically aligned $Ti_3C_2T_x$ films, tested at 0 V. Ragone plots of the two-electrodes $Ti_3C_2T_x$ supercapacitor displaying the gravimetric (e) and areal (f) energy and power

densities achieved by the vertically aligned $Ti_3C_2T_x$ films with the comparison to other MXene/graphene electrodes reported in the literature, [63-1: I-$Ti_3C_2T_x$] [63-2: Y-$Ti_3C_2T_x$] [63-3: Y-Ti_3CNT_x][63] [64: extrusion printed $Ti_3C_2T_x$ micro-supercapacitor][64] [65: spray-coated graphene][65] [66: screen printed $Ti_3C_2T_x$][66] [67: graphene/$Ti_3C_2T_x$ transparent electrode][67].

Galvanostatic charge-discharge (GCD) characteristics of the films at different current densities from 1 to 1,000 A g^{-1} were tested and the representative plots of 2, 5, 10, 20, 50, 100 and 200 A g^{-1} are exhibited in **Fig. 6a**. We can see linear symmetrical triangular charge-discharge lines with negligible IR drop, suggesting good energy storage behaviour and high electrical conductivity of the samples. The highest specific capacitance value of 224 F g^{-1} was achieved at a current density of 1 A g^{-1} for the 150 μm thick sample, originating from the effective utilization of the electrochemically active surface area. As the current density is further increased to an ultrahigh current density of 1,000 A g^{-1}, a high specific capacitance of 137.8 F g^{-1} can still be kept, which is much higher than the rate performances reported in most literature [61–67], showing the excellent rate performance achieved with the vertical microstructure of the electrode. The GCD rate performance of all samples were evaluated and displayed in **Fig. 6b**. The specific gravimetric capacitance value for the 150 μm sample is retained at 89 % and 62 % when the current density is increased from 1 to 100 A g^{-1} and 1 to 1,000 A g^{-1} respectively. Further, 81 % of the specific gravimetric capacitance (from 1 to 100 A g^{-1}) is retained when the thickness of the electrode increases to 300 μm. This is attributed to the porous lamellar structure facilitating the efficient mass transport of the electrolyte ions. **Fig. 6c** demonstrates the areal capacitance at varying scan rates as a function of mass loading (the areal mass loading increase corresponds to the increase in thickness from 150 to 700 μm). At scan rates below 500 mV s^{-1}, the areal capacitance increases almost linearly with mass loading up to 4.5 mg cm^{-2}, indicating the importance of the electrode morphology on the electrochemical behaviour, i.e. the ease of electrolyte transport into the porous electrode and increase of the active surface area participating in the electrochemical response. By increasing the scan rate above 500 mV s^{-1}, the relationship between areal capacitance and mass loading gradually deviates from linearity as the mass of electrodes increases above 3 mg cm^{-2}. Above a scan rate of 1,000 mV s^{-1}, capacitive equilibration is achieved for mass loadings above 2 mg cm^{-2}.

With the aim of investigating the cycling stability of films, a long-term cycling retention test at a high current density of 10 A g^{-1} was carried out (**Fig. 6d**). After 14,000 continuous cycles, the 300 μm thick sample retained 97.7 % of the initial value (after 1,000 cycle pre-activation), indicating that the electrochemical behaviour is highly reversible. The inset of **Fig. 6d** depicts

the electrochemical impedance spectroscopy (EIS) of samples of various thicknesses. The equivalent series resistance of the different electrodes is around 0.5 Ω, regardless of the electrode thickness, demonstrating a fast charge transportation. The plots of all different electrodes are almost vertical in the low frequency region, suggesting an excellent capacitive response in the vertically aligned $Ti_3C_2T_x$ films electrode. The Ragone plots in **Figs. 6e** and **6d** graphically depict the characteristics of the gravimetric, and areal energy and power densities of the corresponding supercapacitors based on the modified $Ti_3C_2T_x$ electrodes. The device made of 150 μm thick $Ti_3C_2T_x$ electrodes exhibits an energy density of 2.8 Wh kg^{-1} at a power density of 150 W kg^{-1}. Furthermore, when the power is increased by 1,000 times (150 kW kg^{-1}), the energy density is maintained at 62 % (1.7 Wh kg^{-1}). When the electrode thickness is increased to 200 and 300 μm, the energy densities can be maintained at 68 % and 51 % respectively, of the initial value while the power density increases by a factor of 300 (to 45 kW kg^{-1}), reflecting the ultrahigh power density potential of these devices. The vertically aligned two-electrode supercapacitors developed in this work are able to achieve one of the highest recorded values of power density compared to other MXene or graphene related works (as seen in **Fig. 6f**). The 150 μm thick electrode at a high-power density of 154 mW cm^{-2}, shows an energy density of 1.8 μWh cm^{-2} without sacrificing the inherent advantage of supercapacitors. On the other hand, a high areal power density of 667 mW cm^{-2} can be achieved at 4,444 mA cm^{-2} for the 700 μm thick electrode. The superior electrochemical performance of these $Ti_3C_2T_x$ electrodes can be attributed to the intrinsically high electrical conductivity of the exfoliated $Ti_3C_2T_x$ flakes (2,963 and 4,279 S cm^{-1} for MXene films made for 45 and 70 mg mL^{-1} slurries respectively) and the vertically aligned architecture produced by the FaTC manufacturing method. The directional channels, which run parallel to the direction of ion transport are an important design factor, as they overcome rate limitations, in contrast to a restacking electrode film produced by conventional electrode casting processes.

4.5 Conclusion

A key challenge with 2D materials conventional electrode preparation methods is their microstructural restacking. In this work, vertically aligned MXene electrodes were prepared via a facile and scalable FaTC method, minimising restacking, and producing a favourable architecture for electrolyte impregnation and diffusion. This enabled the realization two-electrode (up to 300 μm thickness each) supercapacitors with nearly thickness independent electrochemical performance across a wide range of high scan rates and current densities.

Furthermore, the industrially compatible $Ti_3C_2T_x$ films demonstrated remarkable gravimetric and areal power densities for 150 to 700 μm thicknesses. This was possible due to the preparation of MXene slurries with shear thinning behaviour, yet sufficiently retained storage modulus to facilitate the tape casting process while allowing the formation of lamellar ice crystals that template the vertically aligned MXene architecture within films. This work demonstrates the viability of FaTC for potential large-scale fabrication of EES device electrodes with greater thickness without losing performance during fast charge-discharge cycling. Despite encouraging initial results, there are several challenges and opportunities for subsequent work, including optimization of freeze and tape casting parameters to allow for the enhancement of solid loading, choice of substrate, and additives to enhance the energy density in addition to the development of multi-materials fabrication protocols. The authors hope that the processing route showcased within this work highlights its potential for the development of 2D material assemblies in various electronic and composite applications.

Acknowledgements

This work was supported by the Henry Royce Institute for Advanced Materials, funded through EPSRC grants EP/R00661X/1, EP/S019367/1, EP/P025021/1 and EP/P025498/1. The authors would like to acknowledge the University of Manchester for the President's Doctoral Scholar Award. R.A.W.D. thanks EPSRC for funding through the grants EP/R023034/1 and EP/N032888/1. The authors also acknowledge the Henry Mosley X-ray Imaging Facility and the Department of Materials X-ray Diffraction Suite at the University of Manchester and the technical support, advice and assistance provided by Dr. John E. Warren. S.B. would like to thank Heilongjiang Huasheng Graphite Co. Ltd. for funding.

Received: 04 May 2020

Revised: 18 June 2020

Published online: 30 September 2020

Reference

[1] Y. Gogotsi, P. Simon, *Science.* **2011**, *334*, 917.

[2] B. Anasori, M. R. Lukatskaya, Y. Gogotsi, *Nat. Rev. Mater.* **2017**, *2*, 16098.

[3] H. Tang, Q. Hu, M. Zheng, Y. Chi, X. Qin, H. Pang, Q. Xu, *Prog. Nat. Sci. Mater. Int.* **2018**, *28*, 133.

[4] M. R. Lukatskaya, S. M. Bak, X. Yu, X. Q. Yang, M. W. Barsoum, Y. Gogotsi, *Adv. Energy Mater.* **2015**, *5*, 1500589.

[5] C. J. Zhang, B. Anasori, A. Seral-Ascaso, S. H. Park, N. McEvoy, A. Shmeliov, G. S. Duesberg, J. N. Coleman, Y. Gogotsi, V. Nicolosi, *Adv. Mater.* **2017**, *29*, 1702678.

[6] S. Abdolhosseinzadeh, R. Schneider, A. Verma, J. Heier, F. Nüesch, C. (John) Zhang, *Adv. Mater.* **2020**, *32*, 2000716.

[7] M. Q. Zhao, C. E. Ren, Z. Ling, M. R. Lukatskaya, C. Zhang, K. L. Van Aken, M. W. Barsoum, Y. Gogotsi, *Adv. Mater.* **2015**, *27*, 339.

[8] Z. Ling, C. E. Ren, M. Q. Zhao, J. Yang, J. M. Giammarco, J. Qiu, M. W. Barsoum, Y. Gogotsi, *Proc. Natl. Acad. Sci.* **2014**, *111*, 16676.

[9] H. An, T. Habib, S. Shah, H. Gao, M. Radovic, M. J. Green, J. L. Lutkenhaus, *Sci. Adv.* **2018**, *4*, eaaq0118.

[10] S. Korkut, J. D. Roy-Mayhew, D. M. Dabbs, D. L. Milius, I. A. Aksay, *ACS Nano* **2011**, *5*, 5214.

[11] T. Hu, M. Hu, Z. Li, H. Zhang, C. Zhang, J. Wang, X. Wang, *Phys. Chem. Chem. Phys.* **2016**, *18*, 20256.

[12] Y. Xia, T. S. Mathis, M. Q. Zhao, B. Anasori, A. Dang, Z. Zhou, H. Cho, Y. Gogotsi, S. Yang, *Nature* **2018**, *557*, 409.

[13] R. Tian, M. Breshears, D. V Horvath, J. N. Coleman, *ACS Nano* **2020**, *14*, 3129.

[14] M. R. Lukatskaya, B. Dunn, Y. Gogotsi, *Nat. Commun.* **2016**, *7*, 12647.

[15] J. Luo, C. Fang, C. Jin, H. Yuan, O. Sheng, R. Fang, W. Zhang, H. Huang, Y. Gan, Y. Xia, C. Liang, J. Zhang, W. Li, X. Tao, *J. Mater. Chem. A* **2018**, *6*, 7794.

[16] J. Luo, C. Wang, H. Wang, X. Hu, E. Matios, X. Lu, W. Zhang, X. Tao, W. Li, *Adv. Funct. Mater.* **2019**, *29*, 1805946.

[17] J. Luo, W. Zhang, H. Yuan, C. Jin, L. Zhang, H. Huang, C. Liang, Y. Xia, J. Zhang, Y. Gan, X. Tao, *ACS Nano* **2017**, *11*, 2459.

[18] M. R. Lukatskaya, O. Mashtalir, C. E. Ren, Y. Dall'Agnese, P. Rozier, P. L. Taberna, M. Naguib, P. Simon, M. W. Barsoum, Y. Gogotsi, *Science (80-.).* **2013**, *341*, 1502.

[19] Y. Xu, Z. Lin, X. Zhong, X. Huang, N. O. Weiss, Y. Huang, X. Duan, *Nat. Commun.* **2014**, *5*, 1.

[20] Z. Fan, Y. Wang, Z. Xie, D. Wang, Y. Yuan, H. Kang, B. Su, Z. Cheng, Y. Liu, *Adv. Sci.* **2018**, *5*, 1800750.

[21] J. Yang, H. Wu, M. Zhu, W. Ren, Y. Lin, H. Chen, F. Pan, *Nano Energy* **2017**, *33*, 453.

[22] M. R. Lukatskaya, S. Kota, Z. Lin, M. Q. Zhao, N. Shpigel, M. D. Levi, J. Halim, P. L. Taberna, M. W. Barsoum, P. Simon, Y. Gogotsi, *Nat. Energy* **2017**, *2*, 17105.

[23] V. Bayram, M. Ghidiu, J. J. Byun, S. D. Rawson, P. Yang, S. A. McDonald, M. Lindley, S. Fairclough, S. J. Haigh, P. J. Withers, M. W. Barsoum, I. A. Kinloch, S. Barg, *ACS Appl. Energy Mater.* **2020**, *3*, 411.

[24] W. Yang, J. Yang, J. J. Byun, F. P. Moissinac, J. Xu, S. J. Haigh, M. Domingos, M. A. Bissett, R. A. W. Dryfe, S. Barg, *Adv. Mater.* **2019**, *31*, 1902725.

[25] G. Tontini, M. Greaves, S. Ghosh, V. Bayram, S. Barg, *J. Phys. Mater.* **2020**, *3*, 022001.

[26] Y. Yoon, K. Lee, S. Kwon, S. Seo, H. Yoo, S. Kim, Y. Shin, Y. Park, D. Kim, J. Y. Choi, H. Lee, *ACS Nano* **2014**, *8*, 4580.

[27] Z. Bo, W. Zhu, W. Ma, Z. Wen, X. Shuai, J. Chen, J. Yan, Z. Wang, K. Cen, X. Feng, *Adv. Mater.* **2013**, *25*, 5799.

[28] S. Deville, E. Maire, A. Lasalle, A. Bogner, C. Gauthier, J. Leloup, C. Guizard, *J. Am. Ceram. Soc.* **2009**, *92*, 2489.

[29] S. Deville, E. Saiz, A. P. Tomsia, *Acta Mater.* **2007**, *55*, 1965.

[30] N. H. Fletcher, *Philos. Mag.* **1968**, *18*, 1287.

[31] P. Zhang, Q. Zhu, R. A. Soomro, S. He, N. Sun, N. Qiao, B. Xu, *Adv. Funct. Mater.* **2020**, 2000922.

[32] P. Zhang, R. A. Soomro, Z. Guan, N. Sun, B. Xu, *Energy Storage Mater.* **2020**, *29*, 163.

[33] Y. Chen, J. Bunch, T. Li, Z. Mao, F. Chen, *J. Power Sources* **2012**, *213*, 93.

[34] T. Liu, Y. Chen, S. Fang, L. Lei, Y. Wang, C. Ren, F. Chen, *J. Memb. Sci.* **2016**, *520*, 354.

[35] E. P. Gorzkowski, M. J. Pan, B. A. Bender, in *2011 Int. Symp. Appl. Ferroelectr. 2011 Int. Symp. Piezoresponse Force Microsc. Nanoscale Phenom. Polar Mater. ISAF/PFM 2011*, **2011**.

[36] K. Araki, J. W. Halloran, *J. Am. Ceram. Soc.* **2005**, *88*, 1108.

[37] L. Ren, Y. P. Zeng, D. Jiang, *J. Am. Ceram. Soc.* **2007**, *90*, 3001.

[38] L. M. Wang, Z. F. Tang, J. Lin, X. D. He, C. S. Chen, C. H. Chen, *J. Mater. Chem. A* **2019**, *7*, 17376.

[39] A. Daraghmeh, S. Hussain, L. Servera, E. Xuriguera, M. Blanes, F. Ramos, A. Cornet, A. Cirera, *Mater. Res. Express* **2017**, *4*, 025007.

[40] R. A. Susantyoko, F. Parveen, I. Mustafa, S. Almheiri, *Ionics.* **2019**, *25*, 265.

[41] Y. Hwa, E. Yi, H. Shen, Y. Sung, J. Kou, K. Chen, D. Y. Parkinson, M. M. Doeff, E. J. Cairns, *Nano Lett.* **2019**, *19*, 4731.

[42] X. Sang, Y. Xie, M. W. Lin, M. Alhabeb, K. L. Van Aken, Y. Gogotsi, P. R. C. Kent, K. Xiao, R. R. Unocic, *ACS Nano* **2016**, *10*, 9193.

[43] M. Alhabeb, K. Maleski, B. Anasori, P. Lelyukh, L. Clark, S. Sin, Y. Gogotsi, *Chem. Mater.* **2017**, *29*, 7633.

[44] L. Verger, C. Xu, V. Natu, H. M. Cheng, W. Ren, M. W. Barsoum, *Curr. Opin. Solid State Mater. Sci.* **2019**, *23*, 149.

[45] E. Wu, J. Wang, H. Zhang, Y. Zhou, K. Sun, Y. Xue, *Mater. Lett.* **2005**, *59*, 2715.

[46] Swanson, Howard E, *United States Department Of Commerce National Bureau Of Standards* **1967**, *Circular 539 Vol 3*.

[47] J. Lewis, D. Schwarzenbach, H. D. Flack, *Acta Crystallogr. Sect. A* **1982**, *38*, 733.

[48] M. Y. Tashmetov, V. T. Em, C. H. Lee, H. S. Shim, Y. N. Choi, J. S. Lee, *Phys. B Condens. Matter* **2002**, *311*, 318.

[49] B. Bitterlich, C. Lutz, A. Roosen, *Ceram. Int.* **2002**, *28*, 675.

[50] M. Jabbari, R. Bulatova, A. I. Y. Tok, C. R. H. Bahl, E. Mitsoulis, J. H. Hattel, *Mater. Sci. Eng. B Solid-State Mater. Adv. Technol.* **2016**, *212*, 39.

[51] A. M. Anderson, M. G. Worster, *Langmuir* **2012**, *28*, 16512.

[52] A. M. Anderson, M. G. Worster, *J. Fluid Mech.* **2014**, *758*, 786.

[53] T. Waschkies, R. Oberacker, M. J. Hoffmann, *Acta Mater.* **2011**, *59*, 5135.

[54] S. Deville, E. Maire, G. Bernard-Granger, A. Lasalle, A. Bogner, C. Gauthier, J. Leloup, C. Guizard,

Nat. Mater. **2009**, *8*, 966.

[55] W. W. Mullins, R. F. Sekerka, *J. Appl. Phys.* **1964**, *35*, 444.

[56] S. Deville, E. Maire, A. Lasalle, A. Bogner, C. Gauthier, J. Leloup, C. Guizard, *J. Am. Ceram. Soc.* **2009**, *92*, 2497.

[57] H. Bai, Y. Chen, B. Delattre, A. P. Tomsia, R. O. Ritchie, *Sci. Adv.* **2015**, *1*, e1500849.

[58] S. K. Kim, H. J. Kim, J. C. Lee, P. V. Braun, H. S. Park, *ACS Nano* **2015**, *9*, 8569.

[59] J. Yun, D. Kim, G. Lee, J. S. Ha, *Carbon N. Y.* **2014**, *79*, 156.

[60] M. Acerce, D. Voiry, M. Chhowalla, *Nat. Nanotechnol.* **2015**, *10*, 313.

[61] T. H. Chang, T. Zhang, H. Yang, K. Li, Y. Tian, J. Y. Lee, P. Y. Chen, *ACS Nano* **2018**, *12*, 8048.

[62] R. B. Rakhi, B. Ahmed, M. N. Hedhili, D. H. Anjum, H. N. Alshareef, *Chem. Mater.* **2015**, *27*, 5314.

[63] C. J. Zhang, M. P. Kremer, A. Seral-Ascaso, S. H. Park, N. McEvoy, B. Anasori, Y. Gogotsi, V. Nicolosi, *Adv. Funct. Mater.* **2018**, *28*, 1705506.

[64] C. (John) Zhang, L. McKeon, M. P. Kremer, S. H. Park, O. Ronan, A. Seral-Ascaso, S. Barwich, C. Coileáin, N. McEvoy, H. C. Nerl, B. Anasori, J. N. Coleman, Y. Gogotsi, V. Nicolosi, *Nat. Commun.* **2019**, *10*, 1.

[65] H. Li, Y. Hou, F. Wang, M. R. Lohe, X. Zhuang, L. Niu, X. Feng, *Adv. Energy Mater.* **2017**, *7*, 1601847.

[66] C. (John) Zhang, V. Nicolosi, *Energy Storage Mater.* **2019**, *16*, 102.

[67] C. J. Zhang, B. Anasori, A. Seral-Ascaso, S. H. Park, N. McEvoy, A. Shmeliov, G. S. Duesberg, J. N. Coleman, Y. Gogotsi, V. Nicolosi, *Adv. Mater.* **2017**, *29*, 1702678.

4.6 Experimental Section

Synthesis of 2D $Ti_3C_2T_x$

Ti_3AlC_2 powder is the precursor for $Ti_3C_2T_x$ synthesis and was produced in *Laizhou Kai Kai Ceramic Material Co. Ltd*. The etching solution was prepared by dissolving 3 M equivalents of lithium fluoride (LiF, Alfa Aesar, 98+%) in 9 M hydrochloric acid (HCl, Alfa Aesar, 36.5-38.0 % and dilution with de-ionized water) inside a high density poly ethylene (HDPE) reaction vessel at room temperature. 3 g Ti_3AlC_2 powder was slowly added into the solution under vigorous stirring. The reaction vessel was heated and kept at 60 °C for 24 hours. After 24 hours, the reaction mixture was diluted with deionized (DI) water and transferred to centrifuge bottles followed by washing and centrifuging process at 3,500 rpm (Thermo Sorvall Legend XTR Centrifuge). After each centrifuging cycle, the clear supernatant is wasted and more deionized (DI) water is added for further washing, at the same time leading to the delamination of the $Ti_3C_2T_x$ multi-layered flakes. This step was repeated until the supernatant started to become a viscous and black suspension (indicating the presence of suspended single/few layer $Ti_3C_2T_x$ flakes). The black supernatant was separated from the sediment and collected. The cycle of diluting the sediment in DI water, shaking, centrifuging, and collecting the black supernatant was repeated until the supernatant started to become transparent again. Finally, the collected supernatant (about 2 litres of suspension) was washed with DI water and centrifuged at 10,000 rpm several times until pH=6. At the end of the synthesis process, about 3.35 g of solid material (exfoliated $Ti_3C_2T_x$) can be obtained by drying the sediment suspension, while the sediment contains 0.25 g of solid material.

Preparation of $Ti_3C_2T_x$ slurry

After the exfoliation, washing and collecting processes are completed, the final concentration of the obtained $Ti_3C_2T_x$ suspension is measured. The material is then diluted (with DI water) or concentrated (drying it in the vacuum oven at room temperature) as needed to achieve the desired concentrations of 45, 70 and 120 mg mL^{-1}.

Preparation of $Ti_3C_2T_x$ film – Tape casting

The FaTC process can be seen in **Fig. 1** and **3c**. It consists of an aluminium plate as the substrate surface, on top of a cold plate device (Instec Inc.). The temperature of the cold plate (-25°C) was maintained by adjusting the amount of liquid nitrogen being pumped to the plate. A doctor blade assembly (as seen in **Fig. 3c**) was used to manipulate the thickness of the tape casted

films. The $Ti_3C_2T_x$ slurry was subsequently pulled along the substrate using the blade to create a film. The frozen samples were freeze-dried in a Labconco FreeZone 4.5 L console.

Characterization of structure and properties of 2D $Ti_3C_2T_x$ and $Ti_3C_2T_x$ films.

Powder X-ray diffraction (XRD) was undertaken using a PANalytical X'Pert – PRO theta-theta PW3050/60 diffractometer (480 mm diameter) with PW3064 sample spinner (2 rev/s) and X'Celerator (2.122° active length) 1D-detector in Bragg-Brentano geometry employing a Cu Line Focus X-ray tube with Ni kβ absorber (0.02 mm; Kβ = 1.392250 Å) Kα radiation (Kα1=1.540598 Å, Kα2=1.544426 Å, Kα ratio 0.5, Kαav=1.541874 Å). An incident beam Soller slit of 0.04 rad, 2° fixed anti scatter slit, incident beam mask of 10 mm and programmable automated divergence slit giving a constant illuminated length of 10.0 mm and receiving Soller slit of 0.04 rad were used. Freeze-dried powder samples were loaded on standard circular sample holders and data collections from 5° to 75° coupled 2theta/theta at 0.033° step and 67 s/step were undertaken. Phase identification and peak assignment were carried using the Search Match tool (restricted to Li, C, O, Al, and Ti) of the software HighScore Plus [1] with data from the PDF-4 2020 Database [2]. Scanning electron microscopy (SEM) images were taken with Tescan Mira3 LC. Average values for the flake size, pore size and wall opening were obtained from over a hundred measurements of the features using SEM images. TEM samples were prepared by drop-casting diluted MXene solution on a Copper grid covered by lacy carbon film. S/TEM images were collected on FEI Talos F200X instrument with acceleration voltage of 200 kV. X-ray tomography (XCT) was performed using a Zeiss VersaXRM520. Imaging was performed at 60 keV energy and 100 ms exposure time, taking 1601 projections around 180° of sample rotation. A 2560 x 2160 pixel (height x width) 10 μm pco.edge CCD (charge-coupled device) camera was used to collect the X-ray projections, coupled to a 4x microscope objective giving an effective pixel size of 2.6 μm and a field-of-view of approximately 2.5 mm. The sample to detector distance was 15 mm to allow some in-line phase contrast in order to enhance visibility of the aerogel sheets. Reconstruction was performed using a filtered back projection algorithm and visualisation was performed using Avizo (Thermo Fisher Scientific). Powder samples elemental analysis by energy-dispersive X-ray fluorescence (EDXRF) was conducted with data acquisition in a PANalytical MiniPal 4 employing an X-ray tube with Rh anode and quantitative analysis via Omnian software.

Electrochemical testing

To investigate the electrochemical behaviour of the vertically aligned $Ti_3C_2T_x$ films with various thickness, two-electrode symmetrical supercapacitors were prepared with platinum plates as the current collector, a cellulose membrane as the separator, and 3 M H_2SO_4 as the electrolyte. All the electrochemical tests were carried out at room temperature using a PGSTAT302N potentiostat (Metrohm Autolab) and a battery testing system (Germany, BaSyTec). The specific gravimetric capacitance C_{sg1} (F g^{-1}) of the electrode tested by galvanostatic charge-discharge (GCD) was calculated based on the following equation: $C_{sg1} = \frac{2I*\triangle t}{\mathrm{m}*\triangle V}$, where I (A) represents the discharge current, $\triangle t$ (s) and $\triangle V$ (V) are the duration and voltage change during the discharge process, respectively. m (g) is the weight of single electrode. The specific gravimetric capacitance C_{sg2} (F g^{-1}) and specific areal capacitance C_{sa} (F cm^{-2}) of electrode tested by cyclic voltammograms were calculated by equation: $C_{sg2} = \frac{A}{SR*\triangle V*\mathrm{m}}$, where SR is the scan rate (mV s^{-1}), A is the integral area of the CV plot. The EIS curves were recorded by applying a sine wave with 5 mV amplitude under the frequency range of 10^5 Hz to 10^{-2} Hz. Gravimetric energy density E_g (Wh kg^{-1}) and power density P_g (W kg^{-1}) were calculated by using: $E_g = \frac{C_{sg1}*\triangle V^2}{8\mathrm{m}*3.6}$ and $P_g = \frac{E}{\triangle t} * 3600$. Areal energy density E_a (mWh cm^{-2}) and power density P_a (mW cm^{-2}) were calculated by: E_a=E_g*ML, $P_a = P_g$*ML, ML is the mass loading of these electrodes [3,4].

4.7 Supplementary Information

Supplementary Figures

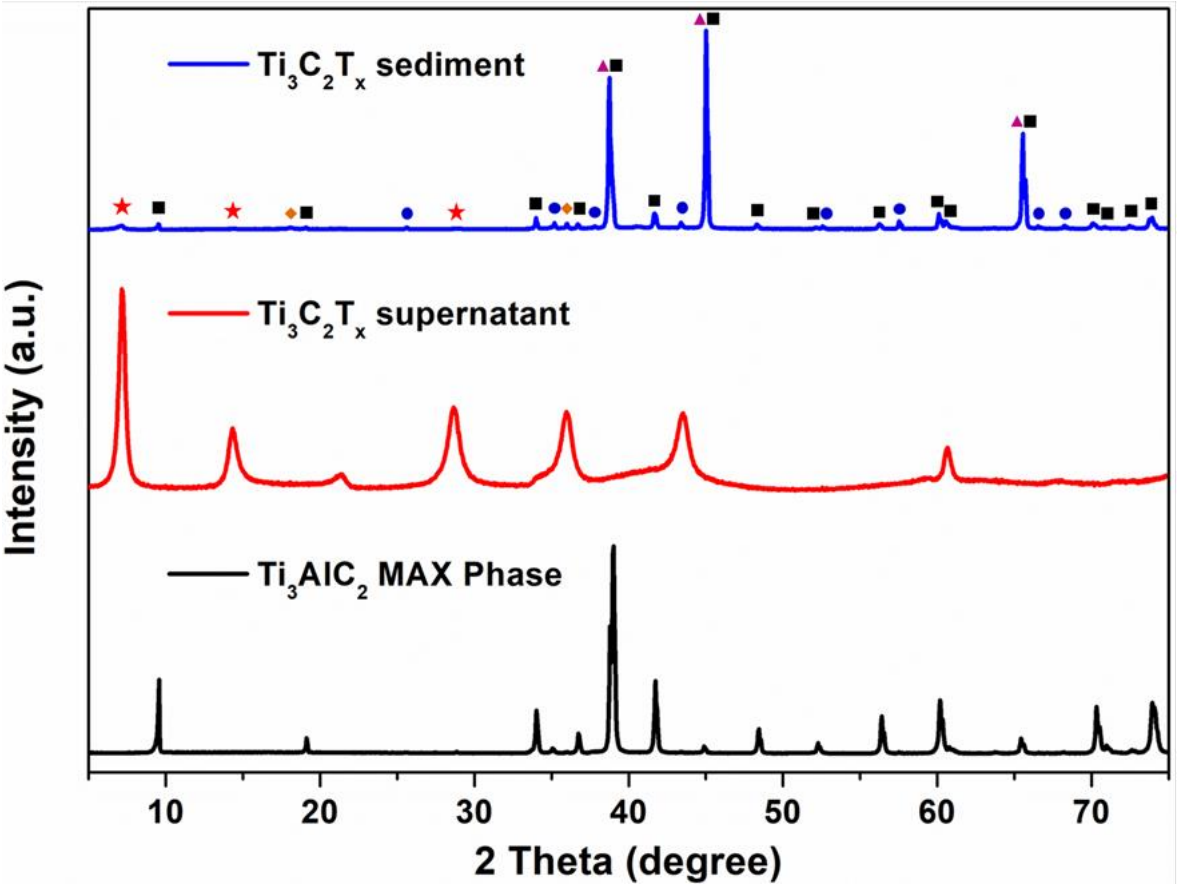

Figure S1 XRD diffraction patterns of the $Ti_3C_2T_x$ sediment, supernatant $Ti_3C_2T_x$ (exfoliated), and precursor Ti_3AlC_2 MAX phase, respectively. Assigned symbols refer to the main representative peaks of the following phases: star (exfoliated MXene [5,6]); square* (Ti_3AlC_2 – JCPDS 04-012-0632 [7]); circle (Al_2O_3 – JCPDS 04-004-2852 [8]); diamond ($TiC_{0.62}$ – PDF 04-017-1603 [9]); and triangle (LiF – JCPDS 00-004-0857 [10]). All peaks in the $Ti_3C_2T_x$ supernatant pattern refer to the basal planes of exfoliated $Ti_3C_2T_x$ (002), (004), (006), (008), (010), (012), and (016) respectively. Ti_3AlC_2 MAX phase pattern is in accordance to JCPDS 04-012-0632 [7].

It is important to note that most main peak positions of a multi-layered $Ti_3C_2T_x$ (i.e. etched MAX phase, but not exfoliated) are undistinguishable from Ti_3AlC_2, which means it is not possible to determine the content of Al in the sediment solely by XRD. However, further elemental analysis by EDXRF of the samples shows an Al:Ti atomic ratio of 1:7, 0:1, and 1:3 for $Ti_3C_2T_x$ sediment, $Ti_3C_2T_x$ supernatant, and precursor Ti_3AlC_2 phases, respectively.

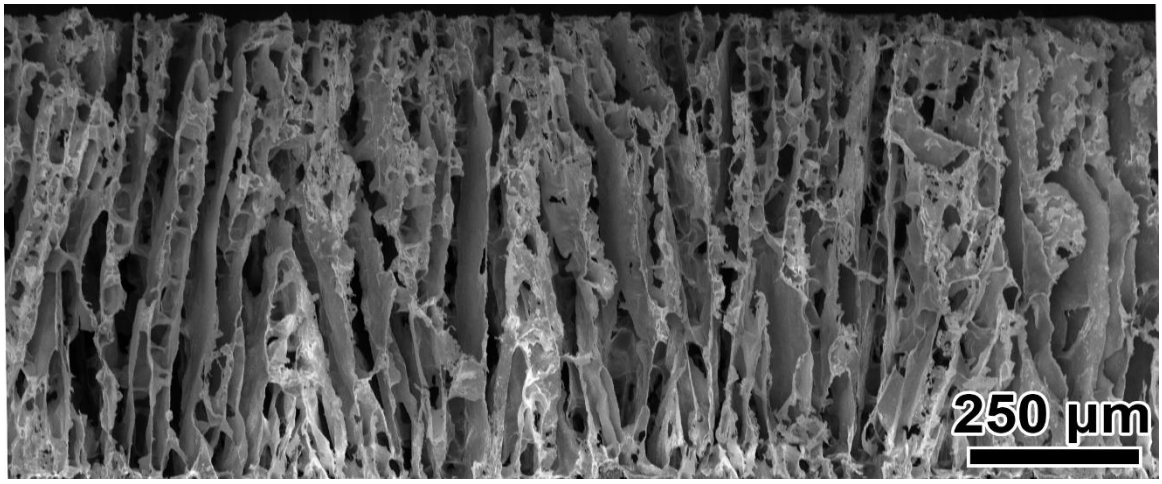

Figure S2 SEM cross-sectional images of the film's internal microstructure for a 500 µm thick sample freeze casted by 45 mg mL^{-1} slurry.

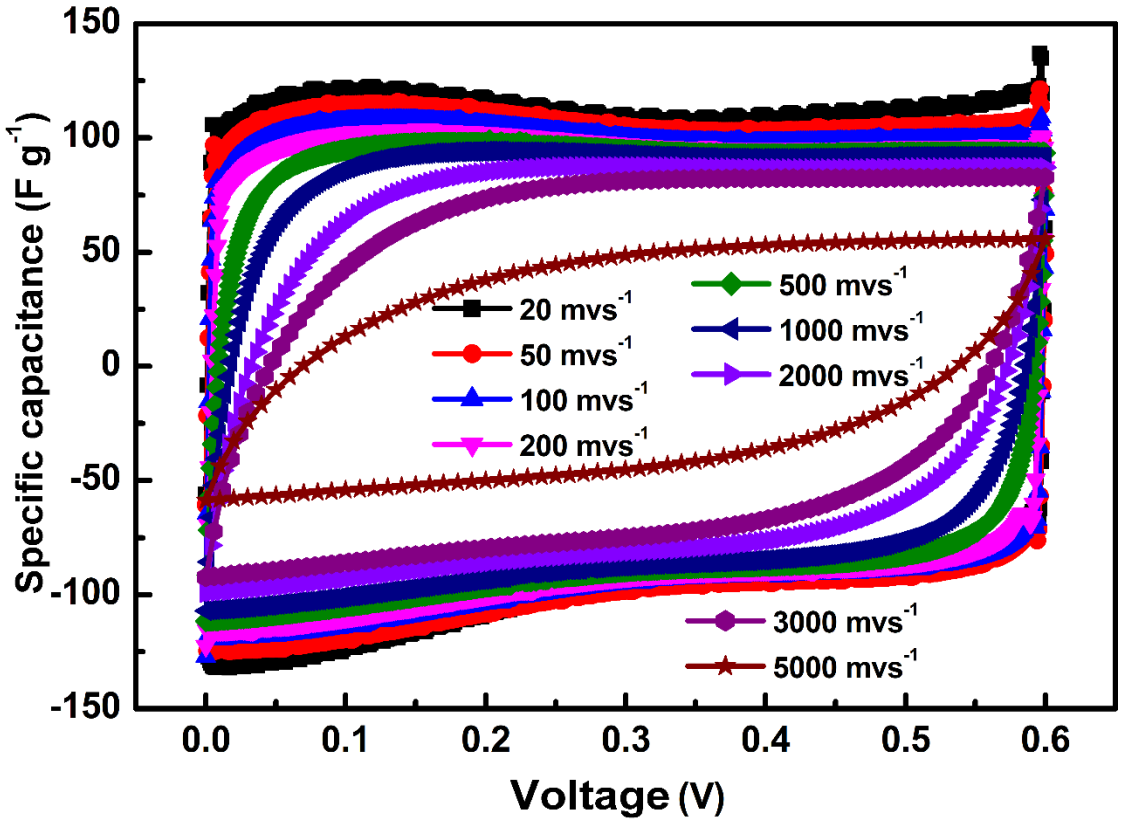

Figure S3 CV curves of the 300 µm thick $Ti_3C_2T_x$ film at scan rates from 20 to 5,000 mV s^{-1}.

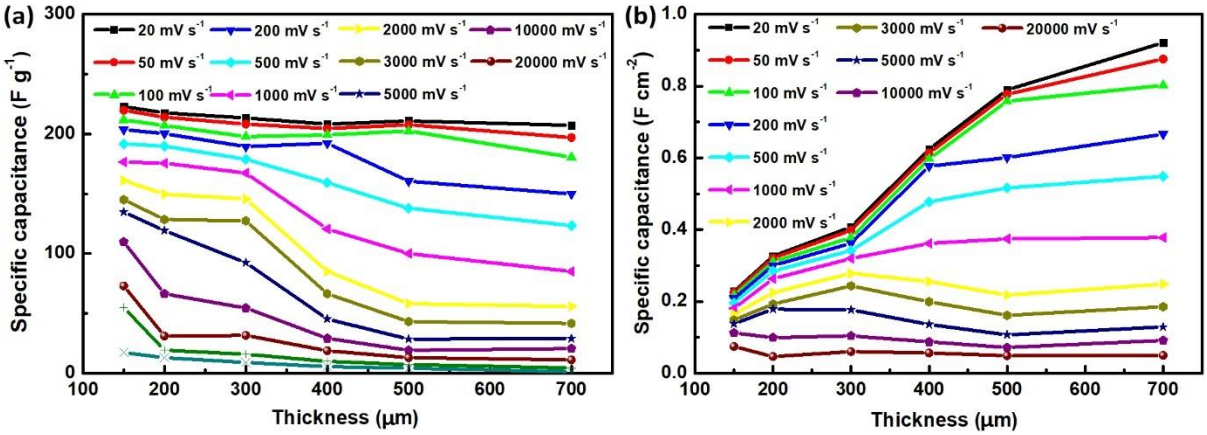

Figure S4 Rate performance (including gravimetric and areal) of the films against the thickness of the electrode.

The gravimetric and areal capacitance of samples against the thickness of the electrode at different scan rates are shown in **Figs. S4a** and **S4b**, respectively. With the increase of the thickness of the elctrode, all the corresponding specific gravimetric capacitance show very modest distortion, especially when the scan rate below 100 mV s^{-1}, specific capacitance of the electrode is independent to the thickness. The areal rate performance against the thickness of the films shows that for scan rate of up to 100 mV s^{-1} the capacitance is roughly proportionate to the increase thickness of the electrode.

Supplementary Table

Table S1 Table illustrating final thickness of $Ti_3C_2T_x$ film.

Doctorblade height setting (μm)	Final Film thickness (μm)
150	149.6
200	191.0
300	286.1
400	375.6
500	483.8
700	672.5

Reference

[1] T. Degen, M. Sadki, E. Bron, U. König, G. Nénert, in Powder Diffr., Cambridge University Press, **2014**, *29*, S13.

[2] S. Gates-Rector, T. Blanton, Powder Diffr. **2019**, *34*, 352.

[3] S. Ji, J. Yang, J. Cao, X. Zhao, M. A. Mohammed, P. He, R. A. W. Dryfe, I. A. Kinloch, ACS Appl. Mater. Interfaces **2020**, *12*, 13386.

[4] W. Yang, H. Zhou, Z. Huang, H. Li, C. Fu, L. Chen, M. Li, S. Liu, Y. Kuang, Electrochim. Acta 2017, 245, 41.

[5] L. Verger, C. Xu, V. Natu, H. M. Cheng, W. Ren, M. W. Barsoum, Curr. Opin. Solid State Mater. Sci. **2019**, *23*, 149.

[6] M. Alhabeb, K. Maleski, B. Anasori, P. Lelyukh, L. Clark, S. Sin, Y. Gogotsi, Chem. Mater. **2017**, *29*, 7633.

[7] E. Wu, J. Wang, H. Zhang, Y. Zhou, K. Sun, Y. Xue, Mater. Lett. **2005**, *59*, 2715.

[8] J. Lewis, D. Schwarzenbach, H. D. Flack, Acta Crystallogr. Sect. A **1982**, *38*, 733.

[9] M. Y. Tashmetov, V. T. Em, C. H. Lee, H. S. Shim, Y. N. Choi, J. S. Lee, Phys. B Condens. Matter **2002**, *311*, 318.

[10] Swanson, Howard E, Standard X-Ray Diffraction Powder Patterns NBS CIRCULAR 539 VOLUME III UNITED STATES DEPARTMENT OF COMMERCE NATIONAL BUREAU OF STANDARDS, n.d.

Chapter 5. All-in-one Mxene-Boron Nitride-Mxene "OREO" for flexible supercapacitor design with integrated structural and functional properties

5.1 Chapter Introduction

The previous chapter focused on the use of freeze casting to enable the alignment of the MXene flakes. Although research on improving the performance of MXene based energy devices and electronics has seen significant advancement in recent years, the consolidation of synergistic manufacturing techniques which effectively exploits the excellent electrochemical properties of the material has considerable challenges to overcome to meet practical usage. Research trends in this area tend to focus on specific elements of the device, with small considerations made on overall compatibility. This makes it more challenging to transition the development to conform with scalable manufacturing process such as roll-to-roll processing normally used in industry. In the pursuit to resolve this, we believe that an essential aspect in the development of the material is an all-in-one fabrication route for structural supercapacitors. This allows for a minimalistic design philosophy and mutability in which the electrochemical energy storage device itself provides some form of the structural framework of the product whilst facilitating a function.

Adhering to the concept of exploring not only the functional properties but also the structural potential of the materials, a MXene ($Ti_3C_2T_x$) based all-in-one flexible supercapacitor with hexagonal boron nitride (*h*BN) separator was assembled with a newly developed concurrent manufacturing process. Fundamentally, an aqueous $Ti_3C_2T_x$ suspension and hexagonal boron nitride-polyvinyl alcohol colloid were concomitantly freeze-tape cast into an integrated $Ti_3C_2T_x$-*h*BN-PVA-$Ti_3C_2T_x$ (THT) 'oreo' structure. The 110 μm-thick THT film reveals anisotropically arranged micropores – which is beneficial for ion transportation and supported by theoretical determination of the tortuosity factor through simulations of the diffusive transport in the XCT rendering of microstructural data.

In this work, the thesis author conceived this study carried out materials fabrication, SEM/EDS/XRD/Rheology and data analysis, making and casting of the MXene/hBN slurries, and finally wrote the paper. Jae Jong Byun assisted with XCT and Yang Jie assisted with

electrochemical measurements. All authors contributed to the review of the manuscript. The original manuscript is presented in the following sections.

Paper: All-in-one MXene-Boron Nitride-MXene "OREO" with Vertically Aligned Channels for Flexible Structural Supercapacitor Design

Wenji Yang[1]*, Jae Jong Byun[1 2], Jie Yang[3 4], Francis Peter Moissinac[1], Yingjie Ma[5], Hui Ding[1], Wei Sun[6], Robert A.W. Dryfe[3 4], Suelen Barg[1 7]*

[1] Henry Royce Institute and Department of Materials, University of Manchester, Oxford Road, Manchester, M13 9PL, UK.

[2] Department of Electrical and Electronic Engineering, University of Manchester, Sackville Street Building, Manchester M1 3BB, UK.

[3] National Graphene Institute, University of Manchester, Oxford Road, Manchester, M13 9PL, UK.

[4] Department of Chemistry, University of Manchester, Oxford Road, Manchester M13 9PL, UK.

[5] Department of Chemical Engineering & Analytical Science, University of Manchester, Oxford Road, Manchester M13 9PL, UK.

[6] Department of Mechanical, Aerospace and Civil Engineering, University of Manchester, Oxford Road, Manchester M13 9PL, UK.

[7] Institute of Materials Resource Management MRM, Augsburg University, Am Technologiezentrum, Augsburg 8 – 86159, Germany.

* Corresponding authors : wenji.yang.hnu@gmail.com ; suelen.barg@mrm.uni-augsburg.de

KEYWORDS: Integration of Functional & Structural; All-in-one; Freestanding & Flexible; MXene; Supercapacitors.

5.2 Abstract

Trends across various fields of energy storage technological advancement call for the development of materials to fulfil both functional and structural requirements. Flexible devices have been an evolutionarily progressive step in this area. Herein, $Ti_3C_2T_x$ and *h*BN are used to build a flexible all-in-one $Ti_3C_2T_x$-*h*BN-$Ti_3C_2T_x$ (THT) integrated composite film for a supercapacitor. The $Ti_3C_2T_x$ layers function as active electrodes (with high electrical conductivity of 8,100 S cm^{-1}) while the *h*BN layer serves as the separator. This design streamlines the manufacturing of a robust supercapacitor, allowing the active materials to self-support, and function independently from additional current collectors or binding agents. The THT film exhibits a Young's modulus of 2.26 ± 0.03 GPa, reflecting the self-supporting nature of the film and suggests the reinforcement of the film by adding MXene layers adjacent to the *h*BN separator. Additionally, it exhibits high capacitance of 0.20 F cm^{-2} at 50 mV s^{-1} and 225.60 F g^{-1} at 10 A g^{-1}. A high-power density of 209.2 mW cm^{-2} can be achieved at 700 mA cm^{-2} with an energy density of 5.6 μWh cm^{-2}. This work highlights a design paradigm and offers a solution to accomplishing roll-to-roll manufacturing for flexible energy storage devices.

5.3 Introduction

Progressing into the technological growth of the 21st century requires the development of materials that exhibit not only novel performance that fulfils functional requirements but also structural advantages. Hence, there is a growing effort in ascertaining the functional and physical properties of a material or its composite configuration and its cumulative effects on integrated performance. Accordingly, a viable route to accomplishing this goal is flexible energy storage devices which function as an ontogenesis to flexible electronics, whether it be for wearable consumer devices [1], soft robotics [2], photonics [3] or integrated sensors [4–6]. As compared to conventional rigid-monolithic energy storage devices, flexibility allows for low volume, lighter device configurations with greater system conformity, in accordance with market requirements. Despite the implicit advantages in flexible digital devices for civil defence hardware or medical accoutrements amongst many other areas, the nominal performance of electrodes fabricated via standard assembly strategies rely on structural formulation additives as well as costly flexible substrates such as aluminium or copper foils [7] to impart structural stability and flexibility to the devices. Therefore, there is impulse for the development of processing routes and novel materials that enable the realisation of self-supporting electrodes, without the need for metallic current collectors or additional structural binders. This can enable a cost-effective delivery of structural and functional properties in energy storage devices, which not only mitigates the risk of impact damage, but also decreases overall manufacturing cost whilst increasing gravimetric energy density of the cell.

A material class that has seen flourishing application in the energy storage field and especially been a good candidate to fabricate self-supporting films for supercapacitor electrodes are two-dimensional (2D) materials such as graphene [8] and MXenes [9]. This is largely attributed to their large lateral aspect ratio, accessible surface sites and good electrical conductivities. Contrastingly, another 2D material *h*BN, has demonstrated promising performance as a separator layer due to its ionic conductivity and electrically insulative nature [10–12]. Additionally, the high temperature stability and chemical inertness [13,14] makes it ideally suited for this application. Several research works using graphene have highlighted the potential for 2D materials for the development of freestanding films for flexible energy storage devices [15–17]. For example, fully solid-state planar asymmetric supercapacitor based on a flexible monolithic film of exfoliated graphene, an ionically conductive boron nitride separator and manganese (IV) oxide has also been explored [18]. The robust nature of their construction was

demonstrated by a 98.8 % initial capacitance retention even when bent at 180 degrees. The design versatility allowed for parallel and series configurations without the need for metal-based interconnections. A related work performed by Z. Li et al. shows that the interlayer spacing of graphene laminate films synthesised by vacuum filtration can be 'tuned' to maximise pore utilisation efficiency in freestanding films [19]. Their symmetric supercapacitor assembly of electrode films managed to deliver an energy density of 88.1 Wh L^{-1} with a capacitance contribution per specific surface area of 47 μF cm^{-2}. This work further highlights the importance of considering the accessibility of surface sites when manufacturing with 2D materials.

MXenes are 2D carbides and nitrides of a transition metal, with the most widely studied being $Ti_3C_2T_x$ [20–22], which is mainly synthesised by the acidic solutions containing fluoride ions such as HF, LiF with HCl or NH_4HF_2. The attractiveness of MXenes over graphene for the development of freestanding electrodes is attributed to the surface charge on $Ti_3C_2T_x$ which contributes to its hydrophilicity [22]. This facilitates more versatile and environmentally friendly fabrication routes. Moreover, its high intrinsic electrical conductivity, large lateral aspect ratio and accessible surface sites contribute cumulatively to excellent capacitive performance [21]. In work by J**.** Yan et. al. supercapacitor electrodes were created by electrostatic self-assembly of reduced graphene oxide (rGO) stabilised in poly(diallyldimethylammonium chloride) and $Ti_3C_2T_x$ nanosheets [23]. It was discovered that the rGO nanosheets inserted between the MXene nanosheet layers mitigated self-restacking and accelerated diffusion of electrolyte ions. This resulted in ultrahigh volumetric energy and power densities of 32.6 Wh L^{-1} and 74.4 kW L^{-1}, which is ideally suited for portable and micro-sized integrated energy storage devices. Another approach was taken by Y. Wang et.al. in which a self-supporting three-dimensionally porous film of MXene and bacterial cellulose was formed by vacuum filtering the mixture, freeze-casting and dried to form the porous interconnected framework which overcomes sluggish ionic kinetics within the electrode film [24].

Additionally, the intrinsic properties of MXene allow it to be readily synthesised into an aqueous additive free colloid which facilitates solution-based roll-to-roll processes and advanced manufacturing methods such as tape casting [25], and three-dimensional (3D) printing [26]. Considering the conventional rigid monolithic designs of commercial supercapacitors, the final assembly of such devices demonstrate diminished gravimetric and volumetric performances [27]. Research has approached this from multiple facets. One being the

preparation of asymmetric solid-state supercapacitors from TiNi shape memory alloys which are body-temperature activatable into watchband-like devices [28]. Although promising, their assembly still required metal foils as the current collector, which cumulatively adds to weight and device cost.

The development of integrated manufacturing processes allow for an incorporative device design where the assembly process is concatenated resulting in a lightweight, damage tolerant product in which potential displacement and delamination of traditional multi-layered architectures are less likely to transpire [27], due to a more seamless interface created between the electrodes and separator. There have been diverse and creative approaches in integrated supercapacitor fabrication. For example, Y. Wang et. al. fabricated an all-in-one supercapacitor by sputtering nickel onto both the top and bottom surfaces of a glass fibre film as the current collector (leaving the core as a separator) [27]. The anode was then formed by vacuum filtration of holey rGO/carbon nanotube composite onto one surface whilst the cathode was formed by electrodeposition of MnO_2 onto the adjacent surface. The all-in-one design of the supercapacitor can then be easily integrated into a 3D system without post-packaging processes. This is similar to the work of L. Lim et. al. who developed a coaxially designed all-in-one graphene and MnO_2 composite supercapacitor device [29]. In this case, a graphene fibre serves as the core of the device, which contributes to its mechanical stability and rapid electron transfer. Differentially, Y. Guo et. al. approached the design from a self-healing perspective, creating a laminated structure with a self-healable polyvinyl alcohol (PVA)/H_2SO_4 electrolyte and SWCNT-PANI electrode layers [30]. The supercapacitor structure managed a capacitance of 15.8 mF cm^{-2} at a current density of 0.044 mA cm^{-2} with a relatively low impedance of 13.2 Ohms. Besides this, a freeze-assisted tape casting (FATC) process in our previous work has also demonstrated potential in scaled fabrication of integrated supercapacitor structures. This processing route aids in the development of vertically aligned 2D sheets via the directional growth of lamellar ice-crystals along the thermal gradient applied to the film, thus avoiding potential stacking of the $Ti_3C_2T_x$ sheets, which facilitates electrolyte ion transportation in the electrodes, enhancing rate performance of the supercapacitor [25,31].

Herein, a scalable fabrication technique for all-in-one integrated supercapacitor is outlined where an aqueous $Ti_3C_2T_x$ suspension and hexagonal boron nitride-polyvinyl alcohol colloid were concomitantly freeze-tape cast into an integrated $Ti_3C_2T_x$-*h*BN-PVA-$Ti_3C_2T_x$ (THT) 'oreo' structure, with $Ti_3C_2T_x$ layers as the symmetric electrodes and *h*BN-PVA layer as the separator. After calendering of the THT film from 800 μm to roughly 110 μm, microstructural

characterisation reveals retention of the micropores – which is beneficial for ion transportation. Additionally, yield stress of ~ 9.5 MPa, alludes to a strong interface between the electrode and separator, whilst a tensile modulus of 2.26 ± 0.03 GPa is testament to the self-supporting nature of the THT film. The integrated THT film exhibited similar electrochemical characteristics to our previous work, in which a commercial separator was used [25]. The integrated supercapacitor demonstrates high specific areal capacitance of 0.20 F cm^{-2} at 50 mV s^{-1} and 0.16 F cm^{-2} at 500 mV s^{-1} with an equivalent series resistance of 0.137 Ω and a stability retention of 92.1 % at 10 A g^{-1} after 12,000 continuous charge-discharge cycles. Furthermore, we fabricated the integrated supercapacitor in series and parallel circuits made of THT films to attain higher voltages of up to 1.8 V, and higher capacitance, respectively. The promising results segue into the potential for functional design in which the all-in-one fabrication route facilitates the creation of structural supercapacitors [32], e.g. integration into carbon fibre composite monocoque of a vehicle. This allows for a minimalistic design philosophy and mutability in which the electrochemical energy storage device itself provides some form of the structural framework of the product whilst facilitating a function.

5.4 Results and Discussion

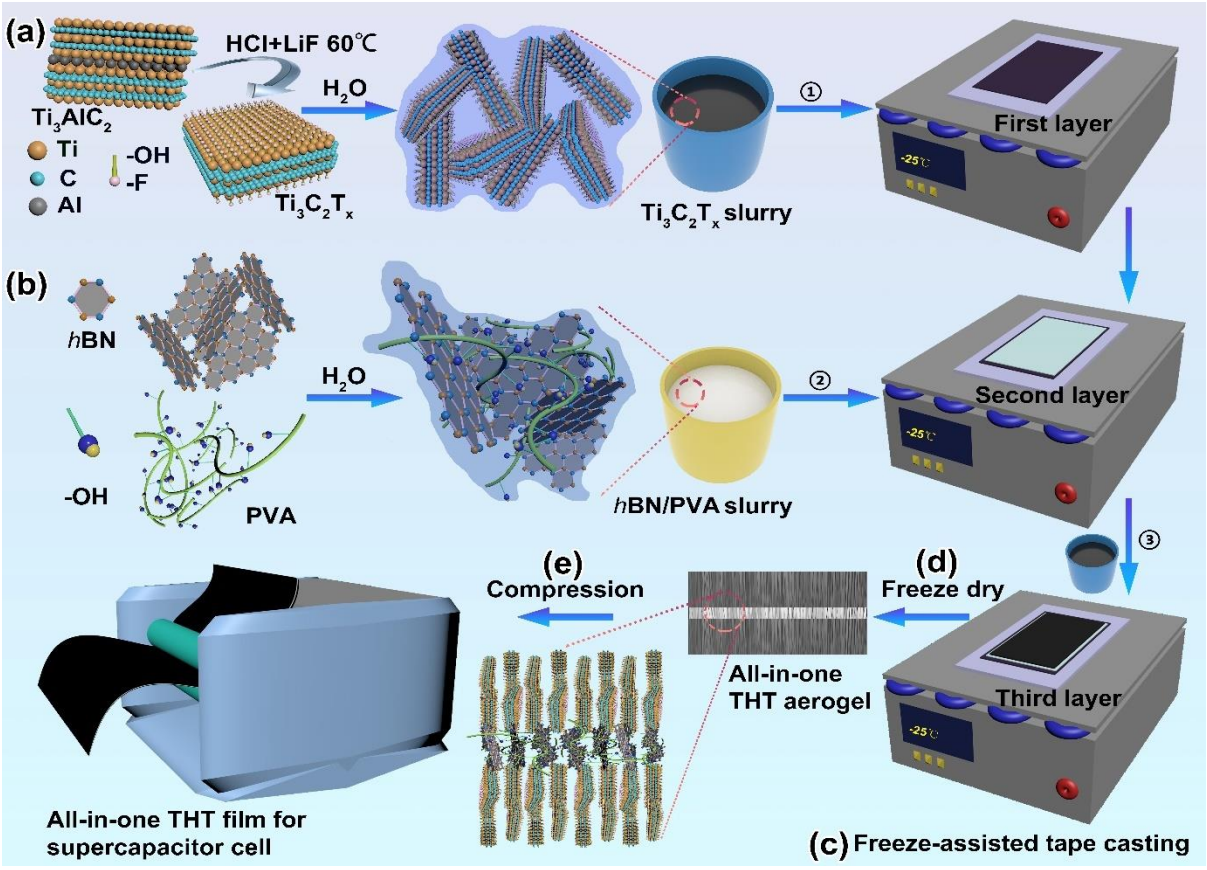

Figure 1 Schematic showing the synthesis and manufacturing of the all-in-one THT film. (a) Synthesis of exfoliated $Ti_3C_2T_x$ flakes and preparation of $Ti_3C_2T_x$ slurry. (b) Preparation of *h*BN-PVA slurry. (c) Freeze-assisted tape casting of three layers: $Ti_3C_2T_x$, *h*BN-PVA, and $Ti_3C_2T_x$ in order. (d) Freeze drying to obtain the all-in-one THT aerogel. (e) Compression of the all-in-one THT aerogel to a film for supercapacitor cell.

To explore the MXene-*h*BN all-in-one-sandwich material for supercapacitor applications, we propose the synthesis and manufacturing steps illustrated in the schematic in **Fig. 1**. The delaminated $Ti_3C_2T_x$ was produced using the MILD method [25], and is described in the experimental section. The concentration of the as-prepared MXene slurry was adjusted to 65 mg mL^{-1} for the subsequent manufacturing steps. The separator in the sandwich structure was formed from a *h*BN-PVA slurry prepared by dispersing *h*BN in a PVA aqueous suspension. As reported in our previous work [25], the 3D hierarchical structures of aligned MXene flakes were fabricated via freeze-assisted tape casting. Initially, the substrate was cooled down to -25 °C, followed by the application of the first layer of $Ti_3C_2T_x$, on the pre-chilled substrate, which behaves as the first electrode. The separator layer was then formed by layering the *h*BN-PVA slurry above this layer. Finally, another $Ti_3C_2T_x$ layer was cast on top to complete the composite supercapacitor design. The freeze cast structure underwent freeze drying to form the all-in-one THT aerogel, which was calendered as the final step, reducing its volume by compressing the THT aerogel into the all-in-one THT film.

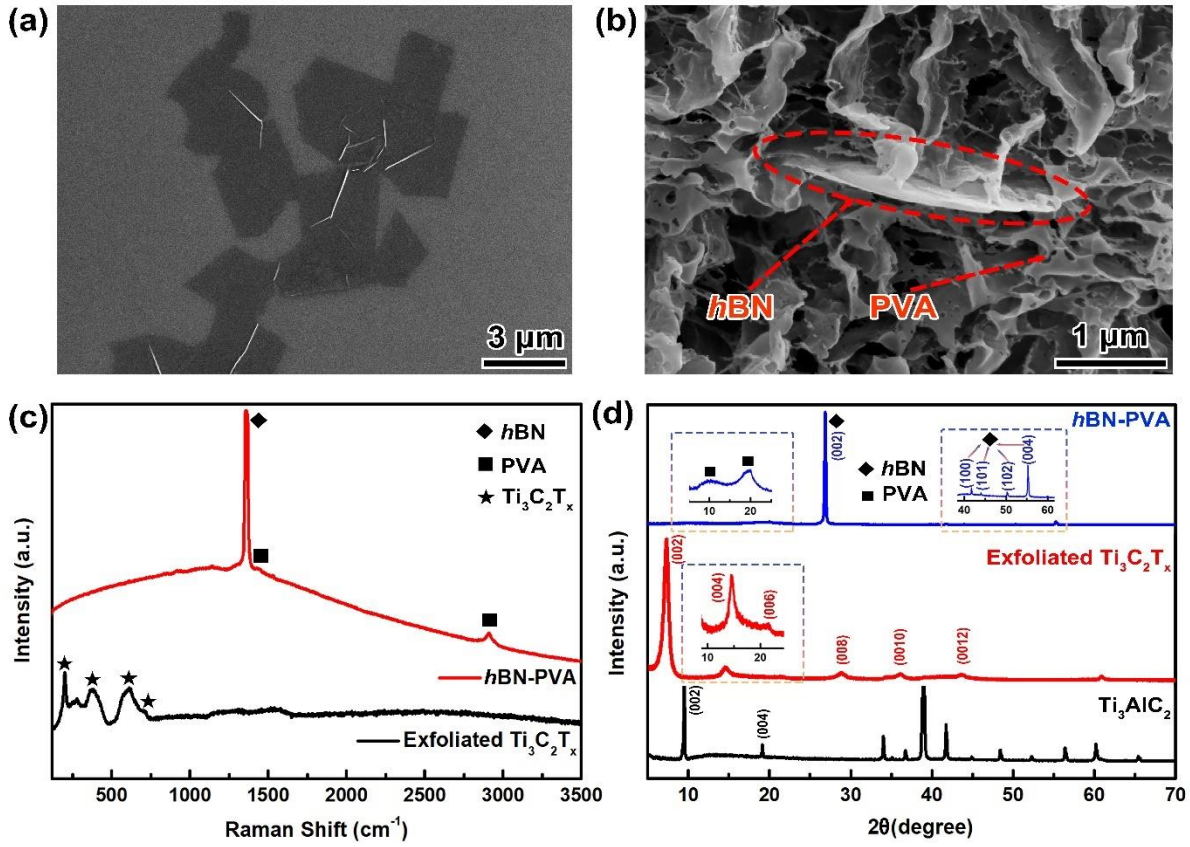

Figure 2 Microstructural and structural characterisations of the delaminated $Ti_3C_2T_x$ and *h*BN-PVA. SEM images of, a delaminated $Ti_3C_2T_x$ flakes, b *h*BN and PVA matrix. c Raman spectra of delaminated $Ti_3C_2T_x$ and *h*BN-PVA mixture. d XRD patterns of the precursor MAX phase Ti_3AlC_2, delaminated $Ti_3C_2T_x$ and *h*BN-PVA matrix.

The microstructure of exfoliated $Ti_3C_2T_x$ flakes and the mixture of *h*BN and PVA were investigated by scanning electron microscope (SEM). In **Fig. 2a**, typical exfoliated $Ti_3C_2T_x$ sheets with a lateral size of ~ 3.7 μm on a silicon wafer are displayed. The surface and edges of the flakes are clean without light white spots, indicating minimal oxidation. From **Fig. 2b**, we can see that the PVA crosslinks to form a reticulate fibrous-structure network and the disk-like shape *h*BN flake is trapped and intercalated within the PVA matrix. In **Fig. S1a**, transmission electron microscope (TEM) reveals the morphology of a few transparent $Ti_3C_2T_x$ flakes with curved edges. Exfoliated $Ti_3C_2T_x$ flakes and *h*BN-PVA were characterised by Raman spectroscopy in the 100-3500 cm^{-1} region (**Fig. 2c**). Characteristic vibrational modes at peaks 202 cm^{-1} and 380 cm^{-1}, a wide peak at around 603 cm^{-1} and a small peak at 720 cm^{-1} are observed from the spectrum of delaminated $Ti_3C_2T_x$ [33]. Furthermore, the peaks associated with the rutile or anatase phase of TiO_2 and amorphous carbon are not observed. **Fig. 2d** demonstrates the X-ray diffraction (XRD) patterns of the precursor MAX phase Ti_3AlC_2, exfoliated $Ti_3C_2T_x$ and the mixture of *h*BN and PVA. For the *h*BN-PVA sample, the peak with

the highest intensity at a diffraction angle of 19.8 degrees indicates the presence of a typical semi-crystalline structure of PVA caused by alternative speed mixing and continuous stirring. Concordantly, it also presents the signature of *h*BN with the main signal peak at around 26.8 degrees, which corresponds to the (002) diffraction peak, according to the PDF00-034-0421 [34]. Comparing the (002) peaks on the spectra of Ti_3AlC_2 and exfoliated $Ti_3C_2T_x$, the $Ti_3C_2T_x$ flakes have been mostly delaminated without observing the typical peaks expected from TiO_2. The X-ray photoelectron spectroscopy (XPS) spectra of *h*BN-PVA and $Ti_3C_2T_x$ are shown in **Fig. S1b**. Ti-C, Ti-OH, Ti-O, Ti (II), Ti-Cl and Ti-F were identified for the delaminated $Ti_3C_2T_x$, suggesting the terminal functional groups which contribute to the hydrophilicity and electrochemical performance.

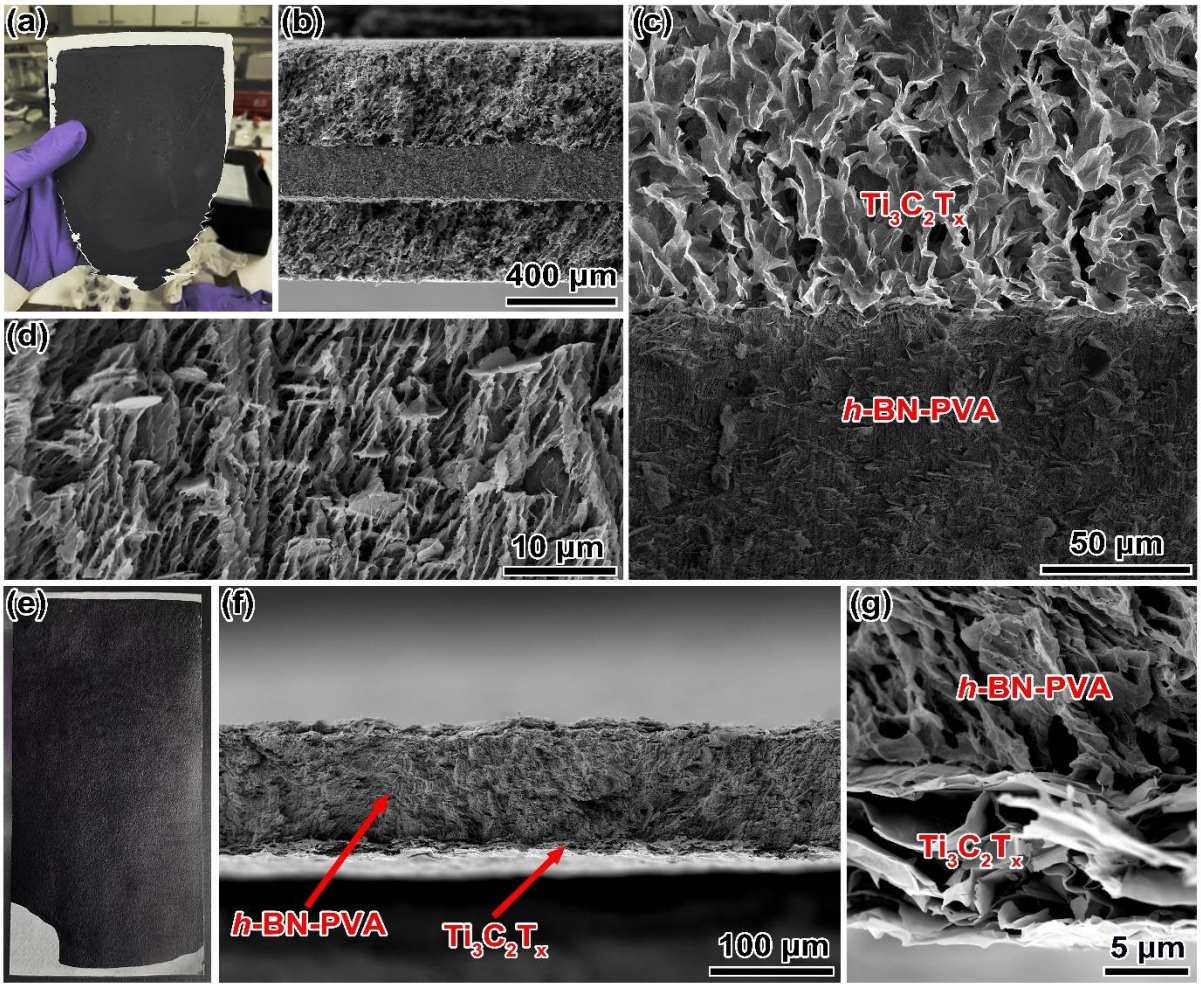

Figure 3 Microstructure of the all-in-one THT film before and after compression. a Digital photograph of all-in-one THT "oreo" aerogel; inset is the cross-sectional view of the film. b SEM images of the all-in-one THT aerogel, c interface of the two different layers, d magnified view of the middle *h*BN-PVA segment, (e) Digital photograph of the compressed all-in-one THT film. f SEM images of the compressed film and, g corresponding magnified interface.

Fig. 3a illustrates a digital photo of an all-in-one THT sandwich with a thickness of 300 μm ($Ti_3C_2T_x$)|200 μm (*h*BN-PVA)|300 μm ($Ti_3C_2T_x$), which was manufactured by concomitantly tape casting a 65 mg mL^{-1} $Ti_3C_2T_x$ slurry and a *h*BN-PVA slurry of 15 % *h*BN & 10 % PVA on a -25 °C cold plate. After freeze-drying, the THT aerogel was removed from the aluminium substrate, and it appeared to have an intact appearance. Referring to the cross-section of this THT aerogel, we can see a distinct three-layer structure. As shown in the SEM image **Fig. 3b**, the central structure of this 'oreo' aerogel, *h*BN-PVA acts as the separator of the all-in-one supercapacitor cell, which corresponds to the white areas in the digital photo. The adjacent sides of this sandwich structure are pure $Ti_3C_2T_x$ based active material for the all-in-one supercapacitor cell, which corresponds to the black areas in **Fig. 3a**. In **Fig. 3c**, we can observe the magnified interface of the uncompressed THT sandwich aerogel. According to principles of the freeze-assisted tape casting process discussed in our previous work [25], the $Ti_3C_2T_x$ layer shows comparatively uniform 3D porous lamellar channels with vertically aligned walls composed of $Ti_3C_2T_x$ flakes. The structure appears to be formed of a central channel which splits into smaller branches. It is further observed that $Ti_3C_2T_x$ and *h*BN-PVA are seamlessly interfaced with no gap. When the former layer was frozen, casting the next layer with room-temperature slurry will cause partial melting of the top surface of the previous layer, which will then instantaneously re-freeze. In this way, a composite with compatible interface will be obtained. Closer inspection of the *h*BN-PVA section (**Fig. 3d**), reveals tens of thousands of smaller channels which also formed in a roughly vertical direction. The large disc-like *h*BN flakes behaves as a supporting framework whilst the PVA develops into an immobilizing reticulate fibrous structure. After compression, by calendering the sandwich aerogel, a thinner all-in-one THT composite film was obtained with a thickness of 10(±1) μm ($Ti_3C_2T_x$)|92 μm (*h*BN-PVA)|10(±1) μm ($Ti_3C_2T_x$), as shown in **Fig. 3e**. **Fig. 3f** illustrates a cross-sectional SEM image of the compressed sample. After calendering, both $Ti_3C_2T_x$ layers present over 96 % reduction in thickness while the separator is compressed to around half of its original size. In the magnified SEM image (**Fig. 3g**), we can observe that the two materials are still well conjoint, with the main channels in the *h*BN-PVA layer still retaining its original alignment. In addition, **Fig. S2** illustrates a top cross-sectional view of the compressed separator. From a lower magnification (**Fig. S2a**), some *h*BN particles can be seen on the flat surface. Upon closer inspection of the PVA areas (**Fig. S2b**), we can observe the presence of some macropores and many micropores, with some of them anchored around the *h*BN flake. These porous structures facilitate electrolyte ion transportation in the electrode and separator. In this image, the previous structure of the $Ti_3C_2T_x$ layer appears to have collapsed, along with the macropores.

Despite this, we cannot conclusively determine that nano- and micropores generated from the freeze-casting process are lost. We consider this further with, XCT characterization and N_2 adsorption/desorption tests.

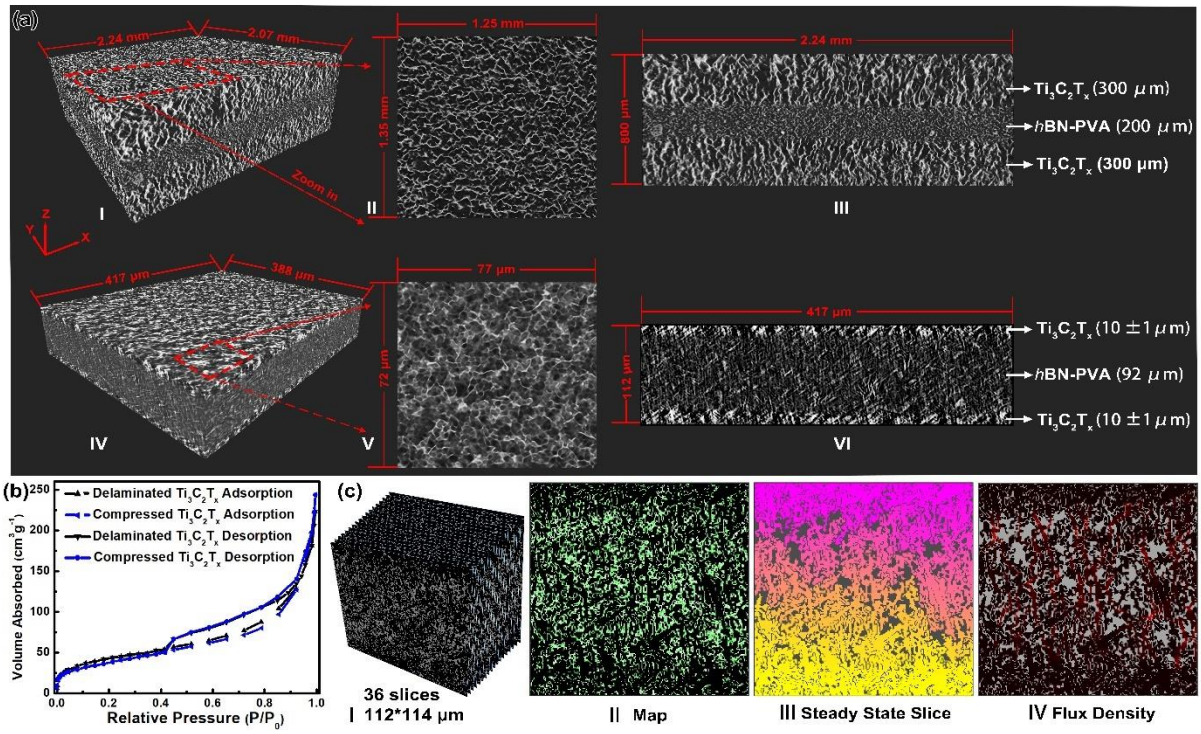

Figure 4 Volume rendering of THT with binary slices in the YZ and XZ planes. (a) I-III THT aerogels; IV-VI THT films. (b) N_2 adsorption and desorption isotherms of non-compressed delaminated $Ti_3C_2T_x$ (specific surface area (SSA) of 147 $m^2\ g^{-1}$) and compressed delaminated $Ti_3C_2T_x$ (SSA of 140 $m^2\ g^{-1}$). (c) Representative volume element (RVE) analysis for each of the separator samples showing that the full volumes of aerogel and film provide representative values for the tortuosity factors of the bulk materials.

Tomographic reconstruction of microstructures in electrochemical devices has become increasingly widespread, offering the possibility to evaluate vital parameters [35,36]. Therefore, the THT aerogel and film structures were imaged using X-ray computed tomography (XCT). The scans performed on the pre-compressed structure (**Fig. 4a I-III**) show vertical alignment within the two MXene layers. The parameters used to produce these structures yielded a porous aerogel structure with an average pore size of 79 ± 6.71 µm which was determined from SEM micrographs and top-down (XZ plane) view of tomography image (**Fig. 4a II**). XCT image of the THT film (**Fig. 4a IV-VI**) demonstrating that the majority of thickness dimensionality loss of the MXene layers after compression, is concordant with the SEM image (**Fig. 3f**). In the case of the separator layer, due to the density of the pre-calendered structure, densification

leads to a loss of roughly 50 % of the original height. Despite the extreme densification of the MXene layers, a further feature noticeable in the XCT of the film is that the pores within the MXene layers are vertically aligned with respect to the separator layer. The pore size decreases to 4.75 ± 1.04 µm. Despite the changes from macropore to micropores, mesoporous features seem unaffected. The specific surface area (SSA) of the THT film is 140 $m^2 g^{-1}$ measured using the N_2 absorption method (**Fig. 4b**). In comparison with the THT aerogel (147 $m^2 g^{-1}$), the SSA has not been affected significantly by reduced macropores from the calendering process. The pore-size distribution (**Fig. S3**) of the THT film averages at around 3.4 nm, which evidences the existence of the mesopores (2–50 nm). This high SSA value demonstrates the effective exfoliation of the MXene nanosheets in the porous film, which is consistent with TEM, XRD, and other results demonstrated above. Additionally, the effect of microstructural parameters on the performance of electrochemical devices has been evaluated by generating synthetic 3D volumes [37]. The purpose of this process is to directly evaluate the effect of specific geometric features such as porosity, pore size distribution, shape or packing orientation of $Ti_3C_2T_x$ and *h*BN-PVA on mass transport of electrolyte. In order to determine tortuosity, an image-based modelling approach was used. 3D rendered volume from XCT scans was processed to produce thresholded volumes representing the THT film's microstructure. From these renders, the objective was to determine the shortest path length through a porous structure by independently evaluating the geometric features. The volumes were meshed into elements which can be directly correlated to the size of a voxel (a 3D pixel in rendered volume), in this case 0.7 µm x 0.7 µm x 0.7 µm. Each element contains a corresponding dataset for the microstructural features within the voxel for the 3D rendering. Information from each element can be extracted to determine the tortuosity of the analysed phase. This computationally generated method for determining tortuosity is outlined by Cooper et al, who developed TauFactor [38], an open-source MATLAB application software package, for the characterisation of microstructural data. **Fig. 4c** summarises the report generated by TauFactor for a tortuosity factor calculation. For the THT film, TauFactor computed a tortuosity factor value of 2.62 ± 0.19. with a high pore volume of 76.2 ± 0.59 %. The tortuosity factor of the sample demonstrated a value comparable to commercial separators which is usually in the range of 2.5 – 6.9 [39]. A low tortuosity factor is favourable for high rate applications, where the resistance to ion transport is low [40]. The FATC approach could be contributing to the higher retained porosity post-calendering. As illustrated in the XCT images of the $Ti_3C_2T_x$, the porous characteristics is retained despite the densification of the pores, thus contributing to the low tortuosity factor.

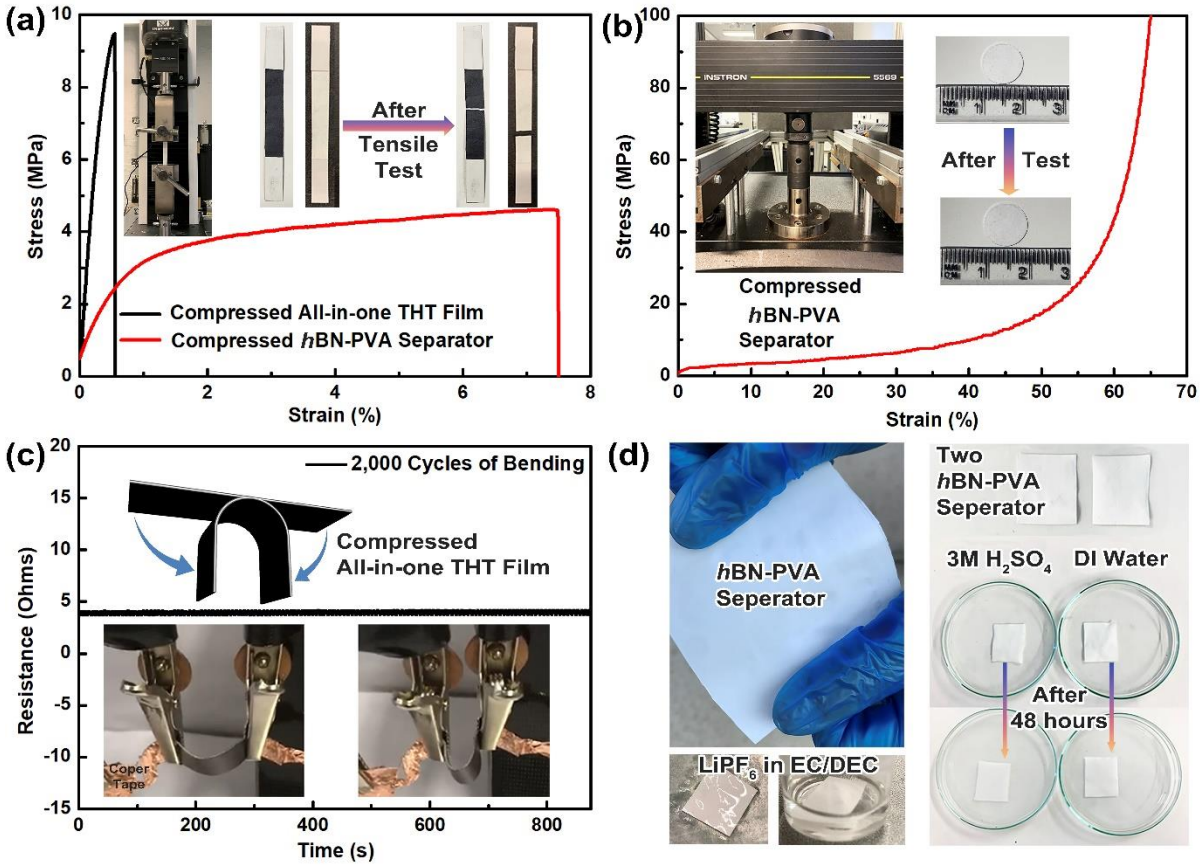

Figure 5 (a) Tensile-strength test for the compressed all-in-one THT sandwich film (110 μm) and compressed *h*BN/PVA separator (90 μm). Inserts are digital photos of the samples before and after the test. (b) Typical compressive stress-strain curve of the rolled *h*BN/PVA separator (90 μm). (c) Electrical resistance testing for the compressed all-in-one THT film. (d) Digital photos of the dry *h*BN/PVA separator, and wet ones in 3 M H_2SO_4 and $LiPF_6$ in ethylene carbonate (EC)/ diethyl carbonate (DEC).

The mechanical strength and flexibility of the THT film electrodes are crucial to their potential applications in wearable and portable energy storage devices. To demonstrate the suitability of THT films in these applications, the electrical and mechanical performance of the THT films were evaluated. As seen in literatures, PVA in 2D material composite films provide flexibility [41,42], and this is observed in the *h*BN-PVA separator in this work, which is able to impart flexibility and strength to the $Ti_3C_2T_x$ layers. **Fig. S4** demonstrates the flexibility of the THT film, as it is bent by roughly 180 degrees and rolled around a 10 mm diameter object. Tensile stress-strain curves for the THT films are shown in **Fig. 5a**. In contrast to a standalone *h*BN-PVA separator, the THT films exhibit significantly increased yield stress and stiffness. The strain at failure of the THT film decreased from 7.5 % to 0.4 %, which is attributed to strengthening of the structure from the addition of the $Ti_3C_2T_x$ layers. Furthermore, the tensile strength increased from 0.49 ± 0.01 GPa to 2.26 ± 0.03 GPa, as a result of the extensive

interfacial interactions between the rigid 2D nanomaterials and the polymer/*h*BN matrix layer. We infer hypothetically that these behaviours could be attributed to the addition of densified MXene layers. Due to the calendering process, there is a densification of meso- and macropores as seen in the XCT images in **Fig 4 II, V**. These smaller pores could be contributing to the increased stiffness. This is seen similarly with honeycomb structures, where the stiffness of the honeycomb structure is increased by increasing the density of the cell i.e. smaller cell size [43,44]. In addition, compressive forces from rolling of the $Ti_3C_2T_x$ would lead to the collapse of the lamellar channel structure. This collapse could manifest in the form of buckling or layering (similar to a domino mechanism) of the $Ti_3C_2T_x$ flakes that make up the channel walls. The crumpling and/or layering of the $Ti_3C_2T_x$ flakes could result in greater interactions between the flakes via van der Waals and hydrogen bonding from the terminal functional groups, cumulatively stiffening the structure.

The compressive mechanical properties of the produced samples were evaluated through in-plane compression tests. The samples were prepared by cutting seven equally sized cylindrical shaped pieces (diameter of 10 mm) using a punch from the compressed *h*BN-PVA film. They were then stacked to form a singular sample of 0.65 mm height. The results from the compression test are reported in **Fig. 5b**. The compressive curves of fabricated samples can be separated into three regions. A small linear elastic region is observed for strains below 5 %. In this region, the pore walls transitioned from an elastic regime to exhibiting more plasticity. An extended yield region follows the linear elastic region for applied strains of up to 40 %. This behaviour is associated with the gradual collapse of aerogel pores due to increasing strains [45]. The subsequent densification region appears for strains greater than 40 %.

THT film's durability is demonstrated by cyclic loading (quick succession of bending illustrated in **Fig. 5c**. The surface resistance is maintained ~ 4 Ω (including the resistance from the interface with copper tape) during the 2,000 cycles (within 900 s). The retention in operating functionality from a large bending curvature denotes that the network of $Ti_3C_2T_x$ flakes remains relatively intact. This shows, how the material developed in this work can be applied to flexible energy storage devices.

In addition to the *h*BN-PVA separator's mechanical properties in dry ambient conditions, the stability of the compressed *h*BN-PVA separator was also examined in inorganic and organic electrolytes. The left top image in **Fig. 5d** illustrates a digital photo of dry *h*BN-PVA separator. Despite crumpling the separator into a dense ball, it is able to recover its original shape with

minimal surface markings (**Fig. S5**). Subsequently, the *h*BN-PVA separator was cut into small rectangular pieces to evaluate its stability in 3 M H_2SO_4, as used in our work to test the electrochemical performance, and also in $LiPF_6$ in EC/DEC (Ethylene carbonate / Diethyl carbonate), which is a commonly used electrolyte in industry. After submerging the *h*BN-PVA in the electrolyte, it was rapidly infiltrated by the electrolyte ions, indicating good wettability of the separator in both the organic or inorganic electrolytes. As the separator is a composite of *h*BN and PVA, it benefits from the hydrophilicity of PVA and hydrophobic nature of *h*BN. Therefore, the *h*BN-PVA separator developed in this work establishes a strong potential for use in diverse energy storage applications.

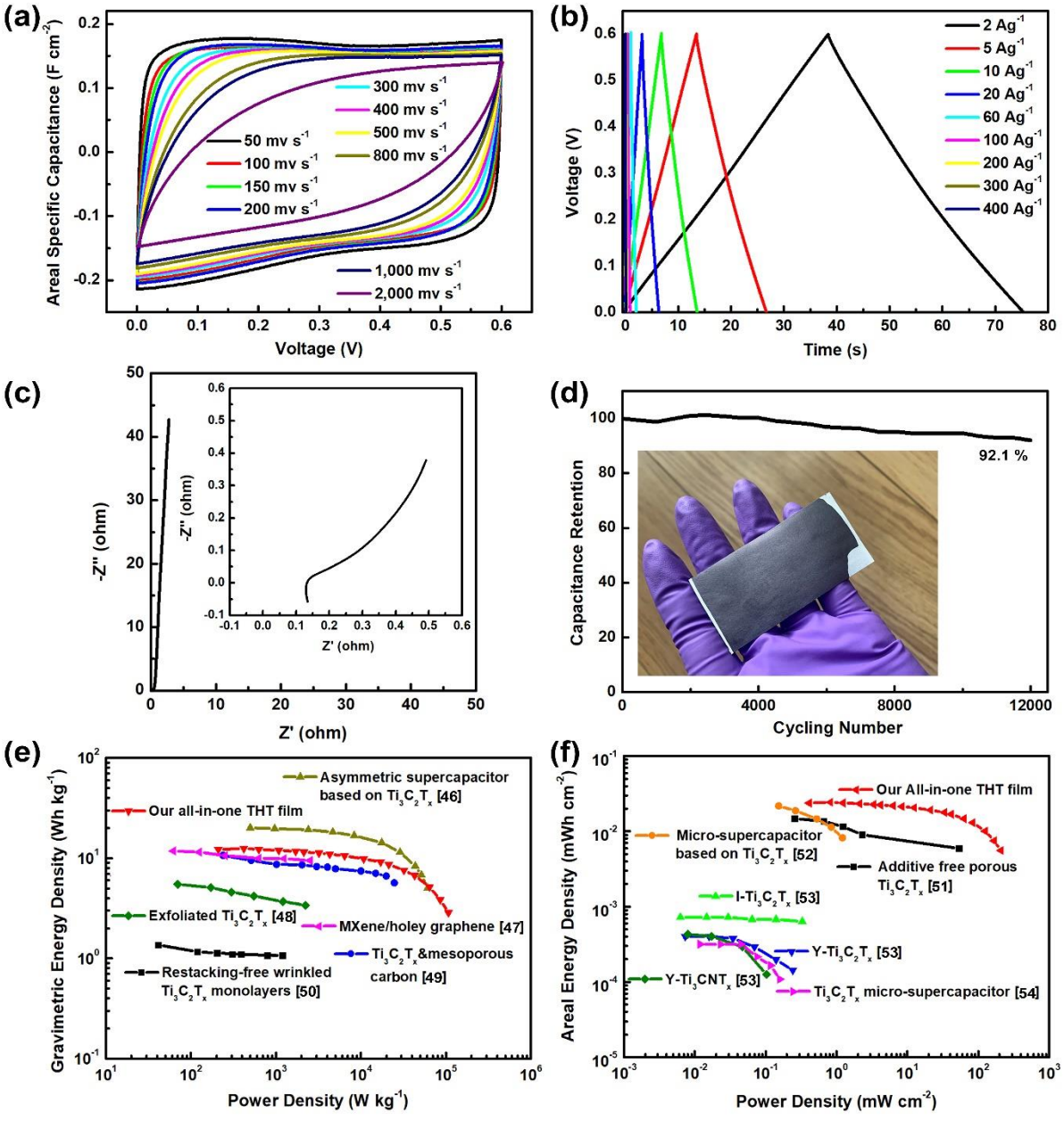

Figure 6 Electrochemical performance of the all-in-one THT film. a Cyclic voltammetry curves at a scan rate ranging from 50 mV s^{-1} to 2,000 mV s^{-1}. b Galvanostatic charge-discharge (GCD) profiles collected ranging from a current density of 2 A g^{-1} to 400 A g^{-1}. c Nyquist plots of electrochemical impedance spectroscopy (EIS) for the all-in-one THT film, tested at 0 V. d Cycling stability of one all-in-one THT film tested by galvanostatic cycling at a current density of 10 A g^{-1} showing over 92.1 % capacitance retention after 12,000 cycles. e and f depict the Ragone plots of the all-in-one THT sandwich cell together with other reported data for comparison: 6e [46–50], 6f [51–54].

To investigate the electrochemical performance of the integrated supercapacitor cell made of the compressed all-in-one THT composite film, we cut the film to small sandwich pieces (about 1.2 cm^2) with two $Ti_3C_2T_x$ layers as symmetric electrodes with *h*BN-PVA layer as the separator, and 3 M H_2SO_4 as the electrolyte for electrochemical testing. In the cell, the $Ti_3C_2T_x$ has a thickness of 10(± 1) μm while the *h*BN-PVA has a thickness of about 91(± 1) μm. **Fig. 6a** is the cyclic voltammetry (CV) curves of the all-in-one THT film at different scan rates. Gradually increasing the scan rate from 50 mV s^{-1} to 500 mV s^{-1}, there is almost no shape change of the rectangular curves, indicating good electrochemical double-layer capacitance, with a high areal specific capacitance of 0.20 F cm^{-2} at 50 mV s^{-1} and 0.16 F cm^{-2} (a retention of 80 %) at 500 mV s^{-1}. Up to 2,000 mV s^{-1}, the CV curve deforms a little but retains its rectangularity with a specific capacitance of 0.10 F cm^{-2}, indicating the integrated all-in-one THT film's good rate performance. Compared with the works that used commercial separator [25], this self-supporting supercapacitor with a pre-assembled *h*BN-PVA separator exhibits similar electrochemical performance. **Fig. 6b** shows the galvanostatic charge-discharge (GCD) tests of the integrated all-in-one THT film. The symmetrical triangular shape of the charge-discharge curves indicates the high coulombic efficiency of this supercapacitor cell. Further, there is no apparent IR drop (electrical potential difference, I: current, R: resistance) observed from the charge-discharge curves, which also implies low resistance of this all-in-one THT film. The kinetic feature of charge transport and ion diffusion were further analysed by electrochemical impedance spectroscopy (EIS). From **Fig. 6c** and the inset, the equivalent series resistance of the THT sandwich cell is around 0.137 Ω, which further confirms low resistance of the integrated all-in-one sandwich system due to the good electrical conductivity of the active material as well as the intimate contact between the electrode layers and separator layer. In addition, the almost vertical line and a phase angle of 86.3 degrees at the low-frequency region demonstrate a good capacitive response of this integrated all-in-one supercapacitor. Following this, the THT film's electrochemical cycling stability is also tested at a current density of 10 A g^{-1} with retention of 92.1 % after 12,000 continuous charge-

discharge cycles and 1,000 cycles of pre-activation (**Fig. 6d**). This indicates the high stability and reversibility of the supercapacitor based on an integrated all-in-one THT sandwich composite design. The Ragone plots in **Fig. 6e** and **6f** graphically demonstrate the gravimetric and areal energy densities against the THT sandwich film's power densities and the comparison with data in other works [46–54]. Our work exhibits a gravimetric energy density of 12.2 Wh kg^{-1} at a power density of 210 W kg^{-1}, and when the power density increases by 500 times to 105,000 W kg^{-1}, the energy density is at 2.95 Wh kg^{-1}. Meanwhile, a high areal power density of 209.2 mW cm^{-2} can be achieved at 700 mA cm^{-2} with an energy density of 5.6 μWh cm^{-2}.

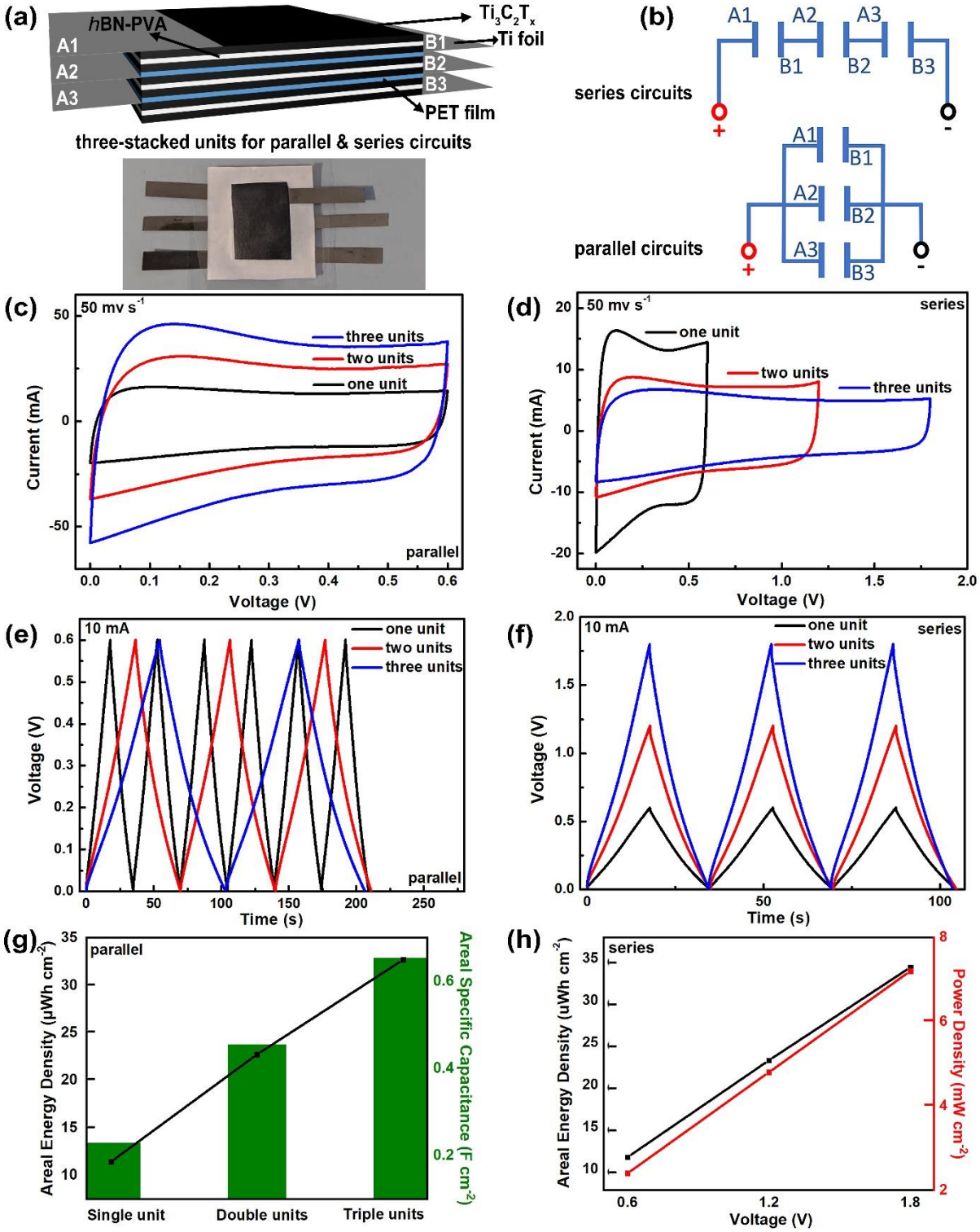

Figure 7. Electrochemical performance of stacked all-in-one THT units, every unit has the same weight of the single electrode of 2.5 mg and the same area of 1.25 cm^2. a Schematic (top) and the digital photo (down) illustrating the design of the stacked all-in-one THT cells. b Schematic diagram of the circuits obtained according to different connections between these electrodes. CV curves at a scan rate of 50 mV s^{-1} for one, c and d show two and three units in a parallel circuit and series circuit, respectively. GCD curves at a current of 10 mA for one, e and f show two and three units in a parallel circuit and series circuit, respectively. g The variation of the areal energy density and areal specific capacitance of

the parallel circuits with one, two and three units. h The variation of the areal energy density and areal power density with increasing potential windows (one, two and three units) in series circuits.

The electrochemical performance of THT cells comprised of multiple units connected in parallel or series was also investigated. All single electrodes have the same weight and area of 2.5 mg and 1.25 cm^2 respectively, with polyethylene terephthalate (PET) films used as separators in the middle of two units to avoid the electrolyte ion transfer. The schematic diagram and the digital photo of the THT cell made of three stacked units are shown in **Fig. 7a**. In order to connect and build specific circuits, titanium foil was used to connect the electrode. We have built circuits made of two and three single units connected in parallel and in series, respectively, as demonstrated in **Fig. 7b**. **Fig. 7c** and **7d** show the parallel and series circuits' CV curves comprised of two and three all-in-one THT units compared with the single unit at a scan rate of 50 mV s^{-1}, respectively. All the curves exhibit a near rectangular shape. In the parallel circuits, the current response increases with the number of the all-in-one units, while the cell's output voltage increases with the number of the units in series circuit configuration. Therefore, the output current or voltage can be effectively tuned using different connections according to specific requirements. Moreover, the GCD test of the corresponding devices was also performed and tested, as shown in **Fig. 7e** and **7f**. As expected, when a parallel circuit consisting of two/three THT films, the device's overall capacitance increases to double/triple times of that in a single unit. In the case of the series circuit (**Fig. 7f**), the voltage can be multiplied with the number of the units in series. The all-in-one THT film exhibits a potential to build efficient energy storage modules to fulfil future industrial requirements. Further, we also calculated the areal energy density and power density of this assembled device. In the parallel circuit, the areal specific capacitance and areal energy density increases, according to the number of units in the circuit (**Fig. 7g**). In terms of the series circuit, both areal energy density and power density show a linearly proportional increase with the amount of the single unit. Thus, this design can satisfy a diverse portfolio in the energy storage area, where parallel or series circuits can be constructed to reach a nominal voltage and capacitance for applications such as emergency power supplies, supporting the peak power density for industrial control, wind generation, transportation equipment.

5.5 Conclusion

This study explored the concept of integrating functional and structural properties of the materials composing the electrodes and separator for supercapacitors. Consequently, we demonstrated a novel manufacturing process to construct an all-in-one integrated electrode|separator|electrode system with $Ti_3C_2T_x$ and *h*BN-PVA as the active materials for electrode and separator, respectively. Freeze-assisted tape casting was employed to fabricate the all-in-one THT composite film. In this way, a highly porous structure with vertically aligned channels was constructed by the 2D flakes of $Ti_3C_2T_x$ and *h*BN-PVA formulation. SEM micrographs, XCT and SSA values demonstrate that even after calendering, the pores and channel structures are retained at the microscale. Furthermore, the THT films exhibited a relatively high stiffness with flexible character, enduring 2,000 bending cycles while maintaining a stable electrical conductivity level. This is an encouraging demonstration of its viability in use for flexible energy storage devices. Further supported by the electrochemical performance of the self-supported THT composite supercapacitor film which had comparable capacitance to a device that used a commercial separator. Arranging THT films into parallel and series configurations to increase the voltage window and areal power/energy density of the integrated supercapacitor, further substantiates the feasibility of these materials to be potentially implemented as commercial energy storage devices. The hope is that this novel and facile approach could offer new scalable solutions to building a new generation of energy storage devices.

Acknowledgements

This work was supported by the Henry Royce Institute for Advanced Materials, funded through EPSRC grants EP/R00661X/1, EP/S019367/1, EP/P025021/1 and EP/P025498/1. The authors would like to acknowledge the University of Manchester for the President's Doctoral Scholar Award. R.A.W.D. would like to thank EPSRC for funding through the grants EP/R023034/1 and EP/N032888/1. The authors also acknowledge the Henry Mosley X-ray Imaging Facility, especially Dr. Julia Benhson for the technical support, advice and assistance provided, and the Department of Materials X-ray Diffraction Suite at the University of Manchester. S.B. would like to thank Heilongjiang Huasheng Graphite Co. Ltd. for funding.

Received: 07-April-2021

Revised: 05-May-2021

Published online: 05-August-2021

Reference

[1] A. E. Ostfeld, A. M. Gaikwad, Y. Khan, A. C. Arias, *Sci. Rep.* **2016**, *6*, 26122.

[2] A. Pal, D. Goswami, R. V. Martinez, *Adv. Funct. Mater.* **2020**, *30*, 1906603.

[3] H. Tang, H. Feng, H. Wang, X. Wan, J. Liang, Y. Chen, *ACS Appl. Mater. Interfaces* **2019**, *11*, 25330.

[4] S. Xu, Y. Dall'Agnese, G. Wei, C. Zhang, Y. Gogotsi, W. Han, *Nano Energy* **2018**, *50*, 479.

[5] Y. Gao, C. Yan, H. Huang, T. Yang, G. Tian, D. Xiong, N. Chen, X. Chu, S. Zhong, W. Deng, Y. Fang, W. Yang, *Adv. Funct. Mater.* **2020**, *30*, 1909603.

[6] K. Wang, Z. Lou, L. Wang, L. Zhao, S. Zhao, D. Wang, W. Han, K. Jiang, G. Shen, *ACS Nano* **2019**, *13*, 9139.

[7] B. Ludwig, Z. Zheng, W. Shou, Y. Wang, H. Pan, *Sci. Rep.* **2016**, *6*, 23150.

[8] M. F. El-Kady, Y. Shao, R. B. Kaner, *Nat. Rev. Mater.* **2016**, *1*, 16033.

[9] Z. Lin, H. Shao, K. Xu, P.-L. Taberna, P. Simon, *Trends Chem.* **2020**, *2*, 654.

[10] M.-T. F. Rodrigues, K. Kalaga, H. Gullapalli, G. Babu, A. L. M. Reddy, P. M. Ajayan, *Adv. Energy Mater.* **2016**, *6*, 1600218.

[11] S. Byun, J. H. Kim, S. H. Song, M. Lee, J. J. Park, G. Lee, S. H. Hong, D. Lee, *Chem. Mater.* **2016**, *28*, 7750.

[12] E. P. Gilshteyn, D. Amanbayev, A. S. Anisimov, T. Kallio, A. G. Nasibulin, *Sci. Rep.* **2017**, *7*, 17449.

[13] N. Kostoglou, K. Polychronopoulou, C. Rebholz, *Vacuum* **2015**, *112*, 42.

[14] Q. Chi, Z. Gao, T. Zhang, C. Zhang, Y. Zhang, Q. Chen, X. Wang, Q. Lei, *ACS Sustain. Chem. Eng.* **2019**, *7*, 748.

[15] W. Huang, P. Wang, X. Liao, Y. Chen, J. Borovilas, T. Jin, A. Li, Q. Cheng, Y. Zhang, H. Zhai, A. Chitu, Z. Shan, Y. Yang, *Energy Storage Mater.* **2020**, *33*, 416.

[16] R. Reece, C. Lekakou, P. A. Smith, *ACS Appl. Mater. Interfaces* **2020**, *12*, 25683.

[17] S. Chen, L. Qiu, H.-M. Cheng, *Chem. Rev.* **2020**, *120*, 2811.

[18] S. Zheng, W. Lei, J. Qin, Z. S. Wu, F. Zhou, S. Wang, X. Shi, C. Sun, Y. Chen, X. Bao, *Energy Storage Mater.* **2018**, *10*, 24.

[19] Z. Li, S. Gadipelli, H. Li, C. A. Howard, D. J. L. Brett, P. R. Shearing, Z. Guo, I. P. Parkin, F. Li, *Nat. Energy* **2020**, *5*, 160.

[20] M. Naguib, M. Kurtoglu, V. Presser, J. Lu, J. Niu, M. Heon, L. Hultman, Y. Gogotsi, M. W. Barsoum, *Adv. Mater.* **2011**, *23*, 4248.

[21] M. R. Lukatskaya, S. Kota, Z. Lin, M.-Q. Zhao, N. Shpigel, M. D. Levi, J. Halim, P.-L. Taberna, M. W. Barsoum, P. Simon, Y. Gogotsi, *Nat. Energy* **2017**, *2*, 17105.

[22] H. Tang, Q. Hu, M. Zheng, Y. Chi, X. Qin, H. Pang, Q. Xu, *Prog. Nat. Sci. Mater. Int.* **2018**, *28*, 133.

[23] J. Yan, C. E. Ren, K. Maleski, C. B. Hatter, B. Anasori, P. Urbankowski, A. Sarycheva, Y. Gogotsi, *Adv. Funct. Mater.* **2017**, *27*, 1701264.

[24] Y. Wang, X. Wang, X. Li, Y. Bai, H. Xiao, Y. Liu, R. Liu, G. Yuan, *Adv. Funct. Mater.* **2019**, *29*,

1900326.

[25] W. Yang, J. J. Byun, J. Yang, F. P. Moissinac, Y. Peng, G. Tontini, R. A. W. Dryfe, S. Barg, *ENERGY Environ. Mater.* **2020**, *3*, 380.

[26] W. Yang, J. Yang, J. J. Byun, F. P. Moissinac, J. Xu, S. J. Haigh, M. Domingos, M. A. Bissett, R. A. W. Dryfe, S. Barg, *Adv. Mater.* **2019**, *31*, 1902725.

[27] Y. Wang, S. Su, L. Cai, B. Qiu, N. Wang, J. Xiong, C. Yang, X. Tao, Y. Chai, *Adv. Energy Mater.* **2019**, *9*, 1900037.

[28] L. Liu, B. Shen, D. Jiang, R. Guo, L. Kong, X. Yan, *Adv. Energy Mater.* **2016**, *6*, 1600763.

[29] L. Lim, Y. Liu, W. Liu, R. Tjandra, L. Rasenthiram, Z. Chen, A. Yu, *ACS Appl. Mater. Interfaces* **2017**, *9*, 39576.

[30] Y. Guo, K. Zheng, P. Wan, *Small* **2018**, *14*, 1704497.

[31] R. Tian, M. Breshears, D. V Horvath, J. N. Coleman, *ACS Nano* **2020**, *14*, 3129.

[32] A. Javaid, K. Ho, A. Bismarck, J. Steinke, M. Shaffer, E. Greenhalgh, *J. Compos. Mater.* **2018**, *52*, 3085.

[33] O. Kaipoldayev, Y. Mukhametkarimov, R. Nemkaeva, G. Baigarinova, M. Aitzhanov, A. Muradov, N. Guseinov, *Eurasian Chem. J.* **2017**, *19*, 197.

[34] S. Gates-Rector, T. Blanton, *Powder Diffr.* **2019**, *34*, 352.

[35] T. M. M. Heenan, C. Tan, J. Hack, D. J. L. Brett, P. R. Shearing, *Mater. Today* **2019**, *31*, 69.

[36] T. M. M. Heenan, D. P. Finegan, B. Tjaden, X. Lu, F. Iacoviello, J. Millichamp, D. J. L. Brett, P. R. Shearing, *Nano Energy* **2018**, *47*, 556.

[37] Q. Cai, C. S. Adjiman, N. P. Brandon, *Electrochim. Acta* **2011**, *56*, 5804.

[38] S. J. Cooper, A. Bertei, P. R. Shearing, J. A. Kilner, N. P. Brandon, *SoftwareX* **2016**, *5*, 203.

[39] J. Landesfeind, J. Hattendorff, A. Ehrl, W. A. Wall, H. A. Gasteiger, *J. Electrochem. Soc.* **2016**, *163*, A1373.

[40] T.-T. Nguyen, A. Demortière, B. Fleutot, B. Delobel, C. Delacourt, S. J. Cooper, *npj Comput. Mater.* **2020**, *6*, 123.

[41] G. A. Salvatore, N. Münzenrieder, C. Barraud, L. Petti, C. Zysset, L. Büthe, K. Ensslin, G. Tröster, *ACS Nano* **2013**, *7*, 8809.

[42] M. M. Rehman, G. U. Siddiqui, J. Z. Gul, S.-W. Kim, J. H. Lim, K. H. Choi, *Sci. Rep.* **2016**, *6*, 36195.

[43] T. Thomas, G. Tiwari, *Int. J. Crashworthiness* **2019**, *24*, 555.

[44] S. K. Sahu, N. D. Badgayan, S. Samanta, D. Sahu, P. S. R. Sreekanth, *Int. J. Mech. Sci.* **2018**, *148*, 284.

[45] A. Tripathi, G. N. Parsons, S. A. Khan, O. J. Rojas, *Sci. Rep.* **2018**, *8*, 2106.

[46] M. Boota, M. Rajesh, M. Bécuwe, *Mater. Today Energy* **2020**, *18*, 100532.

[47] Z. Fan, Y. Wang, Z. Xie, D. Wang, Y. Yuan, H. Kang, B. Su, Z. Cheng, Y. Liu, *Adv. Sci.* **2018**, *5*, 1800750.

[48] M. R. Lukatskaya, O. Mashtalir, C. E. Ren, Y. Dall'Agnese, P. Rozier, P. L. Taberna, M. Naguib, P. Simon, M. W. Barsoum, Y. Gogotsi, *Science (80-.).* **2013**, *341*, 1502.

[49] A. E. Allah, J. Wang, Y. V. Kaneti, T. Li, A. A. Farghali, M. H. Khedr, A. K. Nanjundan, B. Ding, H.

Dou, X. Zhang, B. Yoshio, Y. Yamauchi, *Nano Energy* **2019**, *65*, 103991.

[50] Y. Li, Y. Deng, J. Zhang, Y. Shen, X. Yang, W. Zhang, *J. Alloys Compd.* **2020**, *842*, 155985.

[51] Y. Yang, L. Wu, L. Li, S. Lin, L. Bai, X. Ma, Z. Shao, X. Zhang, *Chinese Chem. Lett.* **2020**, *31*, 1034.

[52] X. Feng, J. Ning, M. Xia, H. Guo, Y. Zhou, D. Wang, J. Zhang, Y. Hao, *Nanotechnology* **2021**, *32*, 035402.

[53] C. J. Zhang, M. P. Kremer, A. Seral-Ascaso, S. H. Park, N. McEvoy, B. Anasori, Y. Gogotsi, V. Nicolosi, *Adv. Funct. Mater.* **2018**, *28*, 1705506.

[54] C. (John) Zhang, L. McKeon, M. P. Kremer, S. H. Park, O. Ronan, A. Seral-Ascaso, S. Barwich, C. Coileáin, N. McEvoy, H. C. Nerl, B. Anasori, J. N. Coleman, Y. Gogotsi, V. Nicolosi, *Nat. Commun.* **2019**, *10*, 1.

[55] N. Fairley, "CasaXPS," **2019**.

5.6 Experimental Section

Preparation of delaminated $Ti_3C_2T_x$

This method is identical to our previous work [25] whereby Ti_3AlC_2 powder (Laizhou Kai Kai Ceramic Material Co. Ltd) is chemically exfoliated to synthesise $Ti_3C_2T_x$. 3 M equivalent of lithium fluoride (LiF, Alfa Aesar, 98.5 %) was dissolved in 60 mL prepared 9 M hydrochloric acid (HCl, Alfa Aesar, 36.5-38.0 %) at room temperature in a high-density polyethylene (HDPE) reaction vessel. 3 g of Ti_3AlC_2 powder was slowly added into the reaction mixture. The reaction was kept at 60 °C under magnetic stirring for 24 hours. The products were subject to centrifugation (Thermo Sorvall Legend XTR) at 3,500 rpm for 5 mins, to remove excess acid and salt (the decanted supernatant). The product was repeatedly washed with deionised (DI) water until the supernatant became viscous and black (an indication of delamination of $Ti_3C_2T_x$). From this point, the supernatant was collected from successive centrifuge cycles until the supernatant became transparent. The delaminated $Ti_3C_2T_x$ supernatant was concentrated and further washed by centrifuging at 10,000 rpm for 60 mins several times until the pH of the supernatant reaches 7. The resultant slurry underwent final mixing (SpeedMixer, DAC 250 SP) to obtain a homogeneous delaminated $Ti_3C_2T_x$ slurry.

Preparation of $Ti_3C_2T_x$ slurry and *h*BN-PVA slurry

The $Ti_3C_2T_x$ slurry concentration was adjusted by adding DI water and further mixing with the Speedmixer to prepare a $Ti_3C_2T_x$ slurry concentration of 65 mg mL^{-1}. The *h*BN-PVA slurry was prepared by adding 15 g of *h*BN (~1 μm, 98 %, Sigma Aldrich) to 10 wt% PVA (M_w 89,000-98,000, 99+% hydrolysed, Sigma Aldrich) aqueous suspension. The slurry was mixed with the Speedmixer and magnetically stirred for 2 days to obtain a homogeneous *h*BN-PVA slurry.

Preparation of all-in-one THT sandwich film and compressed all-in-one THT film

The THT sandwich films were manufactured using freeze-assisted tape casting (FaTC), which was introduced in our previous work [25]. The temperature of the cold plate is maintained at -25 °C using liquid nitrogen. An aluminium plate was used as the substrate upon which the films were formed. A doctored blade assembly (Micrometric Film Applicator, Elcometer UK) was used to control the thickness of each layer. The first layer of a thickness of 300 μm was formed by pulling the $Ti_3C_2T_x$ slurry with the doctored blade, along the pre-chilled aluminium substrate (-25 °C). Thereafter, a 200 μm thick layer was cast from the *h*BN-PVA slurry followed by a

300 μm thick $Ti_3C_2T_x$ layer. These three layers complete the sandwich structure. The frozen sandwich structure is lyophilised using a freeze dryer (Labconco FreeZone 4.5 L console). Once the composite film dries, it is removed from the aluminium substrate. The samples were compressed by passing them through a calendar machine (TMAX-JS-200, Xiamen Tmax Battery Equipments Limited). The gap between the rolling pins was set to 30 μm. The THT films, which were roughly 300 μm|200 μm|300 μm ($Ti_3C_2T_x$-*h*BN-PVA-$Ti_3C_2T_x$) thick, became about 114 μm in thickness, 9~11 μm|90~92 μm|9~11 μm ($Ti_3C_2T_x$-*h*BN-PVA-$Ti_3C_2T_x$).

Characterisation of structure and properties of delaminated $Ti_3C_2T_x$, *h*BN-PVA and non-compressed/compressed all-in-one THT sandwich films

Scanning electron microscopy (SEM) images were taken by Tescan Mira3 LC. $Ti_3C_2T_x$ samples were prepared by drop-casting a diluted $Ti_3C_2T_x$ suspension on a silicon wafer. Cross-sectional images were taken by investigating fracture surfaces of THT. TEM image was collected by FEI Talos F200X microscope with an acceleration voltage of 200 kV. TEM samples were prepared by drop-casting a $Ti_3C_2T_x$ suspension onto a copper grid covered by lacey carbon film. Raman spectroscopy (Confocal Raman Microscope, inVia, Renishaw, Gloucester-shire, U.K.) was used to record the Raman spectra of samples with a 532 nm excitation at a power of 1 mW and a 100X objective. X-ray Photoelectron Spectroscopy (XPS) was performed using an ESCA2SR spectrometer (ScientaOmicron GmbH) using monochromated Al Kα radiation (1486.6 eV, 20 mA emission at 300 W, 1 mm spot size) with a base vacuum pressure of ~1×10−9 mbar. Charge neutralisation was achieved using a low energy electron flood source (FS40A, PreVac). Binding energy scale calibration was performed using C-C in the C 1s photoelectron peak at 285 eV. Analysis and curve fitting was performed using Voigt-approximation peaks using CasaXPS [55]. Powder X-ray diffraction was undertaken using a Proto AXRD θ-2θ diffractometer (284 mm diameter circle) with sample spinner and Dectris Mythen 1K (5.01 ° active length) 1D-detector in Bragg-Brentano geometry employing a Copper Line Focus X-ray tube with Ni kβ absorber (0.02 mm; Kβ = 1.392250 Å) Kα radiation (Kα1=1.540598 Å, Kα2=1.544426 Å, Kα ratio 0.5, Kαav=1.541874 Å) at 600 W (30 kV, 20 mA). X-ray tomography (XCT) was performed using a Zeiss VersaXRM520. Imaging was performed at 60 keV with 100 ms exposure time, taking 1601 projections 180° around the sample. A 2560 x 2160 pixel (height x width) 10 μm pco.edge CCD camera was used to collect the X-ray projections, coupled to a 4x microscope objective giving an effective pixel size of 1.7 μm and a field-of-view of approximately 2.5 mm, and 20x objective giving an

effective pixel size of 0.7 μm and a field of view of approximately 500 μm. The sample to detector distance was 15 mm to allow some in-line phase contrast to enhance the visibility of the THT film layers. Reconstruction was performed using a filtered back projection algorithm, and visualisation was performed using Avizo software (Thermo Fisher Scientific).

The specific surface area and pore size were determined by using a Quadrasorb Evo, using the Brunauer–Emmett–Teller (BET) method for specific surface area and Barrett–Joyner–Halenda (BJH) method for pore size. To ensure the reliability of measurements, more than 75 mg of samples were tested. All samples were degassed for 24 hours under 0.01 mbar and at 433 K before the nitrogen adsorption. The nitrogen adsorption isotherms were performed at relative pressures (P/P_0) between 0.004 and 1 at a bath temperature of 77 K with 40 points for adsorption and 39 points for desorption.

The uniaxial tensile tests were conducted to characterise the mechanical properties of separator using an Instron 3344 fitted with a 100 N loading cell at The Material Testing Laboratory, The University of Manchester. The schematic of strip-shaped sample is shown in **Fig. S6**. The strip-shaped specimens were cut into 80 mm in length and 8 mm in width by Swann Mortan No. 10A Surgical Scalpel Blade and the distance between the two grippers was set to be 40 mm. Afterwards, the two sides of specimens were glued with printing papers to avoid any slippage during the tensile test and then mounted to the Instron grips. A constant prescribed crosshead velocity of 0.2 mm min^{-1} was applied. To ensure that the loading machine recorded sufficient data points, the data recording frequency of the Instron loading machine was set to be 10 Hz. Tests were repeated three times.

The compression testing was conducted on a universal testing machine with a 50 kN load cell (Instron 5569). The setting for the experiments is shown in **Fig. 5b**. The engineering strain is calculated from the relative displacement between two ends of the sample, which is obtained from the crosshead compression after the correction of machine compliance. To increase the accuracy of strain measurement, a stack of separators with 7 layers with a diameter 10 mm was set between the two platens. A pre-compression of 0.5 MPa was applied to remove the gaps between all the layers. A constant loading speed of 0.6 mm min^{-1} was applied, and the machine was automatically stopped when the loading increased to 100 MPa. Tests were repeated three times for this separator.

Microstructural data and modelling/simulation to determine tortuosity (tau factor) of THT film

A greyscale reconstructed volume was segmented into a binary image using a combination of thresholding based on pixel value, watershed algorithms, and background noise reduction. Voxels are then designated as either material or pore for the whole cylindrical volume of the scan. These binarized data sets were used for the various visualisations and extraction of parameters. The MATLAB code TauFactor [38] was used to predict the tortuosity factor on volumes in the XZ plane. TauFactor estimates the tortuosity of a phase by simulating Fickian diffusion and determining an effective diffusion coefficient. The apparent decrease in diffusive transport can be quantified using the Tortuosity factor. This results from the complexities of the flow path through a porous material. Tortuosity factor and tortuosity correspond to two different parameters but they both depict the geometry of the porous media. Tortuosity (τ) equals the ratio of the actual length of the flow path divided by the length of a straight line in the direction of flow. Tortuosity factor and tortuosity both increase proportionally with more tortuous pathways. If the cross-sectional area of the flow stays constant, tortuosity factor is equal to the square of tortuosity. Tortuosity factor and tortuosity tend to a value of 1 which corresponds to their minimal value if the flow path is direct. Values greater than 1 represents a more tortuous geometry which decrease the velocity of the diffusive transport.

A MATLAB application, "TauFactor" facilitates the calculation of the decrease in diffusive transport caused by the complex geometry of the "OREO" structure. It quantifies the tortuosity factor of interconnected porous phases in a three-dimensional volume along three mutually perpendicular axes. In this study, the tortuosity analysis has been carried out in the direction of the channels, i.e. through the layers of the sandwich structure. The XCT of the structures were used in conjunction with the TauFactor Application to quantify the tortuosity of permeable pathways. TauFactor carries out the tortuosity analysis by remapping the XCT voxels onto a set of discrete cuboid volume elements. Within each of these cuboids, the value of tortuosity is calculated using a system of linear equations which describes the relationship with its face-adjacent neighbouring voxels. In addition, Taufactor utilises the vectorisation method to optimise the simulation of the diffusion pathways (as illustrated in the **Fig.S7**)

Electrochemical testing

In order to investigate the electrochemical performance of the integrated all-in-one THT film and the parallel/series circuits made by the films, two-electrode symmetric systems were built with thin titanium plates as the electrically conductive lead to the external circuits. 3 M H_2SO_4 was used as the electrolyte. All the tests were carried out by a potentiostat (PGSTAT320N,

Metrohm Autolab) and a battery testing system (Basytec, Germany). In terms of the calculation of the capacitance, the specific areal capacitance C_{sa1} (F cm^{-2}) of the electrode was tested by CV curves and based on the following equation: $C_{sa1} = \frac{A}{SR*\triangle V*\mathrm{a}}$, where A is the integral areal of the CV plot, SR (mV s^{-1}) is the scan rate, $\triangle V$ (V) is the voltage change and a (cm^{-2}) is the area of one single electrode. The gravimetric capacitance C_{sg1} (F g^{-1}) obtained by GCD is calculated by the following equation: $C_{sg1} = \frac{2I*\triangle t}{\mathrm{m}*\triangle V}$, while I (A) represents the discharge current, $\triangle t$ (s) is the discharge duration. EIS curves were recorded by applying a sinusoidal potential with 5 mV amplitude under the frequency range of 10^5 Hz to 10^{-2} Hz. Charge-discharge cycling stability test was tested at a current density of 10 A g^{-1}. With regards to the Ragone plots, gravimetric energy density E_g (Wh kg^{-1}) and power density P_g (W kg^{-1}) of the single all-in-one THT film are based on the following equation: $E_g = \frac{C_{sg1}*\triangle V^2}{8\mathrm{m}*3.6}$ and $P_g = \frac{E}{\triangle t} * 3600$, while the areal energy density E_a (Wh cm^{-2}) and power density P_a (W cm^{-2}) is calculated by E_a=E_g*ML, $P_a = P_g$*ML, ML is the mass loading of these electrodes. With respect to the parallel/series stacked supercapacitor units, the capacitance C_x (F) of the whole pack is calculated by $C_x = \frac{I*\triangle t}{\triangle V}$ and the areal specific capacitance C_{sax} (F cm^{-2}) is calculated by GCD and the following equation $C_{sgx} = \frac{2I*\triangle t}{\mathrm{a}*\triangle V}$. The areal energy density E_{ax} (Wh cm^{-2}) and power density P_{ax} (W cm^{-2}) are based on the following equations: $E_g = \frac{C_x*\triangle V^2}{2a*3600}$ and $P_{ax} = \frac{E}{\triangle t} * 3600$.

5.7 Supplementary Information

Supplementary Figures

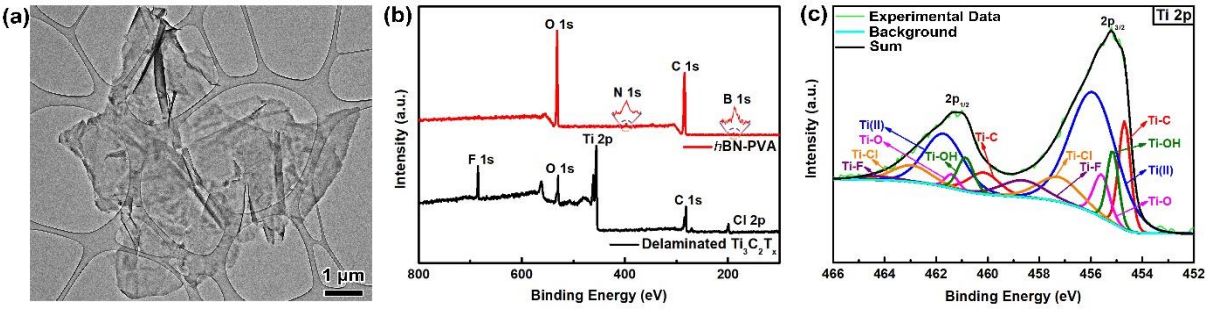

Figure S1 Transmission electron microscope of the delaminated $Ti_3C_2T_x$ (a), X-ray photoelectron spectroscopy spectra (b) of *h*BN-PVA and delaminated $Ti_3C_2T_x$, selected high resolution Ti 2p (c) of the delaminated $Ti_3C_2T_x$.

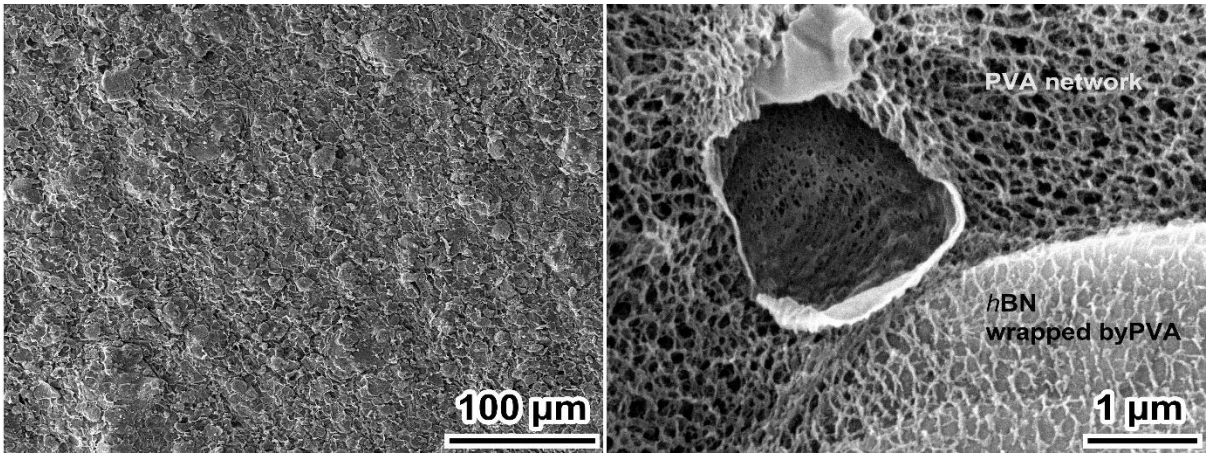

Figure S2 Top view SEM of the compressed *h*BN-PVA separator and high magnification SEM image of one area.

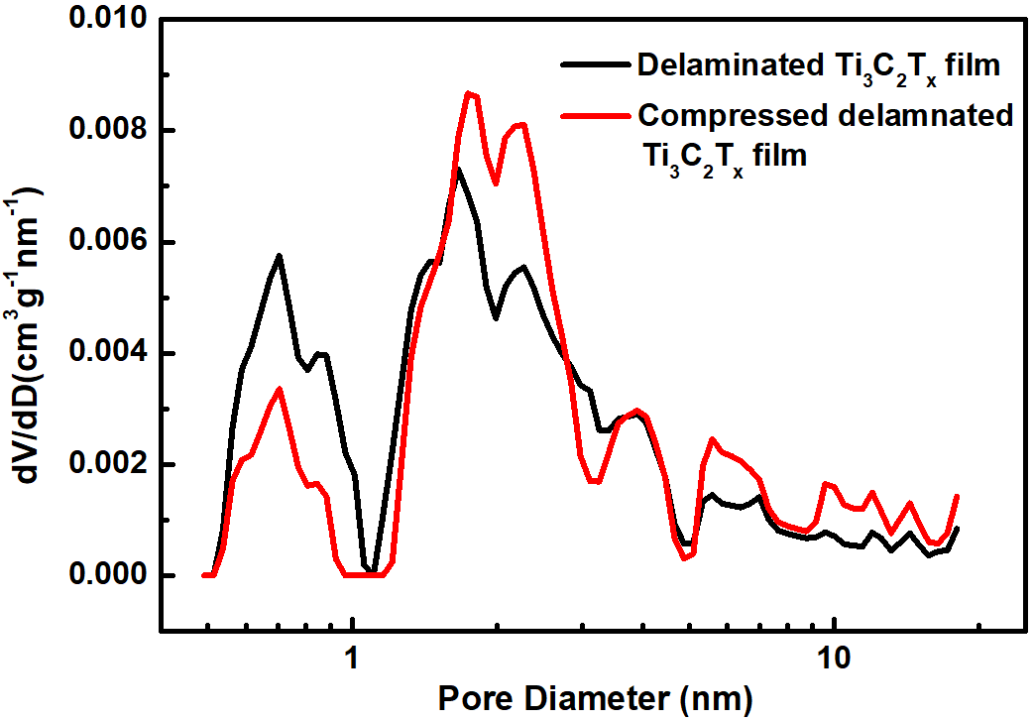

Figure S3 Pore size distribution of non-compressed delaminated $Ti_3C_2T_x$ (specific surface area (SSA) of 147 $m^2\ g^{-1}$) and compressed delaminated $Ti_3C_2T_x$ (SSA of 140 $m^2\ g^{-1}$).

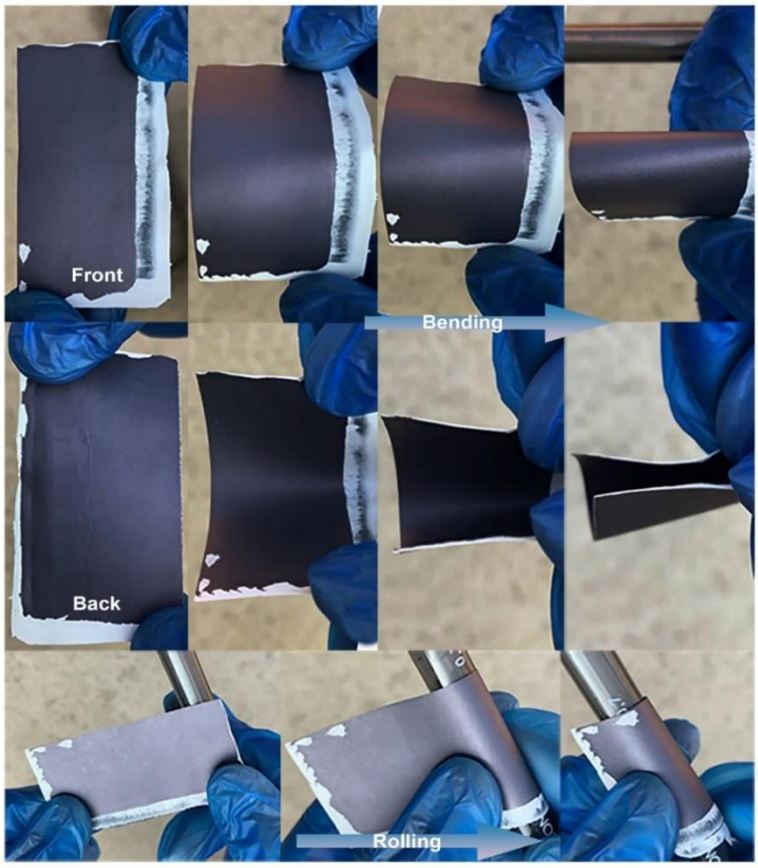

Figure S4 Digital photos of the compressed all-in-one THT film during bending and rolling processes.

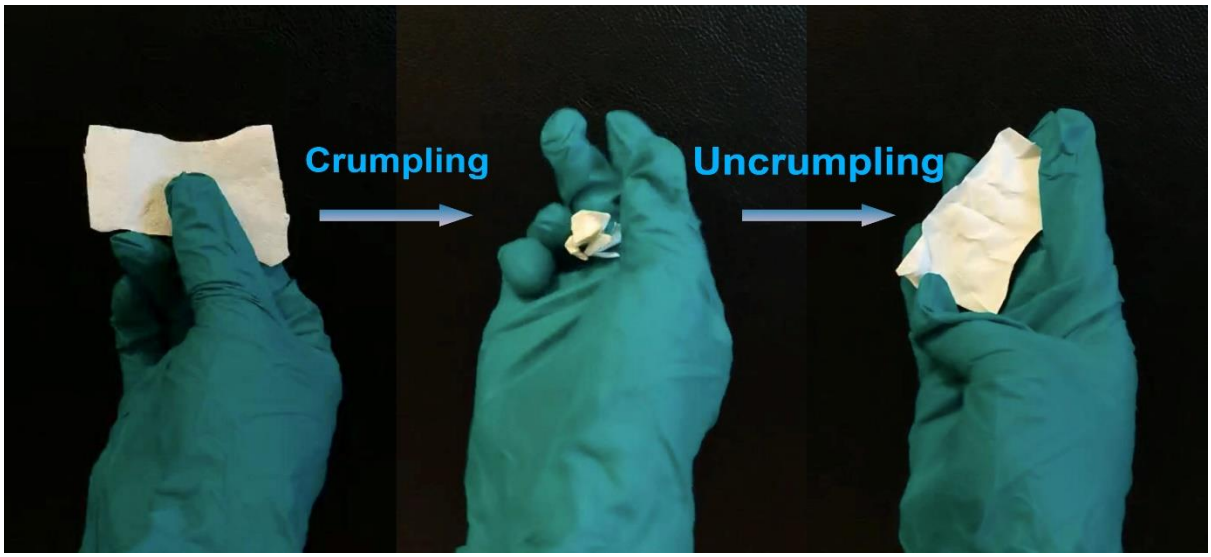

Figure S5 Digital photos of a flat *h*BN-PVA separator (a), a *h*BN-PVA ball after crumpling (b), uncrumpling it to plane (c).

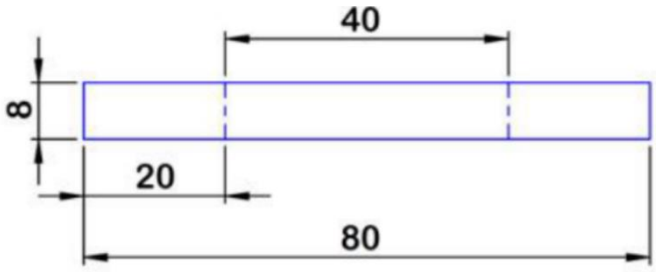

Figure S6 The schematic of the strip-shaped sample.

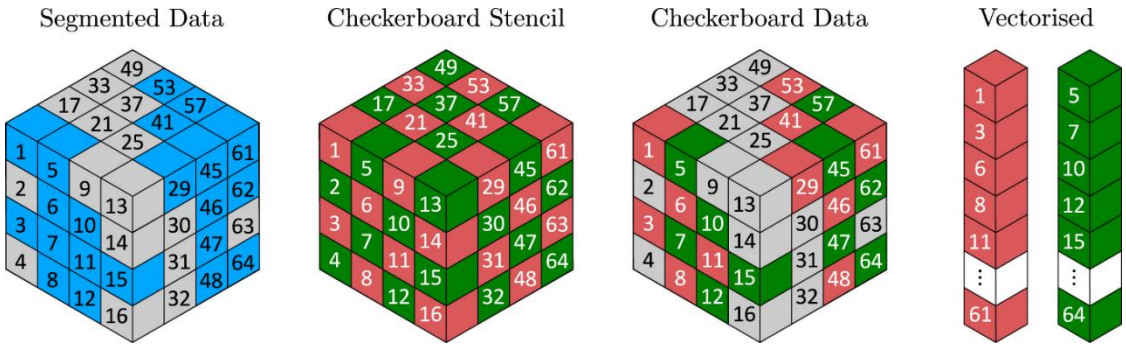

Figure S7 Schematic representation of converting 3D geometric data (where the blue voxels represent the conducting phase) into checkerboard adjusted vectors [1].

Reference

[1] S. J. Cooper, A. Bertei, P. R. Shearing, J. A. Kilner, N. P. Brandon, *SoftwareX* **2016**, *5*, 203.

Chapter 6. Final Conclusions and Perspectives

6.1 Conclusions

The two-dimensional material MXene, with superior thermal, optical, electrical, and electrochemical properties, shows promise to prominently influence various applications ranging from popular energy storage (supercapacitors, batteries), energy conversion, electronics, sensors, antennae (wireless communication), electromagnetic shielding, to capacitive deionization and biomedical engineering. From research and practical experimentation, we have determined that after exfoliation, restacking and re-agglomeration can occur, which impedes the ability of the 2D sheets to exhibit/exploit their outstanding physical, chemical, and optical properties. Therefore, exploring advanced manufacturing methods to construct devices with 3D structure from the 2D nanosheets is essential to achieve better functional performance. As a consequence, fundamental research of the materials is necessary to explore their suitability toward specific manufacturing processes. A significant effort has been put into investigating and improving the capability and versatility of MXenes to transition early laboratory research into practical solutions for commercial applications.

6.1.1 Synthesis of MXene ($Ti_3C_2T_x$ in this project)

In this work, delaminated $Ti_3C_2T_x$ was synthesised by the MILD method. In total, three different batches of the precursor Ti_3AlC_2 have been used. SEM images of all three batches are shown in **Fig. 6-1**. The first two batches were purchased from *Carbon Ukraine* (**Fig. 6-1a** and **b**), and the last batch (**Fig. 6-1c**) was ordered from *Laizhou Kai Kai Ceramic Material Co. Ltd*. The first batch was the one used in the first publication, and the third batch was used in both the second and third publications. The lateral flake size of three batches of MAX phases are ~9, 2 and 4 μm, respectively. After etching, the obtained few-layer $Ti_3C_2T_x$ flakes are roughly 8, 1.8 and 3.5 μm, respectively (shown in **Fig. 6-1d-f**). It can be concluded that the size of MXene flake correlates to the size of its precursor.

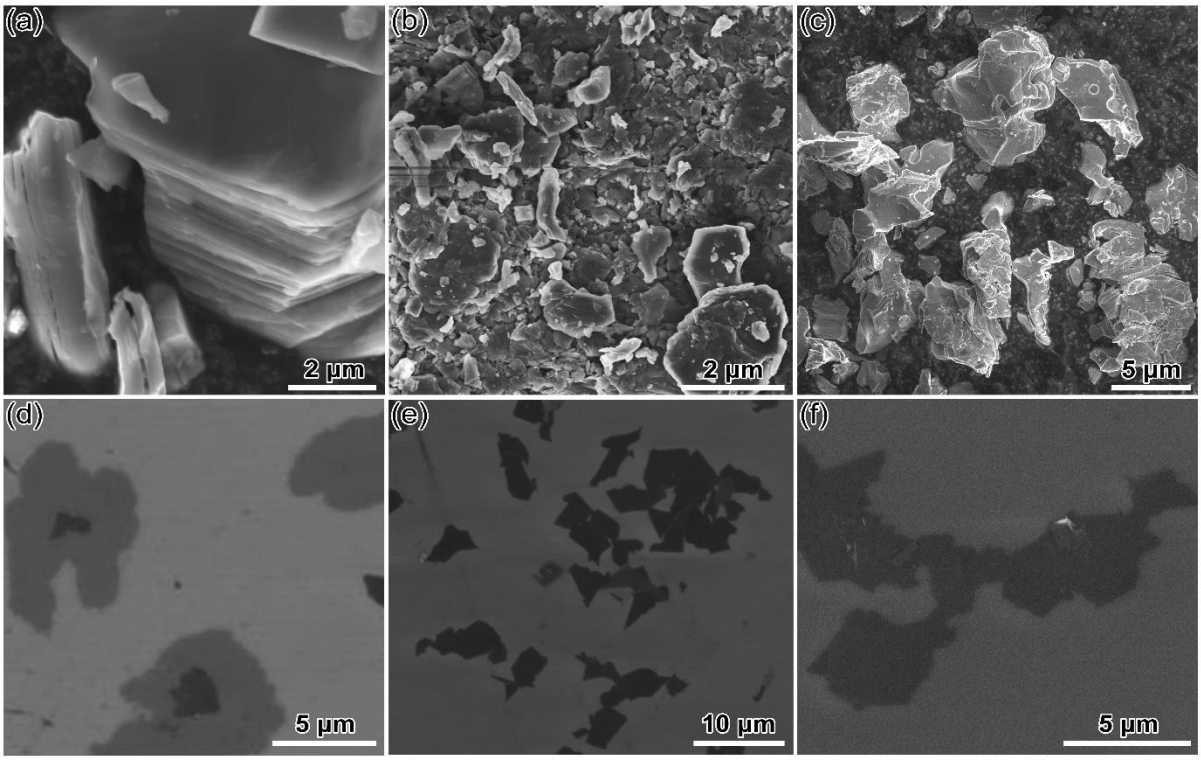

Figure 6- 1 SEM images of Ti_3AlC_2. (a) The first batch ordered from *Carbon Ukraine*. (b) The second batch ordered from Carbon Ukraine. (c) From *Laizhou Kai Kai Ceramic Material Co. Ltd*. (d-f) The SEM images of the $Ti_3C_2T_x$ after etching from the corresponding precursors in (a-c), respectively.

Before etching, the precursor MAX phase has to be ground to a smaller size (ranging from 200 mesh to 500 mesh). By selectively sieving, we can get specific flake sizes that we need. In this project, 400 mesh (roughly 37 µm) was used. In order to carry a comparative study, the Ti_3AlC_2 in the second batch was ground and sieved with 200, 300, 400 and 500 mesh. The SEM images of 200 mesh (roughly 67~75 µm) Ti_3AlC_2 powder are shown in **Fig. 6-2**. Generally (**Fig. 6-2a,b**), it seems that the size of the flakes is controlled well at around 67-75 µm. However, after choosing two flakes and increasing magnification to focus on a small area on the surface (**Fig. 6-2c,d**), we find that the big flakes are made of many small flakes with an average size of 2 µm. This is similar to what we observed from the 400 mesh samples (**Fig. 6-1b**). Consequently, we ascertain that the flake size of MAX phase cannot be fully isolated by the sieving process. It is hypothesized that the flake size of the precursor is controlled by the primary size of the flake. No matter how large the secondary particle is, after immersing it into the *in-situ* HF environment, they would be degraded to the primary nanoflakes with etching of the Al layer occurring concurrently. As shown in **Fig. 6-3**, secondary particles are made of primary particles, and with the addition of etchant, the secondary particle cracks and forms fractured secondary particles. After further time passes, fragmented secondary particles are obtained with Al

interlayer etched. Therefore, in order to control the flake size of MXene, we have to ensure we have the requisite primary particle size in the precursor and then use sieves to further select the size required.

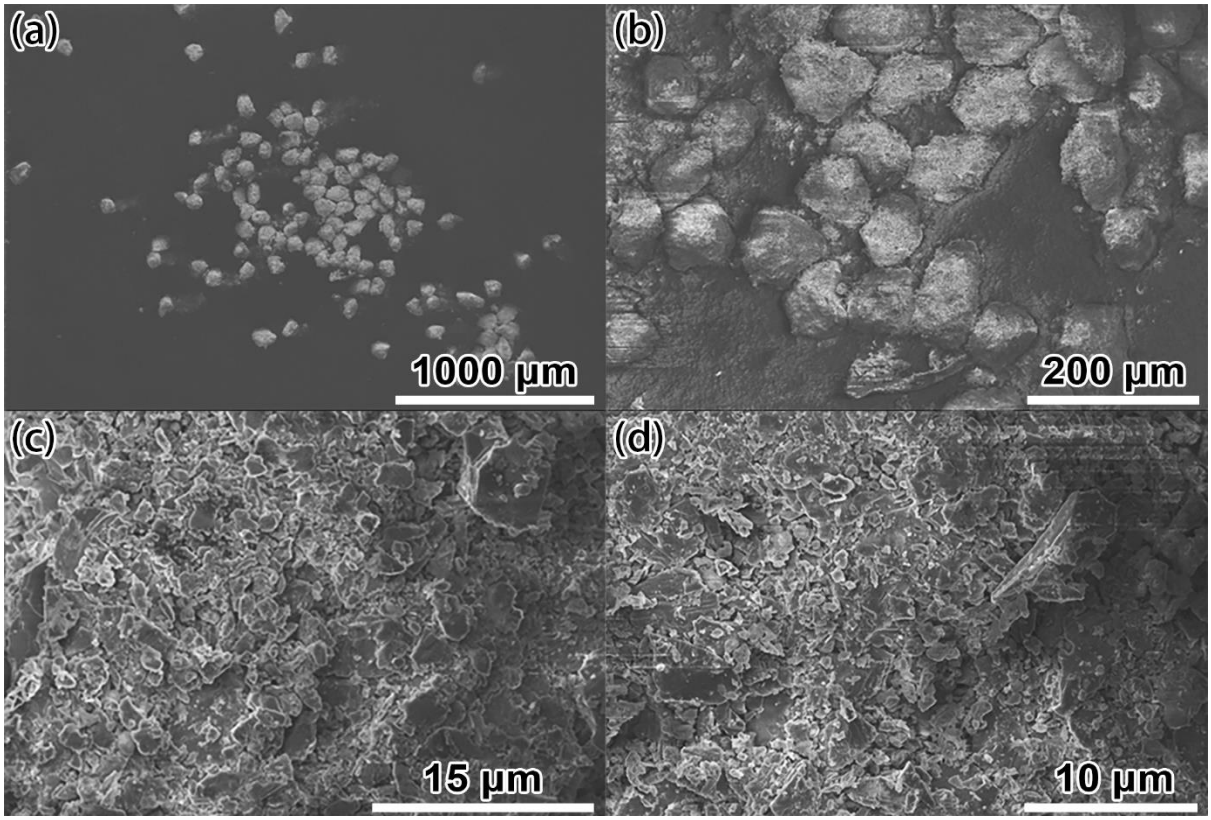

Figure 6- 2 SEM images of the Ti_3AlC_2 after selectively sieving by 200 mesh (67~75 μm).

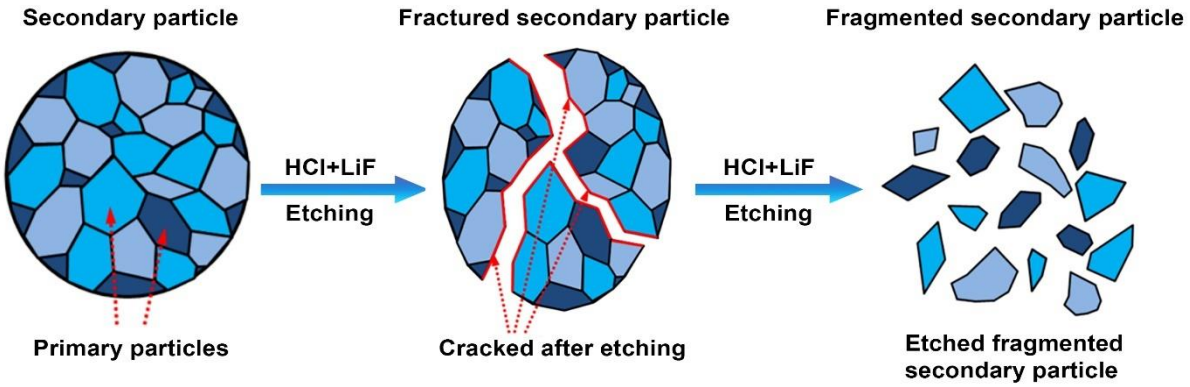

Figure 6- 3 Schematic illustration of the secondary Ti_3AlC_2 particles fragmented to primary flakes after etching enough time [1].

In addition to this, the quality of the precursor has a significant influence on the reaction conditions of the etching. For the first and second batches of Ti_3AlC_2 purchased from *Carbon Ukraine*, Al layers can be etched with the mass ratio of LiF:$Ti_3C_2T_x$:HCl = 2:3:6.6 at 30 ℃ for

24 hours. However, after purchasing the third batch from another company (*Laizhou Kai Kai Ceramic Material Co. Ltd.*), we were unable to etch and obtain the $Ti_3C_2T_x$ by the same experimental parameters used for the first two batches. After reading the literature and carrying out several trials, we eventually removed the Al layers by using a higher ratio of HCl and LiF, with an even higher temperature of 60 ℃. This may not solely be the optimum etching parameter for this batch of Ti_3AlC_2, but it can be concluded that the quality of the precursor has an effect on the etching parameters and ultimately on the characteristics of the resulting MXene.

Moreover, the etching temperature also has a big impact on the etching process. If the temperature is too low, the Al layers cannot be etched efficiently. **Fig. 6-4** shows that the SEM images of $Ti_3C_2T_x$ flakes etched from the first batch of MAX phase by normal (30 ℃) and high (45 ℃) temperatures are shown. It indicates that while the temperature is too high, the MAX phase flakes would be fragmented into small pieces, which also decreases the etching efficiency.

Hence, to have a consistent reaction product, comparable experiments and results, it is crucial to control the quality of precursor and experimental conditions used. The physical, chemical, thermal and rheological electrical performance of MXenes can be adjusted and optimized by choosing the proper precursor and manipulating parameters such as etching temperature, the ratio between reactants, etching duration, etc.

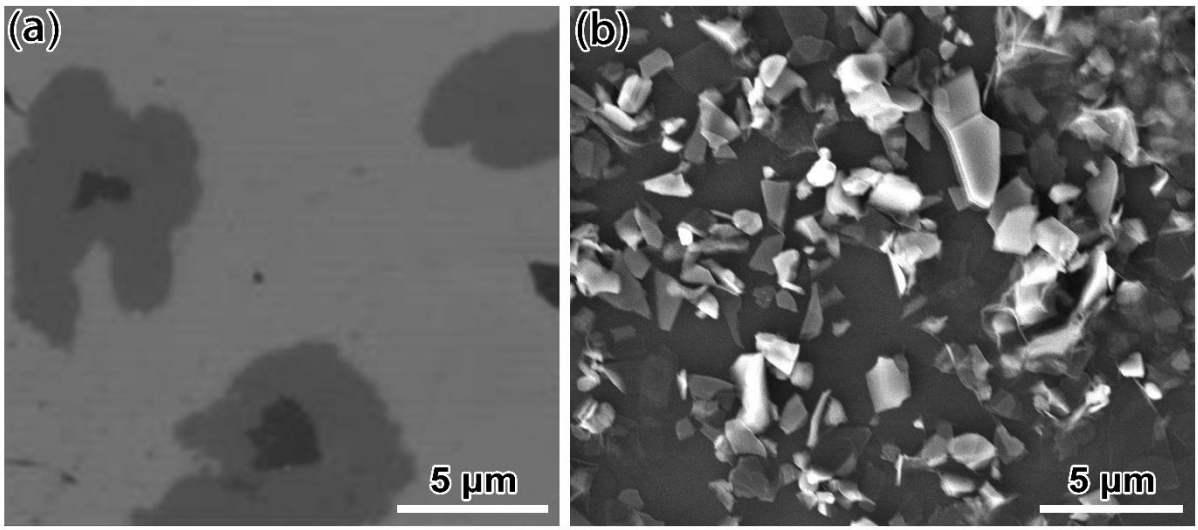

Figure 6- 4 SEM images of $Ti_3C_2T_x$ etched to form the first batch MAX phase at different temperature (a) 30 ℃, (b) 45 ℃.

6.1.2 Chemical stability of $Ti_3C_2T_x$

Due to the instability of MXenes in oxygen, water and warm atmospheres, they are supposed to be used when they are freshly synthesized. In this work, the $Ti_3C_2T_x$ inks and slurries in all three publications were used and tested when they were fresh with little oxidation, which can be supported by SEM, TEM, XRD and Raman characterizations. We performed a stability test by leaving $Ti_3C_2T_x$ slurries (from the third batch) in the fridge at 4 ℃ for five weeks in air and recording the changes by aqueous dispersibility and microstructure. In **Fig. 6-5a-d**, diluted $Ti_3C_2T_x$ suspensions were prepared by handshaking, using fresh $Ti_3C_2T_x$, 1-week after, 3-week after and five-week after, respectively. It was easy to disperse the fresh $Ti_3C_2T_x$ in DI water, and no particles can be seen in the suspension. Further, the SEM of the $Ti_3C_2T_x$ flakes does not show evidence of oxidation. After one week, the $Ti_3C_2T_x$ powder was comparatively harder to disperse but still can be dispersed with very small particles suspended. After three weeks, we can observe obvious large particles in the $Ti_3C_2T_x$ solution. In this case, even though the particles can be suspended for a few moments, they eventually sediment at the bottom after a few minutes. The sample after five weeks cannot be dispersed at all. After shaking, all the particles in the DI water sedimented immediately. There are also large differences between the SEM results of these four samples. After only one week, the sample's SEM results show not much difference compared with the fresh sample. However, after three weeks, obvious oxidative product can be found on the surface and edge of the flakes. In the last SEM image (**Fig. 6-5d**), it is found that the shape of the $Ti_3C_2T_x$ flakes has changed from having sharp edges to more smooth and diffuse edge with the average flakes size being smaller. In this case, we demonstrate that oxidation of the MXene degrades the microstructure of the original $Ti_3C_2T_x$ flakes and form another material (TiO_2) with new morphology (3D particles).

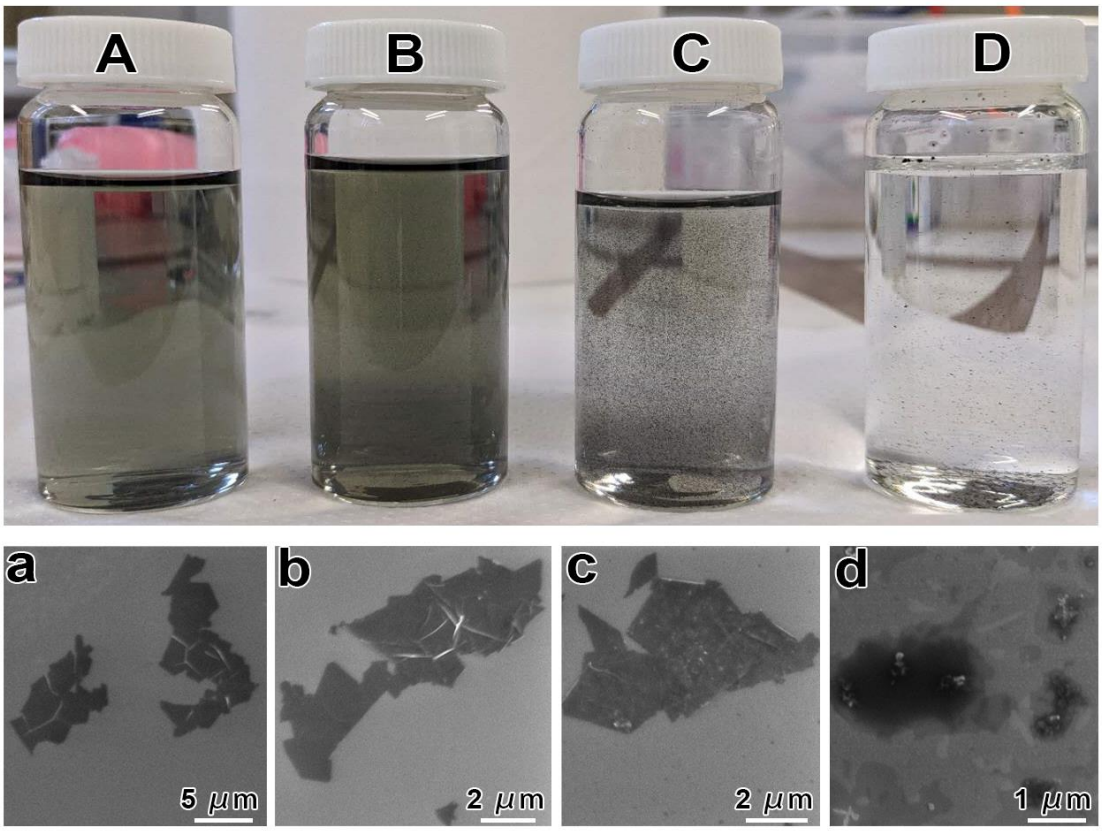

Figure 6- 5 Digital photos and SEM images of diluted $Ti_3C_2T_x$ solutions. A(a), B(b), C(c) and D(d) are the samples fresh, 1 week after, 3 weeks after and 5 weeks after, respectively, which were kept in the fridge at 4 ℃.

When we keep the MXene suspension in the fridge for over one month, we can see a layer of clear water (colourless) on the top of the ink. Therefore, we believe that the water is from the suspension and has been segregated for some reason. If kept for a longer time to half a year or one year, we can see this segregated water layer grows with an observable oxide layer on the top. Therefore, we believe during the exfoliation step of the multilayer $Ti_3C_2T_x$, large amounts of water have been intercalated into the layers of $Ti_3C_2T_x$ nanosheets and is trapped there. This also explains the swelling of the volume of $Ti_3C_2T_x$ slurry during this process, which is shown in **Fig. 6-6**. Besides, in order to disperse the exfoliated, water has another character: solvent. As shown in the **Fig. 6-7**, in a MXene based suspension/slurry/ink, it is assumed that water has two-character states in which it behaves as a solvent and the other in which it is intercalated. The former allows $Ti_3C_2T_x$ to remain well dispersed in the system, while the latter one contributes to the rheological performance of the ink. As shown in **Fig. 6-6**, each time more water is added, the water is initially separated from the initial slurry. However, after mixing them, the water intercalates into the 2D sheets and results in a homogeneous ink state. Due to

the poor stability of $Ti_3C_2T_x$ in water/air conditions, oxidation occurs, which breaks the microstructure and destabilizes the state of the intercalated water. Therefore, intercalated water is removed from the interlayer and 'transforms' to solvent water. This could explain why when the MXene ink is kept for a longer time, the ink appears waterier and the rheological performance decreases with an observed water layer and white layer on the top of the ink. In order to retain the consistency of the rheological properties of the ink in the experiment, we need to use the freshly synthesized MXene as fast as possible in case oxidation affects experimental variables and the results.

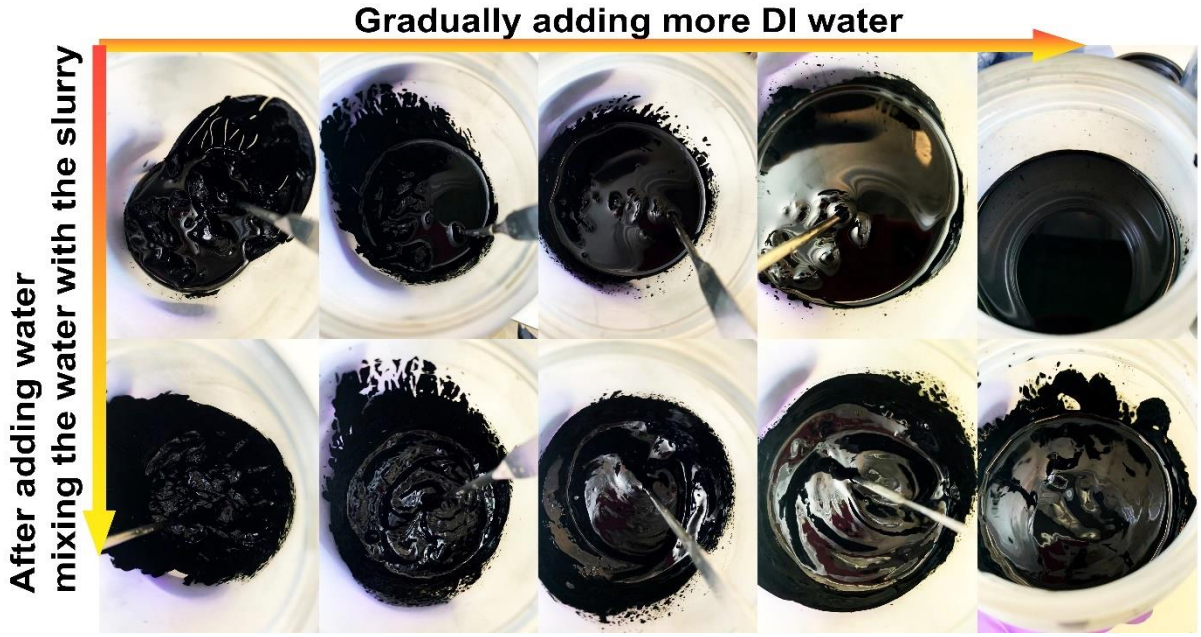

Figure 6- 6 Digital photos of the swelling of $Ti_3C_2T_x$ while adding more and more DI water.

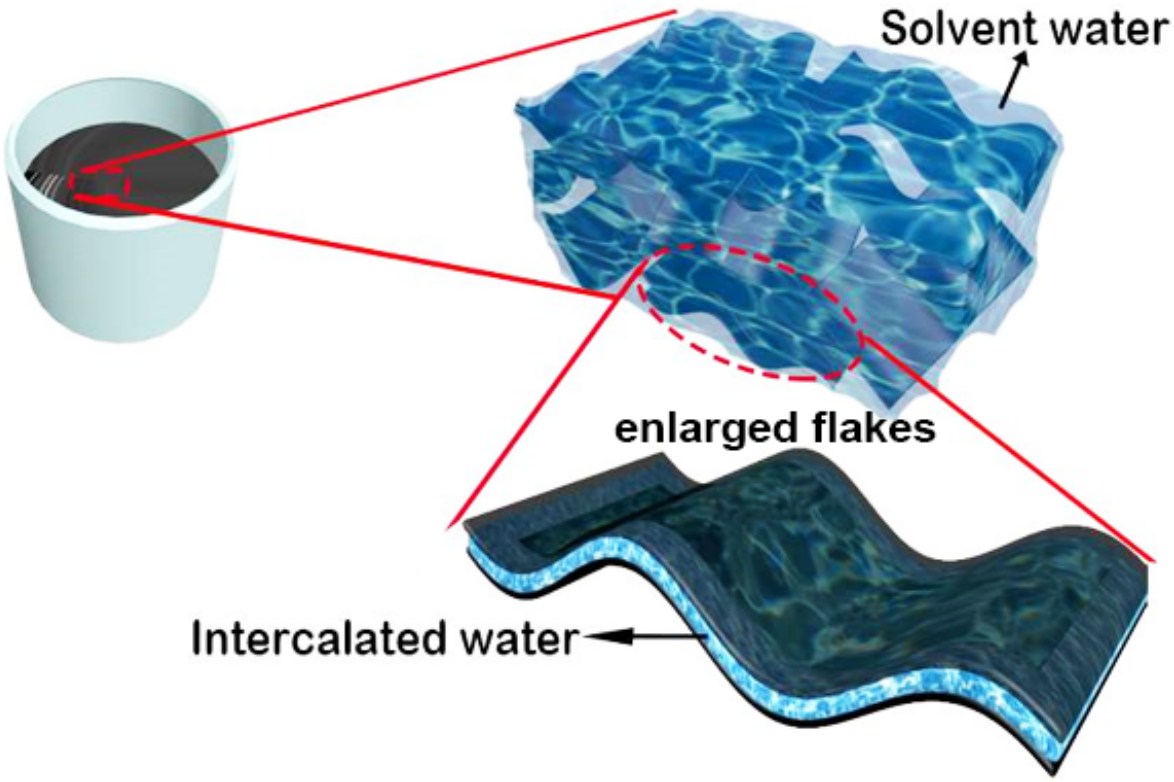

Figure 6- 7 Schematic illustration of the MXene suspension/slurry/ink.

6.1.3 Rheological properties of $Ti_3C_2T_x$

In this work, three different flake sizes of MXene were used to investigate their rheological performance. First of all, all the $Ti_3C_2T_x$ inks with different varying flake sizes and concentrations exhibit shear-thinning behaviour, which enables the inks can be spread on the substrate during manufacturing processes. Besides, inks' viscosity and viscoelasticity are highly related with the concentration of the slurries and also the flake sizes (**Fig. 6-8a-e**). In order to acquire similar rheological data, the concentrations of the inks needed are 15 mg mL^{-1}, 45 mg mL^{-1}, and 80 mg mL^{-1} while flake sizes of the 2D nanosheets are ~8 μm, ~3.5 μm and ~2 μm, respectively. When we increase the concentration of the inks, the same trend is still showing between the inks with different flake sizes. Afterwards, the rheological performance of $Ti_3C_2T_x$ ink was also recorded with the extension of storing duration. The measured viscosity as a function of *versus* shear rate for 300 mg mL^{-1} $Ti_3C_2T_x$ ink with flake size of ~2 μm was checked while it was fresh, and then after 2 months, and then 5 months. Although all the tests were using the same ink (same concentration) and all the lines, demonstrate the shear-thinning behaviour of the ink, but the ink with longer storing duration, the viscosity of the ink shows

decreased from the started slower shear rate to the faster shear rate compare with these shorter-time storing ones. Therefore, to keep the consistent results and products, the characterizations and experiments are better to be done when the MXene is still fresh.

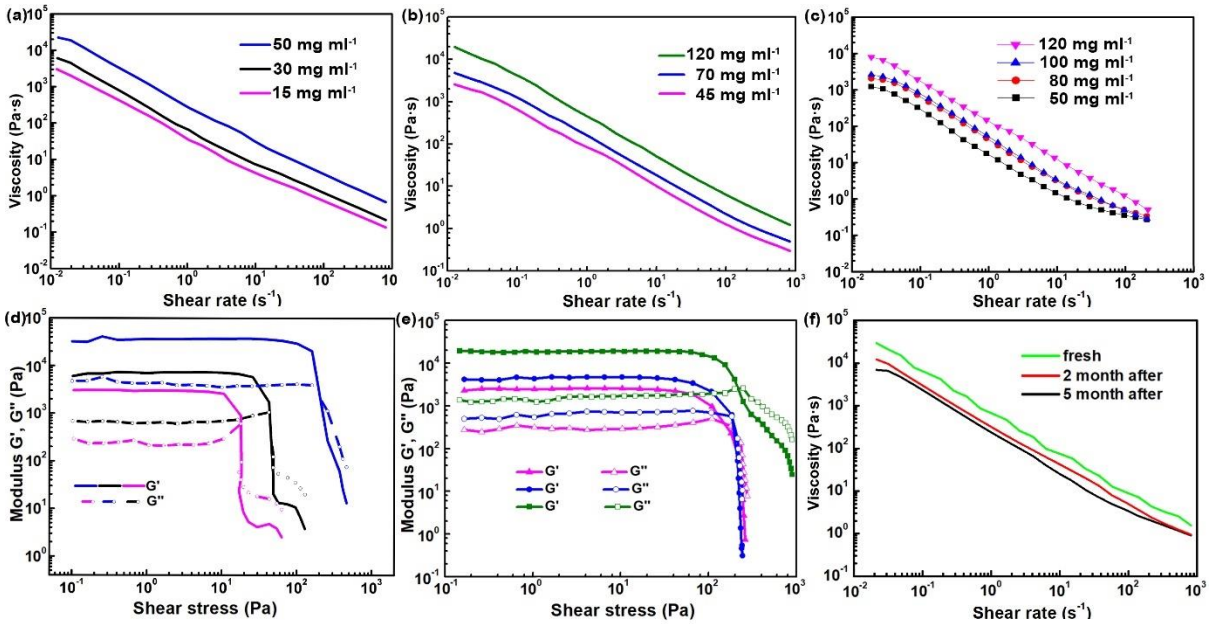

Figure 6- 8 Viscosity versus shear rate (shear thinning behaviour) of MXene inks of different concentrations (a) flake size of ~8 μm, (b) flake size of ~3.5 μm, (c) flake size of ~2 μm. Viscoelastic properties of MXene inks at different concentration: (d) flake size of ~8 μm, (e) flake size of ~3.5 μm. Viscosity versus shear rate of $Ti_3C_2T_x$ 300 mg mL^{-1} ink with flake of ~2 μm at different storing time.

6.1.4 Impact of the techniques while building the three-dimensional microstructure

In this work, 3D printing and freeze-assisted tape casting were used to manufacture the supercapacitor electrode. Both techniques are utilized to assist the construction of the electrode made of 2D nanosheets with three-dimensional microstructure. There is a necessary point to guarantee the 3D porous structure, which is freeze-drying. If, after printing or freeze casting, the slurries on the substrate, we just let it dry in the air or the oven, the 3D structure will not be kept due to the strong interfacial tension. Moreover, eventually, the structure will collapse not because of the viscoelasticity of the ink but the drying process. In addition, freezing methods also have a big influence on the microstructure. In the third chapter, we put the printed structure directly into the freezer or liquid CO_2 box, in which the coldness is from all directions. In this way, the ice crystals are forming from the out surface and extending to the inside. Since the

cold front is directly from all directions, the freezing behaviour in the inner part is difficult to determine. Thus, the microstructure of freeze cast structures built in this way would be non-directional. In the fourth and fifth chapters, the freeze-assisted technique was used during the tape casting process, meaning the sample is frozen immediately as during the casting process. In addition, the directionality of the cold front is controlled so that the ice crystals start to grow from the cold surface. This results in the ice crystal being vertically aligned, which in turn aligns the vertical alignment of the MXene material.

6.1.5 $Ti_3C_2T_x$ for supercapacitor

Although MXene has the potential to be utilized in numerous areas, this work is mainly focused on the energy storage application: supercapacitor. According to the data from this project and also those from others' work, $Ti_3C_2T_x$ based supercapacitor exhibits a capacitance of roughly 200-250 F g^{-1} in a symmetric two-electrode system. For $Ti_3C_2T_x$ this material, these factors: (1) high electrical conductivity; (2) abundant terminal groups on the surfaces and edges of the flakes; (3) hydrophilicity, make it a good candidate to be used in supercapacitor and be processed. Usually, the capacitance exerted in a supercapacitor has two main species: one is electrical double-layer capacitance while another one is pseudo-capacitance. For a $Ti_3C_2T_x$ based supercapacitor, the electrochemical behaviour during charging-discharging should include both mechanisms, and the majority of pseudo-capacitance from the redox reactions happen below 0 V potential. Therefore, when the symmetric two-electrode cell is used, which means a positive working potential range, electrical double-layer capacitance will be the main contributor. Consequently, building a three-dimensional dimensional microstructure is one of the most essential processes to increase the specific surface area of the two-dimensional nanosheets and then enhance the electrochemical performance of an energy storage device.

6.2 Perspectives and Future Work

This PhD has endeavoured to explore the synthesis and methods that mitigate the challenges in fabricating energy storage devices with 2D materials, in particular MXene. Along the way, we have elucidated the versatility of the material and potential advantages that might be gained from the investigated manufacturing methods.

However, as a supercapacitor electrode material, MXenes still has some limitations that need to be resolved. Besides the design of microscopic scale architectures to achieve sufficient

electrolyte infiltration and mass exchange to promote good rate performance and cycling stability of MXenes based supercapacitors, improving the conditions of the electrochemical reaction are also essential. As we all know, compared with batteries, supercapacitors have lower energy density but higher power density. In order to enhance the energy density of a supercapacitor, increasing the capacitance or expanding the voltage window are prerequisites. Currently, H_2SO_4 is the most common electrolyte used in $Ti_3C_2T_x$ based supercapacitors, but it limits the range of the potential window, consequently affecting the energy density of the device. Therefore, changing sulfuric acid to an organic electrolyte or liquid electrolyte becomes a potential solution. Zifeng et al. reached a voltage window of 3 V by using EMI-TFSI as the electrolyte, which increased to 2.4 V compared with the one using aqueous electrolyte (0.6 V). From BET results, the vertically aligned microstructure built by freeze-tape casting showed an average pore size distribution of the MXene electrode at around 3.4 nm, which is big enough for the EMI^+ and $TFSI^-$ ions (the longest dimensions of these ions are 0.76 and 0.79 nm, respectively) to transport in the inner structure while charging and discharging [2]. There is a limited number of studies in this field, thus, this might be an interesting and necessary route to investigate in the future. Despite this, the stability and oxidation mitigation of MXenes also need to be explored further. By using organic/ionic electrolyte, the oxidation problem can be somewhat resolved by sealing MXenes in anhydrous and inert atmospheres. In the previous work, researchers have been more focused on controlling the working environment / storage conditions for MXene. Undoubtedly, this is a good way to prevent the degradation of MXenes. However, looking at it from another perspective, metal is also easily corroded and oxidized in ambient conditions, and a common way to mitigate this is to form a coating layer outside the surface to insulate the metal from this atmosphere, which may cause deterioration. Since a high portion of metal atoms are exposed superficially on the MXenes, they easily react with the active species in ambient environments. Therefore, it also makes sense to treat MXene like a metal, and after finishing the preparation and assembly, a protective coating can be coated on the surface of MXenes. This is also an area that could potentially be studied.

Despite this, the research field is relatively new, and thus there are still a host of potential research investigations that could be expanded upon, leveraging on the discoveries from this PhD.

The primary focus of my investigations was on the $Ti_3C_2T_x$ MXene, which is definitively the most widely applied MXene due to its well-established synthesis route. A facet which I have not explored however, are the influence of the surface terminations as well as how different

chemistries i.e. different transition metals or coordination would influence the capacitive performance of the material or the manufacturing process. An example of this can be seen in the work by Jian Li et. al. in which they explored the influence of cation intercalation and surface modification on the pseudocapacitive behaviour of $Ti_3C_2T_x$ [3]. In addition to this, a review by Xiaobin Hui et. al. provides some insight on the interface chemistry of MXene based materials and how it might enhance the performance of energy storage and/or conversion devices [4]. Topics of specific interest in the review would be targeted surface termination regulation, surface defect engineering and in-situ modification strategies. Moreover, a topical review by Na Li and Jun Fan [5], provides an interesting computational perspective on modulating the performance of MXene based electrode materials for rechargeable batteries. A noteworthy topic that this review touches upon is how varying the composition of MXene might influence specific characteristics in battery performance (e.g. specific capacities, cycling stability, rate performance and so on). Hence, I can gather that there is still much more to explore concerning variations in MXene composition and surface moieties/features, especially on how these influences properties in the final application and potential manufacturing variables.

Besides further explorations on intrinsic and engineered material chemistry, an extension of this work could be to look at the development of asymmetric supercapacitors, which exhibits greater pseudocapacitive behaviour. Various strategies have been explored in employing MXene into asymmetric devices. For example, Qui Jiang et. al. [6], Yagyang Luo et. al. [7] and Kaixin et. al. [8], went the route of doping MXene with metal oxide/complex nanoparticles/quantum dots to create electrodes for asymmetric supercapacitors. The dopants were, ruthenium oxide, nickel-sulfide and FeOOH quantum dots respectively. Alternatively, Ruizheng Zhao et. al. [9] and Jayraj V. et. al. [10] developed nanosheet heterostructures with nickel-cobalt-aluminium layered double hydroxide and tungsten disulphide, respectively. These works are good examples of the versatility of MXenes in how they can be integrated into various asymmetric pseudo-capacitors with greater energy densities. Adapting some of the methods and principles developed in my work, I could develop enhanced devices with similar or greater specific capacitance and enhanced rate performance.

MXenes also have promising applications for batteries which have seen a meteoric increase in global demand within the last few years. An area of interest would be the application of MXenes in metallic lithium anodes, which is an inadvertent natural progression in the development of lithium-ion cells. The main inhibitor of metallic lithium adoption is dendritic

growth that occurs naturally as the cells age, or when operating at high current densities (rates). It can be seen in literature [11–13], that the adoption of parallelly aligned MXene layers or lamellar structures, are able to inhibit dendritic growth to a certain extent resulting in very stable cycling performance. The intrinsic electrical conductivity of MXene and surface chemistry (available nucleation sites) makes them an ideal additive to support the commercial transition to pure metal anodes. The structures formed in the respective works [11–13] bares resemblance to the microstructures attained in our work. Thus, an interesting extension of my current work would be to apply the as-formed freeze-tape casted MXene films into metallic lithium anodes in lithium-ion batteries and observe any potential performance benefits.

Next-generation lithium batteries with alternative chemistries, such as lithium-sulphur (Li-S) cells also see a need for more efficient materials and adaptive microstructures. This is due to the inherent challenges of the cell, especially with regards to the cathode in which electrical conductivity, polysulphide shuttling (loss of active material) as well as contraction/expansion during cycling are hurdles to fully commercializing this technology. Several groups have already researched MXene's application for Li-S cells [14–16], finding that not only does conductive and porous structures of MXene improve cycling and rate performance, but $Ti_3C_2T_x$ (and other MXenes) has the ability to anchor polysulphides (mitigate shuttling) and also serve as an electrocatalyst for Li_2S conversion [14]. This calls into question whether the highly porous and directional electrodes fabricated in our works, would make ideal sulphur-composite host electrodes for Li-S cells, to improve cycling stability and rate performance. Further, an interesting derivative of this research topic, would be in looking at 3D printing complex cell structures (anode, separator/electrolyte, and cathode) for Li-S cells out of MXene ink composites for flexible electronics or micro-energy storage devices. Some of this work is currently being investigated within our research group, with promising results.

Segueing from the potential electrocatalytic performance of MXene for Li-S cells, there is also some novel work into employing MXene for fuel cell applications [17–20]. MXene, on its own, or doped with low loading of homogeneously dispersed monoatomic platinum, has exhibited impressive stability and performance for hydrogen evolution. An interesting investigation would be studying how doped films/membranes developed in my work with platinum or alternative catalytic metal oxides might impact hydrogen evolution/oxygen reduction reactions to enhance the performance of fuel cells whilst reducing costs. A further niche area would also be studying the photocatalytic characteristics of MXene, as well as its stability (considering it

is prone to oxidation once synthesized) – our understanding and results from our work on MXene stability post-synthesis can be applied here, and further developed.

From my works, I have determined that there is still greater room for development in the field of 3D printing and freeze-tape casting. Additive manufacturing is a continuously developing field, and there are many novel innovations. For example, work done by Jennifer Lewis' group in which voxelated soft matter was printed via multi-material multi-nozzle 3D printing [21]. The ability to achieve unique regional/localised compositions opens up a range of possibilities in the advanced manufacturing of energy storage devices. For example, printing supercapacitor arrays with varying concentrations of MXene composite inks. Other works have also demonstrated the diverse geometries and configurations that multi-material printing is able to achieve in order to fabricate bespoke devices with novel properties [22–25]. This is something we can explore with MXene (composite) inks to investigate the material-structure-performance characteristics of electronically designed devices.

The last area that could be expanded upon from this work is the optimization of freeze-tape casting. As mentioned in **Chapters 4** and **5**, this manufacturing method can be easily adapted into a roll-to-roll manufacturing process. However, if this is the case, then the substrate on which the MXene colloid is cast on will have a constant horizontal velocity. This introduces a new variable in the process that can be used to control the templated microstructure. As mentioned in **Chapter 4** of this thesis (and can be seen in the results), orientation domains can and will form when manufacturing the film, which can lead to localized regions of characteristic performance. Introducing a horizontal velocity to the substrate and having a gradient temperature profile on the cold-bed could help form preferential domains to optimize the film performance. In addition to this, controlling the temperature profile depth (how cold it is and how steep the temperature gradient is) allows for further control over microstructural evolution. Furthermore, by adjusting colloid loadings (concentration), we would be able to observe variations in mechanical properties and electronic conductivity of the developed film, as well as determine the limit at which potential ice-lensing might occur for a MXene colloid (and to avoid this). These are some of the potential areas which we could investigate surrounding the freeze-tape casting process, in order to optimize it for a commercial manufacturing line. The potential areas of research that have been mentioned are just a few of a myriad of potential avenues for application development. There are other areas such as integrated electronics, sensors and biomedical devices that have not been specifically mentioned. This PhD has provided the author with insight into the world of 2D materials and

the developments in advanced manufacturing for next generation energy storage and functional devices. With so much more to discover and learn, it is an exciting time to be part of materials science research. There is little doubt that there is a long way to go in order to transition these novel discoveries into commercial products. However, with impetus garnered from observed climatic global events and socioeconomic policy changes, it might not be long before we see these materials and devices making tangible impacts on our daily lives.

Reference

[1] B. Song, T. Sui, S. Ying, L. Li, L. Lu, A. M. Korsunsky, *J. Mater. Chem. A* **2015**, *3*, 18171.

[2] L. Yu, G. Z. Chen, *Front. Chem.* **2019**, *7*, 1.

[3] J. Li, X. Yuan, C. Lin, Y. Yang, L. Xu, X. Du, J. Xie, J. Lin, J. Sun, *Adv. Energy Mater.* **2017**, *7*, 1602725.

[4] X. Hui, X. Ge, R. Zhao, Z. Li, L. Yin, *Adv. Funct. Mater.* **2020**, *30*, 1.

[5] N. Li, J. Fan, *Nanotechnology* **2021**, *32*, 252001.

[6] Q. Jiang, N. Kurra, M. Alhabeb, Y. Gogotsi, H. N. Alshareef, *Adv. Energy Mater.* **2018**, *8*, 1.

[7] Y. Luo, C. Yang, Y. Tian, Y. Tang, X. Yin, W. Que, *J. Power Sources* **2020**, *450*, 227694.

[8] K. Zhao, H. Wang, C. Zhu, S. Lin, Z. Xu, X. Zhang, *Electrochim. Acta* **2019**, *308*, 1.

[9] R. Zhao, M. Wang, D. Zhao, H. Li, C. Wang, L. Yin, *ACS Energy Lett.* **2018**, *3*, 132.

[10] J. V. Vaghasiya, C. C. Mayorga-Martinez, J. Vyskočil, Z. Sofer, M. Pumera, *Adv. Funct. Mater.* **2020**, *30*, 1.

[11] D. Zhang, S. Wang, B. Li, Y. Gong, S. Yang, *Adv. Mater.* **2019**, *31*, 6.

[12] B. Li, D. Zhang, Y. Liu, Y. Yu, S. Li, S. Yang, *Nano Energy* **2017**, *39*, 654.

[13] Z. Cao, Q. Zhu, S. Wang, D. Zhang, H. Chen, Z. Du, B. Li, S. Yang, *Adv. Funct. Mater.* **2020**, *30*, 1.

[14] D. Wang, F. Li, R. Lian, J. Xu, D. Kan, Y. Liu, G. Chen, Y. Gogotsi, Y. Wei, *ACS Nano* **2019**, *13*, 11078.

[15] X. Liang, A. Garsuch, L. F. Nazar, *Angew. Chemie* **2015**, *127*, 3979.

[16] W. Bao, L. Liu, C. Wang, S. Choi, D. Wang, G. Wang, *Adv. Energy Mater.* **2018**, *8*, 1.

[17] J. Zhang, Y. Zhao, X. Guo, C. Chen, C. L. Dong, R. S. Liu, C. P. Han, Y. Li, Y. Gogotsi, G. Wang, *Nat. Catal.* **2018**, *1*, 985.

[18] Z. Li, L. Yu, C. Milligan, T. Ma, L. Zhou, Y. Cui, Z. Qi, N. Libretto, B. Xu, J. Luo, E. Shi, Z. Wu, H. Xin, W. N. Delgass, J. T. Miller, Y. Wu, *Nat. Commun.* **2018**, *9*, 1.

[19] J. Ran, G. Gao, F. T. Li, T. Y. Ma, A. Du, S. Z. Qiao, *Nat. Commun.* **2017**, *8*, 1.

[20] T. Hou, Q. Luo, Q. Li, H. Zu, P. Cui, S. Chen, Y. Lin, J. Chen, X. Zheng, W. Zhu, S. Liang, J. Yang, L. Wang, *Nat. Commun.* **2020**, *11*, 1.

[21] M. A. Skylar-Scott, J. Mueller, C. W. Visser, J. A. Lewis, *Nature* **2019**, *575*, 330.

[22] D. Kokkinis, M. Schaffner, A. R. Studart, *Nat. Commun.* **2015**, *6*, 1.

[23] J. O. Hardin, T. J. Ober, A. D. Valentine, J. A. Lewis, *Adv. Mater.* **2015**, *27*, 3279.

[24] F. Meng, M. Zhang, J. Huang, W. F. Lu, J. M. Xue, H. Wang, *Adv. Funct. Mater.* **2021**, *31*, 1.

[25] J. Xue, L. Gao, X. Hu, K. Cao, W. Zhou, W. Wang, Y. Lu, *Nano-Micro Lett.* **2019**, *11*, 1.